



HAL
open science

The neural substrate of goal-directed locomotion in zebrafish and whole-brain functional imaging with two-photon light-sheet microscopy

Sébastien Wolf

► **To cite this version:**

Sébastien Wolf. The neural substrate of goal-directed locomotion in zebrafish and whole-brain functional imaging with two-photon light-sheet microscopy. Physics [physics]. Université Pierre et Marie Curie - Paris VI, 2017. English. NNT : 2017PA066468 . tel-01787017v1

HAL Id: tel-01787017

<https://theses.hal.science/tel-01787017v1>

Submitted on 7 May 2018 (v1), last revised 22 Oct 2018 (v2)

HAL is a multi-disciplinary open access archive for the deposit and dissemination of scientific research documents, whether they are published or not. The documents may come from teaching and research institutions in France or abroad, or from public or private research centers.

L'archive ouverte pluridisciplinaire **HAL**, est destinée au dépôt et à la diffusion de documents scientifiques de niveau recherche, publiés ou non, émanant des établissements d'enseignement et de recherche français ou étrangers, des laboratoires publics ou privés.

THESE DE DOCTORAT
DE L'UNIVERSITE PIERRE ET MARIE CURIE

Ecole Doctorale Physique en Ile de France

Présentée par
Sebastien Wolf

pour obtenir le grade de
DOCTEUR DE L'UNIVERSITE
PIERRE ET MARIE CURIE



**The neural substrate of goal-directed
locomotion in zebrafish**

**And Whole-brain functional imaging with two-photon
light-sheet microscopy**

Thèse de doctorat de Physique dirigée par Georges Debrégeas

Présentée et soutenue publiquement le 13 octobre 2017
devant un jury composé de:

M. Georges Debrégeas	Directeur de thèse
M. Ruben Portugues	Rapporteur
M. Stéphane Dieudonné	Rapporteur
Mme Cathie Ventalon	Examinatrice
Mme Claire Wyart	Examinatrice
M. Florian Engert	Examineur
M. Jean-François Allemand	Examineur
M. Vincent Hakim	Examineur

A mon enfant

Remerciements

En désordre. Je remercie l'école de la république pour toutes ces années de formation et pour la liberté qu'elle m'a donnée. Je remercie mes parents qui m'ont appris à penser et m'ont montré l'importance du savoir et surtout de la curiosité. Je remercie Noémie de m'avoir poussé à faire cette thèse et de m'avoir aimé toutes ces années. Je remercie mon frère Valentin, nos discussions sur la science. Je remercie tout particulièrement Georges pour la confiance qu'il m'a donné pendant ces années. Je le remercie de m'avoir appris ce que sont l'intuition, et le discernement face aux éléments donnés par les expériences. En bref je le remercie de m'avoir montré ce qu'était être un scientifique.

Je remercie les nombreuses personnes avec lesquelles j'ai pu collaborer pendant ces années de thèse à l'intérieur et à l'extérieure du laboratoire : Raphael, Emmanuel, Willy, Serguei, Jérôme, Alexis, Remi, Simona, Urs, Claire, Sophia, Tomaso, Guillaume, Maryam, Elim, Volker et Geoffrey. Je remercie tout particulièrement Carou, Stephane, Alex et Marie-Nicolle pour leur aide en tout point pendant ces années. Mention spécial à Raphaël O. et Nayelie les chefs de la 417 du LJP 1.0. Je remercie tous les membres du laboratoire Jean Perrin, en particulier Jerome R. pour l'accueil familial et les discussions autour de bières.

Je remercie tous mes amis et les Feu Antoine, Arthur, Clément et Raphaël qui m'ont soutenus sans le savoir lorsque je travaillais sur la route, dans le van ou les loges. Je remercie Maxime et Marlyse conseillers spéciaux dans les montagnes. Je remercie de l'autre côté des frontières Liane et Luizinho, ainsi que Claudine, mes cousin-es et mon filleul. Je remercie particulièrement Bastien et Indiana compagnons à jamais sur la route de cette thèse.

Table of Contents

Remerciements	5
Introduction.....	9
<i>A little personal story</i>	17
Chapter 1	19
Recording the living: an historical overview	19
1.1 Recording the living: a stammering	21
1.1.1 Electrophysiology.....	21
1.1.2 The development of microscopy	22
1.2 Fluorescence and calcium imaging	23
1.2.1 Origins of fluorescence discovery	23
1.2.2 The Green fluorescent protein	24
1.2.3 Calcium indicator	24
1.2.4 GCaMP	26
1.2.5 Limitations.....	28
1.3 Recording the living: Confocal microscopy	30
1.4 Recording the living: 2-photon microscopy	32
1.4.1 The origins.....	32
1.4.2 Struggling the theory	34
1.4.3 A new technique for imaging life.....	37
Chapter 2	41
Whole-brain functional imaging with two-photon light-sheet microscopy .	41
2.1 Recording the living: <i>Light sheet microscopy</i>	43
2.1.1 An old story revealed in the end of the XX th century.....	43
2.1.2 Modern history of light sheet fluorescence microscope.....	46
2.1.3 Resolution of a light-sheet: an analytical framework.....	50
2.2 Recording the living: 2-photon light sheet microscopy	54
2.2.1 The first 2-photon light sheet microscope	54
2.2.2 Comparison 1- and 2-photon light sheet	55
2.3 Imaging zebrafish brain	58
2.3.1 Zebrafish: a model animal for neuroscience	58
2.3.2 Imaging zebrafish brain.....	60
2.3.3 Light sheet imaging of zebrafish brain.....	60
2.2 The 2-photon Light-sheet microscope for zebrafish	64
Chapter 3	83
Principles of goal-directed navigation in motile animals	83
Followed by “Sensorimotor computation underlying phototaxis in zebrafish”	83
3.1 Introduction	87
3.2 Chemotaxis	90
3.2.1 Chemotaxis in <i>Escherichia coli</i> : the klinokinesis example	90
3.2.2 Chemotaxis in <i>Caenorhabditis elegans</i>	92
3.2.3 Chemotaxis in <i>Drosophila melanogaster</i> larva.....	93
3.3 Phototaxis	96
3.3.1 Phototaxis in prokaryotes and eukaryotes:	97
3.3.2 Eyes evolution and phototaxis.....	100

3.3.3	<i>Drosophila melanogaster</i> larvae phototaxis	104
3.3.4	Zebrafish (<i>Danio rerio</i>) larvae phototaxis.....	107
3.4	Sensorimotor computation underlying phototaxis in zebrafish	113
	Introduction	113
Chapter 4		187
Discussion on the neural basis of saccadic eye movements		187
Followed by a discussion on central pattern generator		187
4.1 Introduction		189
4.2 Brainstem/Hindbrain		191
4.2.1	Motor command	191
4.2.2	Premotor command in the brainstem.....	192
4.2.3	Other regions involved in the saccade-command signal	196
4.2.4	Eye-head coordination and gaze shift	200
4.3 The neural integrator		202
4.3.1	Persistent activity and STM	202
4.3.2	Modeling neural integrators: recurrent network models	203
4.3.3	Modeling neural integrators: single-cell approach	208
4.3.4	Zebrafish: new insights in the VPNI	208
4.4 Light-sheet imaging of the oculomotor system in zebrafish		211
4.4.1.	Long lead burst neuron in zebrafish	211
4.4.2.	Discussion on HBO	218
4.4.3.	Discussions on what we could get.....	220
4.5 Discussion on the HBO model: considerations on CPG for the future		222
4.5.1	Why is the circuit rhythmic/periodic?	222
4.5.2	What does determine the timings of the circuit?	225
4.5.3	Comments on possible improvement of HBO model	230
Chapter 5		233
Thermotaxis		233
5.1 Introduction		235
5.2 Thermotaxis in Invertebrates		236
5.2.1	<i>Caenorhabditis elegans</i>	236
5.2.2	<i>Drosophila melanogaster</i> larvae	240
5.2.3	Conclusion.....	244
5.3 Thermotaxis in vertebrates		245
5.3.1	Structure of thermosensation.....	245
5.4 Thermotaxis in zebrafish		248
5.5 Whole-brain imaging characterization of zebrafish heat sensation in zebrafish larva		253
5.5.1	Introduction	253
5.5.2 A heat stimulation apparatus for light-sheet imaging microscope		255
5.5.3	Whole brain imaging of heat-perception in zebrafish larvae	257
5.5.4	Hindbrain oscillator responds to heat stimulation in a phase-dependent manner	263
5.5.5	HBO can be entrained by periodic heat stimuli?.....	266
Conclusion		267
References		273
Annex 1		301
Annex 2		305

Introduction

Modern neuroscience

Neuroscience is undoubtedly one of the most challenging field of biology. The complexity of the brain resides in the huge number of neurons that it comprises, and the dense connectivity of the network that they collectively form (10^{11} neurons and 10^{15} connections in a human brain). From the single neuron physiology to the dynamics of large neuronal circuits, the precise understanding of each level of this structure demands knowledge from many fields, such as cell biology, physiology, computation, genetics or mathematics. Neuroscience also faces tremendous experimental challenges. Until recently, the lack of methods to measure the dynamics of more than a few neurons at once, deterred a detailed description of brain functions to emerge.

During the last decades, progress in genetics together combined with advances in microscopy has propelled neuroscience into a new age. In model animals, it is now possible to genetically encode, in targeted population of neurons, fluorescent molecules that have the ability to emit light with an intensity that varies with the activity of the neurons. Thanks to new optical methods, such as confocal, two-photon or light-sheet microscopy, it is now possible to observe the emitted fluorescence of large regions of the brain at a neuronal resolution. Such non-invasive monitoring of targeted neuronal populations opens a new arena to probe the structure and functioning of the brain.

One may argue that the history of neuroscience has always been the history of its techniques (Yuste 2015). For sure it is not so simple but let's avoid the "tunnel" and examine two paradigms in neuroscience. Cajal's neuron doctrine (Cajal 1988) was a natural consequence of the use of Golgi stain and microelectrode (Golgi 1873). Since the development of new optical and electrophysiological techniques together along with new computational tools, a novel paradigm has opened for neuroscience: neural networks. Neural network approaches assume that brain functions primarily arise from the concerted dynamics of groups or ensembles of neurons, rather than reflecting individual cell properties. Yet general principles of brain functions with the explanatory power to account for behavioral, cognitive states, or to explain mental pathologies, remain elusive with the neural doctrine. It is now widely acknowledged that neuronal networks approaches are the key to understand the emergence of complex cognitive functions. Again technical improvement was the guide leading to this new paradigm.

My research during these years of PhD started with the development of a new imaging tool, which opened a new window on a sensorimotor circuitry in zebrafish larva brain.

The first part of my PhD has been focused on technical developments.

During the last three decades, physicist and biologists have been struggling to find new techniques to image life and in particular the brain. The challenge they are facing could be put this way: how can we record the activity of a (1) specific section/volume of a living tissue (2) at high spatial, (3) high temporal resolution and (4) without damaging the tissue? These four requisites

are the key parameters to understand the short history of microscopy techniques for imaging living tissues like the brain.

In fluorescence microscopy, neurons are tagged with a calcium reporter such that if one shines an excitation light (at wavelength λ_e) onto them, the collected fluorescence signal (at wavelength λ_f) will be indicative of their activity. Thus, in order to respond to the first requisite and record the activity of a specific section/volume of the tissue, scientists use an objective to focus the excitation light on the neurons they want to probe in order to elicit a higher fluorescence from these neurons. However, a large residual fluorescence from the neurons laying above and below the targeted neurons remains, which blurs the recorded signal. A solution to this problem was proposed in the 1960's, that is now a standard technique in biology laboratories: *confocal microscopy*. The confocal microscope uses a pinhole to simply blocks the photons originating from outside the focal volume. Unfortunately, this technique fails in imaging deep in scattering tissues, e.g. the brain, and it requires a large amount of excitation light, which may damage the tissue. These limitations were overcome in 1990, with a new fluorescence imaging technique: *two-photon microscopy*. The so-called two-photon effect warrants that no significant fluorescence will be emitted outside of the focal volume, and because of its long wavelength illumination light ($2\lambda_e$), this imaging technique is a lot less damaging for living tissues and permits to image deeper (as scattering is weaker at longer wavelength).

Despite the high spatial resolution offered by confocal and two-photon microscopy, these two imaging techniques are limited in their temporal resolution. Indeed, these optical techniques are point-scanning microscopes: one needs to scan a small focal volume through the entire sample in order to image an entire specimen. In the years 2000's a third microscopy technique emerged: *light-sheet microscopy*. This method, adapted for transparent tissues, overcomes the temporal limitation of point-scanning techniques by using a thin sheet of light projected sideways onto the sample. The fluorescence of the entire illuminated plane is then collected at once onto the sensor of a camera. In order to image an entire specimen, one only needs to displace the light-sheet in one direction. Moreover, the localization of the excitatory illumination in the light-sheet itself minimizes photodamage.

When I joined the lab at the beginning of my PhD, Georges' group had just published an article describing how light-sheet fluorescence microscopy allowed fast volumetric imaging of the brain of a small vertebrate model: zebrafish larva (*Danio Rerio*). The performances of this new technique were stunning: it was possible to record the whole brain activity of a zebrafish larva (~100 000 neurons) at 0.7Hz at single-cell resolution. However, it suffered a strong limitation: in order to image the brain activity of a zebrafish larva, it was necessary to scan through the animal's brain with an intense blue beam, which strongly disturbs its behaviors. To overcome this visual disturbance while preserving a high temporal resolution, Georges thought to build a light-sheet microscope based on the two-photon effect. Since zebrafish larvae are blind to infrared light, the imaging system would not visually disturb the animal's behavior. Moreover, this system would benefit from the advantages associated with two-photon imaging in terms of penetration depth in the tissue and limitation of photodamage.

That was the objective of the first part of my PhD: to build a two-photon light-sheet microscope to image zebrafish brain activity.

The second part of my PhD has been focused on goal-directed navigation

In order to survive and thrive, organisms ranging from bacteria to humans have developed a myriad of behavioral strategies to find environments where they are more likely to find food, mates, or avoid predators. Many physical or chemical parameters of the environment can affect organisms' behavior such as light, temperature, food concentration, gravitational field, etc. The series of sensory-driven movements that lead towards specific regions of the environment are called taxis behaviors.. The driving stimuli can be light (phototaxis), temperature (thermotaxis), chemical concentration (chemotaxis), fluid flows (rheotaxis), etc. As we will see in chapters 3 and 5, these taxis behaviors can be precisely classified. Animals can actively (*taxis*) or indirectly (*kinesis*) change their orientation when they sense a stimulus change. Moreover, to probe the gradient of a specific stimulus, animals can use two distinct strategies: (i) a comparison of the sensory inputs between two receptors at different location on the animal's body (*tropotaxis*), or (ii) a comparison of the sensory inputs between a unique receptor at two different times of the animal displacement (*klinotaxis*).

During the last decades, phototaxis, thermotaxis and chemotaxis of *E. Coli*, *C. Elegans* and *D. melanogaster* larvae have been thoroughly studied from both behavioral and neuronal perspectives. These works laid the foundations for a global understanding of goal-directed navigation of living organisms. To summarize, *E. Coli* as well as *C. Elegans* navigational strategies are based on a two phases program alternating runs and turning events whereupon the animal randomly reorients itself. The rate of turning events is modulated by the increase or the decrease in intensity of the sensory signals perceived by the animal. Over multiple cycles the animals ends in the preferred region. These strategies are called biased random walks. *D. melanogaster* larvae also use a two phases program modulating the rate of turning events in function of the gradient of the stimuli. However, *D. melanogaster* larvae have the additional capacity to evaluate during the turning events the best direction of reorientation.

When I began the second part of my PhD, zebrafish larvae goal-directed navigation strategies were poorly understood: a few studies had addressed rheotaxis, a unique study existed on thermotaxis. Phototaxis was the only taxis that was precisely described from a behavioral viewpoint. Both tropo and klinotaxis had been shown to coexist in zebrafish and numerous behavioral models had been proposed to account for these complex coordinated motions. However, at that time, no data was available to understand how these behavioral strategies might be implemented at the circuit level in the zebrafish brain. Moreover, no neuronal model had been proposed to account for phototactic behavior.

This was the purpose of the second part of my PhD: to understand the neural basis underlying phototaxis in zebrafish. Using virtual-reality behavioral assays, light sheet functional imaging, optogenetic stimulation, and circuit modeling we demonstrated that a neuronal ensemble called the *hindbrain oscillator* plays a key role for phototaxis. This neuronal population has several properties: (i) it correlates with the gaze (eyes orientation) signal during

spontaneous reorientation of the zebrafish sight (*saccades*) and controls the orientation of successive swim-bouts, (ii) it displays a self sustained oscillating activity in eye-fixed configurations, and (iii) it is sensitive to visual stimuli such that its response to visual inputs varies with the motor context. This peculiar response to visual inputs yields a biased orientation of fish's trajectories towards brighter region: phototaxis.

Openings

Thermotaxis

In the last year of my PhD, we had led our studies on the hindbrain oscillator to a point where we knew that this central pattern generator-like circuit might play an important role for phototaxis. We had also built a simple rate model for this self-oscillatory circuit with inputs coming from visual centers. After a discussion with an editor, we realized that our model of the hindbrain oscillator and its integration of sensory inputs, leading to phototactic behavior, could be more general and may account for other taxis behavior. The reading one of the unique studies (Robson 2013) on thermotactic behavior in zebrafish confirmed our intuition. We thus decided to examine whether the hindbrain oscillator was responsive to heat stimulations, and could therefore be involved in zebrafish navigation toward region of preferred temperature (thermotaxis). I thus built with a graduate student, Guillaume Le Goc, a heat stimulation apparatus adaptable onto the light-sheet microscope and performed some heat-stimulation experiments that ended confirming our original hypothesis.

Global understanding of eye movements circuits in zebrafish

As mentioned above, this hindbrain oscillator has two main properties: it correlates with the gaze signal during spontaneous reorientation of the zebrafish sight (*saccades*) and displays a self-sustained oscillating activity. The first property means that this neuronal ensemble belongs to the oculomotor circuit of zebrafish and the data I collected to identify the HBO may also be useful to dissect the neural circuits controlling zebrafish eye movements. In mammals such as human-primates or cat, neuroscientists have reached an advanced understanding of the anatomy of the brainstem circuits controlling eye movements. However, because of technical issues, they could never monitor the entire circuit at once and thus build a detailed correlation-based model of the neural control of eye movements. We thus thought to exploit our whole brain datasets to examine the homology between zebrafish's hindbrain neural control of eye-movements and the brainstem circuits in mammals. Then we thought that the ability to evaluate the correlations between all the neurons in the eye-movements circuits could help to shed light on some theoretical debates in the eye-movement field.

Other projects

During my years of PhD, I participated in other projects, for which I was not the principal investigator (i.e. not the first author). Here are three of them that "worked".

Blind sparse deconvolution

Jerome Tubiana, a former intern in the lab, now a graduate student in the theoretical physics lab of the ENS, developed with us a spiking inference algorithm to extract the spiking activity from fluorescence signals. Based on a class of algorithm called non-negative sparse deconvolution, which assume that spikes are sparse and non-negative, this so-called “blind sparse deconvolution” algorithm is fast and fully automatic. It ended in Tubiana, J., Wolf, S., & Debregeas, G. (2017). Blind sparse deconvolution for inferring spike trains from fluorescence recordings. bioRxiv, 156364.

Habenula

During my PhD, I also collaborated with Maryam Alavi Naini, a post-doc student from Elim Hong’s group in the Institut de Biologie Paris Seine. Her works on the neuronal transmission dynamics in the habenulo-interpeduncular pathway - an evolutionary conserved neural circuit recently implicated in fear - anxiety and neurobehavioral disorders including substance abuse, led her to use the two-photon light-sheet microscope. I thus helped her to run and analyze experiments in which a zebrafish larva is alternatively submitted to electrical shocks and light flashes. We found that neurons that respond to shocks are inhibited by light flashes, and vice versa. This demonstrates that the two neuronal populations located in the left or right Hb nuclei are indeed part of distinct neuronal circuits that repress each other’s activity.

Rheotaxis

Raphael Olive, a former graduate student in the lab, studied rheotactic behavior of zebrafish larva. Rheotaxis is the ability shared by most aquatic species to orient toward a current and swim to hold their position stable. Using an assay for freely swimming larvae that allows for high experimental throughputs, large statistic and a fine description of the behavior, he detected and characterized two different mechanisms for position holding, one mediated by the lateral line and one mediated by the visual system. This work was published in Olive, R., Wolf, S., Dubreuil, A., Bormuth, V., Debrégeas, G., & Candelier, R. (2016). Rheotaxis of larval zebrafish: behavioral study of a multi-sensory process. *Frontiers in systems neuroscience*, 10.

The dissertation

Before I started working on this dissertation, I thought I would make it simple: I would introduce the two main topics I worked on during these years and attach the two papers that report our results. However, I delved deep into the literature on all these topics: optical microscopy of living systems, goal-directed navigation of organisms, brainstem circuitry of eye movements’ control and central pattern generators. Then only (better late than never) did I understand that I could not finish this PhD without replacing my work in a wider framework. Two-photon light-sheet microscopy for whole brain imaging of zebrafish brain is one small step in the long history of imaging living tissues.

Studies on neural basis of phototaxis in zebrafish is a brick in a rich behavioral and neural literature on goal-directed navigation mostly focused on invertebrates. I thus decided to write three reviews as exhaustive as possible on these subjects. From this bibliographic research many new directions for future works on goal-directed navigation in zebrafish, on the hindbrain oscillator and on the hindbrain circuitry of zebrafish eye-movements appeared. I hope this will be useful for the readers and particularly for my people in the lab.

The technical and experimental results of my PhD are present in the dissertation via the two papers I published as a first author. These papers are detailed enough so they give a fair idea of what I have done these years.

This dissertation is divided in five chapters:

- 1) An historical review of neural recording techniques.
- 2) A specific focus on light-sheet microscopy and its applications to zebrafish neuroscience. This chapter ends with the development I carried out of a two-photon light sheet microscope for zebrafish brain imaging.
- 3) A review on goal-directed navigation behavioral and neuronal mechanisms that ends with phototaxis in zebrafish and more specifically with my work on the neural basis of this behavior.
- 4) (Discussion chapter) A review on the brainstem circuits controlling eye movements in mammals leading to a discussion on possible homologies we could find in our zebrafish recordings. A quick review on central pattern generator that leads to a discussion on the hindbrain oscillator.
- 5) The end of the review on goal-directed navigation with thermotaxis and the recent results we had on the neural basis of this behavior.

The real story is on the next page...

A little personal story

In the following, I want to tell the real story of my PhD, which is, for the sake of clarity, very different from the story we tell in the article...

The following dissertation has a lot to do with chance. When I began my PhD, it was unclear where it would end. Presumably it is a common rule for graduate students.

When I first came to the lab, Georges' group was new to neuroscience and they had just published a new technique to record the activity of the entire brain at single-cell resolution of a small vertebrate called zebrafish. This technique was an adaptation of the light-sheet microscope from Stelzer's group. At that time, Georges had this new idea, after reading a paper from Fraser's team, that this new functional imaging light-sheet technique could also work in two-photon illumination. So he proposed me to join the lab to build this new set-up, adapting the whole-brain recording light-sheet microscope for two-photon illumination and said "after that we will figure out what you will do".

Fortunately, the adaptation of our light-sheet microscope for two-photon illumination worked. After a few tests on the two-photon light-sheet microscope of the Laboratoire d'Optique et Bioscience (Ecole Polytechnique), I built a set-up specific for whole brain functional imaging of zebrafish in our lab. From a biological point of view, the main purpose of this two-photon light-sheet was to avoid the visual disturbance coming from the blue light of the laser in the first light-sheet microscope (one-photon). In the zebrafish community this limitation of the one-photon light-sheet was very problematic since the visual system of zebrafish is widely studied. Indeed, I actually demonstrated this tremendous disturbance recording the brain activity of fish under visual stimulation with the one and the two-photon light-sheet microscope. Hence, after one year we were at that "figure out" point: what would I do during the remaining years?

Luckily, for the two-photon light-sheet paper I had done a lot of whole brain activity recordings under periodic light-flash stimulation. Typically, a zebrafish larva was embedded in agarose and put in front of a LED that flashed every 10s while its brain activity was recorded by the two-photon light-sheet microscope. So I was looking at these data sets. Georges wanted to find a sort of functional structure of the neural activity variability, supposedly reminiscent of the spontaneous activity of the brain. Thus, I was specifically working on the fluctuations of the response to periodic light-flash stimulation. I tried to do clusterisation on whole-brain data set in order to find possible structures of correlation linking several regions in the brain. Nothing seemed really relevant. The clusters obtained were localized within sub-regions of the brain.

However, in classifying the clusters on their level of fluctuation - i.e. on the level of variability - two clusters in the hindbrain always displayed the highest variability. Indeed, I looked at their activity signal (DF/F), and these two clusters were responsive to some light flash but not to others. I remember that one day I came to Georges to show him that I had found two clusters that had a high level of variability in their response to light-flashes. We were looking at their signals separately, and at some point he asked me to superimpose the two signals and to add markers to indicate where the stimulations occurred. When we looked at the graph, we saw that the signal of the second cluster "filled the

blank”, when one was responsive to a light flash, the other was silent. We thus understood that these two clusters encompassed a unique structure. We then looked at the activity of these two clusters in the absence of light stimulation and surprisingly, these two clusters were strongly anticorrelated even in spontaneous activity and they were alternatively active in a periodic manner (period ~20s). Looking in details at the signal of both clusters, we found that it was the already active cluster that would be responsive to the light stimulation.

I remember that it was during these weeks that Alexis presented a paper from Tank’s group in our journal club. The authors recorded the activity of a small subset of neurons in the hindbrain using two-photon point scanning microscopy while the zebrafish larva had its eyes free. They then correlated these signals with the eye position. After the journal club, we thought to reproduce this experiment under our light-sheet microscope in order to have a whole brain map of these eye position neurons. In a few weeks, we recorded hours of whole brain activity on freely eye-moving zebrafish larva. Like in Tank’s group paper we computed correlation maps of the eye-position the neuronal activity of the entire brain. These maps revealed a large structure of neurons in the hindbrain encompassing the subset of neuron discovered by Tank’s group. Surprisingly, this structure also encompassed the two clusters alternatively responsive to light, we talked about before...

The rest of the story is detailed in the paper attached to chapter 3. These two clusters we found in the beginning are actually a key neural structure to understand light-seeking behavior of zebrafish larva. They are correlated to the eye position and to the larva body orientation. The left cluster is correlated to a left body/eyes orientation, the right cluster to a right body/eyes orientation. As we saw, they are responsive to light in a state-dependent manner such that the currently active cluster will have its activity reinforce by a light-stimulation. In the paper attached to chapter 3, we demonstrate that over multiple cycles this process lead to a statistical bias of the body/eye orientation of larval zebrafish towards brighter region.

Georges has never been surprised by the series of chances that led us to study the neural basis of this goal-directed navigation. Maybe it is always the way science goes, following some links of evidence (evident links). As a young student in physics I thought that a scientific research had a program, a question and an assumed answer to this question. What I have learned, beyond the scientific experimental and computational skills, is that in, at least, neuroscience, sometimes we do not even know the question we are asking to the object we are studying. Maybe this is because of the youth of neuroscience.

Chapter 1

Recording the living: an historical overview

A central objective of neuroscience is to understand how neurons of the brain interact, what are the specific functions of these interactions, and how they ultimately give rise to behaviour. To reach this goal, scientists have developed techniques to record neuronal activity in animals' brain. In this chapter, I will review some traditional and more recent techniques for the recording of brain activity at single-cell resolution.

1.1 Recording the living: a stammering

Is the history of neuroscience the history of techniques? When one looks at neuroscience history, he will certainly answer positively (Figure 1.1). During the last century, biology and particularly neuroscience underwent revolution when important technical breakthrough was achieved.

Rafael Yuste described precisely the inextricable link between the techniques and the concepts (Yuste 2015). The list of these achievements begins with the invention of the Golgi staining technique by Camillo Golgi in 1873 (Golgi 1873), which was later used by Cajal to establish the neuron doctrine. By impregnating the tissue with silver nitrate, it was possible to label a random subset of neurons, allowing the entire cell and its processes to be visualized.

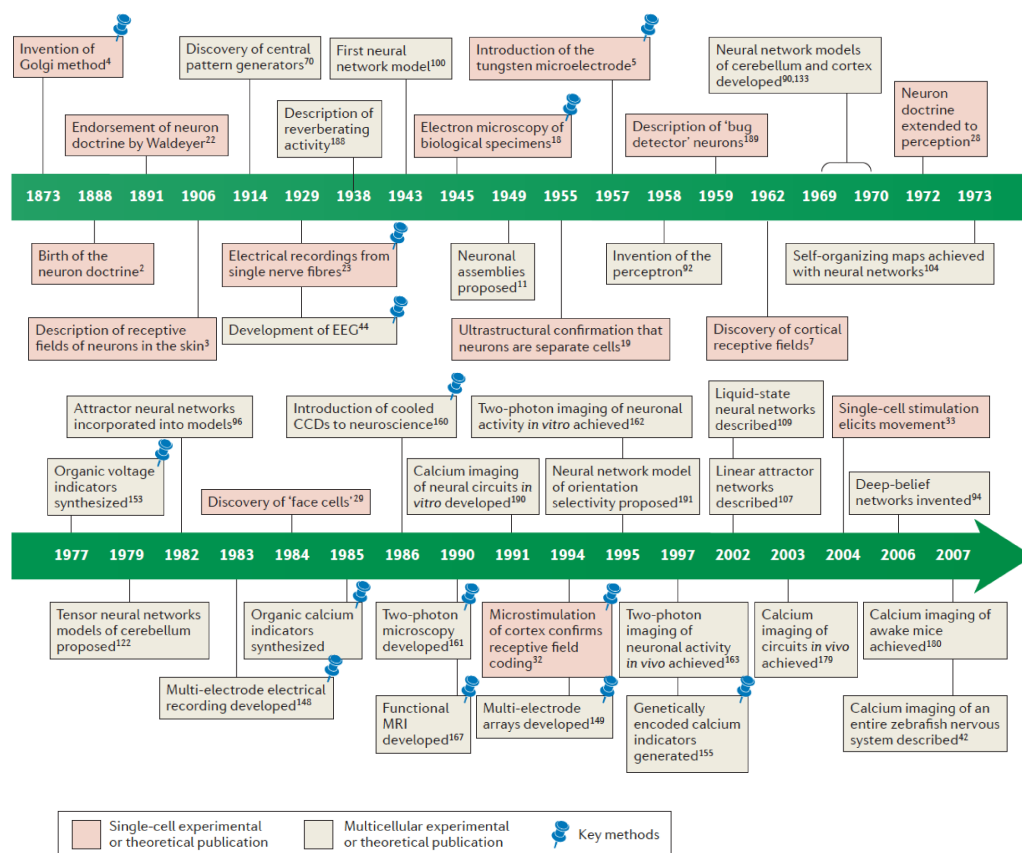


Figure 1.1: Historical evolution of neuroscience. CCD stands for charge-coupled device. EEG for electroencephalography. Taken from Yuste 2015.

1.1.1 Electrophysiology

Later on in the 1920's the premise of patch-clamp offered the first electrical recordings of neuron fibers. Since Galvani and the discovery of animal electricity (Picolino 1998), the behavior of a neuron has been well described in terms of membrane potential and electrical signals. One of the first article on electrophysiology was published in 1957 by Nobel winning David Hubel (Hubel 1957). "An electrode has been developed to fill the need for an easily made,

sturdy device capable of resolving single-neuron action potentials". In figure 1.2 (Hubel 1957), Hubel shows single-unit action potentials recorded from cat.

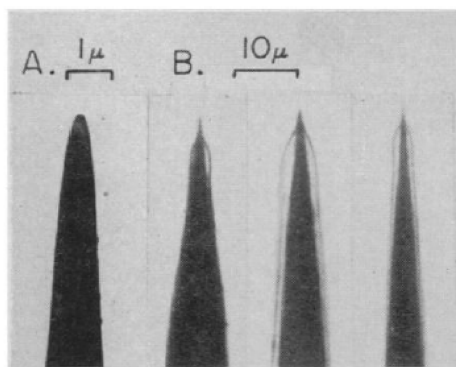


Fig. 1. (A) Electromicrograph of an uncoated, sharpened tungsten wire; (B) optical photomicrographs of coated electrodes immersed in water to show the coating.

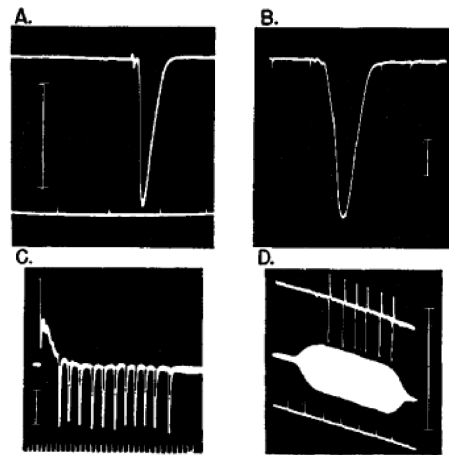


Fig. 2. Single-unit action potentials recorded from cat. (A) S_1 dorsal root, stimulation of same root. (B) Anterior horn cell, spinal cord, S_1 . Stimulation of ventral root. (C) "Renshaw cell," spinal cord, S_1 . Stimulation of ventral root. (D) Response in dorsal cochlear nucleus to a 4000-cy/sec tone. For all tracings, the amplitude is 5 mv, time is in milliseconds; positive deflections are downward.

Figure 1.2: Extract from the reference paper from Hubel 1957.

The so-called patch-clamp technique allows the electrophysiologist to insert an electrode into a single cell and record the intra-cellular or the extracellular electrical currents, and then have access to cell's activity. The main benefit of this technique was the high sampling frequency of the recorded signals, which can be up to several kHz (McNaughton 1983). This high temporal resolution enables one to identify single-action potential in a burst of activity.

However, electrophysiology suffers from some important limitations inherent to the tools used for these recordings: first, the method is invasive as it requires to insert an electrode in the tissue; second, even if the studied area is well understood, it is still impossible to know exactly what cell is recorded during an experiment. This technique is still in constant development to mitigate these limitations (Fujishiro 2014).

During the second part of the twentieth century, fluorescence microscopy offered a new strategy to measure neuronal activity. Before coming to that, let's first take a look back on how microscopy began.

1.1.2 The development of microscopy

Understanding living tissues is the ultimate goal of optical microscopy in biology. During the last centuries the technical improvements in microscopy have always been an important source of new discoveries for biologists. In 1590,

Hans Lipershey and (or) Zacharias Janssen invented the first microscopes. These spectacle-makers were working in the same street in Middelburg, in Holland. While Janssen was trying to find a way to make magnification greater to help people with seriously poor eyesight, he invented a single-lens and later a compound optical microscope.

In the XVIIth and the XVIIIth century, important improvements were made in spatial resolution, and methods to limit for chromatic and spherical aberrations appeared, mostly with Joseph Jackson Lister's (1786–1869) work. Later on, Giovanni Battista Amici (1786–1863) developed the first immersion objective. With Ernst Abbe (1840–1905) (Abbe 1874, 1881, 1883), optical microscopy benefitted from the first analytical theory of aberration. The microscopes were reaching a very high spatial resolution at the beginning of the XXth century, and then the problem of contrast appeared: how can we look at a specific cell within a tissue?

Phase-contrast microscopy proposed by Zernike (Zernike 1942) in 1934 and then interferential-contrast microscopy proposed by Nomarski in 1956 were introduced, both based on refractive index variation of the sample. Still, with these methods it was impossible to visualize a specific object in the field of view of the microscope. In 1873, Golgi used potassium dichromate and silver nitrate to optically target neuron fibers. However, it is with the invention of fluorescence microscopy that the question of contrast was solved. Decades later, the labeling of specific proteins was developed and gave rise to fluorescence microscopy.

1.2 Fluorescence and calcium imaging

1.2.1 Origins of fluorescence discovery

In 1852, Stokes published "*On the Change of Refrangibility of Light* » where he noted that fluorite (CaF_2) is able to change ultraviolet light into blue light. He called this phenomenon "fluorescence", thinking it was a specific property of fluore-based molecules (Stokes 1852). Fluorescence is the emission of light that occurs within nanoseconds after the absorption of light that is typically of shorter wavelength. After an excitation, an orbital electron emits a photon by relaxing to its ground state. This phenomenon is called fluorescence. To visualize the fluorescent objects, one needs to filter out the light at the excitation wavelength.

Fluorophores are molecules that exhibit such fluorescent properties. Many organic substances have auto-fluorescence. In fluorescence microscopes, one take advantage of synthesized compounds that possess conjugated double bonds. These compounds display a small energy difference between the excited and ground states. In general, the more conjugated bonds in the molecule, the lower the excited energy requirement and the longer the excitation wavelength. The fluorescence quantum yield characterizes the efficiency of the fluorescence process. It is defined as the ratio of the number of emitted photons to the number of absorbed photons. This quantity depends on the number of pi bonds of the fluorophore molecule.

1.2.2 The Green fluorescent protein

The Green fluorescent Protein (GFP) is the ultimate fluorophore in neuroscience. In 2008, Roger Tsien, Osamu Shimomura and Martin Chalfie received the Nobel Prize in Chemistry for their discovery and development of the green fluorescent protein. Discovered in the jellyfish *Aequorea victoria* (Shimomura *et al.* 1962), GFP has become one of the most widely studied and exploited proteins in biochemistry and cell biology.

GFP has an amazing ability to generate a highly visible and efficiently emitting internal fluorophore. The work of Tsien (Tsien 1998) on the crystal structures of GFP (Figure 1.3a) offered opportunities to understand and manipulate the relation between protein structure and spectroscopic function. Thanks to Chalfie (Chalfie *et al.* 1994) GFP has become well established as a marker of gene expression and protein targeting in intact cells and organisms.

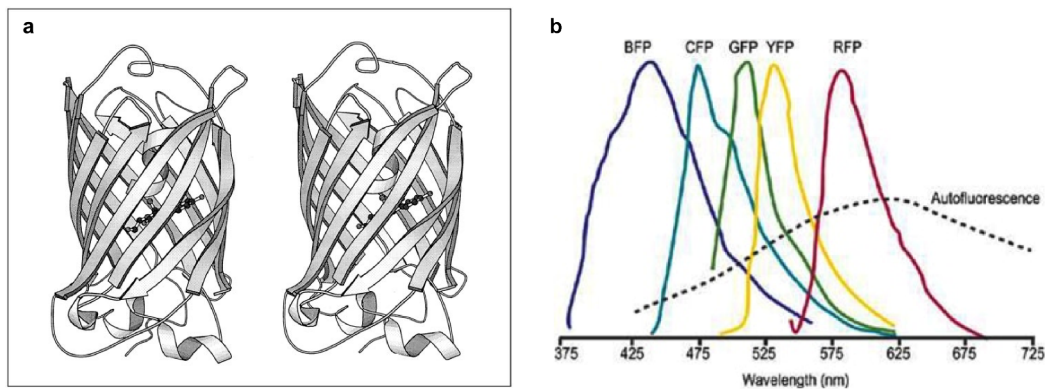


Figure 1.3: **a**, Stereoview of the three-dimensional structure of GFP, showing 11 β -strands forming a hollow cylinder through which a helix is threaded bearing the chromophore. Taken from Tsien 1998. **b**, Fluorescence spectra of different XFPs

In GFP, an imidazolidone ring with conjugated double bonds constitutes the chromophore (Tsien 1998). Mutations in this ring structure that add more conjugated bonds shift excitation and emission to longer wavelengths (Figure 1.3b). The advent of genetically encoded fluorescent proteins (XFPs), based on GFP, allows the tagging of most cellular proteins of interest to measure their spatial distributions and dynamics (Tsien 1998). XFP-based probes can report a vast range of phenomena that are critical for intracellular signal flow, such as protein-protein interactions and the activation of kinases (Miyawaki 2005). XFPs also allow the labelling of specific and sparse subpopulations of cells (Feng *et al.* 2000; Gong *et al.* 2003; Lendvai *et al.* 2000), including neurons.

1.2.3 Calcium indicator

Calcium ions are essential to intracellular signalling pathways and determine a large variety of functions in almost every cell type in biological organisms “*from the control of heart muscle cell contraction to the regulation of vital aspects of the entire cell cycle, from cell proliferation to cell death*”

(Grienberger and Konnerth 2012).

In the nervous system, calcium ions are essential: calcium influx triggers exocytosis of neurotransmitter-containing synaptic vesicles; a calcium transient in dendritic spines is a key step in synaptic plasticity; in the nucleus, calcium regulates gene transcription (Grienberger and Konnerth 2012). The time scale of such processes extends over a wide range, from microsecond for neurotransmitter release to minutes for gene transcription. Thus the understanding of brain function is strongly dependent of our ability to track calcium signals in the brain. Furthermore when the depolarization of the membrane increases enough (when the membrane potential exceed a threshold value around -50mV) calcium channel open and let calcium ions enter in the neuron. In contrast to sodium or potassium ions, which control the depolarization of the neuron and are highly concentrated in the cell (around 12mM for Na^+ and 140mM for K^+), calcium ions are present at a low concentration when the cell is at resting state (around 50nM). An action potential transient increases this value by 10 to 100 fold (Grienberger and Konnerth 2012), whereas the concentration of other ions varies across a way smaller range.

The first generation of calcium indicators comprised a bioluminescent calcium-binding photoproteins, such as aequorin (Ashley and Ridgway 1968; Shimomura *et al.* 1962) or the synthetic compound arsenazo III, an absorbance dye that changes its absorption spectrum upon of calcium binding (Brown *et al.* 1975). Even if these indicators provided insights into calcium regulation in neuron, their implementation was complicated. These indicators were thus rapidly discarded when Roger Tsien *et al.* (Tsien 1980) developed new classes of very sensitive and versatile fluorescent calcium indicators, such as quin-2 or fura-2. Both result from the hybridization of highly calcium-selective chelators like EGTA or BAPTA with a fluorescent chromophore (Tsien *et al.* 1982). Fura-2 became very popular among neuroscientist. Over the years, many more calcium indicators with a wide range of excitation spectra and affinities for calcium have been introduced. The Oregon Green BAPTA and fluo-4 dye families (Paredes *et al.* 2008) are easy to implement and provide a very large signal-to-noise ratio (SNR).

An important breakthrough occurred when Roger Tsien and his team introduced a protein-based genetically encoded calcium indicators (GECIs) in a cell (Miyawaki *et al.* 1997). While the first GECIs had slow response kinetics and low signal-to-noise ratios, quick improvements have been made and the last generations of GECIs like GCaMP6 or 7 are almost as useful as synthetic probes (see next section for a precise description of the GCaMP family).

To summarize: a fluorescent calcium reporter is either injected (synthetic probe) or produced (GECIs) by the animal's neuron. Whenever an action potential is triggered, the calcium concentration quickly rises and decays inside the cell. Reporters bind with the calcium and, owing to a mechanical coupling, become more fluorescent. Hence, the fluorescence signal of the neuron acts as a proxy for the neuron electrical activity. However, because the complexation chemical reaction has a slow kinetics, the fluorescence transient lasts much longer (typically $0.1\text{-}1\text{s}$) than the action potential (5ms).

Synthetic indicators have short rising and decay times and thus require a high sampling rate. They need to be injected by the user and can be used only

during a few hours, after which the intra-cellular concentration of indicator becomes too low. Even if the GECIs are slower than synthetic one, their concentration in a given population of neuron tends to be more homogenous. Moreover GECIs can be expressed under the control of specific promoters, allowing neuroscientists to target defined neuronal classes.

1.2.4 GCaMP

GCaMP is a family of calcium indicators with a cpEGFP molecule, which is a green fluorescent protein modified to be able to circularly permute, the calcium-binding protein calmodulin (CaM) and CaM-interacting M13 peptide (Figure 1.4). The cpEGFP is fluorescent even in the absence of calcium ions with an excitation wavelength of 485nm and an emission wavelength of 515nm. The calmodulin (calcium-modulated protein) is naturally present in the neuron cytoplasm: it is a multifunctional intermediate calcium-binding messenger protein expressed in all eukaryotic cells. It constitutes an intracellular target of the secondary messenger Ca^{2+} , and the binding of Ca^{2+} is required for the activation of Calmodulin. The fixation of Ca^{2+} on CaM induces a conformational change of the peptide M13, which in turn changes the cpEGFP conformation, increasing its quantum efficiency (Figure 1.4b). (Miyawaki 1997, Tian *et al.* 2009).

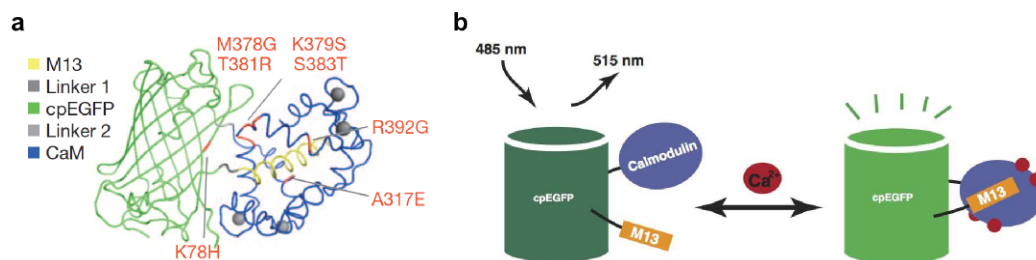


Figure 1.4: **a**, GCaMP structure. Adapted from Tian *et al.* 2009. **b**, Scheme showing how GCaMP can measure Ca^{2+} . The cpGFPs are drawn as simple rigid cylinders, reflecting their crystal structures. The calcium fixation on calmodulin induces a conformational change of M13 peptide which increases the cpGFP fluorescence. Adapted from Nakai *et al.* 2001.

However, the GCaMP indicators are still inferior to synthetic indicators in terms of signal-to-noise ratio (SNR), response linearity, photostability and calcium affinity. The GCaMP indicators also suffer from poor protein stability. Improvements in each of these parameters would facilitate imaging of neural activity.

Since the development of the first generation of GCaMP in 2000 (Nakai *et al.* 2001; Miyawaki *et al.* 1997), several GCaMP reporters have been developed with increased fluorescence baseline and dynamic range, higher affinity for calcium, different rising or decay time, and improved signal-to-noise ratio. In 2009, Looger's team published a new generation of GCaMP indicators (Tian *et al.* 2009). In the first year of my PhD, I have been using this calcium indicator and an improved version, GCaMP5 (which was a lot more sensitive to calcium activity compared to GCaMP 1 and 2 (Figure 1.5).

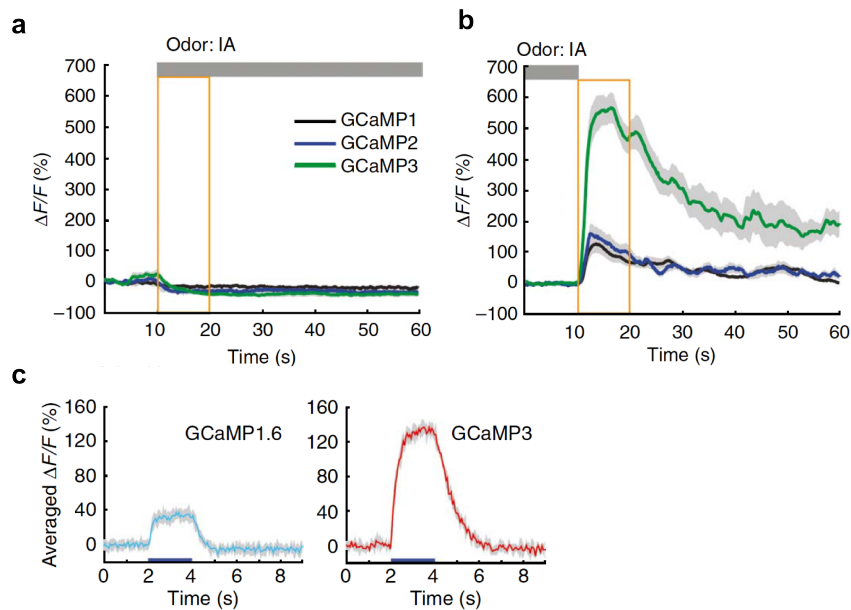


Figure 1.5: *In vivo* imaging of sensory-evoked Ca^{2+} transients with GCaMPs indicators, in *C. elegans*. **a–b** Odour presentation–evoked (**a**) and odour removal–evoked (**b**) responses of GCaMP1, GCaMP2 and GCaMP3 in *C. elegans* olfactory neurons. Transgenic worm lines expressing GCaMPs were imaged after an odour addition–removal sequence. Gray bars denote odour presence. **b**, Comparison of responses of GCaMP1.6 and GCaMP3 to addition of vinegar. Adapted from Tian *et al.* 2009.

In 2013, Looger’s team developed a new class of genetically encoded indicators of neuronal function with greatly improved properties (Chen *et al.* 2013). This new generation of GCaMP indicators, called GCaMP6, crossed important performance thresholds. They have higher sensitivity than commonly used synthetic calcium dyes (for example, OGB1-AM) and can detect individual action potentials with high reliability at reasonable microscope magnifications. (Figure 1.6). These indicators can be used to image large groups of neurons as well as tiny synaptic compartments over multiple imaging sessions separated by months. I used this reporter at the beginning of my PhD. According to the experimental parameters chosen (acquisition frame rate...) 3 different types of GCaMP6 exist with different decay time: GCaMP6f (f for fast) has a decay time of less than a second, GCaMP6s (s for slow) has a decay time of 3s. During the major part of my PhD, I have been using a GCaMP6f with a pan-neuronal promoter (elav13) developed in Engert’s lab by Isaac Bianco and David Hildebrand.

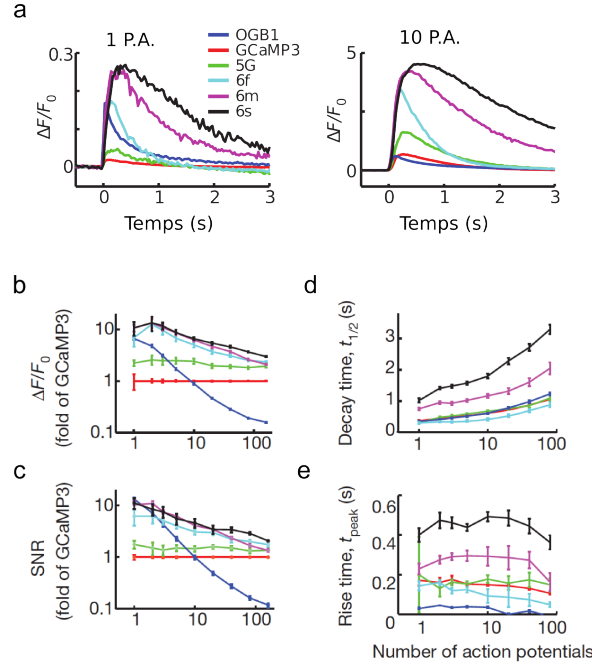


Figure 1.6: **a**. Fluorescence response curves of several calcium indicators belonging to GCaMP family (3, 5G, 6f, 6m, 6s) and OGB. Left: response to 1 action potential. Right: response to 10 action potentials. **b–e**. Comparison of GCaMP sensors and OGB1-AM as a function of stimulus strength (colors as in b). **b**, Response amplitude. **c**, Signal-to-noise ratio (SNR). **d**, Half decay time. **e**, Time to peak (after stimulus offset). Chen *et al.* 2013.

1.2.5 Limitations

An indirect measure of neuronal activity

Functional calcium imaging offers an indirect measure of the neuronal activity. Inference methods can be implemented to recover an approximate spike train from the fluorescence trace.

The fluorescence signal we observe in fluorescence microscopy recordings can be modeled in continuous time by the following equation:

$$F(t) = a \int K(\tau)N(t - \tau)d\tau + b(t) + \epsilon(t)$$

Here

$N(t) = \sum_j \delta_{t,t_j}$ denotes the spike train

$b(t)$ is the baseline fluorescence (spikeless signal)

$\epsilon(t)$ is a Gaussian noise

The convolution kernel modeling the chemical kinetics is of the form $e^{-\frac{t}{\tau_{decay}}} - e^{-\frac{t}{\tau_{rise}}}$. Where the rise and decay time constants τ_{decay} and τ_{rise} depend on the calcium indicator and on the neuron, typically in the range of respectively 10-

100ms and 50ms-1000ms. Every calcium sensor has different rising, decay time and signal to noise ratio.

From this model of fluorescence signal, we can see that what a neuroscientist really seeks to understand neuronal activity is not $F(t)$ but $N(t)$. Spiking inference algorithms have been developed during the last decades to account for this problem and extract $N(t)$ from the measured $F(t)$. A powerful family of algorithms is based on non-negative sparse deconvolution (Vogelstein *et al.* 2009, 2010; Pnevmatikakis *et al.* 2016). In short, it consists in extracting $N(t)$ from $F(t)$ using the a priori knowledge that the spikes are sparse and non-negative. In Annex 1, a submitted manuscript to which I contributed is presented. It describes a novel a new implementation that is fast, robust and blind (automatic).

Photo bleaching

There is no general answer to the question of how much illumination can a biological specimen sustain (Stelzer 2015). But what is sure is the fact that light microscopy can have a very negative effect on living specimen. Light exposure should thus be kept to an absolute minimum. Huisken wrote in 2017: *“The maximum acceptable light level does not deliver the highest quality image but rather the minimum signal-to-noise that still allows the necessary quantitative analyses to be performed”* (Power and Huisken 2017). It summarizes the strategy one experimentalist should choose when doing imaging experiments.

Stelzer (2015) calculated the ‘sun regime’ of energy delivered by a natural environment. In microscopic terms, the sun radiation yields an energy of $100\text{mW}/\text{cm}^2$ around the equator, thus the maximal exposure should be $0.5\text{mJ}/\mu\text{m}^2$. This suggests that cells should not be exposed to more than a few millijoules and a few hundred millijoules for embryos like zebrafish. Furthermore, photodamage originates largely from non-linear processes. Thus spreading the light dose across time and space is an important precaution. As we will see in the next chapter, light-sheet microscopy is one of the sole techniques that follows this rule. Confocal microscopes usually work in a ‘multiple-suns’ regime. Notice also that phototoxic effects tend to be more severe at lower rather than at higher wavelengths. This will be important when comparing one- and two-photon imaging strategies.

1.3 Recording the living: Confocal microscopy

Despite the specificity of calcium indicators, in the first fluorescence microscopes it was impossible to distinguish the focal plane from the others in tri-dimensional sample. Imaging a fluorescent volume was thus impossible since with those so-called epifluorescence microscopes one collects photons from the focal plane of the objective as well as photons coming from out of focus planes. These out-of-focus photons blurred the recorded image.

During the second part of twentieth century, optical techniques have been developed for selectively imaging a thin section within a specimen, a process, called optical sectioning. Two different approaches were successively proposed: confocal imaging and non-linear microscopy.

In the fifties, Marvin Minsky (1955), who later worked on artificial intelligence, invented the confocal microscope when he was a young professor:

« One day it occurred to me that the way to avoid all that scattered light was to never allow any unnecessary light to enter in the first place.

An ideal microscope would examine each point of the specimen and measure the amount of light scattered or absorbed by that point. But if we try to make many such measurements at the same time then every focal image point will be clouded by aberrant rays of scattered light deflected points of the specimen that are not the point you're looking at. Most of those extra rays would be gone if we could illuminate only one specimen point at a time. There is no way to eliminate every possible such ray, because of multiple scattering, but it is easy to remove all rays not initially aimed at the focal point; just use a second microscope (instead of a condenser lens) to image a pinhole aperture on a single point of the specimen.»

Minsky memoir 1988

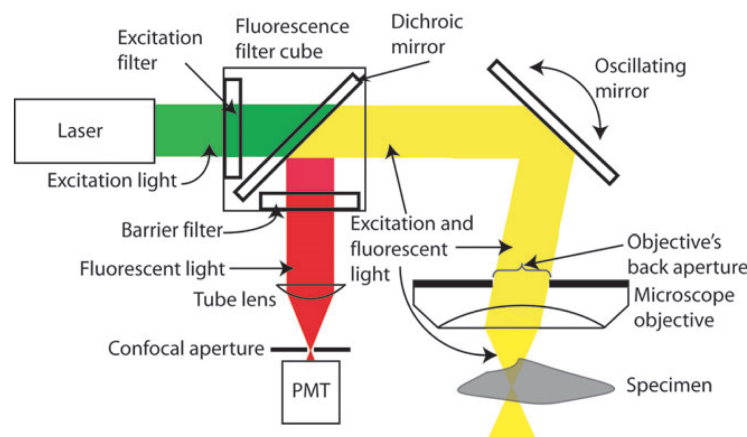


Figure 1.7: Layout of a confocal microscope. The excitation light is directed by the scanning mirror and focused into the specimen. The fluorescent specimen in response to excitation light emits red-shifted photons. This emitted light is separated from the excitation by a dichroic mirror and the barrier filter and goes to the camera through a pinhole. Adapted from Conchello and Litchman 2005.

The confocal microscope uses a pinhole conjugated to the focal point of the objective to block the photon originating from outside the focal volume (Figure 1.7). This enables recording of the fluorescence signal from only one point of the sample. To build a complete image, one has to scan this point throughout the entire sample, moving together the observation (pin-hole) and the excitation arm.

Thus in confocal microscopy, the user needs to find a compromise between the size of the region imaged and the acquisition frame rate f_{acq} . The frame rate is limited by the dwell time of the laser at each point, τ_{exp} , and the number of pixel in the image N , such that:

$$f_{acq} = \frac{1}{N * \tau_{exp}}$$

τ_{exp} depends on the quantum efficiency and concentration of the fluorescence indicators. Typically, it has to be superior to $1\mu s$ to allow for enough photons to be detected by the photo multiplier. Owing to this point-scanning strategy, frame rate thus tends to be low in confocal microscopy.

Another drawback of this approach is that the entire specimen is continuously exposed to the excitation beam although only one voxel is imaged at a given time. The photo-efficiency is thus intrinsically low. Lastly, confocal microscopy has a limited penetration depth in heterogeneous samples.

Another way to produce optical-sectioning is to induce fluorescence only in the in-focus regions, relaxing the need to block photons originating from out-of-focus regions. This strategy is the basis of multiphoton microscopy like 2-photon microscopy and has the advantage to overcome the penetration depth and photo bleaching limitation of confocal-microscopy.

1.4 Recording the living: 2-photon microscopy

2-photon microscopy uses the two-photon quantum transitions effect in atom to optically section tissues that have been labeled with fluorophores. This technique offers a deep penetration in the tissue and low photodamage. For the last decades, the applications of such microscopy have been numerous in biology, especially in neuroscience (Svoboda *et al.* 1996, Trachtenberg *et al.* 2002, Ahrens *et al.* 2012), in immunology (Schwickert *et al.* 2007) or in developmental biology (Squirrell *et al.* 1999, Amy McMahon *et al.* 2008, Olivier *et al.* 2010). Here I present a quick overview of how this technique became so essential to our labs.

1.4.1 The origins

In 1931, Maria Göppert-Mayer published her doctoral dissertation in Göttingen:

“The first part of this work considers the coaction of two photons in an elementary process. [...] Namely the simultaneous emission of two photons, is calculated. It appears that a nonzero probability exists that an excited atom divides its excitation energy into two photons, whose energies in sum prove to be the excitation energy but are otherwise arbitrary. When light falls upon the atom with a frequency smaller than the corresponding atomic eigen-frequency, another stimulated double emission occurs during which the atom divides its energy into one incident and one frequency-difference photon.”

Maria Göppert-Mayer, 1931

Two years before her doctoral defense, Göppert-Mayer published a report (Göppert-Mayer 1929) where she predicted the theoretical existence of a virtual state leading to two-photon transition. She concluded that the probability for the two-photon absorption process was proportional to the square of the light intensity.



Figure 1.8: Maria Göppert-Mayer during her PhD

In her doctoral thesis, Maria Göppert-Mayer extended the quantum

mechanical treatment of Dirac to obtain the transition probability of a 2-photon electronic process. She showed that the process of two-photon absorption involved the interaction of two photons and an atom via an intermediate virtual state. This interaction had to occur within the lifetime of this virtual state, of the order of 0.5fs. The first photon induces a transition to a virtual state, the second to the excited state, the relaxation from the excited state to ground state emits a unique photon (Figure 1.9 and 1.10).

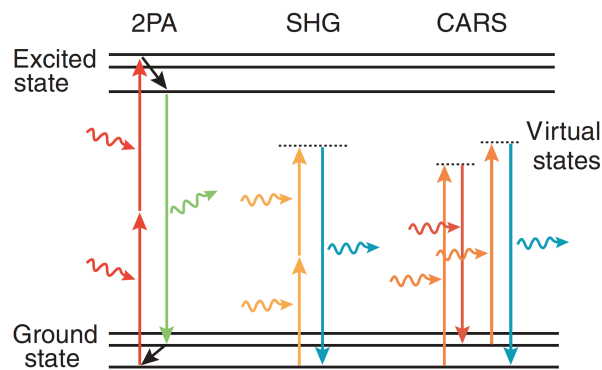


Figure 1.9: Jablonski diagram illustrating two photon absorption (2PA), second harmonic generation (SHG) and coherent anti-Stokes Raman scattering (CARS). Taken from Helmchen and Denk 2005.

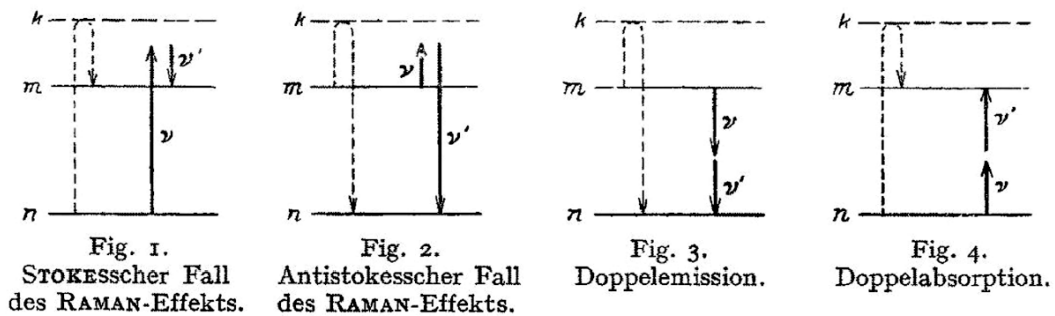


Figure 1.10: Diagram illustrating different common non-linear effects. Stokes Raman effect (I), anti-Stokes Raman effect (2), two-photon emission (3) and two-photon absorption (4). Taken from Göppert-Mayer's dissertation.

This non-linear process has a transition probability extremely low at normal light intensity. For example a molecule of the natural chromophore rhodamine B excited by the sunlight will have a 2-photon absorption transition every 10^7 years (Mahou 2012). Observing this phenomenon thus requires the use of spatially and temporally focused light, in order to increase the probability of interactions of several photons with the same molecule. Focusing a laser beam through high numerical aperture objective easily generates high spatial density. To have a concentration in time, one needs a laser that emits short pulses of high intensities as is now possible with femto-laser technology which currently provides ~ 100 fs-long high-energy pulses at 80MHz repetition rate.

1.4.2 Struggling the theory

The Oxford group

The experimental investigation of the 2-photon absorption only became possible 30 years after the theoretical prediction of Göppert-Mayer, with the development of lasers that could deliver intense monochromatic, coherent light (Maiman 1960). Following Maiman's invention, stimulated Raman scattering was discovered in 1962. During the early sixties, non-linear spectroscopy was on fire: Franken *et al.* observed the first second-harmonic generation (Franken *et al.* 1961) focusing light onto a quartz crystal, then they settled the basis of optical mixing. The first step towards non-linear microscopy occurred in Bell Laboratories. In 1961, Kaiser and Garrett made the first experimental observation of two-photon excitation fluorescence (Kaiser and Garrett 1961). They generated blue fluorescent light at a wavelength of 425 nm by illuminating crystals of $\text{CaF}_2:\text{Eu}^{2+}$ with red light at 694 nm from a ruby optical maser. The next step in the application of nonlinear optics was the development of a nonlinear optical microscope (Figure 1.11) for the examination of the polycrystalline microscopic structure ZnSe (Hellwarth and Christensen 1974).

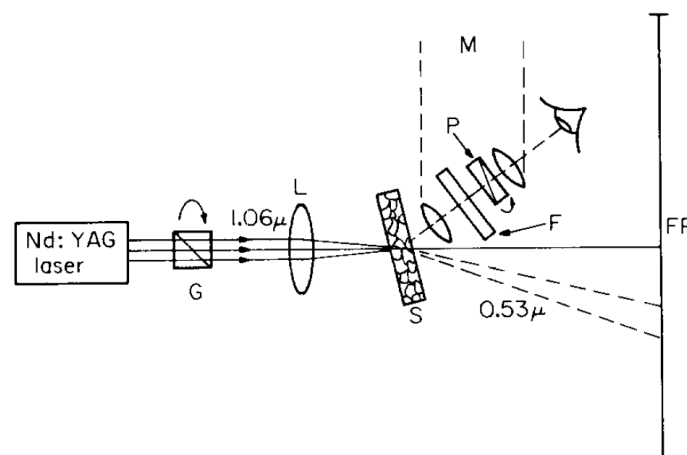


Figure 1.11: Schematic of second-harmonic microscope used by Hellwarth and Christensen in 1974. The unpolarised laser output could be polarized by a Glan prism (G) and focused by lens (L) onto the sample (S). The green second harmonic is viewed by microscope (M) or on screen (FP), sometimes through a polarizer sheet. Taken from Hellwarth and Christensen 1974.

In 1977 at Oxford University, Sheppard, Kompfner, Gannaway, Choudhury, and Wilson suggested that a nonlinear optical phenomenon could be incorporated into a three-dimensional scanning laser microscope. Their idea was to develop a nonlinear scanning optical microscope where the excitation light is focused onto a small volume and an image is generated by raster scanning of either the beam or the specimen (Figure 1.12). With this they almost invented the 2-photon scanning microscope.

“In the scanning optical microscope nonlinear interactions are expected to

occur between the object and a highly focused beam of light, which we hope will open new ways of studying matter in microscopic detail hitherto not available. Nonlinear interactions include the generation of sum frequencies, Raman scattering, two-photon fluorescence, and others. We feel that the method will be of particular interest in studying biological materials, some of which have large second harmonic generation coefficients, and the wide range of these coefficients should give very strong contrast in the images formed. Furthermore, frequency mixing should give information concerning the chemical structure of the object.”

Sheppard and Kompfner 1978

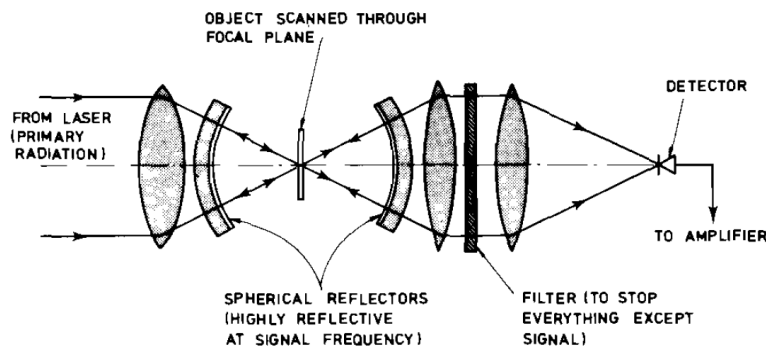


Figure 1.12: The nonlinear scanning optical microscope from the Oxford group. Taken from Sheppard and Kompfner 1978.

Excited volume: an intrinsic optical sectioning

In non-linear microscopy, the signal is localized in a restricted volume centered on the focal point, which gives an intrinsic optical sectioning to the excitation. To illustrate this point let's calculate in cylindrical coordinates the function $S^n(z) = \int_0^{+\infty} I^n(r, z) r dr$ which characterizes the localization of emission at n photons in the (r, θ) plane.

Since the laser beam has a Gaussian intensity distribution, its intensity profile can be written:

$$i(r, z) = i_0(z) \cdot e^{\frac{-2r^2}{w(z)^2}} \quad \text{with} \quad i_0(z) \propto \frac{1}{\pi w(z)^2}$$

and

$$w(z) = w_0 \sqrt{1 + \left(\frac{z}{z_0}\right)^2}$$

(See light-sheet section for details)

This yields the following expression for $S^n(z)$:

$$S^n(z) \propto \frac{1}{n} \left(\frac{1}{\pi w(z)^2} \right)^{n-1}$$

Then for $n = 1$ i.e. 1-photon excitation, $S(z) = cste$. The same number of photon originates from all the planes. In contrast, for 2-photon excitation

$$S^2(z) \propto \frac{1}{\pi w(z)^2}$$

i.e.

$$S^2(z) \propto \frac{1}{1 + \left(\frac{z}{z_0} \right)^2}$$

The fluorescence intensity thus rapidly decays as one moves away from the focal plane, leading to the sectioning effect. It's easy to understand then the advantage in term of optical sectioning of 2-photon microscopy compared to 1-photon (figure 1.13).

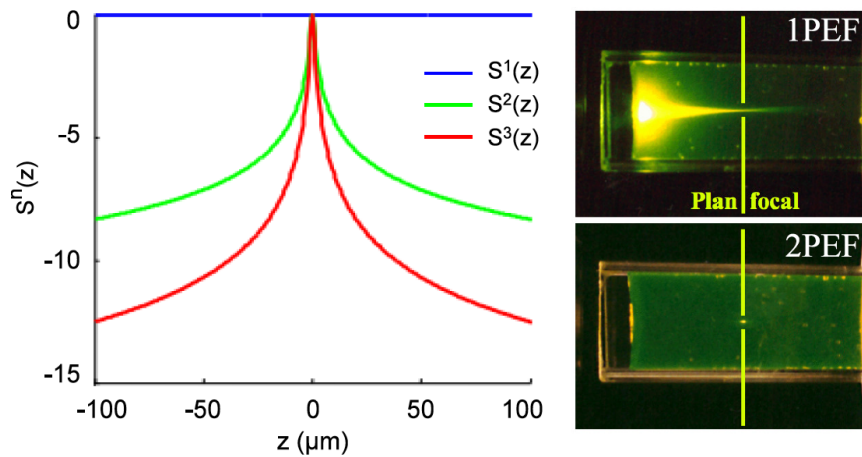


Figure 1.13: Right: Localization curves in non-linear microscopy for 1, 2 and 3-photons absorption. Left: Single-photon excitation of fluorescein by focused 488-nm light (0.16 NA). (b) 2-photon excitation using focused (0.16 NA) femtosecond pulses of 960-nm light. The 2-photon excitation has an intrinsic localization. Adapted from Mahou 2012 and Zipfel *et al.* 2003.

Limitation: toward modern two-photon microscopy

The Oxford group pointed out the main advantages this new technique would have compared to conventional microscopy: the nonlinear dependence of the emission signal with the excitation light would bring super resolution and depth discrimination. They also claimed that such a laser microscope would lead to nonlinear effects like Raman scattering or two-photon fluorescence which could be used to investigate the molecular structure of the specimen. In Gannaway and Sheppard 1978, the authors predicted that this new technique would be used to image biological structures with high contrast. They evaluated the temperature rise for a small biological sample and suggested scanning the

laser beam and not the sample: “Fast-scanning of the beam results in the whole specimen reaching an equilibrium temperature”.

In the end, Sheppard *et al.*'s microscope reached a resolution of 20-200 μm , but they did suggest that the development of pulsed lasers would improve the performance: “*It is possible to increase the harmonic signal for a given specimen temperature rise by pulsing the laser*“. Their suggestion was right and with the invention of a colliding-pulse 80-MHz mode-locked dye laser that generated 100-fs pulses (Valdmanis and Fork 1986) and a few years later the development of the Ti-sapphire femtosecond laser, two-photon excitation microscopy became practical (Spence *et al.* 1991).

1.4.3 A new technique for imaging life

Denk et al. 1990

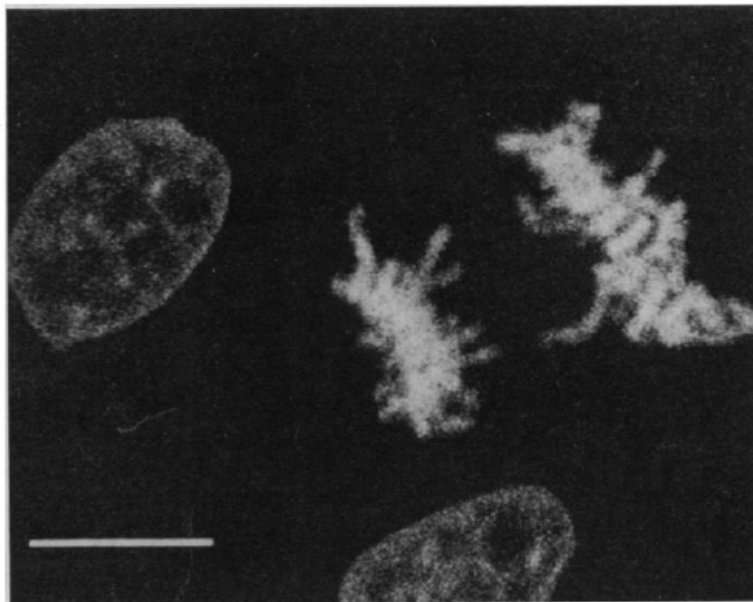


Figure 1.14: A 2-photon optical section through chromosomes of live cultured pig kidney cells. Two cells are seen in interphase and one cell is in anaphase. The image is taken from a 13 s recording. Scale bar 10 μm . Taken From Denk *et al.* 1990.

In 1990, Winfried Denk, James Strickler, and Watt W. Webb published a revolutionary paper in *Science*. Combining a laser scanning microscope and a mode-locked laser that generated pulses of near-infrared light, they created the 2-photon fluorescent microscope (Denk *et al.* 1990). The high-intensity (25mW) and the short pulses (100fs at a repetition rate of 100 MHz) of near-infrared light caused significant multiphoton excitations. In the report Denk *et al.* demonstrated the numerous benefits of 2-photon microscopy: improved background discrimination, optical sectioning, reduced photobleaching of the fluorophores, and minimal photodamage to biological specimens (Figure 1.14):

"The fluorescence emission increased quadratically with the excitation intensity so that fluorescence and photo-bleaching were confined to the vicinity of the focal plane as expected for cooperative two-photon excitation. This technique also provides unprecedented capabilities for three-dimensional, spatially resolved photochemistry."

Denk *et al.*, 1990

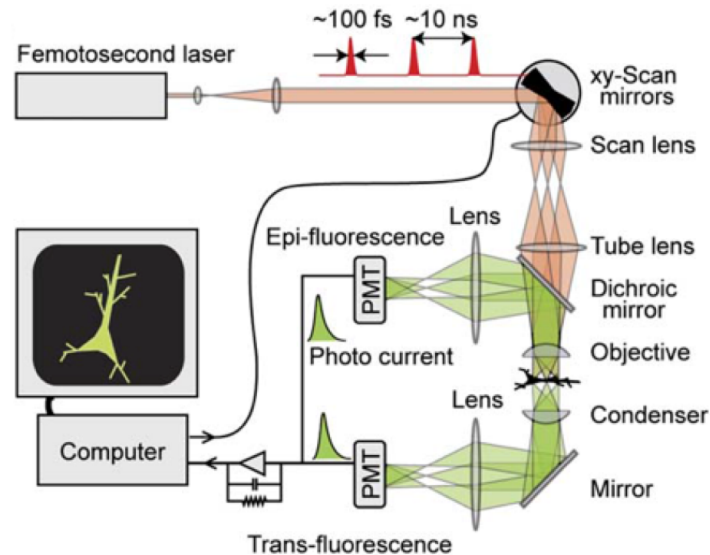


Figure 1.15: Schematic of a typical 2-photon microscope. Taken from Svoboda and Yasuda, 2006.

During the decades following this invention, 2-photon microscopy became the ultimate microscope for biologists. Thousands of publications have employed, developed, or reviewed 2-photon microscopy. Let us examine in more details the main advantages of the technique: optical sectioning, deep in tissue.

A light scattering comparison, confocal vs. 2-photon microscopy

Optical sectioning in non-linear microscopy comes from the non-linear dependency of the detected intensity with the illumination intensity. This property allows to maintain optical sectioning even in scattering tissue, since scattered photons are unlikely to contribute to the fluorescence. Non-linear microscopy has three main advantages for imaging through scattering tissues compared to one-photon techniques like confocal microscopy, (1) One can image deeper in tissue since light penetration depth increase with the wavelength, (2) The localization of excitation in non-linear microscopy implies that all fluorescence light coming from the tissue (ballistic and scattered) contributes in a useful way to the signal, (3) Non-linear linear technique induces less photodamage on biological tissues.

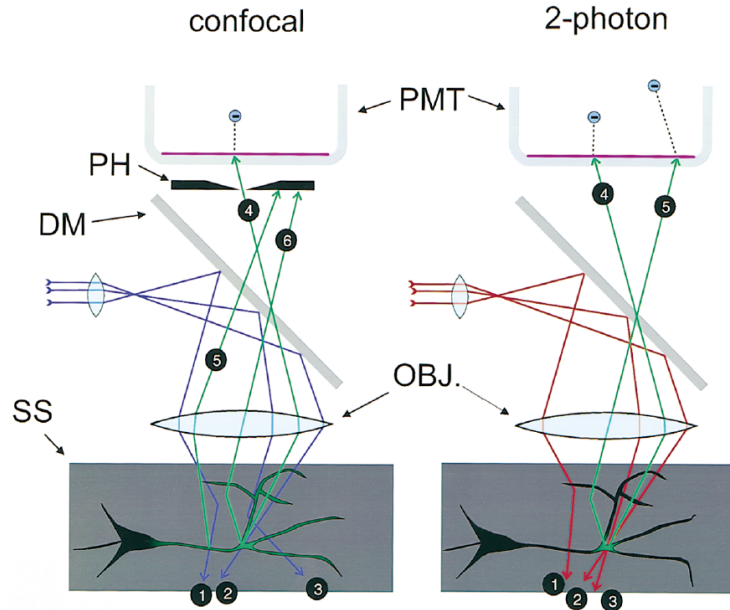


Figure 1.16: Imaging in scattering media. In the confocal configuration (left), the excitation photons have a higher chance of being scattered (1 and 3) because of their shorter wavelength. Off the fluorescence photons generated in the sample, only ballistic (i.e., unscattered) photons (4) reach the photomultiplier detector (PMT) through the pinhole, which is necessary to reject photons originating from out-of-focus regions (5) but also rejects photons generated at the focus volume but whose direction and hence seeming place of origin have been changed by a scattering event (6). Excitation, photobleaching, and photodamage occur throughout a large part of the cell (green region). In the multiphoton case (right), a larger fraction of the excitation light reaches the focus (2 and 3), and the photons that are scattered (1) are too dilute to cause 2-photon absorption, which remains confined to the focal volume where the intensity is highest. Ballistic (4) and scattered photons (5) can be detected, as no pinhole is needed to reject fluorescence from off-focus locations. Taken from Denk and Svoboda 1997.

1) On the macroscopic scale, light scattering in tissue is quantified by the mean free path (l_m), which is the average distance between scattering events and by the anisotropy parameter g , which is the average direction along which the photons are diffracted. l_m depends on refractive index variation in the tissue, object size and light wavelength. Basically $g = \langle \cos(\alpha) \rangle$ where α is the diffusion angle of a specific event. In biological tissue such as gray matter in brain, l_m is around $200\mu\text{m}$ for a wavelength at 800nm (Helmchen and Denk 2005). The parameter g is generally high in brain tissue (≈ 0.9).

The effects of scattering leads to a decay of the intensity that follows a Beer-Lambert law:

$$i(z) = i_0 \cdot e^{\frac{-2 \cdot z}{l_m}}$$

thus in power :

$$P(z) = P_0 \cdot e^{\frac{-2 \cdot z}{l_m}}$$

Diffusion coefficients decrease with the wavelength as $1/\lambda^\alpha$ with $\alpha \geq 1$. These effects are thus mitigated in 2-photon (infrared light at 930-1300nm) (Kobat *et al.* 2009) compared to one-photon (Figure 1.17).

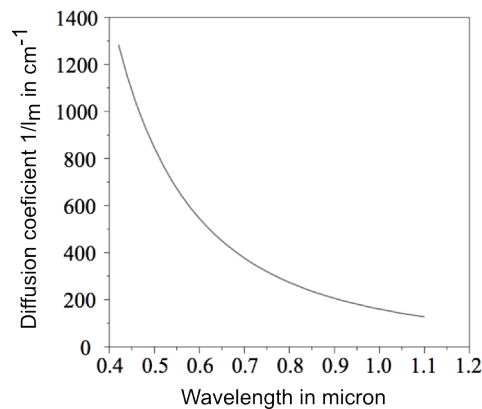


Figure 1.17: Diffusion in tissue. Data from Mahou 2012.

2) In 2-photon microscopy, light scattering does not affect the spatial confinement of the excitation (Figure 1.16). Experiments where imaging is performed at a depth of less than three times l_m , i.e. less than $500\mu\text{m}$ in the brain at 930nm, only ballistic photons contribute to signal generation in the focal volume (Ying *et al.* 1999).

3) Photodamage limits fluorescence microscopy. In non-linear microscopy, the nature of the non-linear excitation implies that excitation photons are too dilute to produce fluorescence. Fluorescence is limited to a small focal volume, which in turn limits photodamage to this small volume. Hence, in 2-photon microscopy it is possible to use very high laser power without photodamage. In Tomer *et al.* (2012), the authors use 300mW for 2-photon excitation at 940nm vs. 0.36mW for 1-photon excitation at 488nm, for identical imaging performances in *Drosophila*.

The advantages of 2-photon approaches in microscopy are thus numerous. Without using any pinhole, 2-photon microscopy provides optical sectioning. This technique allows for deeper penetration into thick, highly scattering tissues, and confines photobleaching and photodamage to the focal volume (Figure 1.16).

However, 2-photon microscopy is not perfect and important limitations remain. To produce a sufficient amount of emitted photons, a high-power laser is needed. Furthermore, to build a complete image of a sample, one needs to scan through the entire sample. Thus, like in confocal microscopy, the user needs to find a compromise between the size of the region imaged and the acquisition frame rate. Finally, the technique is not suitable for imaging highly pigmented cells and tissues that absorb near-infrared light.

A third optical technique emerged in the years 2000's has allowed to overcome these limitations of 2-photon microscopy. This new fluorescent microscopy technique, called light-sheet microscopy, has been the central theme of the beginning of my PhD.

Chapter 2

Whole-brain functional imaging with two-photon light-sheet microscopy

Limitations of confocal and 2-photon microscopy led scientists to the development of a new fast and less photodamaging microscopy technique: light-sheet microscopy. In this chapter, after reviewing the basis of light-sheet microscopy, I will discuss the particular assets of zebrafish for circuit neuroscience and why this animal is particularly well adapted to light-sheet based functional imaging. I will then motivate the development of the two-photon light-sheet microscope, which I carried out during the first year of my PhD, in order to record whole brain activity at a cellular level of zebrafish larvae under controlled visual stimulation. The details of this method is provided in the attached paper (Wolf, S., Supatto, W., Debrégeas, G., Mahou, P., Kruglik, S. G., Sintes, J. M., Candelier, R. (2015). Whole-brain functional imaging with two-photon light-sheet microscopy. *Nature methods*, 12(5), 379-380).

2.1 Recording the living: *Light sheet microscopy*

Light sheet fluorescence microscopy uses a thin sheet of light to optically illuminate transparent tissues or whole organisms that have been labeled with a fluorophore. This technique offers high acquisition speed and low photodamage. Let's have a quick reminder of how this technique appeared.

2.1.1 An old story revealed in the end of the XXth century

In 1902, Siedentopf and Zsigmondy published an article in *Annalen Der Physik* (Siedentopf and Zsigmondy 1902) describing a technique to measure the size of gold particles. They projected sunlight through a slit aperture in the focal plane of an observation objective. The light in the sample was thus projected orthogonally to the observation objective (Figure 2.1), and they collected the scattered photons. They called this technique ultramicroscopy due to its ability to image object smaller than the diffraction limit.

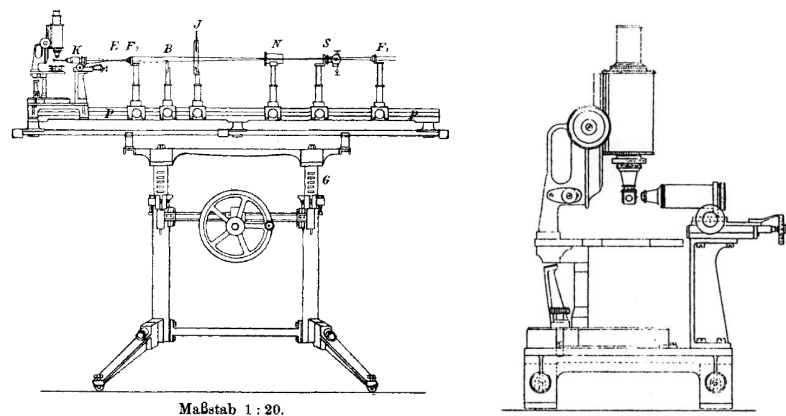


Figure 2.1: Part of the light sheet microscope developed by Siedentopf and Zsigmondy with an upright microscope containing a specimen holder that appears to be mounted to its objective lens and orthogonal illumination at 90° from what appears to be an illuminating objective. Adapted from Siedentopf and Zsigmondy 1902.

Although in 1925, Zsigmondy received the Nobel Prize for Chemistry in part for this invention, it remained for a long time confined to the domain of colloids. In 1993, Voie, Burns and Spelman (Voie *et al.* 1993) reintroduced this optical method but in a completely different context, renaming it: the orthogonal-plane fluorescence optical sectioning (OPFOS), Figure 2.2. Inspired by side illuminating photomicrography, Spelman's team developed the OPFOS device and used it to optically section, for the first time, whole fluorophore-stained and cleared cochleas (Voie *et al.* 1993; Voie and Spelman 1995; Voie 1996, 2002).

« Another approach to optical sectioning involves the use of a planar illumination beam. Planar illumination has been used in other imaging

modalities such as flow cytometry and flow visualization. The illumination beam is focused into a plane with a cylindrical lens, and aligned to be co-planar with the depth of field of the imaging detector. The beam is thus orthogonal to the imaging axis. The region where both the imaging system and laser illumination focus coincide is the system focal zone. »

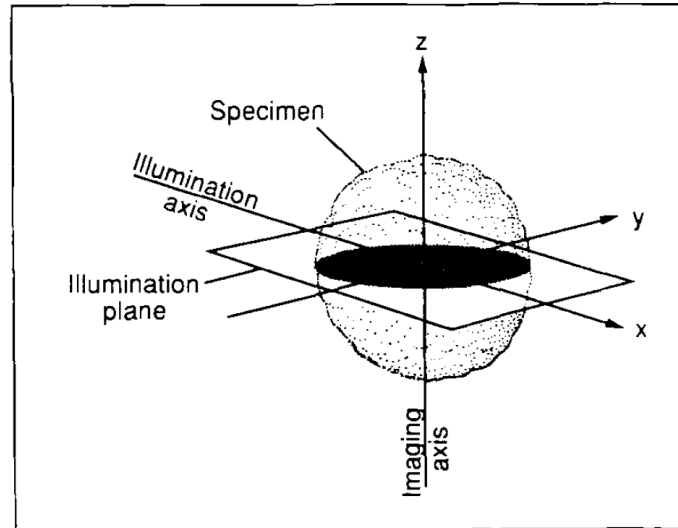


Figure 2.2: Orientation of the illumination axis, imaging axis and specimen for OPFOS imaging. Taken from. Voie *et al.* 1993.

In 1994, Ernst Stelzer's laboratory was trying to improve the axial resolution of confocal microscopy. They developed an oblique illuminating confocal microscope called a confocal theta microscope (Lindek *et al.* 1994; Lindek and Stelzer 1994; Stelzer *et al.* 1995). Their 1995 article cited Voie's work on OPFOS, and theta confocal microscopy appeared to lay the foundation for their subsequent version of a light sheet microscope device called selective or single-plane illumination microscopy (SPIM).

In 2004, a publication from Stelzer's group (Huisken *et al.*) demonstrated the usefulness of light-sheet fluorescence microscopy for investigating embryonic development. This article also showed images of developing Medaka embryos and *Drosophila Melanogaster* embryo and ganalion cells monitored during 17 hours. The spatial resolution announced was $6\ \mu\text{m}$ with a field of view of $1.5 \times 0.9\text{mm}$. Although Voie and colleagues published several articles (Voie *et al.* 1993; Voie and Spelman 1995; Voie 1996, 2002) claiming that light-sheet was very efficient, it is the Huisken *et al.*'s paper that imposed light-sheet microscopy among biologists. (Figure 2.3)

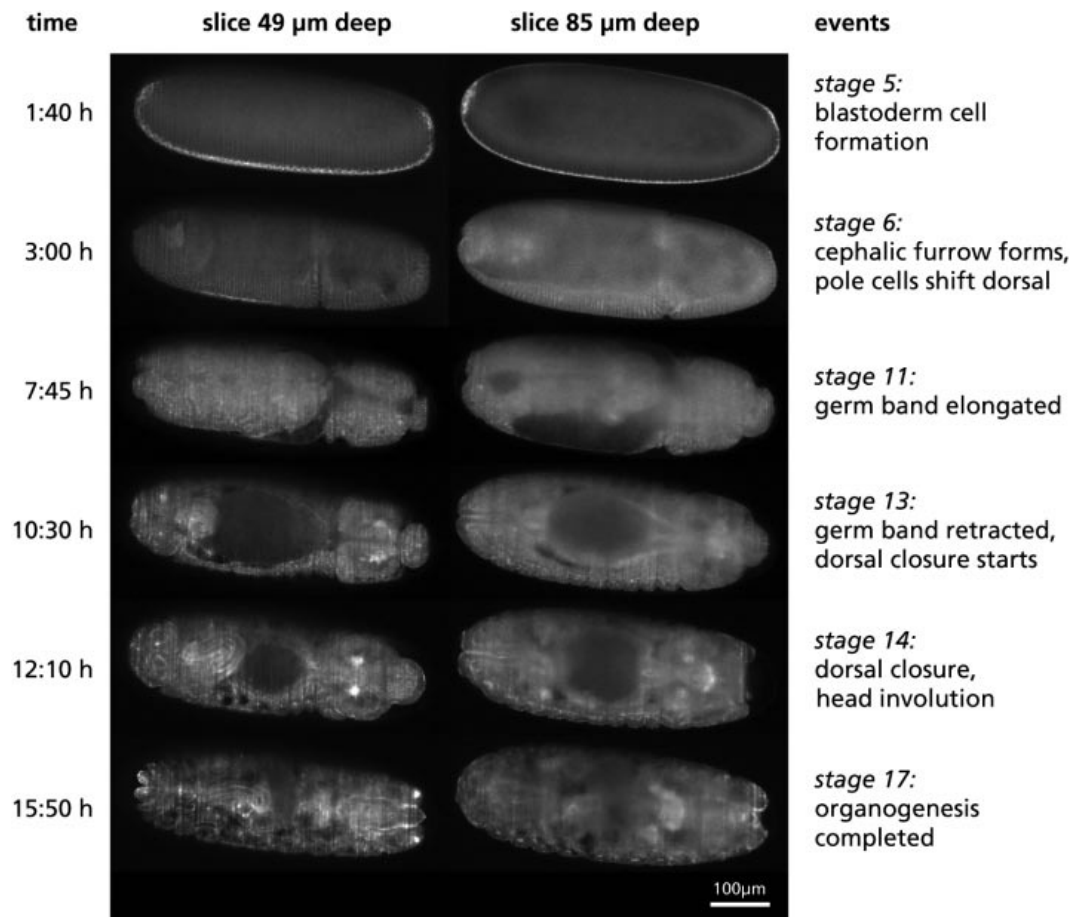


Figure 2.3: Time-lapse imaging of *Drosophila melanogaster* embryogenesis. Six out of 205 time points acquired are shown. At each time point, 56 planes were recorded, from which two (at depths of 49 μm and 85 μm below the cortex) are shown. Taken from Huisken et al 2004.

Name	Signal	Resolution	Fluorescent	Size	Imaging Time	Cost (\$)	Photobleaching	Citation
Magnetic resonance imaging	Magnetic	mm	No, contrast agent	M	hr	Millions	NA	Lauterbur 1973
Computed tomography	Radioactive	<mm	No, contrast agent	cm	min	Millions	NA	Kalender 2006
Confocal	Laser	<micron	Yes	micron	msec	200,000	Yes	Minsky 1961
2-Photon	Laser	<micron	Yes	mm	msec	500,000	Less	Denk et al. 1990
Light sheet fluorescence microscopy	Laser	micron	Yes	>cm	msec	30,000	Least	Voie et al. 1993

Figure 2.4: Microscopes comparison. Adapted from Santi 2011.

Fluorescent refers to whether the instrument is capable of detecting fluorescent probes. Size refers to the size of the specimen that can be imaged. Time refers to the average time it takes to make a stack of the specimen that is within the size range of the imaging device. Cost is approximate, and photobleaching refers to how quickly the fluorescent probe fades. NA not applicable.

2.1.2 Modern history of light sheet fluorescence microscope

A number of other light sheet fluorescence microscopes have been developed since Voie's original description.

In 2007, Dodt *et al.* (Dodt *et al.* 2007; Becker *et al.* 2008) added a dual-sided illumination to light-sheet microscope. Becker's team wanted to image large specimens such as an entire brain and make the illumination more uniform. This was the first publication on light sheet fluorescent microscopy with two sheets. This improvement minimized shadow artifacts, which are dark objects in the final image that are produced when the sheet encounters an opaque structure during its travel across the sample.

A digital scanned laser light sheet fluorescence microscope

In 2008, Keller *et al.* (Keller *et al.* 2008; Keller and Stelzer 2008; Keller *et al.* 2010) proposed another type of light-sheet microscope called a digital scanned laser light sheet fluorescence microscope (DSLM) to record an entire zebrafish embryo (Figure 2.5):

« To achieve the imaging speed and quality for recording entire embryos, we developed digital scanned laser light sheet fluorescence microscopy (DSLM). The idea behind DSLM is to generate a “plane of light” with a laser scanner that rapidly moves a micrometer thin beam of laser light vertically and horizontally through the specimen. »

Keller *et al.* 2008

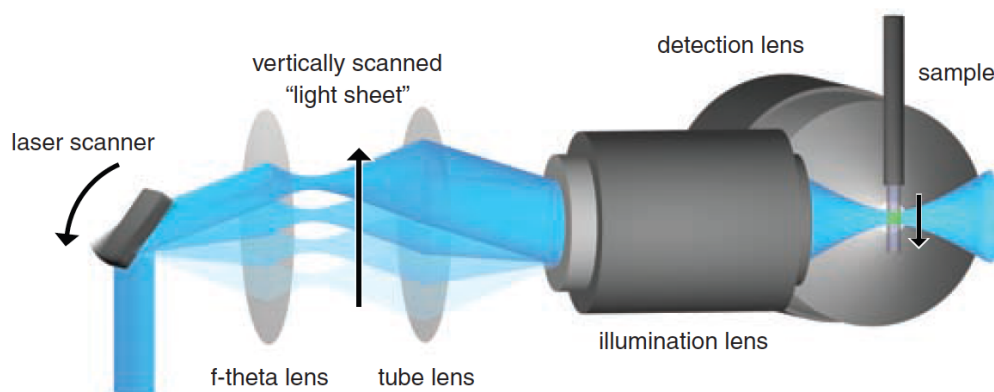


Figure 2.5: Digital scanned laser light sheet microscopy. The laser beam illuminates the specimen from the side and excites fluorophore along a single line. Keller *et al.* 2008.

In contrast to what was standard light sheet at that time, this new technique had several advantages. For example, in DSLM each line in the specimen was illuminated with the same intensity, crucial for quantitative imaging of large specimens. Also, since in DSLM a scanning mirror creates the sheet of light, the microscope does not rely on apertures to form the laser profile, which reduces optical aberrations and provides a better image quality. DSLM

allows generating illumination patterns and thus was later used in structured illumination. In the 2008 article, Keller *et al.* claimed to image 63 million voxels per second, with a signal-to-noise ratio of 1000:1, with a lateral and axial resolution of 300 and 1000nm, respectively and a total field of view of 700 μ m x 700 μ m. Using a very low energy excitation, they could image zebrafish embryos during 24h and subsequently track cell displacement.

Rigidly coupling illumination lens and observation objective

In order to record an entire specimen, the light sheet needs to be displaced along the z-axis. Before 2008, the specimen itself was moved. This strategy resulted in a strong limitation in acquisition rate. To overcome this limitation, in Holy's lab, Holekamp *et al.* (2008) created a light sheet microscope where the illumination lens and the observation objective were rigidly coupled that both could be rapidly translated together to attain fast three-dimensional imaging. They called their device objective-coupled planar illumination (OCPI) microscopy. Notice that this paper is the first recording of neuronal activity with a light-sheet microscope. The authors used a synthesized calcium indicator Oregon Green BAPTA injected in an excised mouse brain. 88 neurons recorded at 200Hz. Due to the geometry of the sample, Holekamp *et al.* decided to put excitation and detection arms of the microscope at +/- 45° to the z-axis. In Turaga and Holy (2008), they improved the OCPI trying to avoid low-order aberrations that arise from bulk index mismatch: the immersion fluid has a refractive index $n=1.33$, while the tissue sample typically has an average refractive index of 1.40.

An oblique plane microscope

In 2008, Dunsby inspired by the Highly Inclined Laminated Optical sheet microscopes that had been recently reported by Tokunaga *et al.* (2008), developed a light sheet fluorescence microscope that used a single, high numeric aperture (NA) objective to both illuminate a plane in a sample and to collect the fluorescence. He called this technique the oblique plane microscopy. The microscope from Tokunaga *et al.* is similar to SPIM but with two significant differences: the illumination and detection beams are not at 90° and the sheet of illumination does not align in the focal plane of the imaging system used to collect fluorescence (Figure 2.6).

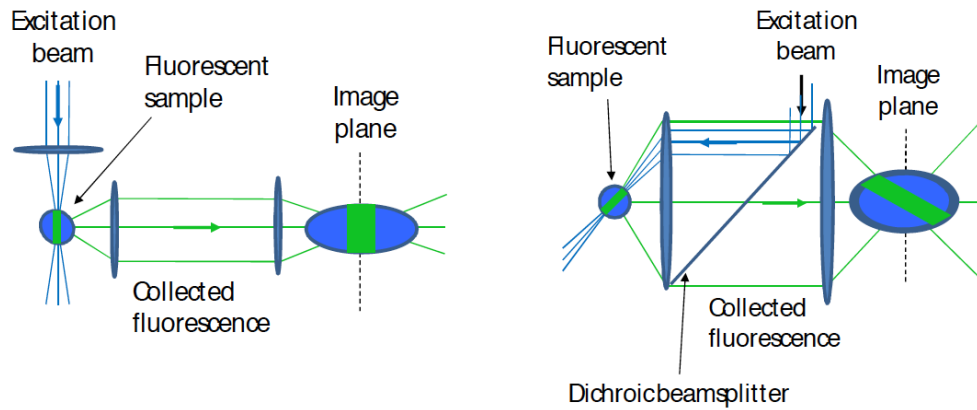


Fig 2.6: Left: Experimental geometry for SPIM. Right: Simplified experimental geometry for HILO. The green stripe on the fluorescent sample illustrates the region where fluorescence is excited. Adapted from Dunsby 2008.

Scattering limitations of light-sheet

As we mentioned before, residual index of refraction mismatches undermine the performance of light-sheet microscopy, because it deteriorate the illumination quality and thus the optical sectioning by introducing out-of-focus background. Image resolution is also degraded due to scattering and aberration. In the following part of this chapter, we will see that the use of two-photon illumination in light-sheet microscopy can overcome these limitations.

Photodamage: confocal vs. light-sheet microscopy

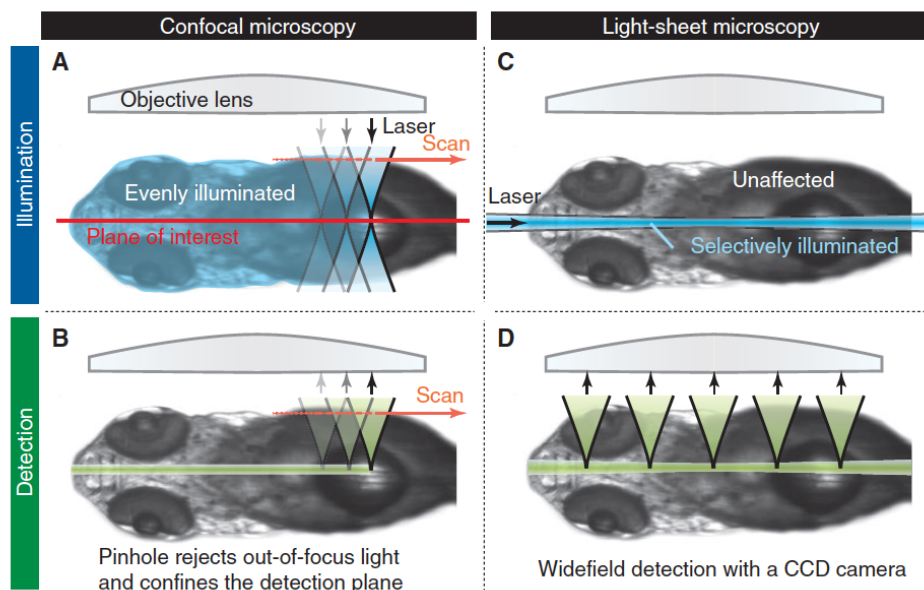


Figure 2.7 Advantages of light-sheet microscopy compared with confocal microscopy. To illustrate the difference between laser scanning confocal microscopy (A, B) and light-sheet microscopy (C, D), the processes of

illumination (A, C) and detection (B, D) are split. In confocal microscopy, a tightly focused laser beam is scanned across the sample (A), thereby exposing the sample to high-intensity light not only in the plane of interest, but also above and below. (B) A pinhole rejects much of the excited fluorescence and confines the image to the plane of interest. In light-sheet microscopy, a light sheet from the side (C), which overlaps with the plane of interest, illuminates the sample in a thin slice. Photobleaching is thereby considerably reduced. (D) All the fluorescence is collected and imaged onto a CCD camera. From Huisken and Stainer 2009.

2.1.3 Resolution of a light-sheet: an analytical framework

In the following, we summarize the analytical framework of light sheet microscopy and show how to evaluate the spatial resolution of this imaging technique.

For spatially invariant blurring, image formation through an optical system can be expressed as

$$I(x, y)]_{z=0} = O(x, y, z) \otimes PSF(x, y, z)$$

Where $I(x, y)]_{z=0}$ is the image formed with the imaging lens focused at $z = 0$, $O(x, y, z)$ is the 3-D structure of the object that is imaged and $PSF(x, y, z)$ is the point spread function of the microscope. In any optical system, the point-spread function is the product of i the illumination intensity and g the blurring function of the lens (Hiraoka 1990):

$$PSF(x, y, z) = i(x, y, z) \cdot g(x, y, z)$$

In most optical imaging techniques, the illumination is coaxial with the imaging axis and uniform upon or through the object. In these cases the illumination intensity distribution is constant, and thereby the PSF reduces to $g(x, y, z)$. In our case - light sheet imaging - there are two differences: the illumination arm is orthogonal to the imaging axis and the illumination intensity distribution follows a gaussian shape and depends on the optical system. The illumination system is aligned so that the intensity distribution is co-planar with the depth of field of the imaging camera.

Diffraction limitation

In the case of diffraction-limited optical components, g the blurring function of the lens is described by

$$g(x, y, z) = \left[\frac{2 * J_1 \left(\frac{2\pi}{\lambda} \sqrt{x^2 + y^2} * \sin(\alpha) \right)}{\frac{2\pi}{\lambda} * \sqrt{x^2 + y^2} * \sin(\alpha)} \right]^2$$

Where J_1 is the first-order Bessel function, α is the acceptance angle of the lens.

The radius of the central bright spot (Airy pattern) gives the lateral resolution of a diffraction limited imaging system:

$$r_0 = \frac{0.61 * \lambda}{n * \sin(\alpha)}$$

Pixellation

In the case of a digital imaging set-up, the effect of pixelisation can be characterized by the function $p(x, y)$ equal to one inside of a square pixel, null otherwise. Then:

$$I(x, y)_{z=0} = (O(x, y, z) \otimes [i(x, y, z) \cdot g(x, y, z)]) \otimes p(x, y)$$

Thus the square sides length p_0 of the pixel must be taken into account.

Gaussian optics

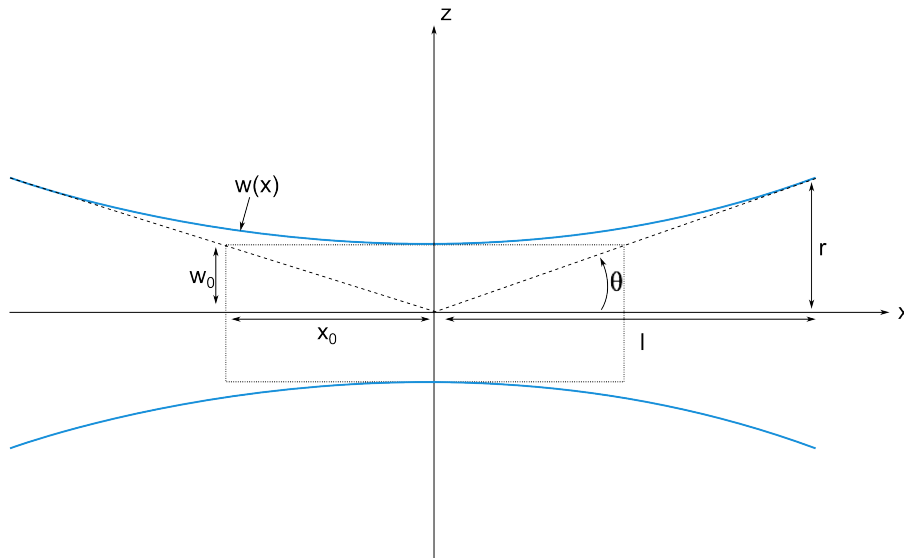


Figure 2.8: Scheme of a light sheet where l is half width of the field of view in the sample. The thickness of the beam waist is $2a$, and the confocal parameter length of the beam is $2b$

In the focal zone, the laser spot has a Gaussian intensity distribution. In the x - z plane, the variation in the intensity can be expressed as

$$i(x, z) = i(x, z = 0) \cdot e^{\frac{-2z^2}{w(x)^2}}$$

The spatial extent of the laser spot is the positions at which the intensity is superior to $1/e^2$ of its maximum value.

In Gaussian optics, the shape of the beam, $w(x)$, is hyperbolic and follows the Cartesian equation of an hyperbole:

$$\frac{w^2}{w_0^2} - \frac{x^2}{x_0^2} = 1$$

Where

$$w_0 = \frac{2 * \lambda * f}{\pi}$$

With λ the excitation wavelength and f the focal length of the lens. Or

$$w_0 = \frac{\lambda}{\pi * NA}$$

With NA the numerical aperture of the illumination arm.

Thus the full width half maximum (FWHM) of the beam profile, often used to designate the minimum lateral size that a diffraction-limited focused beam of light can reach, is

$$FWHM = \sqrt{2\ln 2} * w_0 = \sqrt{2\ln 2} * \frac{\lambda}{\pi * NA}$$

Note that consequently, a laser beam with a waist thickness of $w_{0,i}$ has, after crossing a lens with a focal f , a waist thickness $w_{0,s}$

$$w_{0,s} = \frac{f * \lambda}{\pi * w_{0,i}}$$

From the hyperbole equation, one can easily understand that then:

$$w(x) = w_0 \sqrt{1 + \left(\frac{x}{x_0}\right)^2}$$

The focal region of the beam, called the Rayleigh length, where the size of the beam is almost constant, is by definition limited by $\pm x_0$. Thus:

$$x_0 = \frac{n * \pi * w_0^2}{\lambda}$$

With n the refractive index

Resolution of a light sheet

In light sheet microscopy the *lateral* and *axial* resolutions of the final image are decoupled: the lateral resolution is fixed by the detection optics and the axial resolution is determined by both the thickness of the light sheet and the detection optics.

The *lateral resolution* of a light sheet is given by two terms: a diffraction term and a pixellation term p_0 . If p_0 is less than $r_0/2$, then the lateral resolution only depends on the diffraction effects given the Nyquist criterion for spatial sampling. Thus the lateral resolution is given by the diffraction term $r_0 \sim \frac{\lambda}{n * \sin(\theta)}$

Then by definition of the numerical aperture, $r_0 \sim \frac{\lambda}{NA}$ with λ the excitation wavelength and NA the numerical aperture of the illumination arm.

The *axial resolution* of the light sheet is limited by two terms: a diffraction term r_0 (the lateral resolution) and a divergence term r due to the gaussian beam. Like for the lateral resolution, the diffraction effect is given by λ/NA . The field of view of the light sheet microscope is defined as the extent in the x-direction where the thickness of the light sheet remains below x_0 , the so-called confocal parameter of the illumination focus.

To evaluate the *best accessible axial resolution* at a distance l along the x-axis from the waist center, let L be the maximum axial height of our light sheet.

$$L = r + r_0$$

$$L = l * \tan(\theta) + \lambda/NA$$

In the small angles limit,

$$L \approx l * \sin(\theta) + \lambda/NA$$

Since by definition, $NA = n * \sin(\theta)$ with n the refractive index, we thus have

$$L \approx l * NA/n + \lambda/NA$$

Thus L is minimal when

$$NA = \sqrt{\frac{n * \lambda}{l}}$$

With this one can easily calculate what numerical aperture one should use to have the best axial resolution.

Thus in the small angles limit,

$$L \approx 2 \sqrt{\frac{l * \lambda}{n}}$$

If you assume we are in the case of a gaussian beam profile, the exact minimization of L , without any hypothesis, leads to:

$$L(l) = \sqrt{\frac{2 * l * \lambda}{\pi * n}}$$

2.2 Recording the living: 2-photon light sheet microscopy

2.2.1 The first 2-photon light sheet microscope

Compared to both confocal and 2-photon point scanning microscopy, light sheet microscopy has the advantage of combining low phototoxicity and high acquisition speed with a good spatial resolution. Still when one needs to image deep in scattering tissues, the use of light-sheet microscopy remains limited because it is a linear microscopy technique.

As we saw before, choosing the good microscope to image living tissue is fundamental in biology. The biologist's list of concerns could be: spatial resolution, temporal resolution, light scattering, tissue absorption and photodamage. Often optimizing any one of these parameters means sacrificing the others. For example, 2-photon microscopy offers a high penetration depth in scattering tissue but a low acquisition speed. Whereas light-sheet microscopy excels in acquisition speed but scattered photons limit its penetration depth into tissue and decrease its axial resolution

In 2011, Fraser's (Truong *et al.* 2011) team developed a two-photon scanned light-sheet microscopy combining the advantages of 2-photon point scanning microscopy and light-sheet microscopy. They used near-infrared laser pulses to create a two-photon excitation light sheet, exploiting both non-linear excitation to achieve high penetration depth and the orthogonal geometry of light sheet illumination to achieve high acquisition speed and low photodamage. They used this technique to record drosophilae embryos development.

The 2-photon light sheet offers many advantages compared to 1-photon light sheet:

- Spatially confined volume of excited fluorophore due to 2-photon transition makes scattered emitted light less important and preserves axial resolution of the sheet
- Infrared wavelength of the illumination arm reduces the scattering of excitation (Figure 2.9)
- Spatially confined volume of excited fluorophore also leads to less fluorescent background

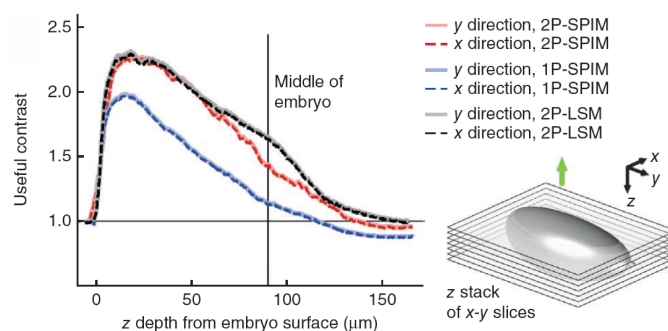


Figure 2.9: Quantitative analysis of the z depth penetration performance of the three imaging modalities. 2-photon light-sheet microscope (2P-SPIM), 1-photon

light-sheet microscope (2P-SPIM), 2-photon laser scanning microscope (2P LSM). Taken from Truong *et al.* 2011.

Several other implementations were recently proposed. For example, the use of Bessel beam illumination in Fahrbach *et al.* 2010 is very promising. It reduces artifacts, and increases image quality and penetration depth in dense sample. Also the recent development of adaptive optics coming from Betzig's lab allows to correct aberration artifacts using pupil segmentation (Ji *et al.* 2010).

Two years after Fraser's team paper, I began my PhD. As we will see in the next section of the chapter, my main purpose was to develop a two-photon scanned light-sheet microscope and adapt it to record the brain activity of zebrafish larvae.

2.2.2 Comparison 1- and 2-photon light sheet

Resolution and field of view

The fluorescence signal rate of 2-photon light sheet is proportional to the squared illumination light intensity:

$$F_{2p} \sim i^2 \sim \left(\frac{P}{\pi * w^2} e^{-\frac{2r^2}{w^2}} \right)^2 = \frac{P^2}{\pi^2 * w^4} e^{-\frac{4r^2}{w^2}} = \frac{P^2}{\pi^2 * w^4} e^{-\frac{2r^2}{(w/\sqrt{2})^2}}$$

Whereas for 1-photon:

$$F_{1p} \sim i \sim \frac{P}{\pi * w^2} e^{-\frac{2r^2}{w^2}}$$

As we saw before, the *FWHM* for 1-photon light sheet is written:

$$FWHM_{1p} = \frac{\sqrt{2 \ln 2} * \lambda_{1p}}{\pi * NA_{1p}}$$

For the 2-photon light sheet, F_{2p} is a gaussian but with a width reduced by a factor $\sqrt{2}$, then the *FWHM* reads:

$$FWHM_{2p} = \frac{\sqrt{\ln 2} * \lambda_{2p}}{\pi * NA_{2p}}$$

Note that the wavelength in 2-photon is twice the 1-photon wavelength ($\lambda_{2p} \sim 2 * \lambda_{1p}$) thus

$$\frac{FWHM_{2p}}{FWHM_{1p}} = \frac{\sqrt{2} NA_{1p}}{NA_{2p}}$$

With a $NA_{2p} = \sqrt{2} NA_{1p}$ one reach the same axial resolution.

Illumination

We can also compare static and scanned light sheet under 1-photon ($\lambda_{1p} = 488$ nm) or 2-photon ($\lambda_{2p} = 927$ nm) excitation as in Power and Huisken 2017. Let us characterize the fluorophore photo-physics in both cases. Taking the example of the fluorophore eGFP used in GCaMP lines, we have a molecular cross-sections and quantum efficiencies of:

$$\begin{aligned} \sigma_{1p} &= 2.26 \times 10^{-20} \text{ m}^2, \phi_{1p} = 0.6 \text{ SI for the 1-photon excitation} \\ \sigma_{2p} &= 3.9 \times 10^{-56} \text{ m}^4 \cdot \text{s}, \phi_{2p} = 0.77 \text{ SI for the 2-photon excitation (2photon} \\ &\text{absorption Drobizhev } et al.) \end{aligned}$$

The number of photons produced by fluorescence per second and per fluorophore is (for the exact calculation see Pawley et al 1996):

$$\begin{aligned} n_{1p} &= \left(\frac{\pi NA^2}{hc\lambda_{1p}} \right) * P * \sigma_{1p} * \phi_{1p} \\ n_{2p} &= \frac{0.664}{f_p \tau_p} \left(\frac{\pi NA^2}{hc\lambda_{2p}} \right)^2 * \langle P \rangle^2 * \sigma_{2p} * \phi_{2p} \text{ if the pulse distribution of the laser is} \\ &\text{a Gaussian} \end{aligned}$$

Where h is the Planck constant, c light speed in vacuum, P the laser power, NA the numerical aperture of the illumination arm, f_p the pulse frequency of the femto laser τ_p the pulse duration and $\langle P \rangle$ the average laser power.

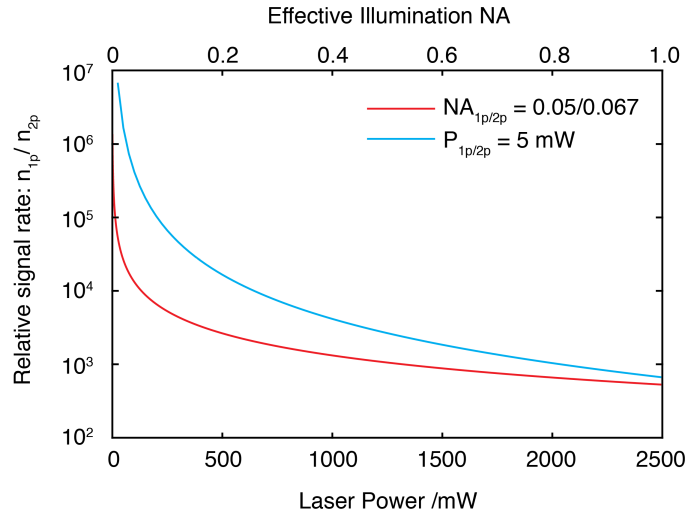


Figure 2.10: Relative rates of signal for 1 or 2-photon excitation as a function of numerical aperture (red) and laser power (blue). In these curve, the signal rate is calculated such that $NA_{2p} = NA_{1p} * (\lambda_{2p} / (\sqrt{2} \lambda_{1p}))$ to avoid contribution due the different beam waist, since in 2-photon excitation the light sheet is thinner by a factor of $\sqrt{2}$ and thicker by a factor of $\lambda_{2p} / \lambda_{1p}$. Here $f_p = 80$ MHz and $\tau_p = 140$ fs.

As we could expect, at a given laser power the signal level for 1-photon excitation is very superior to the 2-photon case. However, in 2-photon light sheet it is possible to use very high laser power without photodamage. For example Tomer *et al.* (2012) use 300mW for 2-photon excitation at 940nm vs. 0.36mW for 1-photon excitation at 488nm, for identical imaging tasks in *Drosophila*. In our lab, we use 250mW for 2-photon excitation at 930nm vs. 1mW for 1-photon excitation at 488nm to record zebrafish neuronal activity with single-cell resolution at 20 Hz, using GCaMP5 calcium indicator.

2.3 Imaging zebrafish brain

2.3.1 Zebrafish: a model animal for neuroscience

For the last two decades, zebrafish has become an important new model system in neuroscience. Native from Asia, *Danio rerio* is today a very popular organism in scientific labs (Figure 2.12). There are multiple reasons to use this species in biology and in neuroscience. Zebrafish displays a rich repertoire of behaviors even at larval stage and it presents high physiological and genetic homologies to mammals. Its genome is fully sequenced and a large panoply of genetic tools is now available for zebrafish. Zebrafish reproduction is quick and abundant such that each female can lay a hundred of eggs once a week. Zebrafish was originally used mostly in developmental biology since the main organs develop within the first day post fertilization and the development process can be easily monitored. At this early stage, zebrafish is indeed transparent - pigments are only present in the eyes and a few on the skin - which permits exceptional optical access to the brain. The identification of a new mutation that could block the apparition of pigments outside of the eyes (Lister *et al.*, 1999) lead to the design of the so-called Nacre zebrafish line that lacks skin pigments, thus improving the advantages of zebrafish larvae for imaging approaches.

The zebrafish larval brain is relatively small (of the order of 10^5 neurons at 6 dpf), yet the animal already possesses a large variety of behaviours such as optomotor response, optokinetic reflex, goal-directed navigation (phototaxis, chemotaxis, thermotaxis...), prey capture, rheotaxis, etc. The small size of the zebrafish brain and its transparency has enabled the development in the last few years of whole brain imaging techniques (Ahrens *et al.* 2012, Portugues *et al.* 2014, Ahrens *et al.* 2013, Panier *et al.* 2013, Wolf *et al.* 2015) to record the neuronal activity of the entire brain. Combined with virtual reality assays where the fish is fixed under the microscope in a virtual world, these techniques provide a unique opportunity to unravel the neuronal substrate of complex behaviors. Furthermore, recent progress in genetics and automated behavioral phenotyping methods have led to important results in characterizing which neuronal types are involved in particular behaviors (Zhang *et al.* 2017, Muto *et al.* 2017).

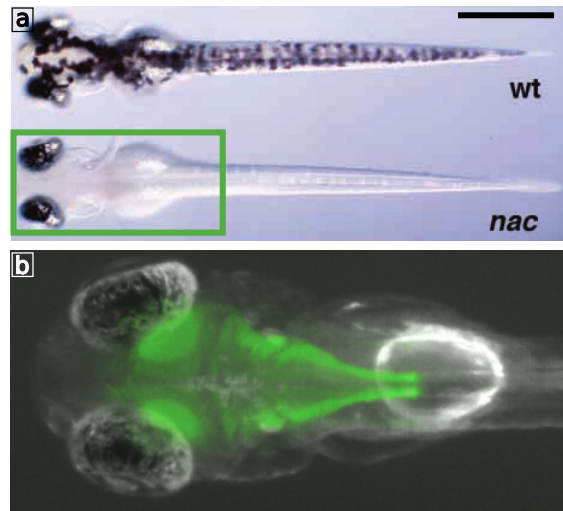


Figure 2.11: **a**, Comparison between a wild type zebrafish larva (up) and larva from the *nacre* genetic line (down). Bar line: 500µm. **b**, Brain of a zebrafish larva imaged with a light sheet microscope. The protein GCaMP is expressed under the control of the HUC promoter in almost all neurons. Taken from LJP.

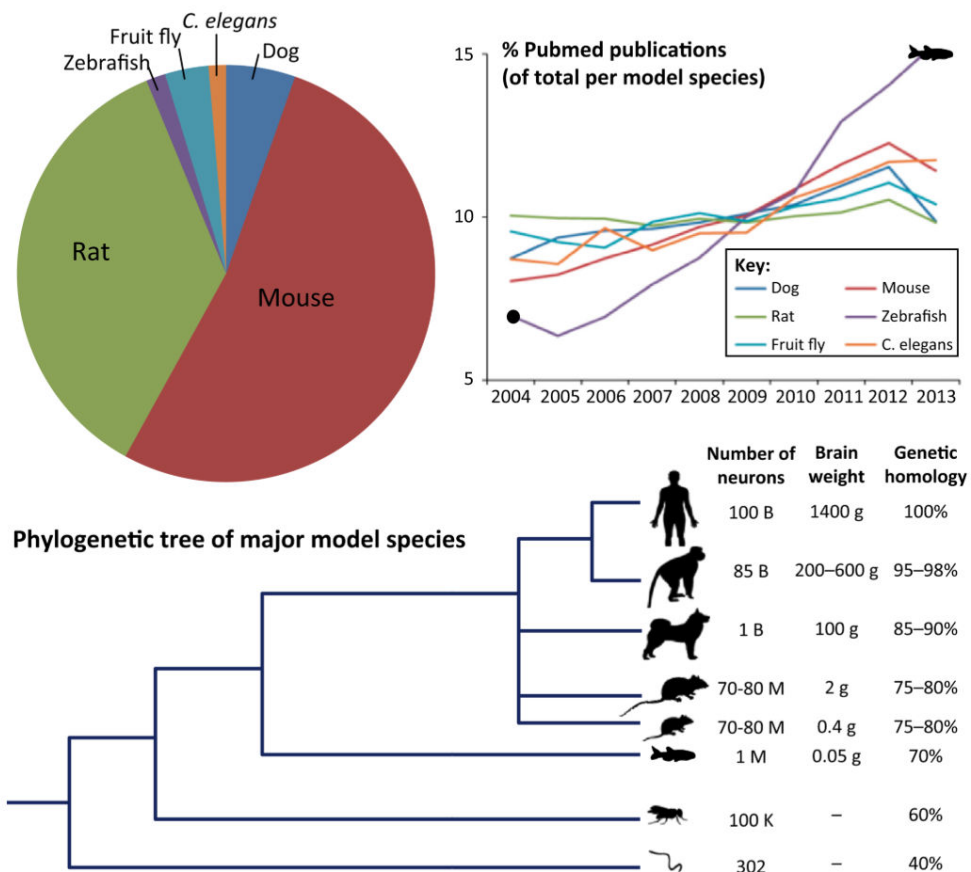


Figure 2.12: Left : Number of PubMed publications in 2004-2013 for various model animals. In total 532 000 publications for mice, 361 000 for rats, 54 000 for dogs, 34 000 for fruit flies, 15 000 for zebrafish, and 13 000 for nematodes

(*Caenorhabditis elegans*). Right Up: Number of publications per species normalized by the total number of publications in 2004-2013. Right Down: Phylogenetic tree of major model species. Taken from Stewart *et al.* 2014.

2.3.2 Imaging zebrafish brain

Brain functions rely on multiple interactions between several regions of the nervous system. The number of neurons involved in a given function is highly variable going from a few tens to thousands of cells. To reach a detailed understanding of this complex system requires to record population activity at cellular level of the entire circuit, ideally at millisecond resolution.

As illustrated in chapter 1, the past decade have seen the development of numerous techniques to monitor the development of living systems (Denk *et al.* 1990; Huisken *et al.* 2004; Keller *et al.* 2008) and later the functions of these systems, taking advantage of protein engineering that enables optical-based measurement of neuronal activity (Siegel and Isacoff 1997; Chen *et al.* 2013; Cao *et al.* 2013). Confocal (Minsky 1955) and then two-photon microscopy (Denk *et al.* 1990) have been the most common methods to perform such functional imaging. To increase the number of neurons that could be simultaneously monitored, several “strategies” have been developed including high-speed random-access imaging using acousto-optical deflectors (Salome *et al.* 2006; Katona *et al.* 2012; Grewe *et al.* 2010) or simultaneous multi-point excitation (Quirin *et al.* 2014). Still these methods proved to be too slow to record the entire brain of zebrafish larvae. Whole brain imaging thus required to successively record different part of the brain, in different animals, and then to patch together these different regions (Ahrens *et al.* 2012). Such a sequential approach only provided a mean activity pattern, but did not allow to analyze correlated activities between distant brain regions or large-scale dynamic fluctuations.

2.3.3 Light sheet imaging of zebrafish brain

When I started my PhD in 2013, a new imaging set-up for zebrafish had just been developed independently by the Laboratoire Jean Perrin (Panier *et al.*) and the HHMI Janelia farm, USA (Ahrens *et al.* 2013), which overcame the two-photon point scanning and confocal limitations. As we saw in chapter 1, since 2004 (Huisken *et al.* 2004) light sheet microscopy emerged in developmental biology (Huisken *et al.* 2004; Stelzer *et al.* 2007; Keller *et al.* 2008) as a new tool to do volumetric recording at high imaging speed with a good spatial resolution (see chapter 1). In 2008, Timothy Holy was the first to use this technique to record the neuronal activity on an ex-vivo mouse preparation. LJP and Janelia groups implemented this technique in zebrafish larvae expressing GcaMP calcium reporter panneurally, to record the activity of almost 80 000 neurons at 0.7 Hz, or 25 000 neurons at 4Hz. This new technique thus offered the possibility to identify large-scale functional ensembles of neurons spanning several brain regions (figure 2.13 and figure 2.14), using activity correlation

analysis. With these new sets of data, rich structure in space and time were accessible, offering a new insight in brain functions.

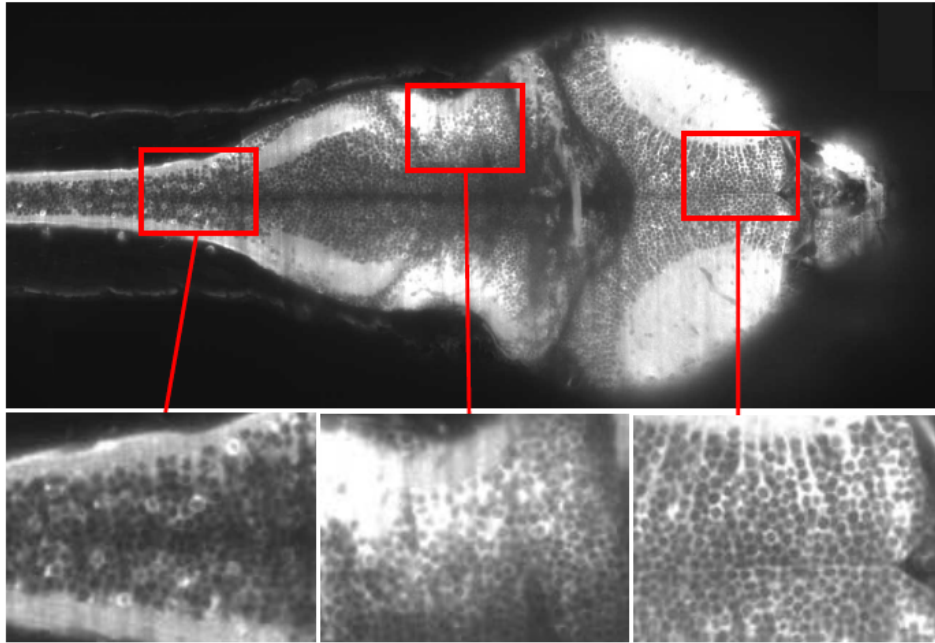


Figure 2.13: Image of zebrafish brain recorded with light-sheet microscopy at an acquisition frequency of 10 Hz. Adapted from Panier *et al.* 2013.

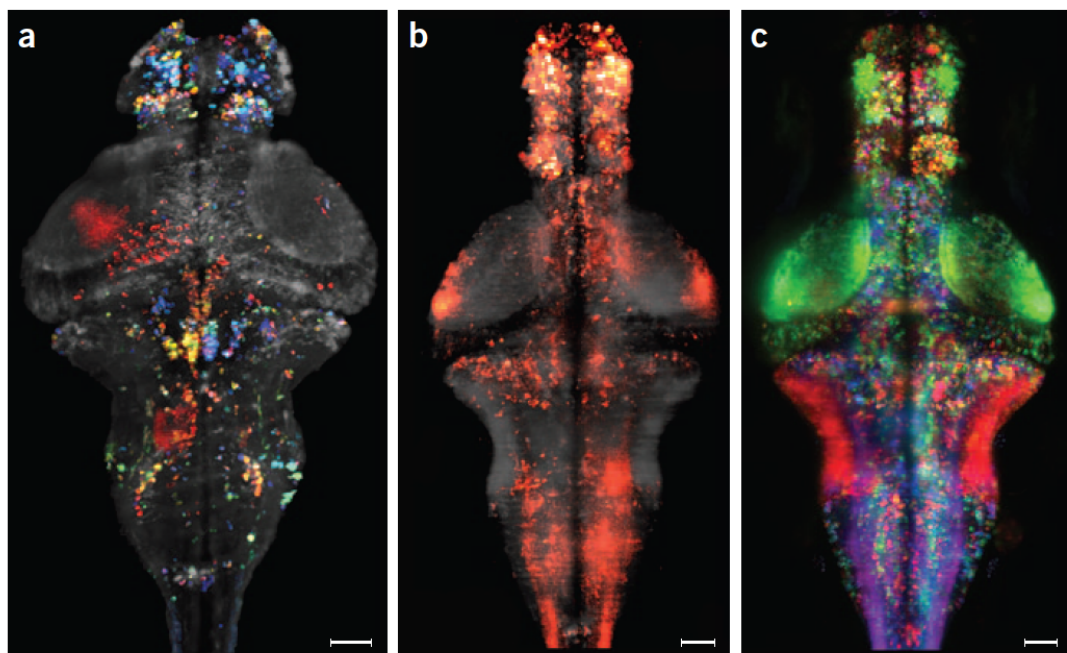


Figure 2.14: Modern light-sheet microscopy in systems neuroscience. **a.** Activity in the brain of a larval zebrafish expressing a genetically encoded calcium indicator, imaged with a light-sheet microscope. Each color represents neural activity at a different time point. **b.** Activity in the brain of a larval zebrafish at a single time point, measured with a genetically encoded calcium indicator. **c.** Computational map of correlated activity across the same brain as in b. 50 μm . Taken from Ahrens *et al.* 2013.

Data analysis limits

Analyzing and navigating through the massive datasets produced by whole brain recordings pose significant computational and theoretical challenges. The first step consists in morphological registration. In order to compare activity obtained from different animals, one needs to align several volumetric brain images onto a unique reference brain. This can be done using the Computational Morphometry Toolkit (CMTK), an algorithm that was originally developed for Magnetic Resonance Imaging data. Another ongoing problem is clusterisation. In these data sets, one always seeks for stereotyped patterns of correlated population activity. Numerous mathematical tools are available to do so, but they generally fail to provide a clear estimate of how much information is lost upon clusterisation. Quantifying, standardizing and optimizing these clusterisation techniques is becoming more and more necessary to analyze these large data sets. Beyond these clusterisation approaches, the ultimate goal for neuroscientist is to infer the effective connectivity within these large populations. Knowing where the links are and then what are the weights of these links may eventually enable neuroscientists to build microscopic models of neural computations at the brain scale. During the last decade several methods (Cocco *et al.* 2017; Schneidman *et al.* 2006) were developed to infer the connectivity matrix from population recordings but the size of whole brain activity recordings currently limits the use of these inference methods. The outcome of these inference methods needs to be confronted with ground truth data. Recently Hildebrand *et al.* (2017) demonstrated the possibility to trace axonal and dendritic arborization across the zebrafish larva using high-resolution serial-section electron microscopy. By combining whole brain functional imaging with connectomics and computational inference methods, one may hope to unravel computational principles underlying complex behaviors.

Limitations

Despite the significant increase in data throughput brought by light-sheet functional imaging techniques, some important limitations still remain. The current acquisition speeds are far below the temporal resolution of single neuronal spikes (1-10ms). This limitation owes both to the frame-rate of CCD cameras and to the intrinsically slow dynamics of calcium sensors (in the order of a few tens of milliseconds). This second issue might be solved in the near future with the use of voltage indicators, which directly report membrane potential. It will likely motivate the development of even faster volumetric imaging methods. The latter might also benefit from post-processing computational techniques such as super resolution, that allow to reach effective temporal resolution beyond the sampling rate (Tubiana *et al.* 2017, see Annex 1 for more details).

When I started my PhD, current implementations of light-sheet based functional imaging suffered from one strong limitation in the particular context of behavioral neuroscience. Since the photoreceptors of zebrafish eyes are extremely sensitive to blue light (Fernandes *et al.* 2012; Risner *et al.* 2006), the intense 1-photon excitation produced a significant visual stimulation. This issue

precluded the use of this technique to study visually-guided behaviors. In 2014, Vladimirov et al showed that, provided that the light-sheet was not directed towards the animal eyes, it was still possible to evoke the OMR behavior under 1P light-sheet imaging. However, this robust behaviour is not driven by the blue and UV cones (Portugues *et al.* 2014) and is not even affected by ablation of the optic tectum (Roeser and Baier 2003), the largest visual center in fish. To have a better control over the visual stimulation, we developed a 2-photon version of the light sheet microscope. Since the zebrafish is blind to infrared light, this configuration guarantees that the illumination beam does not evoke any visual response.

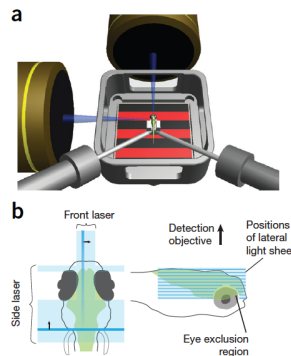


Figure 2.15: Whole-brain functional light-sheet imaging of fictively behaving zebrafish used by Vladimirov et al, 2014. **a.** Illustration of experimental setup in which two laser beams enter through windows in a custom chamber and scan the brain of a paralyzed larval zebrafish positioned above a diffusive screen on which visual scenes are projected. Two extracellular suction electrodes record fictive swimming from the tail. The detection objective located above the chamber is not shown. **b.** Schematic of the laser-scanning strategy. Taken from Vladimirov et al 2014.

Note:

Since the first results obtained in 2013, several labs tried to improve light-sheet microscopy for zebrafish, like Yang et al 2015 with their dual-slit confocal light sheet microscopy which increase the axial resolution. Also Chhetri *et al.* improved the spatial and the temporal resolution of the traditional light sheet developing an isotropic multiview (IsoView) light-sheet microscopy, which rapidly images large specimens via simultaneous light-sheet illumination and fluorescence detection along four orthogonal directions.

2.2 The 2-photon Light-sheet microscope for zebrafish

To overcome the visual disturbance of the 1-photon light-sheet microscope and to evaluate the relevance of 2-photon excitation for whole-brain visual studies we built a 2-photon light-sheet microscope. We performed first tests with Pierre Mahou, Willy Supatto and Emmanuel Beaufreire at the Laboratoire d'Optique et Biosciences of Ecole Polytechnique. I then built a 2-photon light-sheet microscope (Figure 2.16) specifically designed for zebrafish functional imaging in the Laboratoire Jean Perrin, and ran whole brain activity recordings under visual stimulation. To compare 1P and 2P excitation regimes, I ran the same visual stimulations protocols for the same fish under both 1-photon and 2-photon light-sheet imaging.

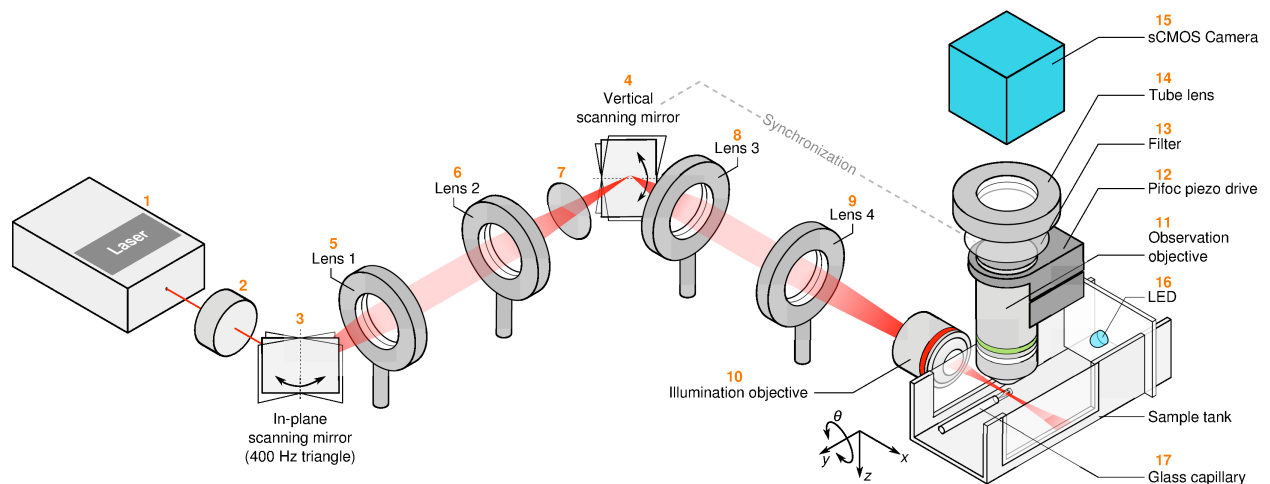


Figure 2.16: Scheme of the 1P/2P light-sheet microscopy setups. The optical components are listed in Supplementary Table 1 of Wolf *et al.* 2015.

We published this new technique in Wolf, S., Supatto, W., Debrégeas, G., Mahou, P., Kruglik, S. G., Sintes, J. M., Candelier, R. (2015). Whole-brain functional imaging with two-photon light-sheet microscopy. *Nature methods*, 12(5), 379-380.

Whole-brain functional imaging with two-photon light-sheet microscopy

To the Editor: Several studies recently demonstrated that one-photon (1P) light-sheet imaging gives access to the spontaneous activity of a large fraction of the zebrafish larval brain at nearly single-cell resolution^{1–3}. This imaging method, however, requires an intense and extended illumination at a wavelength ($\lambda = 488 \text{ nm}$) that lies within the most sensitive region of the fish visible spectrum⁴ and therefore likely stimulates the blue photoreceptors in the retina as well as other photosensitive cells⁵. As an alternative, we report on brain-wide three-dimensional (3D) neural recordings during visuomotor integration in zebrafish larvae using two-photon (2P) light-sheet imaging⁶ at a wavelength of 930 nm combined with visual stimulation.

The extent to which 1P illumination interferes with visually driven processes is critical as it determines the suitability of light-sheet imag-

ing for behavioral neuroscience. Vladimirov *et al.* recently showed that the optomotor reflex and the associated motor-adaptation behavior could be normally evoked during 1P light-sheet imaging³. However, these robust behaviors are not driven by the blue and UV cones⁷ and are not even affected by ablation of the optic tectum, the largest visual center in fish⁸. To evaluate the relevance of 2P excitation for whole-brain visual studies and directly compare 1P and 2P excitation regimes, we implemented a twin light-sheet system (Fig. 1a, Supplementary Figs. 1 and 2, and Supplementary Table 1). This system provided similar axial and lateral resolutions in the 1P and 2P configurations and enabled functional imaging with cellular resolution in ~80% of the brain volume (Supplementary Figs. 3 and 4), without measurable photobleaching during long-term (1-h) recordings. We exposed 4- to 6-d-old zebrafish larvae expressing the calcium indicator GCaMP5G to a series of blue flashes of increasing intensity. We successively recorded evoked neural activity at 4 Hz using 1P and 2P imaging in approximately the same layer of the

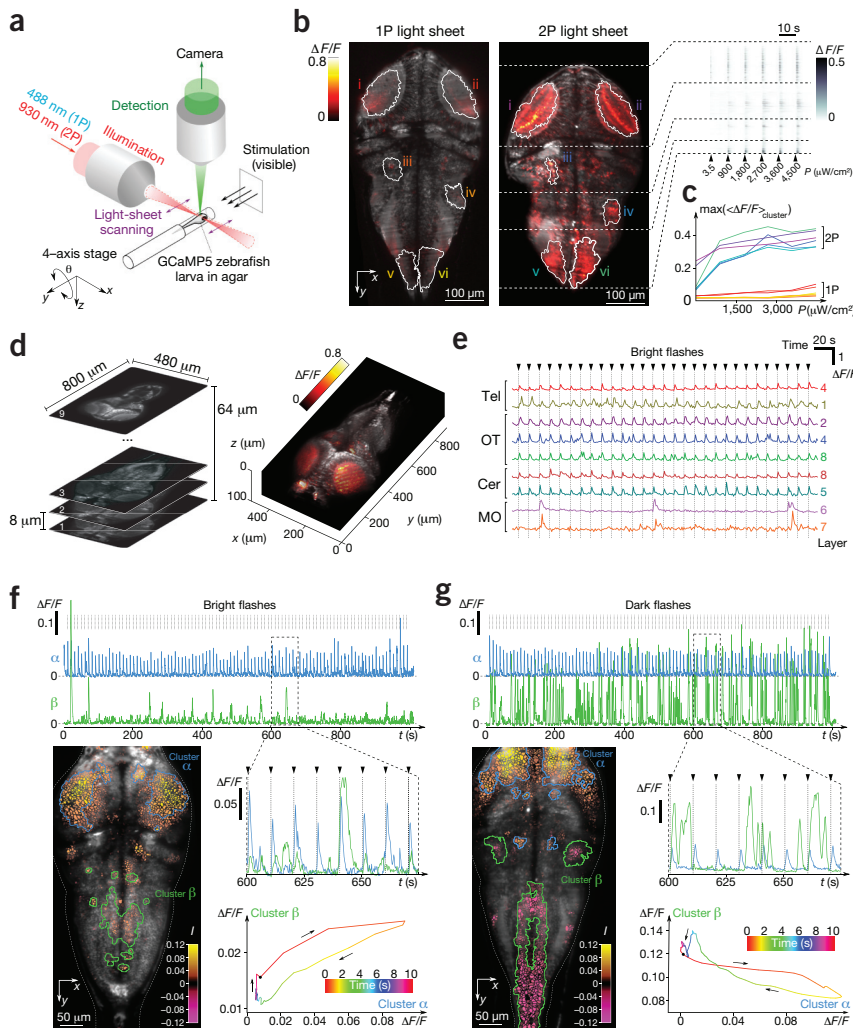


Figure 1 | Two-photon (2P) light-sheet functional imaging of visually evoked neural activity. **(a)** The 1P/2P light-sheet imaging system. **(b)** Left, brain-wide section of a 5-d-old larva overlaid with the flash-evoked neural response ($\Delta F/F$, 250 ms after the flash) measured with 1P and 2P light-sheet imaging. Images were recorded at 4 Hz and averaged over 20 successive flash presentations at 4,500 $\mu\text{W cm}^{-2}$. Right, post-stimulus raster plot of 3,283 neurons and neuropil regions. Data are averaged over 20 flash presentations for each stimulus intensity. **(c)** Post-stimulus response of the regions contoured in **b** for various stimulus intensities. Data in **b,c** are representative of $n = 9$ larvae. **(d)** 3D recording of activity evoked by 3,600 $\mu\text{W cm}^{-2}$ flashes. A stack of nine layers with 8- μm intervals was recorded every second, yielding a total of 36,063 neurons monitored at 1 Hz. The 3D volume rendering of the fish brain shows the $\Delta F/F$ response measured immediately after the flash. **(e)** Typical signals of flash-responsive neurons in different brain regions (Tel, telencephalon; OT, optic tectum; Cer, cerebellum; MO, medulla oblongata). **(f,g)** Network analysis of flash-induced neural responses. The images display the stimulus-averaged response to a 200-ms-long bright flash (**f**) or a 1-s-long dark flash (**g**). The color code in the micrographs represents the variation of $\Delta F/F$ averaged over the first 1.5 s after the flash. The blue and green lines delimit the two most prominent neuronal clusters responding to bright and dark red flashes as computed using the k -means algorithm ($k = 12$), whose time dynamics are shown in the three associated graphs. For bright flashes, the activity of the hindbrain cluster was enhanced after the flash onset, whereas dark flashes induced a transient reduction of its activity.

same fish. The imaged section was chosen so as to avoid direct exposure of the eyes to the illumination beam. During 2P imaging, the flashes elicited acute neural responses in various regions of the brain (Fig. 1b and Supplementary Video 1) even at the lowest flash intensity ($3.5 \mu\text{W cm}^{-2}$). At an illumination intensity compatible with 3D imaging, the response during 1P imaging was either abolished or greatly attenuated (Fig. 1b and Supplementary Video 2). To quantify this observation, we extracted the maximum of the post-stimulus signal in the five most responsive regions in both experiments. In 2P imaging, all regions displayed a substantial response at the lowest stimulus intensity, which rapidly reached a plateau as the visual stimulation became more intense (Supplementary Figs. 5 and 6, and Fig. 1c). During 1P imaging, the visually evoked activity was mostly confined to the tectal neuropil, the region that receives direct projections from retinal ganglion cells. To elicit measurable signals in other brain areas, the stimulus intensity had to be increased up to $4,500 \mu\text{W cm}^{-2}$, beyond physiologically relevant levels.

The exact mechanism by which 1P illumination leads to the observed reduction in visual sensitivity remains to be elucidated. The photoreceptors in the retina may receive excitation light scattered by the observation chamber or by the brain tissue, increasing the response threshold to subsequent visual stimuli. Alternatively, the visually evoked neural response may be attenuated owing to direct activation of light-sensitive cells throughout the brain. In any case, our results highlight the potential problems associated with visible illumination wavelengths and argue for the use of near-infrared wavelengths when studying visually driven processes.

2P light-sheet imaging combines the advantages of near-infrared illumination with the high speed of light-sheet microscopy. We produced 3D maps of flash-responsive neurons in a single experiment by sequentially moving the recorded plane across the brain and simultaneously recorded >36,000 individual neurons at 1 Hz (Fig. 1d,e, Supplementary Fig. 7 and Supplementary Video 3), without compromising signal-to-noise ratio. Brain-wide parallel recording of multiple brain regions opens the possibility of identifying extended clusters of neurons by analyzing the structure of the correlation matrix (Supplementary Methods and Supplementary Fig. 8). Cluster dynamics can then provide a low-dimensional description of the post-stimulus time sequence of brain activity (Fig. 1f,g and Supplementary Fig. 9).

In conclusion, we demonstrated that near-infrared 2P light-sheet imaging is suitable for 3D brain-wide functional imaging in zebrafish larvae at cellular resolution. Notably, this imaging method eliminates the photostimulation associated with 1P functional imaging. Although the latter does not abolish robust visuomotor reflexes, we showed that it compromises visual perception in the blue domain. Therefore, 2P light-sheet imaging is a suitable alternative method for whole-brain network analysis of neural processes that require fine control over the visual stimuli or that are sensitive to the photic environment.

Note: Any Supplementary Information and Source Data files are available in the online version of the paper (doi:10.1038/nmeth.3371).

ACKNOWLEDGMENTS

We thank F. Engert (Harvard University) for providing the Huc:GCaMP5G strain. The study was partly supported by Agence Nationale de la Recherche (contracts ANR-2010-JCJC-1510-01, ANR-11-EQPX-0029, ANR-10-INBS-04), Fondation Louis D. de l'Institut de France, European Union Seventh Framework Program (Marie Curie International Reintegration Grant no. 268379).

COMPETING FINANCIAL INTERESTS

The authors declare no competing financial interests.

Sébastien Wolf^{1,2}, Willy Supatto³, Georges Debrégeas^{1,2}, Pierre Mahou³, Sergei G Kruglik^{1,2}, Jean-Marc Sintès³, Emmanuel Beaurepaire³ & Raphaël Candelier^{1,2}

¹Sorbonne Universités, Université Pierre et Marie Curie Paris 06, Paris, France.

²Centre National de la Recherche Scientifique (Unité Mixte de Recherche 8237), Laboratoire Jean Perrin, Paris, France. ³Laboratoire Optique et Biosciences, Ecole Polytechnique, Centre National de la Recherche Scientifique (Unité Mixte de Recherche 7645) et Institut National de la Santé et de la Recherche Médicale (U1182), Palaiseau, France.

e-mail: georges.debregeas@upmc.fr or raphael.candelier@upmc.fr

1. Panier, T. *et al. Front. Neural Circuits* **7**, 65 (2013).
2. Ahrens, M.B., Orger, M.B., Robson, D.N., Li, J.M. & Keller, P.J. *Nat. Methods* **10**, 413–420 (2013).
3. Vladimirov, N. *et al. Nat. Methods* **11**, 883–884 (2014).
4. Risner, M.L., Lemerise, E., Vukmanic, E.V. & Moore, A. *Vision Res.* **46**, 2625–2635 (2006).
5. Fernandes, A.M. *et al. Curr. Biol.* **22**, 2042–2047 (2012).
6. Truong, T.V., Supatto, W., Koos, D.S., Choi, J.M. & Fraser, S.E. *Nat. Methods* **8**, 757–760 (2011).
7. Portugues, R. & Engert, F. *Curr. Opin. Neurobiol.* **19**, 644–647 (2009).
8. Roeser, T. & Baier, H. *J. Neurosci.* **23**, 3726–3734 (2003).

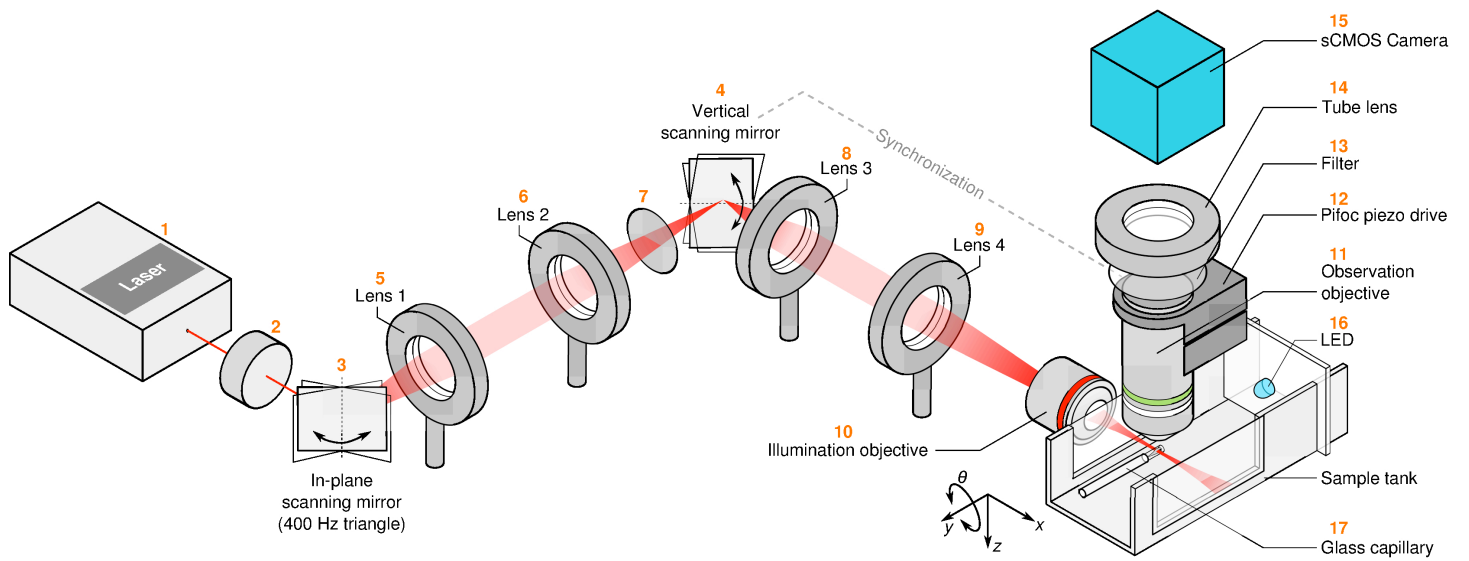
MiXCR: software for comprehensive adaptive immunity profiling

To the Editor: High-throughput sequencing is gaining importance in adaptive immunity studies, demanding efficient software solutions for immunoglobulin (IG) and T-cell receptor profiling¹. Here we report MiXCR (available at <http://mixcr.milaboratory.com/> and <https://github.com/milaboratory/mixcr/>), a universal framework that processes big immunome data from raw sequences to quantitated clonotypes. MiXCR efficiently handles paired- and single-end reads, considers sequence quality, corrects PCR errors and identifies germline hypermutations. The software supports both partial- and full-length profiling and employs all available RNA or DNA information, including sequences upstream of V and downstream of J gene segments (Fig. 1, Supplementary Note 1 and Supplementary Table 1).

In contrast with previous software^{2–5}, MiXCR employs an advanced alignment algorithm that processes tens of millions of reads within minutes, with accurate alignment of gene segments even in a severely hypermutated context (Supplementary Note 2 and Supplementary Tables 2–6). In paired-end sequencing analysis, MiXCR aligns both reads and aggregates information from both alignments to achieve high V and J gene assignment accuracy. It handles mismatches and indels and thus is suitable even for sequences with many errors and hypermutations. MiXCR employs a built-in library of reference germline V, D, J and C gene sequences for human and mouse based on corresponding loci from GenBank⁶.

MiXCR further assembles identical and homologous reads into clonotypes, correcting for PCR and sequencing errors using a heuristic multilayer clustering. Additionally, it rescues low-quality reads by mapping them to previously assembled high-quality clonotypes⁷ to preserve maximal quantitative information (Supplementary Note 3). The Illumina MiSeq platform currently allows for deep full-length IG repertoire profiling with ~20 million long paired-end reads. MiXCR captures all complementarity-determining regions (CDRs) and framework regions of immune genes and permits the assembly of full-length clonotypes. Flexibility to analyze partial-length data is also provided, allowing, for example, users to group reads into clonotypes

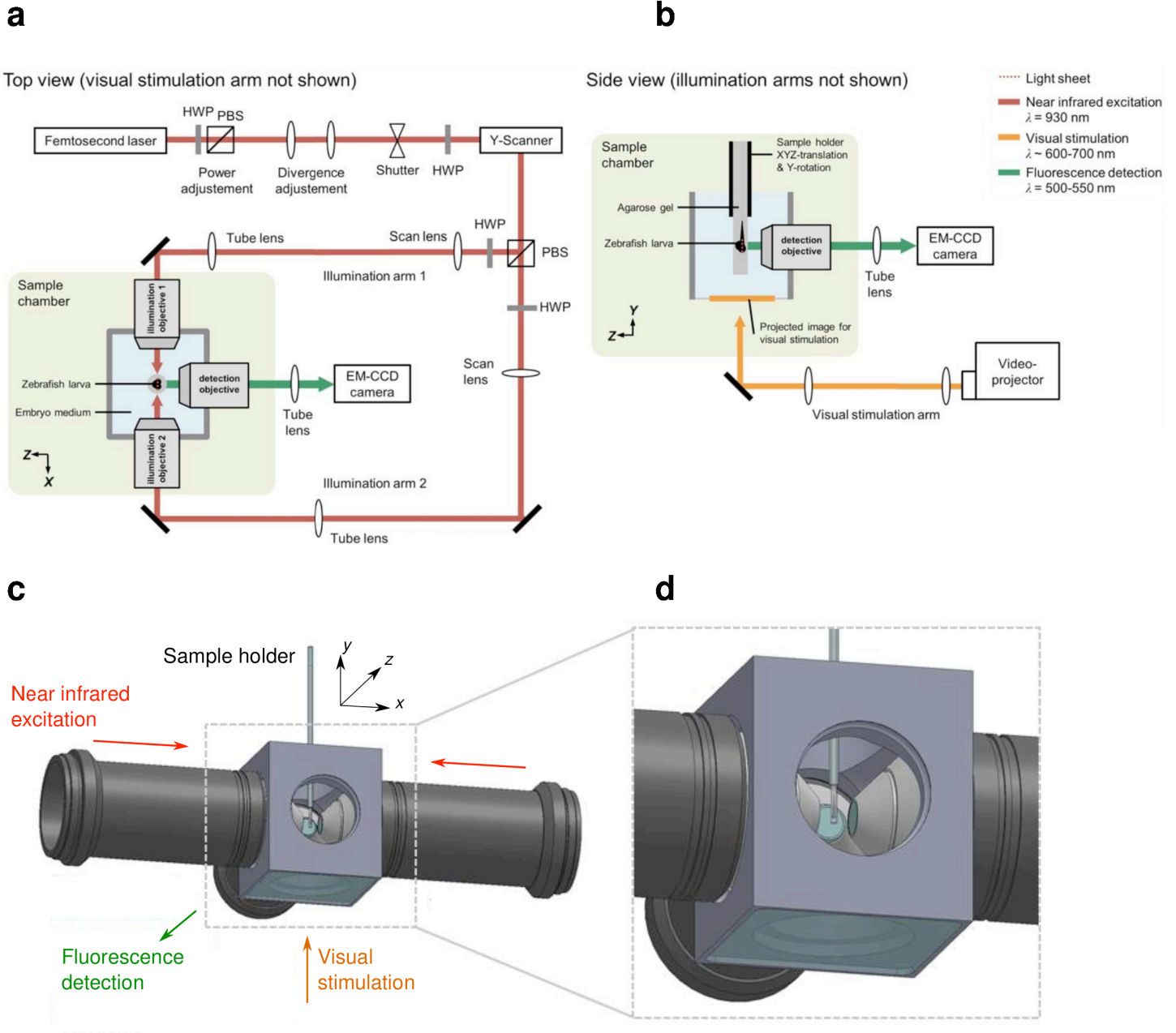
Copyright of Nature Methods is the property of Nature Publishing Group and its content may not be copied or emailed to multiple sites or posted to a listserv without the copyright holder's express written permission. However, users may print, download, or email articles for individual use.



Supplementary Figure 1

Scheme of the 1P/2P light-sheet microscopy setups.

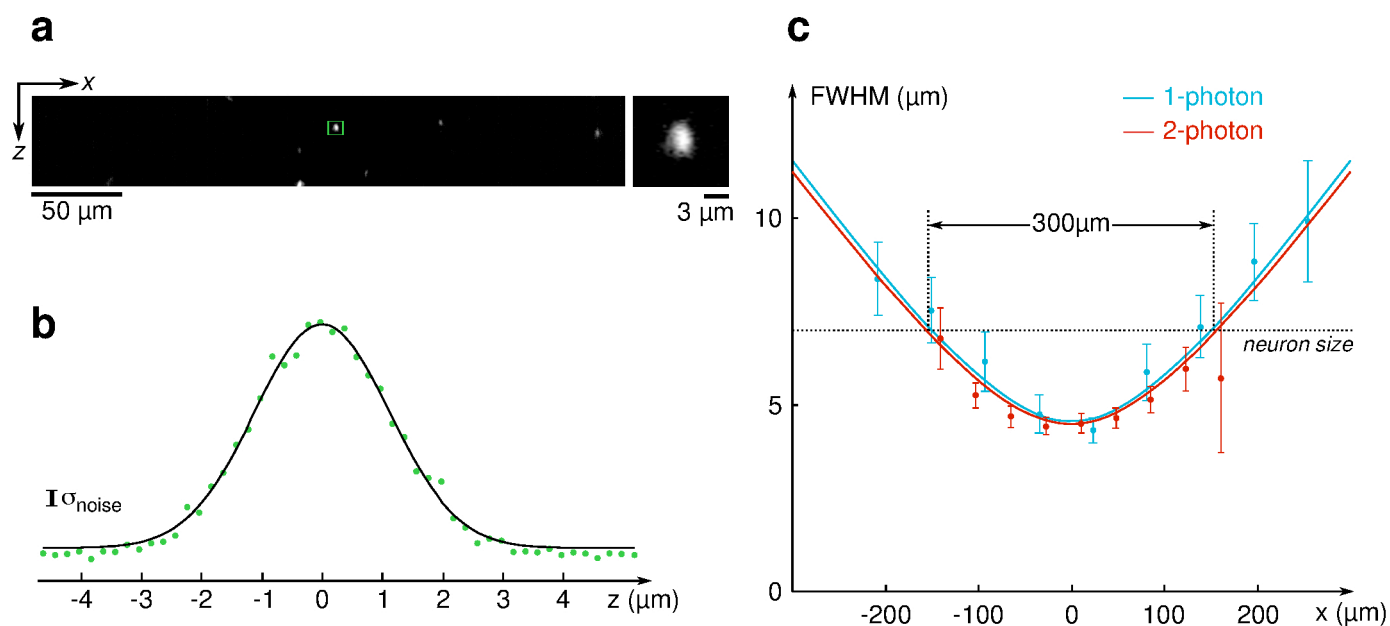
The optical components are listed in **Supplementary Table 1**.



Supplementary Figure 2

Two-photon light-sheet microscope with visual stimulation.

(a,b) Scheme of the two-photon light-sheet microscope with visual stimulation used to perform cluster analysis of dark- and bright-flash induced responses. HWP: half wave plate; PBS: polarization beam splitter; EMCCD: electron-multiplying charge-coupled device camera. (c) 3D-rendering of the liquid-filled specimen chamber with objective lenses on the lateral sides, sample held from the top and transparent screen for visual stimulation at the bottom. (d) Blow-up of the specimen chamber.

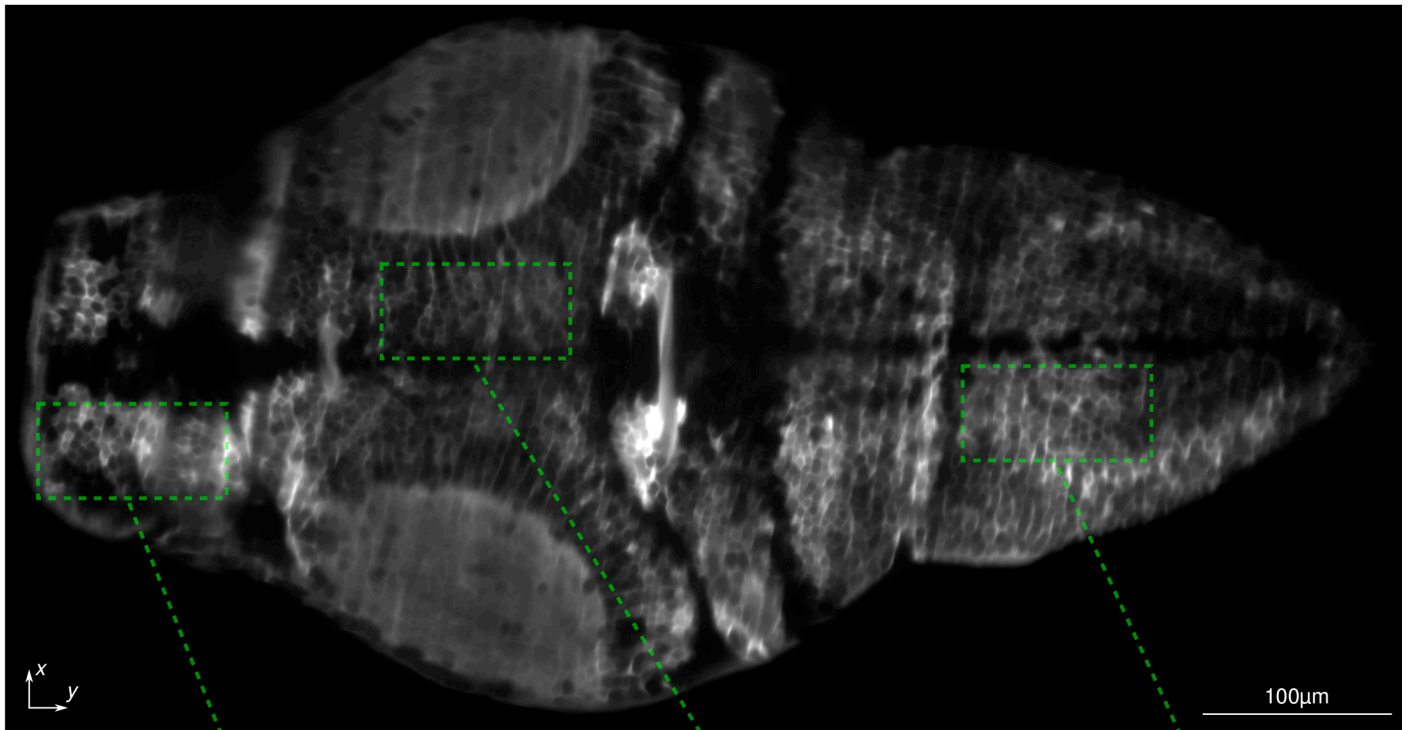


Supplementary Figure 3

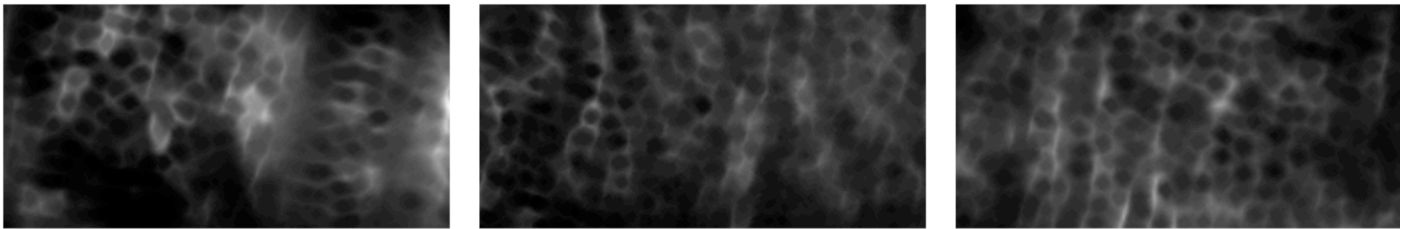
Axial resolution.

(a) Vertical cross-section of an agarose gel cylinder containing 100 nm in diameter fluorescent beads. The image was reconstructed from a series of horizontal sections, separated by 0.2 μm intervals, imaged using the 2P light-sheet setup. (b) Axial profile of the fluorescence intensity of the bead identified in (a) by the green rectangle. The solid line shows the best gaussian fit to the profile. (c) Full width at half maximum (*FWHM*) of the measured fluorescence profile, for 1P and 2P light-sheet imaging, as a function of the bead position along the illumination axis. The profiles are fitted with equations (1) and (2). The *FWHM* in the region delimited by the two vertical lines falls below the typical inter-soma distance in zebrafish larvae ($\approx 6.5 \mu\text{m}$). In this region, the optical sectioning is thus compatible with single-cell resolution.

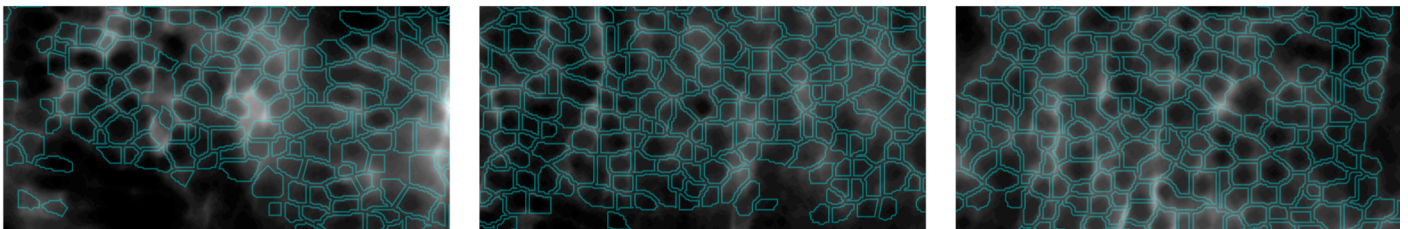
a



b



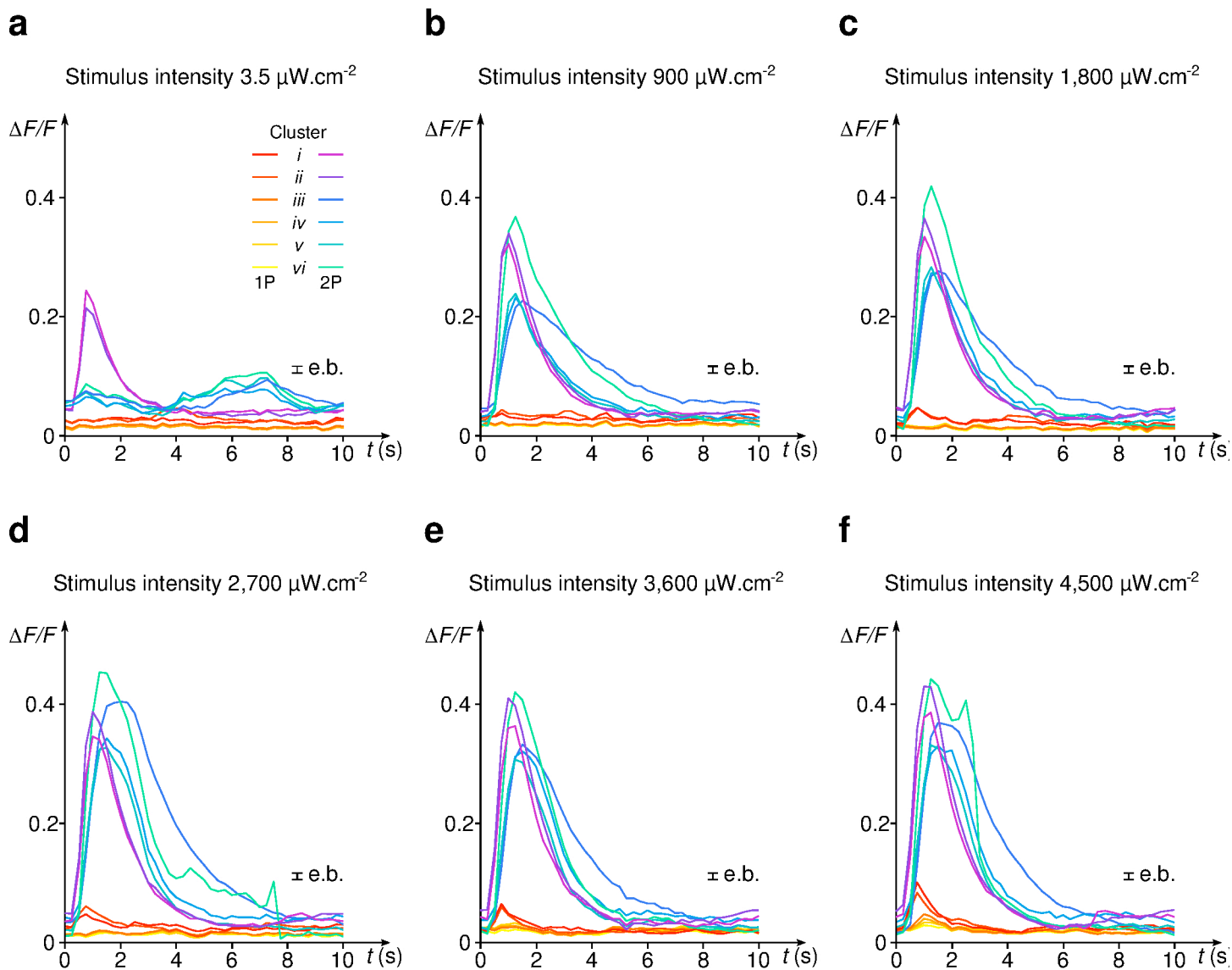
c



Supplementary Figure 4

Automatic image segmentation.

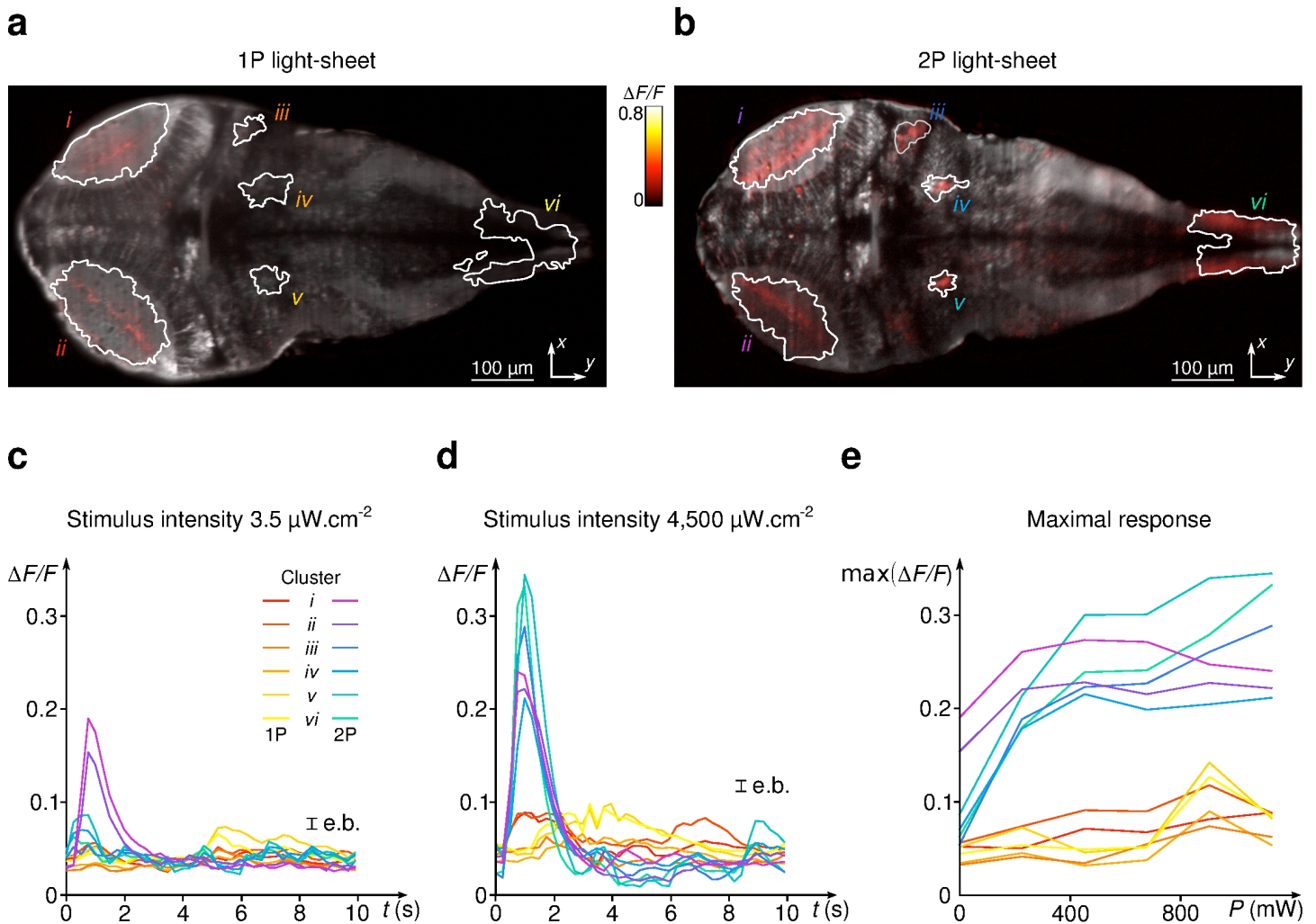
(a) Characteristic brain-wide section of the larva's brain obtained using 2P light-sheet imaging. (b) Blowups of different regions. From left to right: telencephalon, optic tectum, hindbrain. (c) Result of the automatic segmentation procedure leading to the identification of ROIs associated with individual somas.



Supplementary Figure 5

Comparison between flash-evoked response under 1P vs 2P imaging (1P illumination power, $500 \mu\text{W}$).

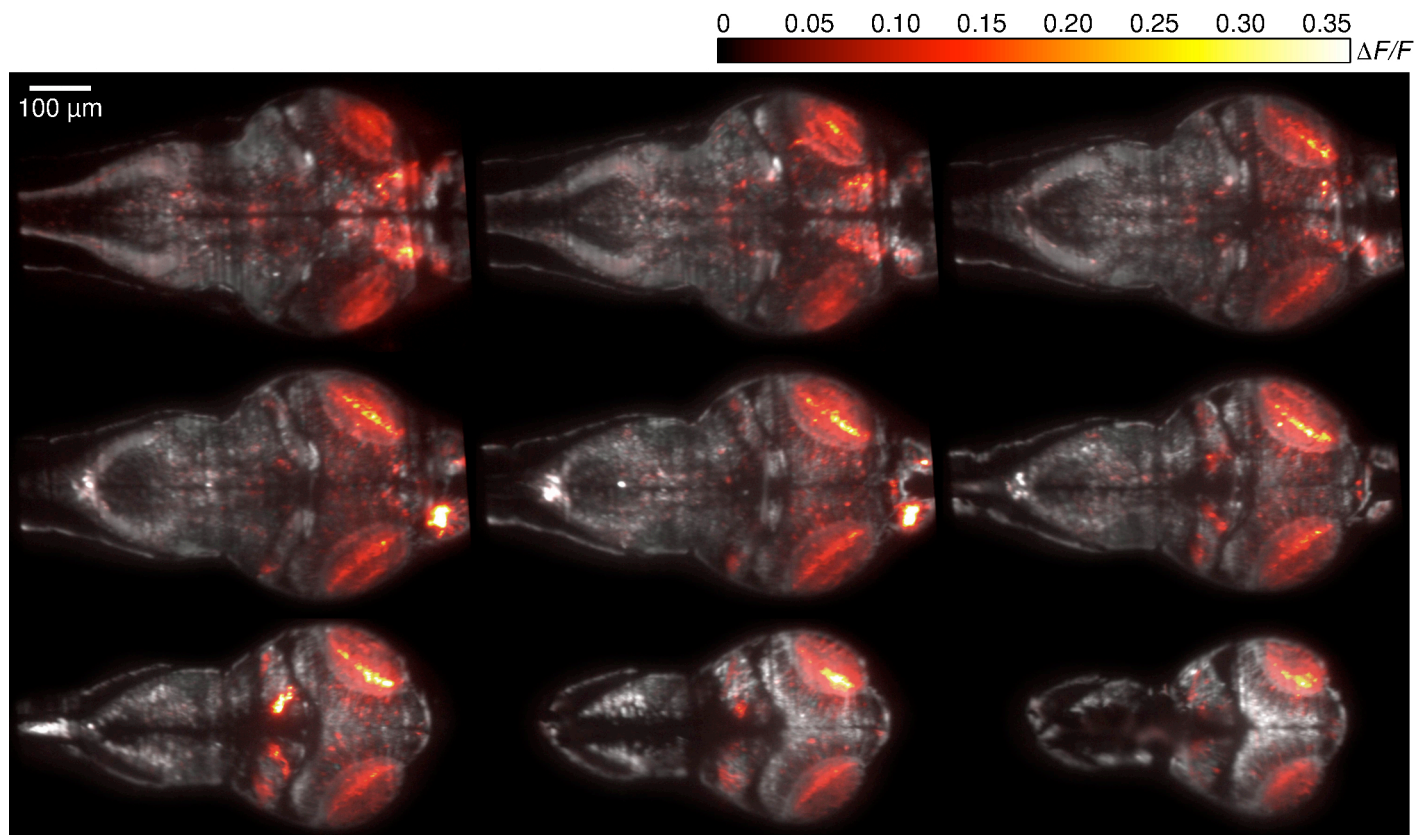
(a-e) Post-stimulus response averaged over the 5 most responsive subregions contoured in **Fig. 1**, for 6 increasing stimulus intensity. The graphs show that for all tested stimulus intensities, the response is either abolished or greatly reduced in 1P imaging, with respect to 2P imaging.



Supplementary Figure 6

Comparison between flash-evoked response under 1P vs 2P imaging at low 1P illumination power (100 μW).

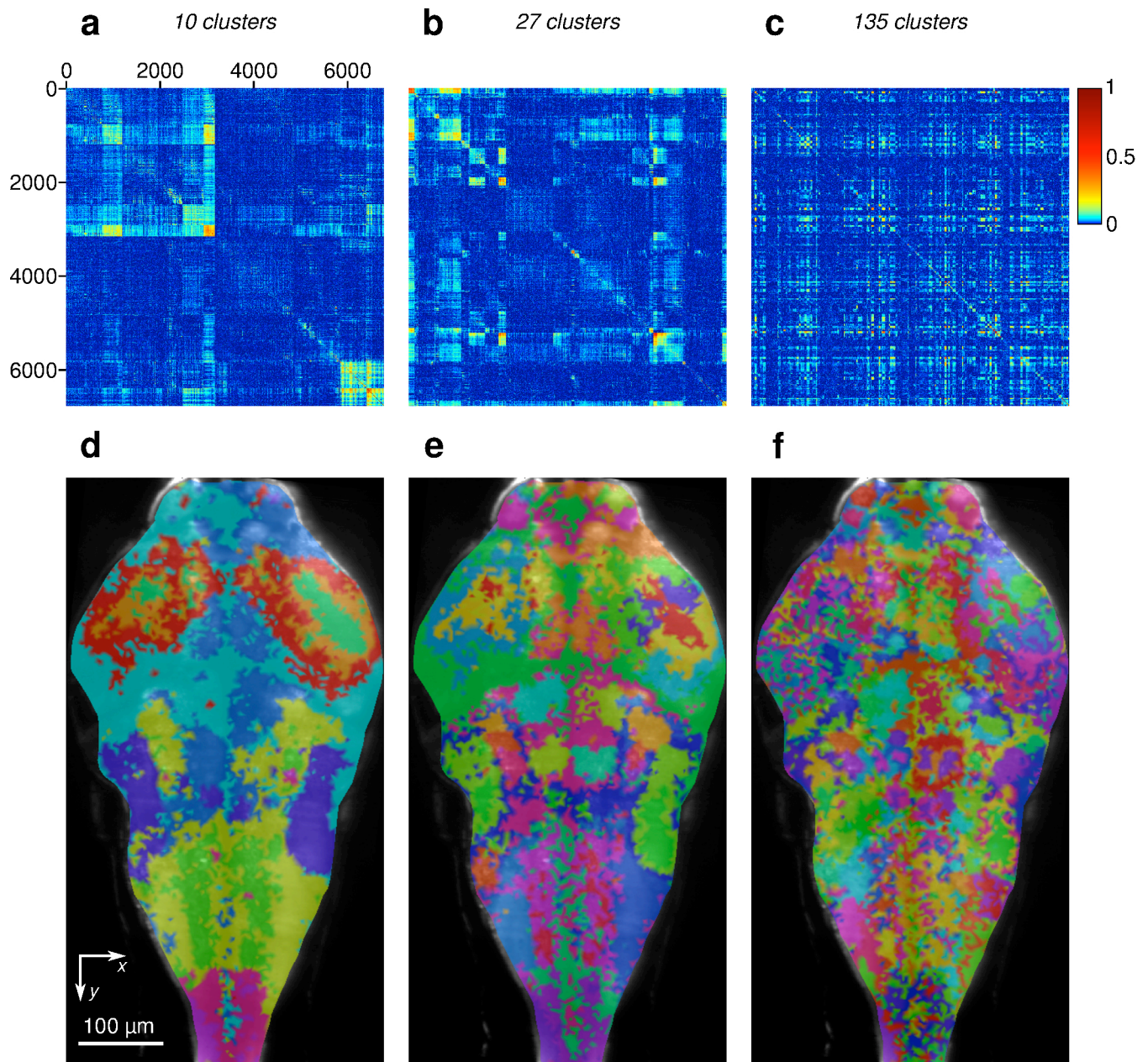
(a-b) Stimulus-averaged response, measured 250 ms after the flash in 1P and 2P imaging, respectively ($\Delta F/F$ in color code). (c-d) Post-stimulus response averaged over the 5 subpopulations contoured in (a-b) (most responsive regions), for the lowest (c) and highest (d) stimulus intensity. (e) Evolution of the maximum response for each contoured region as a function of the stimulus intensity. Even at this low illumination power, 1P light-sheet imaging still induces a severe reduction of visual sensitivity.



Supplementary Figure 7

3D imaging.

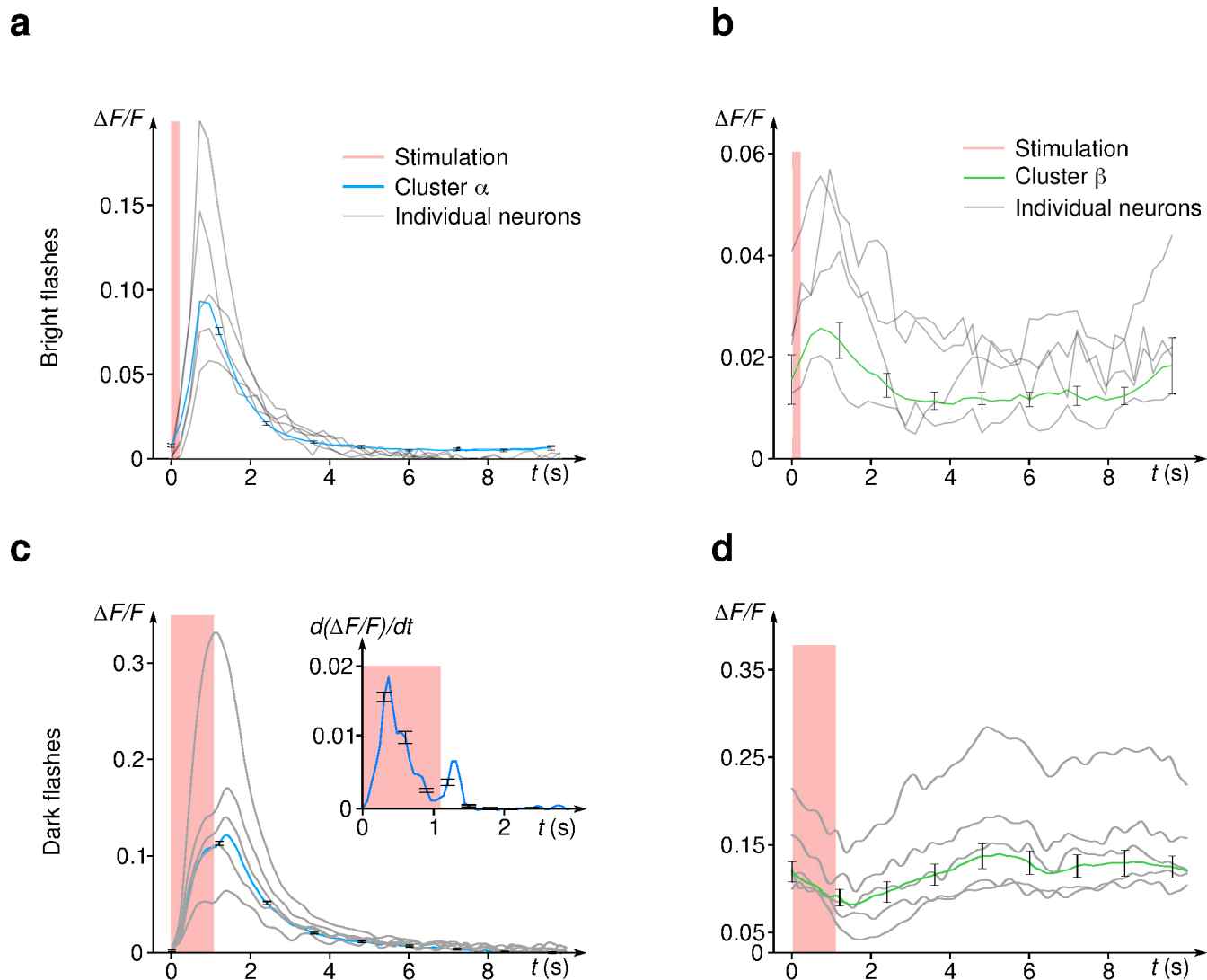
Nine layers were acquired at 1 Hz across a 5 day old larva brain (90 ms exposure per layer). On the sections shown, the average neural response ($\Delta F/F$), measured in the first second following a $3,600 \mu\text{W}\cdot\text{cm}^{-2}$ flash, is color coded (120 flashes, 10 s intervals between flashes).



Supplementary Figure 8

Cluster analysis performed on a 1,050 s-long, 100 bright flashes recording.

(a-c) The k-means algorithm is computed for different k-values on the Pearson matrix that conveys neuron-neuron correlations. The clusters appear as square blocks in the re-ordered Pearson matrix. (d-f) The spatial structure of the different clusters is shown: each color corresponds to one cluster. These maps reveal the functional organization of the brain at different scales.



Supplementary Figure 9

Bright vs dark flash-induced response.

Using the k-means algorithm ($k = 12$), we identified the two most prominent neuronal clusters whose topography is shown in **Fig. 1g-h**. Across-stimuli responses of the (a) visual α and (b) hindbrain β clusters for 200 ms-long bright flashes. The blue curve is the cluster-averaged response. Characteristic traces of individual neurons from the clusters are shown in grey. (c-d) Similar analysis performed for 1 s-long dark flashes on a different larva. The inset in (c) reveals that the visual cluster shows a positive transient response to both the onset and offset of the stimulus. In all graphs, the red rectangle indicates the stimulation period.

Supplementary tables

	Part	1P light-sheet microscope	2P light-sheet microscope
1	Laser	488 sapphire, Coherent	Mai Tai, Spectra-Physics
2	Precompensator	-	Deep See
3	Galvanometer mirror (xy)	8315K, Cambridge Technology	8315K, Cambridge Technology
4	Galvanometer mirror (xz)	8315K, Cambridge Technology	8315K, Cambridge Technology
5	Scanning lens (Lens 1)	$F = 50$	$F = 50$
6	Tube lens (Lens 2)	$F = 150$	$F = 150$
7	Polarization beam splitter	-	CM1-PBS252, ThorLabs
8	Scanning lens (Lens 3)	$F = 100$	$F = 150$
9	Tube lens (Lens 4)	$F = 200$	$F = 300$
10	Illumination Objective	Zeiss EC Plan-Neofluar 5x	IR 5x Olympus LMPLS5xIR
11	Observation Objective	20x Olympus XLUMPlanFLN	20x Olympus XLUMPLFLN
12	Objective piezo drive	Mipos 500 SG, Triptics	Mipos 500 SG, Triptics
13	Emission filter	Notch-filter, 488 nm	Low-pass filter (cut-off 800 nm)
14	Camera tube lens	$F = 150$	$F = 150$
15	sCMOS camera	PCO.edge 5.5	PCO.edge 4.2
16	LED	470 nm, 5 cd, 15° aperture	470 nm, 5 cd, 15° aperture
17	Capillary	Internal diameter 1 mm	Internal diameter 1 mm

Supplementary table 1 | Main components of the 1P and 2P twin light-sheet microscopes.

Supplementary Methods

Larvae preparation

The experiments were performed on zebrafish *nacre* mutant expressing the calcium indicator GCaMP5G⁹ under the control of the pan-neuronal promoter *elavl3*. The embryos were collected and raised at 28.5°C in E3 embryo medium, and kept under 14/10h on/off light cycles. Larvae aged 4–6d.p.f. were mounted in a 1 mm in diameter cylinder of low-melting point agarose (1.8% in concentration)¹. To prevent movements of the animal during functional imaging, the agarose contained a paralyzing agent (Pancuronium bromide, 0.3 mg/mL). All experiments were approved by *Le Comité d'Ethique pour l'Expérimentation Animale Charles Darwin*.

Optical setup for 1P/2P comparison

In order to compare visual responses during 1P and 2P imaging, we built a twin light-sheet microscope (**Supplementary Fig. 1** and **Supplementary Table 1**), with similar optical configurations, using the same specimen chamber and visual stimulation device.

Two-photon light-sheet microscopy. A titanium:sapphire laser (Mai Tai, Spectra-Physics) was used to deliver a near infrared pulsed excitation at the sample with 100–200 fs pulse duration, 80 MHz repetition rate and $\lambda = 930$ nm central wavelength. The excitation power at the sample was adjusted using a half wave plate and a polarization beam splitter (CM1-PBS252, Thorlabs) to 280 mW (measured before the illumination objective). This power allowed for a contrast and a signal-to-noise ratio close to what we obtain with the 1P setup at similar exposure time, and was low enough to avoid damage in brain tissues. The light-sheet microscope included two galvanometer mirrors (6215H/8315K, Cambridge Technology), associated with two pairs of scan and tube lenses, and a low NA illumination objective (5 x 0.1NA, LMPLNXIR, Olympus). The weakly focused laser beam was scanned at 400 Hz over 800 μm in the Y-direction by the galvanometer mirror, creating an illumination light-sheet in the XY-plane.

The detection arm consisted of a water-immersion objective (20 x 1.0NA, XLUM-PLFLN, Olympus) mounted vertically onto a piezo nanopositioner (Piezosystem Jena MIPOS 500), allowing precise adjustment of the focus plane with the light sheet. The fluorescence light was collected by a tube lens (150 mm focal length, Thorlabs AC254-150-A) and passed through a low-pass filter (NF488-15, Thorlabs) to eliminate 930 nm photons. The image was then formed onto a sCMOS sensor (PCO.edge 4.2, PCO). The 20x magnification yielded a field of view of 0.8 x 0.8 mm², with a pixel area of 0.4 x 0.4 μm^2 . The 3D recordings were performed at a rate of 10 frames per second.

One-photon light-sheet microscopy. The one-photon light-sheet microscope was a modified version of a system described earlier¹. It used a 488 nm solid-state diode laser (488 Sapphire, Coherent) at a power of 500 μW (measured before the illumination objective), two galvanometer mirrors (6215H/8315K, Cambridge Technology), associated with two pairs of scan and tube lenses, and a low NA illumination objective (5 x 0.16 NA, Zeiss EC Plan-Neofluar).

The detection arm consisted of a water-immersion objective (20 x 0.95 NA, XLUMPlanFL, Olympus) mounted vertically onto a piezo nanopositioner (Piezosystem Jena MIPOS 500). The fluorescence light was collected by a tube lens (150 mm focal length, Thorlabs AC254-150-A) and passed through a notch filter (NF488-15, Thorlabs) to eliminate 488 nm photons. The image was then formed onto a

sCMOS sensor (PCO.edge 5.5, PCO). The 20x magnification yielded a field of view of 1 x 0.8 mm², with a pixel area of 0.4 x 0.4 μm².

Specimen chamber and visual stimulation. Both setups included a lab-built chamber filled with E3 embryo medium, and connected to the specimen holder *via* a soft membrane. This allowed us to position the larva using a combination of translation and rotation stages, while maintaining the chamber fixed with respect to the optical system. A blue LED (5 cd, 15° aperture angle), was positioned inside the chamber 6 cm in front of the fish eyes. The stimulus intensity was calibrated by measuring the radiance at a similar distance as a function of the applied voltage. In a typical experiment, we applied twenty successive 30 ms-long flashes at each intensity (3.5 ; 900 ; 1,800 ; 2,700 ; 3,600 ; 4,500 μWcm⁻²), separated by 10 s intervals (120 flashes, 1,200 s). Image acquisition, mirror scanning, objective motion and visual stimulation were synchronized using a D/A multifunction card (NI USB-6259 NCS, National Instruments) and a custom-written program in LabVIEW (National Instruments).

Lateral and axial resolution

In light-sheet imaging, the axial and lateral resolutions are decoupled. The lateral resolution is set by the optical properties of the detection arm (detection objective and camera sensor). With our configurations, it is thus similar in both imaging methods. The axial resolution is mostly controlled by the thinness of the light sheet. In one-photon, the axial resolution, defined as the full width at half maximum (*FWHM*) of the fluorescence profile, is directly given by the light-sheet profile, which reads¹:

$$FWHM_{1P}(x) = \sqrt{2\ln(2)} \frac{\lambda_{1P}}{\pi(NA)_{1P}} \sqrt{1 + \left(\frac{x}{b_{1P}}\right)^2} \quad (1)$$

where λ_{1P} is the wavelength, NA_{1P} the numerical aperture of the illumination objective, and $b_{1P} = 2n\lambda_{1P}/\pi(NA)_{1P}^2$ defines the characteristic distance over which the axial resolution can be considered uniform.

In two-photon imaging, the fluorescence signal is proportional to the square of the illumination profile, such that the fluorescence profile reads:

$$FWHM_{2P}(x) = \sqrt{\ln(2)} \frac{\lambda_{2P}}{\pi(NA)_{2P}} \sqrt{1 + \left(\frac{x}{b_{2P}}\right)^2} \quad (2)$$

where $b_{2P} = 2n\lambda_{2P}/\pi(NA)_{2P}^2$. Since $\lambda_{1P} \cong \lambda_{2P}$, it is possible to obtain the same axial resolution between the two imaging systems across the entire field of view, by setting $(NA)_{2P} = \sqrt{2}(NA)_{1P}$ through appropriate filling of the back aperture of the illumination objectives.

The fluorescence axial profile was characterized by imaging 100 nm in diameter fluorescent beads embedded in an agarose gel cylinder as they were scanned vertically across the laser sheet (**Supplementary Fig. 3a**). The recorded intensity signal of each bead exhibited a Gaussian profile from which the *FWHM* was extracted (**Supplementary Fig. 3b**). The profiles were found invariant along the scanning direction and were correctly described by equations (1) and (2) (**Supplementary Fig. 3c**). In our configuration $(NA)_{1P} = 0.04$ and $(NA)_{2P} = 0.055 \cong \sqrt{2}(NA)_{1P}$ such that the two systems yield the same axial resolution across the field of view, as evidenced by the superposition of the measured *FWHM* profiles. If we define, as a criterium for single-cell resolution, the fact that *FWHM* is less than 6.5 μm

(the typical distance between neighboring somas), then both techniques are single-cell resolved over a band of width of 250 μm , a region that encompasses $\approx 80\%$ of the brain volume.

Data pre-processing

Image processing was performed offline using Matlab (The MathWorks). We first corrected for specimen drift by registering each image with the initial one. We implemented a semi-automatic segmentation procedure, adapted from (ref. 2), to identify individual somas and neuropil subregions (**Supplementary Fig. 4**). We then extracted the $\Delta F/F$ signal from the fluorescence trace of each ROI.

Comparative analysis of brain-wide visual response during 2P vs 1P imaging

In order to quantitatively compare the visually-evoked response measured using 2P and 1P light-sheet imaging, we manually selected, in each experiment (performed successively on the same fish, in approximately the same layer), five subregions that exhibited the strongest response. We then averaged the $\Delta F/F$ signal over the neurons within each region, and finally produced a post-stimulus averaged signal over the successive flash presentations, for each stimulus intensity (**Supplementary Fig. 5**). Notice that the level of spontaneous activity measured with either technique was found comparable, which indicates that 1P illumination does not impede measurement of neural activity but induces a massive reduction in visual sensitivity.

We finally run a comparative test in which the illumination intensity of the 1P light sheet was reduced down to 100 μW (as measured before the illumination objective). Even for such a low illumination power, the reduction in visual sensitivity induced by 1P imaging remains severe (**Supplementary Fig. 6**).

Cluster analysis of bright and dark flash-induced response

Optical setup. These experiments were performed on a 2P light-sheet imaging setup (**Supplementary Fig. 2**, see also ref. 10). The average laser power at $\lambda = 930 \text{ nm}$ was adjusted to 160 mW before the objective of a single illumination arm. Green fluorescence was detected with a laser rejection filter (FF01-680/SP, Semrock) and a green detection bandpass filter (FF01-525/50, Semrock). Images spanning 335 x 667 μm^2 of the sample with 0.67 μm pixel size, were acquired at a rate of 4.2 frames s^{-1} . We specifically designed a liquid-filled chamber to enable visual stimulation of the sample. This chamber was directly suspended to the water immersion objective lenses, and provided access to the specimen from six directions of space. The agarose cylinder embedding the larva was held from the top, and the transparent bottom of the chamber was used for visual stimulation. Visual stimuli consisted of bright (200 ms) and dark (1 s) flashes in the 600-700 nm wavelength range, generated by a video projector (Vivitek Qumi Q5) and projected onto a small screen positioned at the bottom of the microscope specimen chamber using a 1/20 magnification relay optics and covering 60° of the animal visual field. Stimulation patterns were generated at a frame rate of 60 Hz by a custom C++ program using OpenGL. Image acquisition and visual stimuli were synchronously triggered using TTL pulses.

Clustering procedure. In order to identify clusters of correlated neurons, we computed the $N \times N$ Pearson correlation matrix M , where N is the number of monitored neurons. The distribution of the elements M_{ij} , *i.e.* the neuron-neuron activity correlations, displayed a systematic bias towards positive values as a result of minute fluctuations of the laser intensity. This uniform correlated noise was reflected in the existence of a large eigenvalue λ of the matrix M , associated with an eigenvector V . We corrected for this effect by subtracting $\lambda V_i V_j$ from each element M_{ij} . We used the k-means

algorithm to identify clusters of correlated neurons from the corrected Pearson matrix. In this clustering method, the total number k of clusters is manually set. It defines the level of coarse graining in the description of the neural dynamics. We obtained cluster maps for arbitrary numbers of clusters ($k=10, 27$ and 137 clusters in **Supplementary Fig. 8**). We computed the clusters' neuronal activity by averaging the $\Delta F/F$ signals of the associated neurons (**Supplementary Fig. 8**). The low-dimensional representation of the network dynamics was then obtained by computing the across-trial averages of each identified cluster.

Analysis and statistical methods

All analyses were done in MATLAB (The MathWorks). Error bars in figures show the standard deviation. The comparative experiments between 2P and 1P imaging were replicated on $n=9$ larvae. We checked that the order in which the two experiments were performed had no influence on these observations. The visual/hindbrain clusters dynamics evoked by bright and dark flashes were qualitatively reproduced in $n=3$ fishes, although the exact morphology of the clusters identified by k-means may vary from run to run.

Online methods references

1. Akerboom, J. *et al.*, *J. Neurosci.* **32**, 13819-13840 (2012)
2. Mahou, P., Vermot, J., Beaufrepire E. & Supatto, W., *Nat. Meth.* **11**, 600-601 (2014)

Chapter 3

**Principles of goal-directed
navigation in motile animals**

**Followed by “Sensorimotor
computation underlying phototaxis
in zebrafish”**

On serait fort embarrassé pour citer une découverte biologique due au raisonnement pur. Et, le plus souvent, quand l'expérience a fini par nous montrer comment la vie s'y prend pour obtenir un certain résultat, nous trouvons que sa manière d'opérer est précisément celle à laquelle nous n'aurions jamais pensé.

One would be very embarrassed to quote a biological discovery that resulted from pure reasoning. And, more often than not, when the experiment has finally shown us how life proceeds in order to obtain a certain result, we find that its mode of operation is precisely that to which we would never have thought.

Bergson, *L'Evolution créatrice*

3.1 Introduction

In order to survive and thrive, motile organisms use sensory cues to navigate towards environments where they are more likely to survive, obtain food or find mates. These series of movement directed relative to some sensory gradient $\vec{\nabla}\mathcal{S}$ are called taxis behaviour. The driving stimulus can be light (phototaxis), heat (thermotaxis), food (odortaxis or chemotaxis), gravity (geotaxis) or moisture (hydrotaxis). The movement can be directed toward (*positive* taxis) or away (*negative* taxis) from the stimulus. The transformation of sensory cues into a motor command that will consequently change the position in space of the organism and thus the sensory inputs constitute a closed-loop mechanism that coordinates motor action and sensory perception. This mechanism is at play in organisms ranging from bacteria to nematodes and insects but also among humans (Jékeli *et al.* 2008; Kane *et al.* 2013; Luo *et al.* 2014; Sawin *et al.* 1994; Chen and Engert 2014).

Taxis or kinesis

In order to achieve these taxis, animals have developed various strategies. They all use the same incoming information: the organism needs to infer a sensory gradient $\vec{\nabla}\mathcal{S}$ to evaluate whether it is navigating towards the right direction. The comparisons of sensory cues can induce two different consequences: (1) an active (i.e. direct, deterministic) change in the orientation of the animal: when it detects a stimulus gradient, the animal reorients its movement accordingly, (2) an indirect change of the orientation: when it detects a stimulus gradient, the animal does not change its direction, but rather modulates the locomotion speed or the rate of turning, which leads to statistically biasing its trajectory. Taxis strategies are thus divided in two groups: (real) *taxis* and *kinesis*. The first group encompasses the navigation strategy with directed reorientation. The second group corresponds to the navigation strategies with no direct orientation bias (Figure 3.1).

Tropotaxis or klinotaxis

All taxis strategies necessitate to probe the spatial gradient of a stimulus $\nabla\mathcal{S}$. Two strategies can be implemented. First, a *tropotaxis* strategy where the animal evaluates $\vec{\nabla}\mathcal{S}$ directly using two sensors at different locations (for example the two eyes): the animal computes $\vec{\nabla}\mathcal{S}$ by probing $\mathcal{S}(x_1, t)$ and $\mathcal{S}(x_2, t)$ where x_1 and x_2 corresponds to the different locations of the receptors. Second, a *klinotaxis* strategy where the animal evaluate $\vec{\nabla}\mathcal{S}$ using a unique sensor that measure \mathcal{S} at two different time points before and after a displacement corresponding to two different locations: the animal thus infers $\vec{\nabla}\mathcal{S}$ by probing $\mathcal{S}(x(t), t)$ and $\mathcal{S}(x(t + \Delta t), t + \Delta t)$ with a unique receptor, where $x(t)$ and $x(t + \Delta t)$ corresponds to the location of the animal respectively before and after a movement that lasted Δt . In the literature, some articles use *spatial comparison* and *spatio-temporal sampling* instead of *tropotaxis* and *klinotaxis* (Sawin *et al.* 1994; Chen and Engert 2014). In doing taxis behaviors, the organisms sometimes use a klinotaxis strategy, sometimes tropotaxis, sometimes both.

Distinguishing the contribution of each strategy is difficult, as will be illustrated in the following (Klein *et al.* 2015; Robson 2013; Chen and Engert 2014; Wolf *et al.* 2017) (Figure 3.1).

There are many examples of kinesis (chemotaxis in *E. coli*, *C. elegans*), klinotaxis (thermotaxis in *C. elegans*, *D. melanogaster* larva, *Danio rerio* larva), less of tropotaxis (phototaxis in adult marine zooplankton *Platynereis dumerilii* and *Danio rerio* larva, chemotaxis in walking bees). It seems obvious that a tropotaxis behavior relies on the existence of several sensors spatially distributed to allow a spatial comparison. Phototaxis is an intuitive example where the difference in instantaneous perceived intensity at two different angles (two eyes) of the visual field provides the desired information. Later in this chapter, we will discuss about this “eyes necessity”.

Stimulus is a vector or a scalar

Another important distinction between taxis behaviors is based on the dimension of the stimulus. Stimuli like chemoattractants (chemotaxis) or temperature (thermotaxis) are scalars whereas light (phototaxis), the gravitational field (geotaxis) or sound are vectors. An appropriate measure of a vectorial stimulus can offer more than its intensity: the direction of the source. For example, the shape of the ears is actually suited to measure the intensity of sound and evaluate the position of the source at once. In the same way, the presence of two eyes, with directionally variable visual sensitivity, is ideal to evaluate the direction of a light source.

Conclusion

What are the strategies implemented by organisms to perform goal-directed navigation (kinesis, klinotaxis or tropotaxis)? What are the neural circuits involved in these various behaviors linking sensory inputs to motor output? How does the central nervous system contribute to this goal seeking process? What can navigational strategies tell us about the evolution of the brain?

These are the question we will try to address in the following with a short review of important strategies developed by organisms in order to achieve goal-directed behavior. We will first focus on chemotaxis and then on phototaxis in bacteria (*Escherichia Coli*), marine zooplankton (*Platynereis dumerilii*), nematodes (*Caenorhabditis elegans*), insects (*Drosophila melanogaster*) and fish (*Danio rerio*). In Chapter 5 a specific review on thermotaxis is provided. The last part of this chapter presents the results I obtained during my PhD on the neural basis of phototaxis in zebrafish larva.

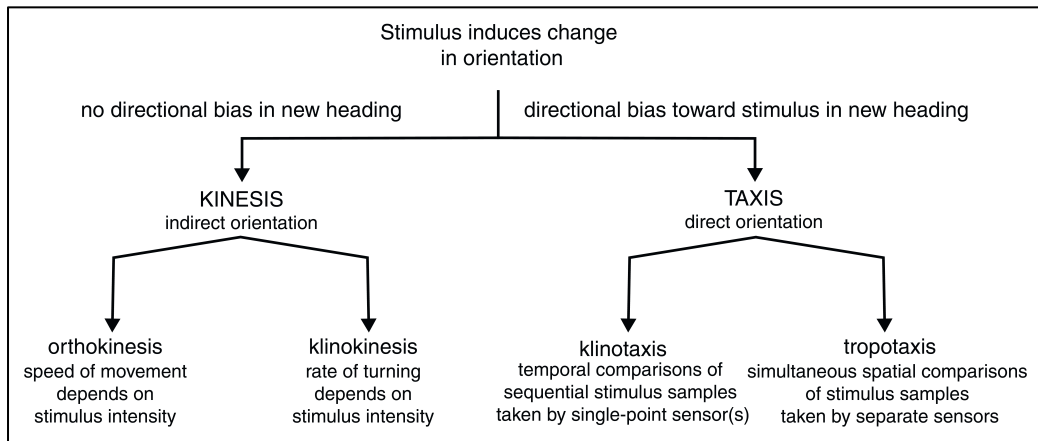


Figure 3.1: Classification of navigational strategies. Adapted from Gomez-Marin and Louis 2012.

Small idea: why navigation strategy is a key issue in neuroscience paradigm evolution? *Passive or Active Perception*

For a very long time (fifty years – which is in fact not so much in science), neuroscience has thought the brain as a passive recording studio. Seeking for so-called *receptive fields* was the ultimate goal in neuroscience. A typical experiment consisted in recording activity of individual cells in an animal while delivering series of stimulations in order to characterize their responses. To do so scientist needed to anaesthetize or paralyze the animals to be able to record their brain activity. During decades neuroscientist thus mapped receptive fields in various regions of the brain. This approach was tedious and time-consuming yet it did not yield much knowledge regarding the computation performed by the brain. But at that time, it was technically impossible to do better.

Improvement in the speed of camera and computer made possible to very precisely monitor the animal's behavior. Again, it is with the development of new techniques that a new paradigm emerged. Recent works on the navigation strategies of animals in a specific sensory environment (Luo *et al.* 2006, 2010, 2014; Gomez Marin *et al.* 2011; Ahrens *et al.* 2012) demonstrates that the brain, rather than being a passive recorder, actively acquires sensory inputs (Luo *et al.* 2010; Gomez Marin *et al.* 2011). Perception is more than reception of inputs: it is a closed loop between the detection of external sensory stimulations, the processing of these inputs by the brain leading to a motor command. In turn motor action leads to movement of the detectors, which changes the perceived stimuli (Ahissar and Assa 2016). This continuous loop between stimulation, brain and motor control is a key point in understanding simple sensorimotor tasks such as the navigation of *Drosophila melanogaster* larva in chemical gradients, or the navigation of a zebrafish larva towards a light source.

3.2 Chemotaxis

3.2.1 Chemotaxis in *Escherichia coli*: the klinokinesis example

Chemotaxis in *Escherichia coli* is one of the most studied goal-directed navigation in biology (Berg and Brown 1972; Berg and Purcell 1977; Baker *et al.* 2006; Tu 2013; Micali and Endress 2016). From the molecular transduction pathway to the physics of diffusion of small molecules, chemotaxis in *Escherichia coli* is one of the best example of what biology will be in a (near?) future: highly precise in the description of the molecular biological cascade and highly quantitative with a beautiful mathematical model.

In 1972, Berg published a pioneering study showing that *E. Coli* was able to navigate up a gradient of chemoattractant. *E. Coli* swims using 5-8 flagellar rotary motors, which rotate either clockwise or counterclockwise. *E. Coli* locomotion encompasses two phases: “runs” during which the bacteria moves forward and “tumbles”, which are random reorientation events. In the absence of any chemical gradient, the trajectory of *E. Coli* is a random walk. To move up a concentration gradient the bacteria suppresses tumble events whenever the perceived concentration of chemoattractant increases. This leads to longer runs, which eventually drive the animal towards the chemoattractant source.

To achieve this biased random walk, a precise chemosensory molecular pathway is implemented. A chemical process defines the frequency of tumble events. The chemotaxis protein CheA is associated with dimeric chemoreceptors which are methyl-accepting chemotaxis proteins (MCP). The decrease in concentration of a chemoattractant induces a phosphorylation of CheA, which in turn phosphorylates CheY called the response regulator. Phosphorylated CheY diffuses to the flagellar motor complex and changes the sense of rotation of the flagella, triggering tumble events. In reverse, the presence of chemoattractants perceived by chemoreceptors can stabilize the complex MCP-CheA and reduce the rate of CheY phosphorylation, leading to a suppression of tumble events.

Despite the simplicity of this mechanism, chemotaxis pathway is extremely sensitive and *E. Coli* can detect three molecules (Micali and Endress 2016) in a volume of the bacteria’s size. Another important property of this system is its adaptation to persistent stimulation, which allows *E. Coli* to sense relative changes in concentration and still be sensitive to minute concentration changes.

Chemotaxis in bacteria illustrates how a complex navigation behavior can be implemented in a unique cell. This taxis behavior belongs to the category of *klinokinesis*: the animal probe $\vec{\nabla}\mathcal{S}$ by evaluating the stimulus \mathcal{S} at different times (*klino*), then the animal regulates its trajectory in a stochastic way by modulating the rate of turning (*kinesis*).

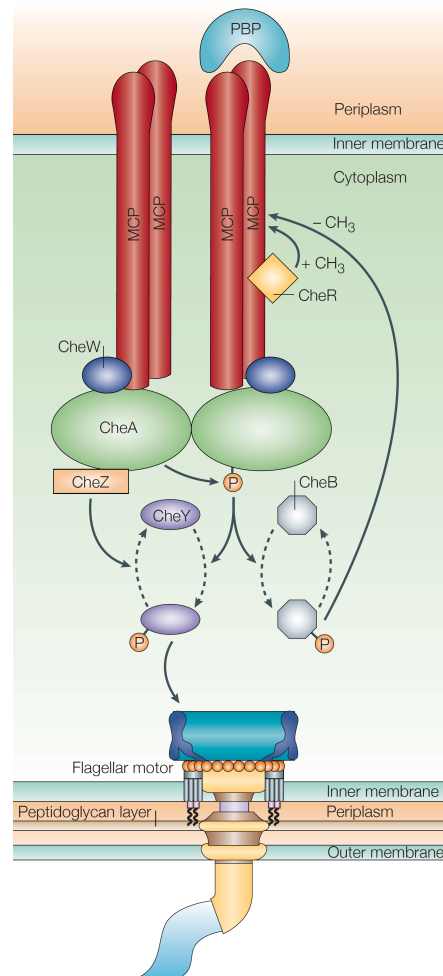


Figure 3.2: Schematic diagram of the chemosensory system of *Escherichia coli*. Two dimeric chemoreceptors - methyl-accepting chemotaxis proteins (MCPs) - are shown. In addition, two chemotaxis protein CheW monomers and a CheA dimer are shown interacting with the highly conserved signaling domain of the MCPs in the cytoplasm. A decrease in attractant concentration induces trans-autophosphorylation of the CheA dimer, which phosphorylates the response regulator CheY. Phosphorylated CheY then binds to the flagellar motor to bring about a change in direction. Phosphorylated CheA also phosphorylates another response regulator - the methyl-erasure CheB. Phosphorylated CheB competes with a constitutive methyltransferase, CheR, to control the degree of methylation of specific glutamates in the MCPs. This resets the signalling state of the receptors and allows them to adapt to the present concentration of attractant and to sense subsequent changes. The dephosphorylation of phosphorylated CheY is accelerated by the phosphatase CheZ. P=phosphoryl group. Taken from Wadhams and Armitage 2004.

3.2.2 Chemotaxis in *Caenorhabditis elegans*

C. elegans is a model animal with many assets for circuit neuroscience: its entire brain comprises only 302 neurons, whose complete connectome is known, its genetics is well controlled and it possesses a large repertoire of behaviors.

A klinokinesis strategy ?

Chemotaxis in *C. elegans* is very similar to *E. Coli* strategy; both are also biased random walks. *AE. Coli* worms have a two-phase navigation, alternating runs and pirouettes (Bargmann and Horvitz 1991; Pierce-Shimomura *et al.* 1999; Luo *et al.* 2014), which are random reorientation events. As for bacteria, the rate of pirouettes events is modulated by the gradient of concentration in chemoattractant, such that chemotaxis in *C. elegans* is a *klinokinesis*.

One important difference with *E. Coli* is the fact that *C. elegans* can do either positive or negative chemotaxis and has a preferred concentration of chemoattractant, which depends on its environmental conditions of growth. A worm grown at 50mM concentration of NaCl will seek region at that concentration (Figure 3.3a and b). Recently, another important difference with *E. Coli* has been discovered by Lino and Yoshida (2009). Re-examining chemotaxis navigation, the authors found that worms slightly bias their curvature during runs towards region of higher concentration. It is today accepted that chemotaxis in *C. elegans* is a mix of the traditional biased random walk and a slight bias during runs. This new result may change the class of *C. elegans* chemotaxis from *klinokinesis* to *klinotaxis*.

A chemosensory pathway

A chemosensory pathway has been proposed in the literature (Suzuki *et al.* 2008; Luo *et al.* 2014). ASE chemosensory neurons are activated by a positive gradient (ASEL) or a negative gradient (ASER) of NaCl concentration (Suzuki *et al.* 2008). This ON/OFF pattern of activity is then encoded by downstream interneurons AIY, AIZ and AIB, which constitute a downstream comparator (Figure 3.3c). These interneurons may inhibit or not the pirouettes events and then lengthen or shorten the runs.

C. elegans chemotaxis appears to be very similar to its thermotaxis. A more detailed description of the latter is provided in Chapter 5.

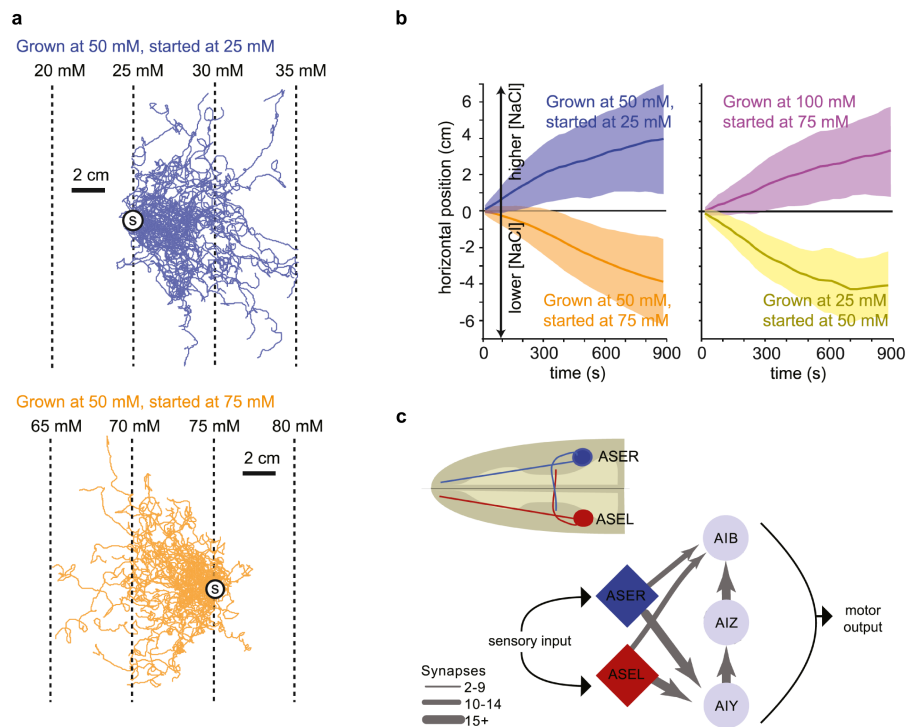


Figure 3.3: *C. elegans* performs chemotaxis in linear NaCl gradients. **a**, Navigation trajectories of wild-type animals in linear NaCl gradients with 2 mM NaCl/cm steepness. Animals were grown at 50mM NaCl and started at 25 mM (blue) or 75 mM (orange). **b**, Average horizontal position of worms grown at specific salt concentrations and started at different salt concentrations on 2 mM/cm NaCl steepness linear gradients. Solid lines and shading indicate the mean ± 1 STD of horizontal displacement. $n > 280$ animals for each measurement. **c**, Simplified synaptic connections for the salt-sensing ASE neurons. Taken from Luo *et al.* 2014.

3.2.3 Chemotaxis in *Drosophila melanogaster* larva

Drosophila melanogaster larva is an important model animal for the study of goal directed navigation. Flies, at the larval stage are small, optically transparent and genetically tractable. Furthermore the knowledge of their anatomy, behavior and genetics is immense. *D. melanogaster* larva is thus an ideal animal to use modern tools like high speed behavioral imaging, fluorescence microscopy or optogenetics and to study the sensorimotor circuit underlying goal-directed navigation such as chemotaxis.

Locomotor behavior of D. melanogaster larva

The navigation of *D. melanogaster* larvae comprises two alternating motor programs: runs and turns (Figure 3.4). During the first phase, the larva runs forward and its head is aligned with the rest of its body. During turns, the larva pauses its forward movement and sweeps its head left and right one or multiple times. In the end of a turning event, the head is oriented in a new

direction, which will be the direction of the next run. Chemotactic navigation results from a sensory-driven modulation of the statistics of runs and turns.

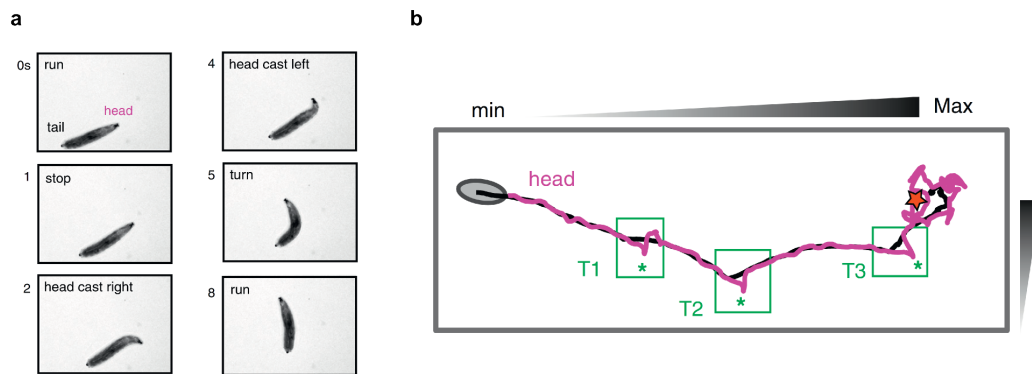


Figure 3.4: **a**, Top view of body posture changes. A sequence of behavioral transitions encompassing active sampling and turning. At time $t = 1$ s, the larva interrupts its motion. Next, it implements a head cast to the right ($t = 2$ s) followed by a head cast to the left ($t = 4$ s). Finally, a turn is initiated upon resumption of peristalsis. **b**, Trajectory of a larva navigating toward the odor source in the odor gradient is shown in panel (a). The position of the head and the center of mass are indicated in magenta and black, respectively. We focus on three illustrative turns (corresponding to time points T1, T2 and T3). Adapted from Gomez-Marin and Louis 2012.

Chemotaxis strategy

1. Like in the biased random walk of *E. coli* or *C. elegans*, during chemotaxis, *D. melanogaster* larvae bias run duration towards regions of higher concentration of chemoattractant. Modulating the probability of triggering a turning event by integrating the time course of the sensory inputs, the larva increases the duration of run towards high concentrations regions.

2. Unlike *C. elegans*, turning events are actual decision points. The animal actively samples the local gradient of concentration. When larvae pause and begin head sweep, the direction of the first head sweep is biased toward higher concentration but with a large error rate (Gomez Marin). If the head sweeps toward high concentration region it is more likely to interrupt its turning phase and to run again. During head cast the larva performs an association between increase and decrease of concentration perceived and the head position. This process requires a temporal integration of the sensory inputs across the cast period. In 70% of cases, larvae need only two head casts to identify the good direction. Gomez Marin *et al.* summarized this active sampling of the concentration in its environment with a model shown in figure 3.5a).

The circuit involved in the active seeking of high concentration during head sweeps remains unknown.

A spatial strategy? Not really...

Even if *D. melanogaster* larva has bilateral chemoreceptors, Louis *et al.* and Gomez-Martin *et al.* showed that with their olfactory function restricted to one side, larvae can still perform chemotaxis. In fact, owing to the small size of the larvae, the left/right difference in concentration is close to the physical threshold for detection (Gomez-Marin *et al.* 2011). Bilateral olfactory inputs are thus not required to do chemotaxis but they enhance turning decision success rate.

In conclusion, the chemotaxis strategy of *D. melanogaster* larvae is a two phases program with (i) runs whose duration is biased by the concentration gradient (*klinokinesis*) and (ii) head casts whereupon, after a seeking phase, the final direction of turns is set towards high concentration regions (*klinotaxis*).

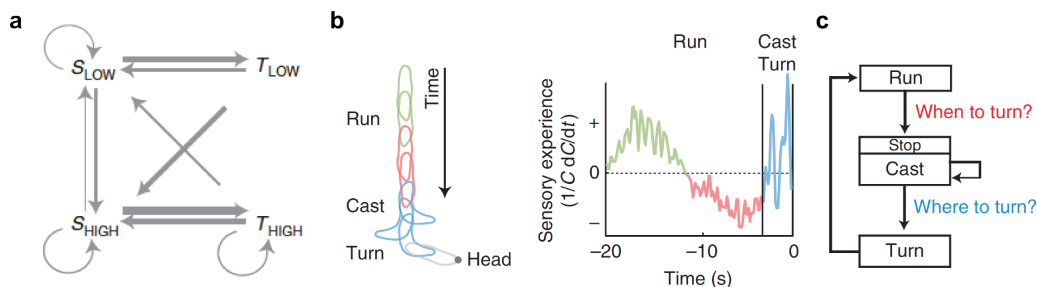


Figure 3.5: **a**, Ethogram classification of odor-search behaviour as proposed by Gomez Marin *et al.* 2011 consisting of four elementary ‘action - perception’ states: turns (T) and head casts (S) towards low (L) and high (H). Illustration of the 4 behavioral states of the model. Transition probabilities between states calculated on the basis of a first-order Markov chain trained on the experimental data. Arrow thicknesses are proportional to the transition probabilities. **b**, Left panel: Schematic of a trajectory segment consisting of a run followed by a turn. The sequence of body postures corresponds to forward locomotion oriented up gradient (green) and down gradient (red) followed by a series of head casts (blue) and a turn (gray). Right panel: Sensory experience associated with the trajectory segment depicted in the left panel. During up-gradient motion (green), the sensory experience detected at the larva’s head region is positive. On motion down gradient (red), the sensory experience is negative for several seconds, which triggers a transition from running to head casting (blue). Head casts are associated with short and contrasted changes in odor concentration. **(c)** Diagram of the basic computation and rules controlling larval navigation in odor gradients. Chemotaxis consists of two main types of decision: when and where to turn. Gomez-Marin *et al.* 2011.

3.3 Phototaxis

Light is a variable that affects biological systems. From predator avoidance to foraging, changes in environmental light level can affect the behavior of organisms. Phototrophic organisms, like photosynthetic algae, have a direct need of light for their metabolism. Other feed on phototropic animals – fish larvae feed on paramecium for instance – and they thus need to navigate towards light in order to find food. Phototaxis is used to increase gamete encounters in marine green alga (Togashi and Cox 2004). Positively phototactic, gametes reach the surface of the water because they are more likely to find a mate in a plane than in a volume.

Phototaxis differs from chemotaxis because of the dimension of its stimulus. Chemical concentration is a scalar whereas light is a vector. The vectorial nature of light stimuli is essential to understand the development of a directional sensory-receptor organ, such as the eyes. Even if prokaryotes have kept their simple run and tumble (klinokinesis) strategy to reach brighter region, during evolution, organisms rapidly developed a specific receptor that could probe the intensity of light and the direction of the source at once. We will see that such an evolutionary perspective can help us understanding phototactic behaviors.

In the last decades, phototaxis has been studied in many organisms such as algae (Togashi and Cox 2004), prokaryotes (McCain *et al.* 1987), marine zooplankton *Platynereis dumerilii* (Jekeli *et al.* 2008), invertebrates like *C. elegans* (Ward *et al.* 2008) or *D. melanogaster* larva (Sawin *et al.* 1994, Kane *et al.* 2013), as well as vertebrates like *Danio rerio* larva (Burguess and Granato 2007, Burguess *et al.* 2010, Chen and Engert 2014, Zhang *et al.* 2017). In the following I will focus on the phototaxis strategies at play in marine zooplankton *Platynereis dumerilii*, *C. elegans*, *D. melanogaster* and *Danio rerio* larva (zebrafish). I will try to relate these phototactic strategies with current knowledge regarding the evolution of the eyes. In the last part of the chapter, I will try to classify the different phototactic behaviors using the kinesis/taxis and tropo/klino terminology.

Prior: how do eyes sense light?

The light enters in the eye through the pupil, which size is controlled by a set of muscles encompassing the iris. These muscles are controlled by parasympathetic and sympathetic neurons. The retina - located in the back of the eye - is the location of the photoreceptors, which convert light into electrical signal. Rods are necessary for black and white vision under low light intensity whereas cones provide colour vision in bright light. Rods and cones contain photopigments that absorb light; they are made of proteins called rhodopsin (rods) or opsin. Rhodopsin and Opsin have a 11-cis-retinal as a chromophore and are coupled with a G-protein. The chiral part of these opsins is sensitive to light and photon absorption changes their conformation from *cis* to *trans*. Photoisomerization of 11-cis-retinal to all-trans-retinal results in the activation of the G-protein cascade, a process called phototransduction. This process ultimately activates ion channels and results in a change in the membrane

potential and corresponding neurotransmitter release, which initiates the electrical transduction.

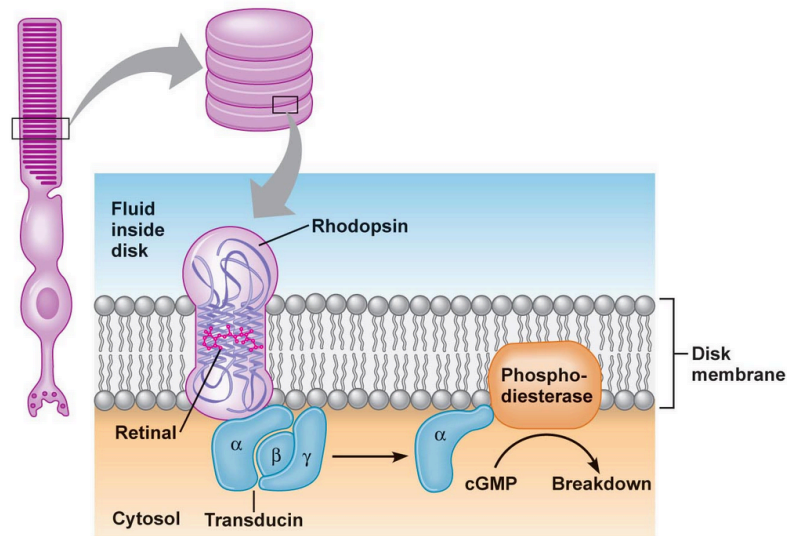


Figure 3.6: Phototransduction for the rhodopsin case.

3.3.1 Phototaxis in prokaryotes and eukaryotes:

Prokaryotes

The majority of prokaryotes do not have any detector to sense light direction. However some species like archaeobacteria and eubacteria are phototactic (Scharff and Wolff 1994). For example, the archaeobacterial *Natronobacterium pharaonis* developed pigments control of its movements mediated by two retinal-dependent proteins, sensory rhodopsin I and rhodopsin II, and are attracted by light gradients above 520nm. In general, the phototaxis mechanism in archaeobacteria is very similar to chemotaxis as described before: it is a biased random walk (McCain *et al.* 1987). If light intensity decreases the bacteria tumbles and reorients itself in a random direction; if the bacteria is moving up the gradient of light, the runs are prolonged (*klinokinesis* strategy).

Numerous studies have described in details the chemical pathway leading to motor switch and modulation by light intensity in archaeobacteria (McCain *et al.* 1987). Light triggers an isomerization of retinal rhodopsin, which initiates the phototransducing pathway leading to swimming reversals. Spudich (2006) summarizes the phototactic pathway in prokaryotes (see Figure 3.6):

“Sensory rhodopsins I and II form 2:2 complexes in haloarchaeal membranes with their cognate transducers, HtrI and HtrII, respectively. The transducers, which are homologous to bacterial chemotaxis receptors, contain two transmembrane helices and a large cytoplasmic domain that, at its distal end, binds to the histidine kinase CheA. The SR–Htr complexes modulate the CheA kinase activity, thereby controlling the extent of phosphorylation of a cytoplasmic flagellar-motor switch regulator, CheY. Orange-light activation of SRI elicits an attractant response by transiently inhibiting kinase activity. The resulting decrease in phospho-CheY concentration reduces the probability of

motor switching and, therefore, the cells continue to swim in the direction of increasing orange light. Blue-light activation of SRII has the opposite effect and transiently activates CheA. The increased phosphorylation of CheY increases the probability of a reversal in swimming direction and, therefore, the swimming path of the cells is biased towards lower intensities of blue light. An unusual twist is that SRI also mediates strong repellent responses when it is activated by two sequential photons (i.e. orange followed by near-UV light)”

Eukaryotes use a strategy for phototaxis that is a fundamentally different from that of prokaryotes. They can follow light gradient in three dimensions. They possess several photosensors, allowing them to scan the space and periodically alter the beating of the cilia. Thus, rather than a *kinesis*, eukaryote organism developed a *taxis* strategy (the direction of the navigation is changed during in live). Let us focus on the example of an eukaryote organism: marine plankton.

An Opsithokont phototaxis: a real taxis

Opsithokont is a group of eukaryotes encompassing fungi, multicellular animals and protozoan taxa. Phototaxis is present in a large number of these organisms, especially ciliated marine zoospores like *Platynereis dumerilii*.

Marine zooplankton phototactic behavior accounts for the largest transport of biomass on earth (Hays 2003; Giometto *et al.* 2015; Jekeli *et al.* 2008). This vertical migration of phytoplankton occurs everyday and strongly affects the ecology of aquatic ecosystems. These populations of phytoplankton are essential because they are responsible for half of the global photosynthetic activity on earth (Behrenfeld *et al.* 2006).

The “simplest animal eyes”

In order to swim toward light, *Platynereis* larva uses the “*simplest animal eyes*” (Jekeli *et al.* 2008). This pair of “proto-eyes”, considered to be the first eyes in animal evolution (Randel and Jekeli 2016), comprises only two cells per side: a pigment cell and a rhabdomeric photoreceptor (figure 3.7). The structure of each eyespot restricts the view angle of *Platynereis*. This kind of photoreceptor makes use of the vectorial nature of light and allows the organism to probe the intensity of light stimulation and the direction of light source at once.

Phototaxis mechanism

The phototactic behavior begins at 25h of development and is sensitive to the wavelength of the light. *Platynereis* larva is sensitive to light between 365nm to 545nm with a maximal efficiency of phototaxis at 410nm and 490nm.

Platynereis larva navigates thanks to a ciliary band. During rotational swimming along the helical axis in the presence of a distant light source, each photoreceptor receives a periodic signal with a peak value every 2π rotation. Having two eyes, the entire system thus experiences a periodic peak value every π rotation. The beat frequency of the ciliary band is changed in function of the increase or decrease of the periodic peak value measured by the photoreceptor.

Kinesis or taxis?

Using an electron-microscopy sectioning technique (Briggman and Bock, 2012), an axonal connection between the eyespots and an extension of the photoreceptor into a basal axon that forms synapses on the cilia has been discovered. Moreover, upon light exposure, the cholinergic neurotransmission by the photoreceptor slows down the beating of adjacent cilia of the ciliary band in less than 80ms, resulting in the reorientation of the helical trajectory towards the light (Jekeli *et al.* 2008). These elements demonstrate that eyespots are sensory neurons that directly modulate cilia's beating. Thus phototactic behavior of *Platynereis* is a *taxis* and not a *kinesis* as for prokaryotes.

Klinotaxis or tropotaxis?

Through ablation of the eyespots, Jekeli *et al.* showed that, (i) larvae cannot swim toward light without eyespot, (ii) with only one eye spot, half of the larve still perform phototaxis. The latter results indicate that larvae do not only compare light intensity between eyespots. *Platynereis*'s strategy is thus a mix of *klinotaxis* and *tropotaxis*.

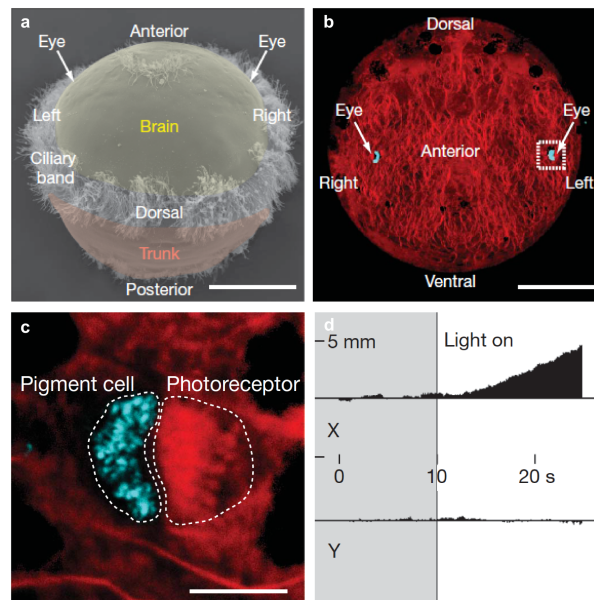


Figure 3.7: Larval eyespots mediate phototaxis in *Platynereis*. **a**, Scanning electron micrograph of a 48h old larva. **b**, Anterior view showing pigment autofluorescence (cyan). Boxed region is enlarged in **c**. **c**, Pigment (cyan) with bodipy564/570-propionic acid (red), the image is an enlarged view of the region indicated in **b**. Cell outlines are shown. **d**, Quantification of average phototactic displacement with directional light after 10 s. Positive phototaxis is indicated as positive X values ($n > 200$ larvae). Adapted from Jekeli *et al.* 2008.

An evolutionary perspective

Several other animals equipped with ciliated bilateral eyespots are believed to use the same phototaxis strategy. Spiral swimming, eyespots and phototaxis have been observed in many zooplankton larvae and also in single cell alga *chlamidomonas* (Witman 1993). In this navigational process, cilia-driven helical swimming and eyespots are functionally linked and co-adapted for

efficient phototaxis, reflecting a direct sensory-motor coupling between photoreceptors and locomotor cells. In more simple organisms like jellyfish larvae or sponge, the photoreception and the steering functions are combined in one unique cell. From an evolutionary perspective, Jékeli estimates that:

“Such direct sensory-motor coupling between a light sensor cell and effector cilia mediating phototaxis represents an ancestral condition in the evolution of animal eyes”.

In an impressive article, Jékeli (2009) reviewed all the literature on phototactic eukaryotes. The large variety of independent groups that do phototaxis suggests that it is somehow “easy” to evolve this behavior. Indeed phototaxis appeared after eukaryotes evolved to planktonic organism with ciliary and fixed shape. The phylogenetic analysis of photopigments (Jékeli 2009) indicates that they were acquired from a prokaryote source. Evolutionary scientists believe that first photopigments served to mediate a photophobic response. Then it evolved to phototaxis when orientation-dependent illumination of the photopigments was provided by a shading body or shading stigmata to give an information on the direction of the light.

Important to know

Some species display a positive phototactic behavior at a certain larval stage and switch to negative phototaxis at other developmental stage. In some cases, the organism is able to switch from positive to negative phototaxis in function of environmental factors like temperature, light intensity, chemicals, etc. (Randel and Jékeli 2016).

3.3.2 Eyes evolution and phototaxis

Eyes evolution: an old question

“To suppose that the eye with all its inimitable contrivances for adjusting the focus to different distances, for admitting different amounts of light and for the correction of spherical and chromatic aberration, could have been formed by natural selection, seems, I freely confess, absurd in the highest degree”. But then he continues: “Reason tells me, that if numerous gradations from a simple and imperfect eye to one complex and perfect can be shown to exist, each grade being useful to its possessor, as is certainly the case; if further, the eye ever varies and the variations be inherited, as is likewise certainly the case; and if such variations should be useful to any animal under changing conditions of life, then the difficulty of believing that a perfect and complex eye could be formed by natural selection, though insuperable by our imagination, should not be considered as subversive of the theory”

Charles Darwin, 1859

In the field of evolutionary and developmental biology, the origin of the eyes is still unknown. What was the first precursor of the eyes? Which of the brain or the eyes did come first during evolution? And beyond that why?

600 million years ago, organisms evolved photoreceptors to sense light, certainly to mediate phototaxis and avoid dark shadows of predators. 60 million years later the first visual systems emerged (Lamb *et al.* 2007). Four phyla independently evolved a high-resolution vision (Nilsson 2009) offering entirely different strategies to solve the optical problems of vision. Thus, the last common ancestor of bilaterians had to only possess proto-eyes, even early bilaterians (Randel and Jékeli 2016). The universal deployment of opsins in eyes reinforces this idea and suggests that eyes must have a common ancestry. Gehring, Ikeo and later Arendt (Gehring 2004, Arendt 2003) proposed that a proto-eye made of a photoreceptor and a pigment cell per side is the origin of the eyes mediating directional photoperception.

A unique common ancestor

One simple approach to understand the evolution of eyes is to look at the evolution of photoreceptors. From simple to complex eyes, every visual system comprises rhabdomeric or/and ciliary photoreceptors associating two molecular types of opsins: r-opsins and c-opsins (Erclik *et al.* 2009). Despite the fact that rhabdomeric photoreceptors are often found in insects whereas ciliary photoreceptors are more present in vertebrates, many animals possess both photoreceptors suggesting that early bilaterian already evolved both photoreceptors. The literature on more downstream elements of the visual system evolution suchn as interneurons suggests that visual circuits may have already evolved in early bilaterians (Randel and Jékeli 2016). However, the understanding of this evolution process is still very partial.

In the following, we will review some evolutionary articles that address phototaxis sensorimotor processing in various organisms as a way towards the understanding of eyes evolution.

Nilsson's framework on evolution and phototaxis

Evolution is driven by the need to perform new sensory tasks requiring the system to integrate and interpret now external information. For Nilsson, “*sensory evolution is a task-punctuated process* “ (Nilsson 2009). Improvement in the processing of sensory information can lead for the same sensory task to the replacement of an old strategy. The transition, as in phototaxis, from temporal comparison strategy (*klinotaxis*) to spatial comparison (*tropotaxis*) is an example of such an improvement. It is often called in the literature the transition from non-vision to vision (Arendt 2003 Jékeli 2009, Nilsson 2009, Randel and Jékeli 2016,). The schematic diagram (Figure 3.8) proposed by Nilsson accounts for this transition.

Nectochaete larva provides an illustration of such a task-driven improvement of the visual system. This larva uses helical strategy (temporal strategy) for phototaxis when swimming or performs spatial comparison phototaxis when gliding on a surface (Randel and Jékeli 2016).

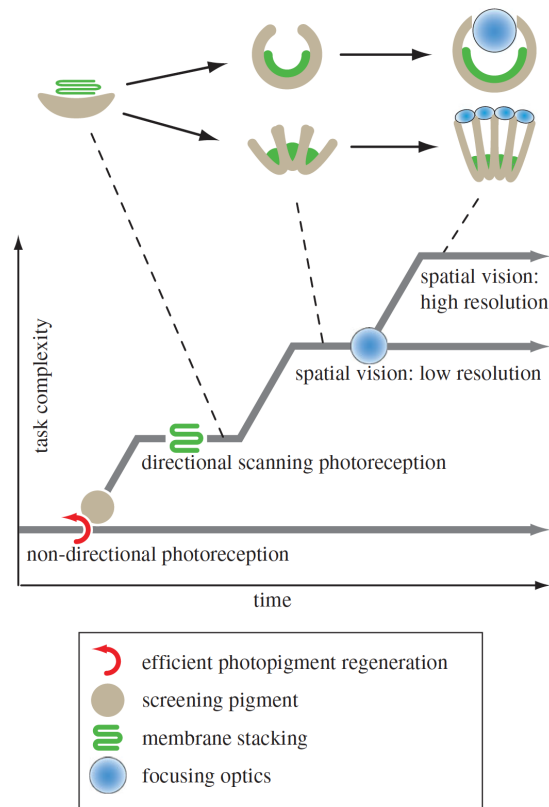


Figure 3.8: Key innovations in eye evolution. Directional photoreception is assumed to have evolved from nondirectional monitoring of ambient luminance by a cell duplication event and an opsin gene duplication leading to a receptor opsin and photoisomerase pair of proteins. This was followed by the introduction of screening pigment and soon also by membrane stacking to allow for better contrast discrimination, increased speed and more directional photoreception. Multiple receptor cells would then allow for true spatial vision and the scanning mode of operation could be abandoned. To collect enough photons for spatial vision with higher resolution, lenses must be introduced, but the new high-resolution tasks are expected to add to rather than replace the older low-resolution tasks. Taken from Nilsson 2009.

Randel and Jékeli draft on eyes evolution in *Platynereis dumerilii* eyes

In Randel and Jékeli (2016), the author proposed a “conjectural” scenario for the evolutionary transition from helical phototaxis with proto-eyes to spatial comparison phototaxis with a complex circuitry in the case of *Platynereis dumerilii*. Summarized in figure 3.9, the scenario begins with an eyespot comprising a sensorimotor photoreceptor and a pigment. The photoreceptor directly modulates the beat frequency of cilia in function of perceived light intensity (Figure 3.9a). The second step is the development of a second photoreceptor called cerebellar photoreceptor with projection towards the contralateral part (Figure 3.9b). This process, visible in the development of *Platynereis dumerilii* larva (Randel and Jékeli), enables the larva to also perform negative phototaxis. These new bilateral connections represent a step towards tropotaxis. The third step could have been the duplication of these photoreceptors to form the *Platynereis dumerilii* adult eyes consisting of four

photoreceptors (Figure 3.9c).

Although these three first steps are well supported by developmental study of *Platynereis dumerilii*, the rest of the proposed evolutionary process is really conjectural. The authors suggest that the development of motor neurons (Figure 3.9d) lead to the loss of direct connections from sensory perception to motor control. Then, duplications of photoreceptors could have progressively formed interneurons (Figure 3.9e, f, g), creating contralateral and ipsilateral connections. These new connections “*may have allowed more complex turning decisions and the ability to switch from negative to positive phototaxis*” (Randel and Jékeli 2016).

Beyond phototaxis, the visual system evolved to allow more complex tasks such as motion detection, opto-motor and opto-kinetic reflex or predator avoidance. Certainly, the neural circuitry evolved from phototaxis visual system to a high-resolution visual system.

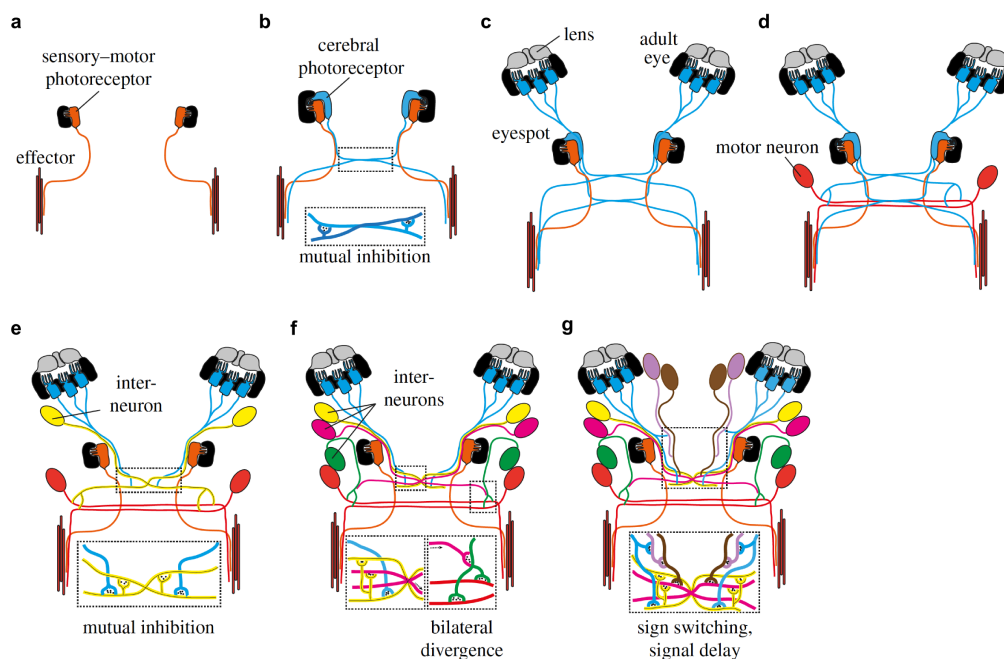


Figure 3.9: Transition scenario for the evolution of low-resolution visual eyes from two-celled sensory-motor eyes. **a**, Larval eyespot with a single photoreceptor cell (orange) mediates positive helical phototaxis by directly innervating an effector (muscle and ciliated cells are not distinguished for simplicity). **b**, A duplication event leads to the development of a second photoreceptor cell (blue), which is able to mediate negative phototaxis. The development of mutual synaptic contacts between the contralateral photoreceptors allows contrast enhancement, representing the first step towards vision. **c**, Relocation and duplication of the second photoreceptor cell (blue) results in the development of the cerebral eyes. The duplication of photoreceptors improves the signal-to-noise ratio, the development of a lens improves photon collection. **d**, Integration of a motor neuron into the circuit and bilateral circuit divergence enables the signal to reach either the left or the right motor organ (effector). With this circuit, the animal is able to switch between positive and negative phototaxis, using the same eye. **e**, **f** Integration of one to several interneurons improves computational power and provides further possibilities for modulation (e.g. integration of other sensory inputs). **g** The

development of a new type of primary interneuron (magenta, directly postsynaptic to the photoreceptor cells), which transmits the signal with a delay. This second primary interneuron might work together with the first primary interneuron (yellow) to form the first motion detector. Orange: sensory–motor photoreceptor of the eyespot and motor neurons; blue: adult eye photoreceptors; yellow: primary interneuron; pink, green, magenta, other interneurons. Adapted from Randel and Jékeli 2016.

3.3.3 *Drosophila melanogaster* larvae phototaxis

Phototaxis of fly larvae has been studied for a long time as the ultimate example of goal directed navigation (Mast 1911, Sawin, *et al.* 1994 Kane *et al.* 2013, Fraenkel and Gunn 1961). During most of their development, *D. melanogaster* larva does negative phototaxis and navigates away from light (Sawin *et al.* 1994, Kane *et al.* 2013). Light avoidance is dramatically reduced in the late larval stages and young adult flies become photoneutral. Adult flies are then strongly attracted by light and do positive phototaxis (Keene and Sprecher 2012).

Locomotor behavior of D. melanogaster larva

As we already mentioned, the trajectory of *D. melanogaster* larvae consists in two alternative motor programs: runs and turns (Figure 3.10). During this second phase, the animal actively probes its environment using head sweeps. Phototactic strategy is a behavior that modulates the statistics of runs and turns.

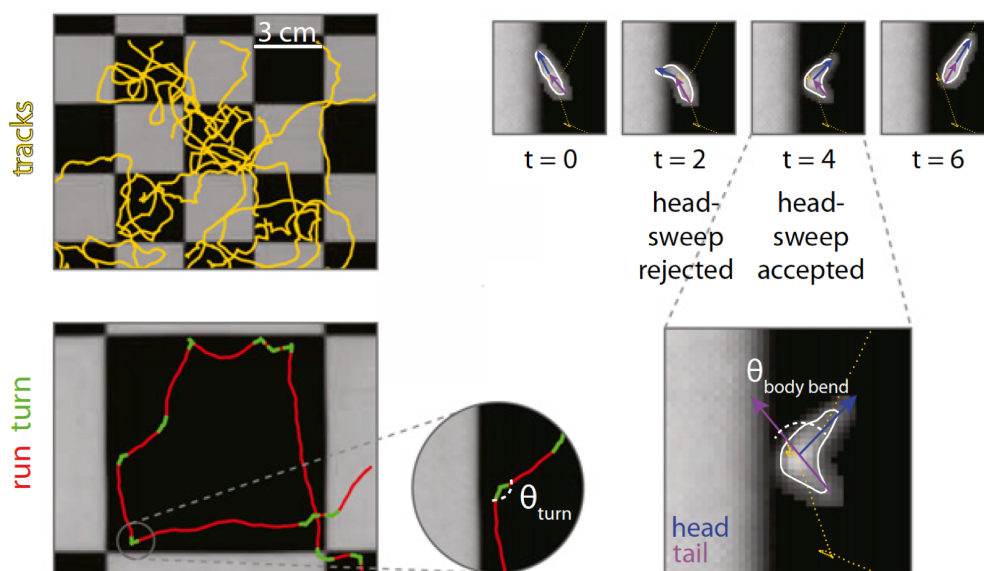


Figure 3.10: Right top panel: Representative negative phototactic trajectories of *D. melanogaster* larvae. Right bottom panel: zoom of an individual trajectory showing turning events in green and runs in red. Left top panel: Representative-turning events at the border of a light/dark square. The larva sweeps its head on

the left side, encounters a positive gradient of light, which is not what it wants. Thus the larva sweeps its head on the right and encounters a negative gradient of light, which is favored, so the larva runs. Adapted from Kane *et al.* 2013.

Photosensors

To sense the light, *D. melanogaster* larvae have two eyes called the “Bowling organ”. This organ is composed of 12 photoreceptors (Keene and Sprecher 2012 review on fly eyes) expressing *rhodopsin* that mediate phototaxis at low light level. Remarkably, at very high level of light, larvae lacking eyes can still perform negative phototaxis. Indeed, the non-rhodopsin multidendritic neurons located in the larva body respond to intense light levels (Xiang *et al.* 2010).

Negative phototaxis

1. Like in the biased random walk of *E. coli* or *C. elegans*, during phototaxis, *D. melanogaster* larvae bias run duration towards darker region. Modulating the rate of turning events, the larva increases or decreases the duration of runs towards dark or bright regions. In Kane *et al.* the authors show that the probability of turning events is a lot higher when larvae go from dark to bright regions, as compared to when they move from bright to dark regions or when they stay in regions of constant illumination level (Figure 3.11a).

2. As for chemotaxis, *D. melanogaster* larvae use turning events to correct the orientation of their body towards darker regions. These are decision points whereupon the larva biases its direction of motion. In Kane *et al.* (2013), the authors showed that the size of head sweep is biased such that larvae will make larger turns if they are in a bright region. Hence, it will increase the probability to explore new regions (Figure 3.11b).

3. When larvae pause and begin a head sweep, the direction of the first head sweep is random (Kane *et al.* 2013) whereas the probability of terminating the turning events and run again is biased by its direction. If the head sweeps toward a dark region, it is likely that the larva will interrupt the turn and run again (Figure 3.11).

4. Larvae are able to find the light source orientation using directional cues. This property is given by the position of the Bowling organ and its photoreceptors (Figure 3.11c). Located in a “pigment cup”, the BO allows to decode the direction of the source.

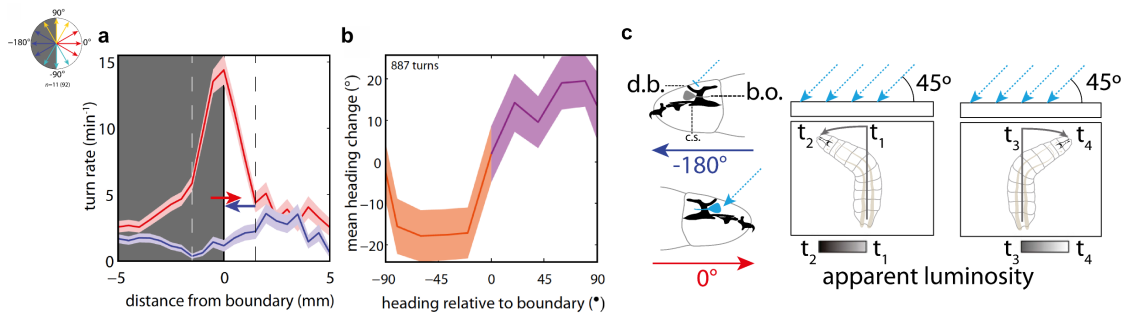


Figure 3.11: Larvae bias the frequency, size, and direction of turns to remain in the dark. Top right: Schematic of heading angles relative to boundary. **a**, Turning rate vs. distance of head from the boundary of dark/light region for -180° and 0° headings. Dashed lines indicate boundary region. **b**, Mean heading change achieved by turns vs. initial heading relative to the boundary. **c**, Directional illumination navigation. Schematic of differential view angle of the BO conferred by cephalopharyngeal skeleton. Adapted from Kane *et al.* 2013.

Spatial vs. Temporal strategy

Is *D. melanogaster*'s phototactic behavior a klinotaxis (temporal comparison) or a tropotaxis (spatial comparison)? Does *D. melanogaster* compare the difference in light intensity between their Bowling organs (the eyes) during runs? The response to the second question is probably negative, as indicated by the fact that when a larva is at the border between a dark and a light region, the first head sweep is randomly oriented toward the dark or the illuminated region. Kane *et al.* (2013) confirmed this result by submitting larvae to time-varying illumination, in the form a square-wave or triangle-wave temporal pattern. In both cases, the authors observed that larvae respond to a temporal gradient of light intensity and display a modulation of both turn rate and turn amplitude. This result demonstrates that larvae use temporal comparisons of light intensity to perform phototaxis.

Moreover this klinotaxis only occurs during head-sweeps (Kane *et al.* 2013). Turning events are the key point of decision in phototactic behavior. During these phases, the larva evaluates the direction of the darker region.

Modeling the circuit

The Bowling organ encompasses 12 photoreceptors (8 express rhodopsin 6, 4 express rhodopsin 5) that send signals to tectal neuropil of the larvae (Keene and Sprecher 2012). One neuronal class receiving synaptic inputs from these photoreceptors is the fifth lateral neurons (LN). It has been shown that the 5th LN is a major relay for phototaxis; an inactivation of these neurons disrupts phototaxis (Kane *et al.* 2013). No evidence has been found so far that would indicate that a comparison is made between the left and right Bowling Organs, excluding for the moment a possible tropotactic mechanism. No detailed circuit-level analysis has been proposed but all these results provide a first step towards a precise understanding of phototaxis in *D. melanogaster* larva.

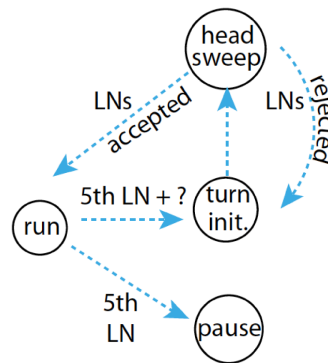


Figure 3.12: Models for the phototaxis navigational strategy and photosensory processing of *D. melanogaster* larvae. Adapted from Kane *et al.* 2013.

Conclusion

Phototaxis in *D. melanogaster* larva is reminiscent of chemotaxis. It is a two phases process: runs whose duration is modulated by light stimuli (*klinokinesis*) and head casts where, after an active exploration phase, the final direction of the turn and its magnitude is biased by light (*klinotaxis*).

3.3.4 Zebrafish (*Danio rerio*) larvae phototaxis

As we saw before in this manuscript (Chapter 2), zebrafish larva is a model vertebrate animal for neuroscience and developmental biology with many advantages: small size, transparency, multiple behaviors at larval stage, genetics tractability and amenability to *in vivo* fluorescence microscopy. I made use of this model during my PhD to investigate phototactic neural circuit in vertebrates.

Despite pioneering studies in invertebrate animals like *Platynereis dumerilii* or *Drosophila melanogaster* (see above for more details), behavioral and neuronal mechanisms underlying phototaxis in vertebrates is still poorly understood. Some publications on zebrafish phototaxis exist, which mainly focus on the behavioral aspects of this behavior. But to date, no data are available to understand how these behavioral strategies might be implemented at the circuit level in the vertebrate brain.

Here I will quickly review the literature on phototaxis in zebrafish. This was the starting point of my work on this behavior.

Prior: spontaneous locomotor behavior of zebrafish larva

Zebrafish locomotion is very different from flies' larvae locomotion. It consists in a series of discrete movements called swim bouts. During spontaneous navigation, swim bouts can be classified as forward swim, turning, C turn, j turn (Kalueff *et al.* 2013, Orger 2016). In Dunn *et al.* (2016), the authors showed that during spontaneous navigation, zebrafish larvae make a swim bout every 1.2s. A change in the direction (left/right) of the navigation

occurs in periodic manner every 5-6 swim bouts i.e. every 6-7.2s (Dunn *et al.* 2016). Thus zebrafish larvae thus tend to maintain the same turing state for 6-7.2s.

To quantify the locomotion of larval zebrafish, these series of movement can be characterized by: (1) the *dwelt time*, which is the time between two swim bouts, *displacement*, which is the distance between the beginning and the end of a swim bout, (2) the *turn magnitude*, which is the absolute value of angle variation during a swim bout and (3) the *turn direction*, which is the sign of angle variation during a swim bout.

Prior: how does zebrafish larva sense light?

Zebrafish larvae strongly relies on visual cues, thus displaying a large range of visually-guided behaviors as early as 3dpf (Brockerhoff et al 1995). Zebrafish eyes possess four cone types, which makes them tetrachromatic animals. They possess three “classical” long cones containing blue, red and green sensitive photopigments and a short cone with a UV-sensitive photopigment. Zebrafish larvae also possess rod photoreceptors allowing vision at low intensity levels. The organization of the zebrafish visual system is similar to that of other vertebrates. Moreover zebrafish larvae possess a melanopsin class of deep brain photosensors that mediates dark photo-kinesis in the absence of eyes (Fernandes *et al.* 2012).

Zebrafish larvae demonstrate positive phototaxis

Zebrafish larvae exhibit a positive phototactic behavior: when placed in a gradient of light intensity, they tend to navigate towards regions of higher intensity (Figure 3.13) (Orger and Baier 2005, Serra *et al.* 1999, Burgess et al 2010). After a prior habituation phase in an homogenously lit environment, an imposed gradient of light drives larvae to swim towards the region of higher intensity (positive phototaxis)..

To reach the target light source in the case of positive phototaxis, larvae display two types of movements: turns and swim forward. Burgess *et al.* precisely analyzed the first movements of larval zebrafish when a gradient appears in its environment. They showed that the dwell time of the first turn is slightly modulated by the distance to the target but is strongly dependent on the orientation of the larvae relative to the target when the gradient appears. The frequency of turn increases if the larva is oriented away from the target. They also showed that the turn magnitude is modulated by the orientation of the larva relative to the target such that if the larva is away from the target, the turns will be larger in amplitude.

Regarding the swim forward movements: larvae already facing the target will decrease drastically (3 times) the dwell time between forward swim bouts and thus increase the swim bout rate.

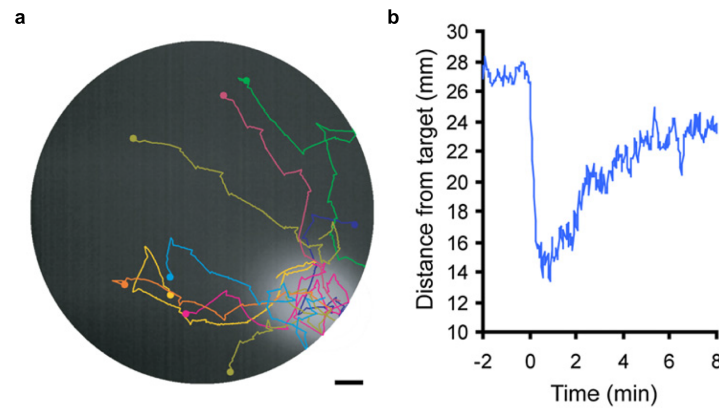


Figure 3.13: Zebrafish larvae perform positive phototaxis. **a**, Swim tracks for nine larvae during phototaxis superimposed over an image of the arena showing the position of the target light. Circles indicate starting positions. The scale bar represents 5mm. **b**, Mean distance from target is minimal after 60 s of phototaxis (total 180 larvae). Adapted from Burgess *et al.* 2010.

Zebrafish larvae can display negative phototaxis

If the light intensity is very high, larvae turn away from the light source and move slowly away displaying a negative phototactic behavior (Burgess *et al.* 2010). It seems that negative phototaxis in zebrafish is a mix of freezing behavior and taxis behavior.

Phototaxis of adult zebrafish

Phototactic behavior in adult zebrafish is more complicated. It has been shown (Serra *et al.* 1999, Gerlai *et al.* 2000) that adult fish have a preference for bright regions the first minute following a change in illumination. After ten minutes the fish prefers to stay in a darker environment, certainly to hide from possible dangers.

Photoreceptors

Photoreceptors in vertebrates sort light by wavelength and bipolar cells encode increments and decrements of light (Orger and Baier 2005). Short (UV/blue) and high (red) wavelength cones mediate phototactic behavior. The former do not contribute to motion detection but are involved in phototaxis (Orger and Baier 2005).

Separate population of ON and OFF cells drive phototaxis

Vertebrate retina channels visual stimuli into an ON-pathway activated by an increase in light intensity and an OFF-pathway activated by a decrease in light intensity. Using a mutant line with a disrupted ON-pathway, Burgess *et al.* showed that approaching the target light during a positive phototactic sequence is mediated by the ON-pathway: the mutant animals do not display increased

swim bout frequency when facing the light source. This process also explains why during negative phototaxis, the swim bout rate does not increase when the larvae swim away from the light source.



Figure 3.14: Schematic illustrating information flow through retinotectal ON and OFF pathways when the target light is in the blind visual field. The OFF pathway enables larvae to reorient toward the target light by turning away from the eye perceiving a light decrement. Taken from Burgess *et al.* 2010.

Ablating one side of the optic tectum, Burgess *et al.* further showed that the OFF-pathway triggers turns away from the eyes perceiving the highest decrease in light intensity: half-blind larvae will turn in the right direction if the light is on the blind half of the visual field and will be mistaken if the light is on the intact part of the visual field. Confirming this idea, the authors also showed that the turn frequency is higher if the blind half of the larvae faces the bright side of the experimental chamber. This OFF-turn and ON-approach strategy is very similar to the OFF-turn pathway used by *C. elegans* in odortactic behaviors when worms undergo a decrease in odor stimulus.

A tropotaxis strategy?

Owing to the presence of two eyes in zebrafish larvae, one might expect that a spatial comparison of intensities between both eyes would mediate phototaxis (*tropotaxis* strategy). It is maybe because this result seems evident that no precise characterization of this tropotactic behavior is reported in the literature. The few insight on this issue are the following.

Burguess *et al.* (2010) showed that larvae submitted to a gradient of light, with the light source on the right side, will preferentially turn to right and vice-versa for the left eye. Huang *et al.* (2013) showed that a larval zebrafish under a left/right illumination contrast fixed on its antero-posterior body axis, will turn towards the bright side robustly (Figure 3.15a). Chen and Engert (2014) showed that a zebrafish larva freely swimming in an arena where an opaque black ring surrounds a bright disk in the center will stay in the middle of the chamber without crossing the border (Figure 3.15b).

This shows that a purely spatial difference in luminosity is sufficient to elicit a phototactic behavior in larval zebrafish.

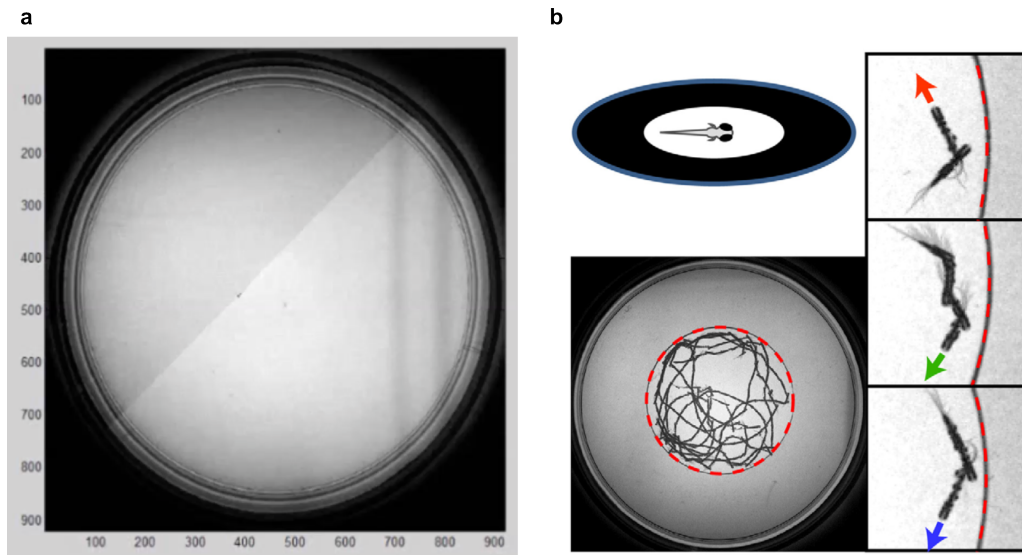


Figure 3.15: Spatial phototaxis. **a**, A freely swimming larval zebrafish is exposed to a visual stimulus that is dark on the right side and bright on the left side. The stimulus is locked to the location and orientation of the fish. Larval zebrafish turns robustly toward the white region. (Snapshot of a movie from Huang *et al.*). **b**, Larval zebrafish prefer light over darkness in the spatial comparison assay. Upper left: a diffusive (scattering) white screen surrounded by an opaque black ring is placed beneath the arena (a transparent dish) and illuminated from below. Lower left: the full trajectory of a fish over a session of 8min. Right panels: close-up views of trajectory segments close to the border. Three example segments are shown (rotated into the same orientation), with swim direction indicated by the red, green, and blue arrowheads; circular border indicated by the dashed red line. Note that the fish does not cross the border. Taken from Chen and Engert 2014.

A klinotaxis strategy?

As we saw before the spatial comparison (*tropotaxis*) strategy evolved as an improvement of the temporal comparison strategy (*klinotaxis*, see paragraph on evolution). In general animals that developed a spatial comparison strategy may still preserve a temporal strategy (*Platynereis dumerilii* or *Drosophila melanogaster*). Can zebrafish larvae also use temporal comparison to perform phototaxis? In Chen and Engert (2014), the authors developed a behavioral assay to isolate the purely temporal component of light stimulation. Zebrafish larvae navigate freely in a uniformly lit chamber. When the larva moves beyond a certain radius from the center of the arena, the light is turned off creating a “virtual circle“ (or virtual disk) of light. In this experiment the only information to which the fish has access to probe the gradient of light is temporal. Analyzing fish trajectories, the authors showed that the temporal gradient modulates swim turns, effectively restricting the trajectory within the virtual circle.

The *turn-magnitude* is strongly modulated by a Light to Dark transition. In this case, the average turning angle is highly increased just after the transition. Then, if the fish is still in the dark region, even if it does not have any spatial information, it keeps turning with a high turning magnitude distinct from the

baseline during 3 bouts (Figure 3.16b). This process is thus a short-time memory process.

The *turn direction* is also biased. Just after a Light to Dark transition, fish are more likely to turn in the direction opposite to its last turn. Then the following turns are always in the same direction as the first turn after the transition (Figure 3.16c).

These different behavioral elements suggest that temporal phototaxis is present in larval zebrafish and could be mediated by a short-term memory process.

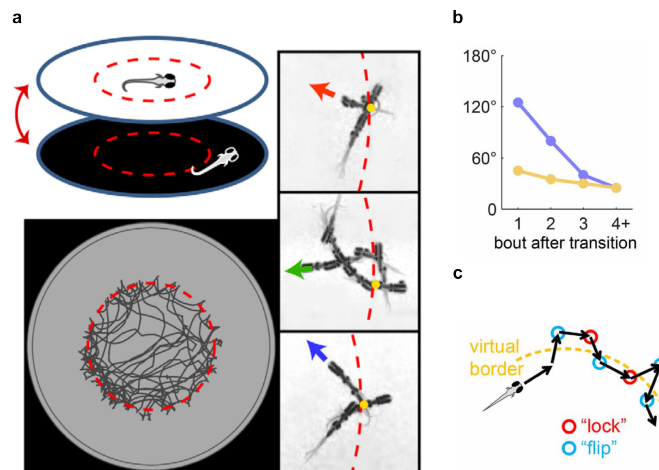


Figure 3.16: **a**, Temporal comparison assay, i.e., the Virtual Circle (VC) assay. The uniform illumination is turned off when the fish exits the virtual circle (dashed red circle, invisible to fish), and turned on again when the fish returns. Close-up view as in Figure 3.15b. Yellow dots marking the point where the fish exits the virtual circle. **b**, Mean turning angle of the n -th turn after a light to dark transition (violet) or a dark to light transition (yellow). **c**, Illustration of a model in which the fish tend to go back toward the virtual border flipping (“flip”) and then keeping turning in the same direction (“lock”) or making a big flip. Taken from Chen and Engert 2014.

3.4 Sensorimotor computation underlying phototaxis in zebrafish

Introduction

Multiple goal-directed navigation

There is a large variety of strategies developed by organisms to achieve goal-directed navigation. The behavioral aspects of these strategies have been precisely described. A *klinokinesis* strategy that relies on a biased random walk for *E. Coli* and *C. elegans* chemotaxis and thermotaxis and for prokaryotes phototaxis. A two phase program that consists of a *klinokinesis* biased random walk during runs and a *klinotaxis* to seek the preferred direction of turns during head casts for chemotaxis, thermotaxis and phototaxis in *D. melanogaster* larvae. A mixed *klino* and *tropotaxis* strategy that relies on a direct sensory-motor coupling of the photoreceptor to the cilia in planktons. A mixed *klino* and *tropotaxis* strategy for phototaxis in zebrafish larva. (Figure 3.17)

From the neuronal circuit point of view, navigational strategies are poorly understood. *E. Coli* and in part *C. elegans* are the only organisms for which a precise qualitative and quantitative description of the neuronal/molecular cascade has been provided. When I started my PhD, new tools had just appeared in neuroscience and particularly in the zebrafish community (whole brain imaging, optogenetics, electron microscopy, high speed behavioral monitoring). Thanks to these new techniques, it may finally become possible to dissect the neural circuits underlying navigational strategies in vertebrates. Several groups (Samuel in Harvard, Gershow at NYU, Louis in UCSB) used these new tools to dissect the circuitry subserving *D. melanogaster* larvae navigation. Our objective was to do the same with phototaxis in zebrafish.

Zebrafish phototaxis behavior

To simplify, we can think about zebrafish locomotor spontaneous navigation as a two phases program that is reminiscent of *D. melanogaster* larvae locomotion: a forward navigation phase with swim bouts occurring every 1.5s (similar to runs) and a reorientation phase that occurs every 10s (similar to head sweep). As we saw, the running phase is biased in the presence of a light gradient: the dwell time is shortened. The turning events are also modulated in the presence of a light gradient: the rate of reorientation events increase, the turn direction is biased such that larvae navigate for a longer time in the direction of a positive gradient of light. This second phase of zebrafish behavior is reminiscent of the head cast phase in melanogaster phototaxis.

Neural basis of phototaxis in zebrafish

In order to find the neural basis of phototaxis in zebrafish, we focused on the second phase of the locomotor program, i.e. we sought to understand orientational phototaxis. We looked for a neural ensemble whose dynamics could explain the bias in reorientation events towards a light source. This neural ensemble should account for both tropotaxis and klinotaxis strategy and bias the orientation of the larval navigation. Combining virtual-reality behavioral assays, volumetric calcium imaging, optogenetic stimulation, and circuit modeling we revealed that a self-oscillating hindbrain population (HBO) acts as a pacemaker for ocular saccades and controls the orientation of the turning events. This hindbrain population is sensitive to visual stimuli in a state-dependent manner, i.e. its response to visual inputs varies with the motor context. The HBO self-sustained oscillations allow zebrafish larvae to actively explore the light angular gradient. Its response to an asymmetric or symmetric visual stimuli lengthens the navigation in the current direction such that this activity bias is equivalent to a bias of the fish orientation towards a light source. We also developed a rate model that reproduces our observations and demonstrates how this sensorimotor processing accounts for phototaxis in zebrafish larva.

We published these results in **Wolf, S., Dubreuil, A. Berton, T., Böhm, U., L., Bormuth, V., Candelier, R., Karpenko, S., Hildebrand D. G. C., Bianco I. H., Monasson, R., Debréas, G.. Sensorimotor computation underlying phototaxis in zebrafish. *Nature Communications*. 2017 (in press)**

		Escherichia Coli and Prokaryote		Caenorhabditis elegans		Marine Zooplankton Platynereis dumerilii		Drosophila melanogaster larva		Zebrafish Danio rerio larva	
		Runing phase	Turning phase (tumble)	Runing phase	Turning phase (pirouettes)	Runing phase	Turning phase	Runing phase	Turning phase (head casts)	Runing phase	Turning phase (saccades)
Chemotaxis ∇_C	Locomotor parameters modulated by the stimulus	Duration of runs	Turns are randomly oriented	Duration of runs	Turns are randomly oriented			Duration of runs	First casts direction		
	Category	Klinokinesis		Klinokinesis with a slight klinotaxis				Klinokinesis and klinotaxis			
	Category	Klinokinesis		Klinokinesis with a slight klinotaxis				Klinokinesis and klinotaxis			
Phototaxis ∇_T	Locomotor parameters modulated by the stimulus	Duration of runs	Turns are randomly oriented			Speed of run		Duration of runs	Turn magnitude	Dwell time	Turn magnitude
	Category	Klinokinesis				Orientation of run		Final casts direction			Turn direction
	Category	Klinokinesis				Mixed klinotaxis and tropotaxis (2 eye-spots)		Klinokinesis and klinotaxis		Mixed klinotaxis and tropotaxis	
Thermotaxis ∇_T	Locomotor parameters modulated by the stimulus	Duration of runs	Turns are randomly oriented	Duration of runs	Turns are randomly oriented	Speed of run		Duration of runs	Turn magnitude	Dwell time	Turn magnitude
	Category	Klinokinesis		Orientation of run for isothermal tracking	Turns suppression for isothermal tracking	Orientation of run		Orientation of run	Final casts direction	Displacement	Turn direction
	Category	Klinokinesis		Klinokinesis or klinotaxis for isothermal tracking		Mixed klinotaxis and tropotaxis (2 eye-spots)		Klinokinesis and klinotaxis		Mixed klinotaxis and tropotaxis	

Figure 3.17: Summary of the different goal-directed navigation strategy discussed in the chapter

Refreshing the spirit

What was known on zebrafish phototaxis when I began my PhD (we just saw that in 3.3):

1. Light gradient modulates larvae behavior:

- Turn direction is modulated by light gradient (Burguess *et al.*)
- Turn magnitude is modulated by light gradient (Burguess *et al.*)
- Frequency of turning events is modulated by light gradient (Burguess *et al.*)
- Frequency of swim bouts forward is modulated by light gradient (Burguess *et al.*)

2. Light spatial or temporal gradient modulates larvae behavior; phototaxis uses a mix of tropotaxis and klinotaxis:

- Asymmetric illumination drives phototaxis (Huang *et al.*)
- Pure temporal gradient drives phototaxis (Chen *et al.*)

3. Temporal phototaxis relies on short-term memory:

- Turn magnitude is modulated by pure temporal light gradient for a few seconds (Chen *et al.*)
- Turn direction is modulated by pure temporal light gradient for several turns (Chen *et al.*)

4. Neural circuit:

- ON pathway drives the modulation of the frequency of swim bouts forward (Burguess *et al.*)
- OFF pathway drives turning events (Burguess *et al.*)

Sensorimotor computation underlying phototaxis in zebrafish

Authors: Sébastien Wolf^{1,2*}, Alexis M. Dubreuil^{3*}, Tommaso Bertoni^{1,2}, Urs Lucas Böhm⁴⁻⁷, Volker Bormuth^{1,2}, Raphaël Candelier^{1,2}, Sophia Karpenko^{1,2}, David G. C. Hildebrand⁸⁻¹⁰, Isaac H. Bianco¹¹, Rémi Monasson³, Georges Debrégeas^{1,2}.

Affiliations:

- 1. Sorbonne Universités, UPMC Univ. Paris 06, UMR 8237, Laboratoire Jean Perrin, F-75005 Paris, France**
- 2. CNRS UMR 8237, Laboratoire Jean Perrin, F-75005 Paris, France**
- 3. Laboratory of Theoretical Physics, Ecole Normale Supérieure, CNRS, PSL Research University, Sorbonne Universités UPMC, 24 rue Lhomond, 75005 Paris, France**
- 4. Institut du Cerveau et de la Moelle épinière, 75013 Paris, France;**
- 5. UPMC Univ. Paris 06, 75005 Paris, France**
- 6. Inserm UMR 1127, 75013 Paris, France**
- 7. CNRS UMR 7225, 75013 Paris, France**
- 8. Program in Neuroscience, Department of Neurobiology, Harvard Medical School, Boston, Massachusetts, 02115, United States of America**
- 9. Department of Molecular and Cellular Biology, Harvard University, Cambridge, Massachusetts, 02138, United States of America**
- 10. Present address: Laboratory of Neural Systems, Rockefeller University, New York, New York, 10065, United States of America.**
- 11. Department of Neuroscience, Physiology & Pharmacology, University College London, London WC1E 6BT, UK.**

28

29 *** These authors contributed equally to the work.**

30 **Correspondence: georges.debregeas@upmc.fr**

31

32

33

34

35

Abstract:

Animals continuously gather sensory cues in order to move towards favourable environments. Efficient goal-directed navigation requires sensory perception and motor commands to be intertwined in a feedback loop, yet the neural substrate underlying this sensorimotor task in the vertebrate brain remains elusive. Here, we combine virtual-reality behavioural assays, volumetric calcium imaging, optogenetic stimulation, and circuit modelling to reveal the neural mechanisms through which a zebrafish performs phototaxis, *i.e.* actively orients towards a light source. Key to this process is a self-oscillating hindbrain population (HBO) that acts as a pacemaker for ocular saccades and controls the orientation of successive swim-bouts. It further integrates visual stimuli in a state-dependent manner, *i.e.* its response to visual inputs varies with the motor context, a mechanism that manifests itself in the phase-locked entrainment of the HBO by periodic stimuli. A rate model is developed that reproduces our observations and demonstrates how this sensorimotor processing eventually biases the animal trajectory towards bright regions.

63 In order to survive and thrive, motile organisms use sensory cues to navigate towards
64 environments where they are more likely to avoid predators, obtain food or find mates. Efficient
65 goal-directed locomotion requires closed-loop coordination between motor action and sensory
66 perception. Each movement induces a new sensory signal, which in turn modulates the
67 forthcoming motor output. This mechanism is at play in a number of goal-directed behaviours, in
68 organisms ranging from bacteria¹ to nematodes^{2,3} and insects^{4,5}, but also among humans⁶.
69 Numerous models have been proposed to account for this complex coordinated motion, but to date
70 no data are available to understand how these behavioural strategies might be implemented at the
71 circuit level in the vertebrate brain.

72 Here, we take advantage of the accessibility of zebrafish larvae to whole-brain imaging^{7,8,9} to
73 investigate the neural sensorimotor computation at play during phototaxis. This behaviour, which
74 drives the animal towards illuminated regions, is already present at 5 days post-fertilization and is
75 thus likely to be hard-wired in the larval brain^{10,11,12}. To obtain information regarding the direction
76 of a light source, larvae use two complementary strategies: stereo-visual comparison¹² and spatio-
77 temporal sampling¹³. The first mode relies on the difference in instantaneous perceived intensity at
78 two different angles to infer the direction of the source. In the second mode, the illumination
79 spatial gradient is extracted from two successive samplings obtained before and after a gaze-
80 reorienting movement. This latter approach requires that the visual and motor information are
81 integrated in a timely fashion.

82 We thus postulated the existence of a central neural circuit that would drive spontaneous gaze
83 shift while integrating unilateral and bilateral changes in illumination so as to bias reorienting
84 bouts towards a light source. We first established, through behavioural assays, that the gaze and
85 turning bout orientations are robustly coordinated, and that the statistics of gaze orientation are
86 biased towards illuminated regions. We then used volumetric functional imaging and optogenetic
87 activation to identify a bilaterally distributed neuronal ensemble in the rostral hindbrain that
88 appears to be a strong candidate for the control of spontaneous gaze dynamics. We further
89 investigated in detail how the self-oscillatory dynamics of this population are modulated by

90 bilateral and unilateral changes in illumination. Finally, we developed a rate model of this circuit
91 that reproduces most of our observations and provides the first comprehensive description of how
92 phototaxis can be implemented in the vertebrate brain.

94 **Visually induced modulation of gaze shift dynamics**

95
96 Larvae can redirect their gaze by triggering coherent angular excursions of both eyes—a
97 process called a saccade—or through whole-body reorientation. We examined the endogenous
98 temporal structure of both processes by monitoring tail deflections and eye orientations in the
99 absence of visual cues in larvae partially restrained in agarose. Spontaneous ocular saccades in
100 zebrafish larvae are highly stereotyped (Fig. 1a-d, Supplementary Figure 1), with a quasi-periodic
101 alternation between leftward and rightward gaze periods. This property is reflected by the quasi-
102 bimodal distribution of gaze orientations and a distribution of delays between successive
103 reorientations peaked at ~ 12 s (12.2 ± 3.5 s mean \pm std, $N = 29$). The orientations of the gaze and
104 the turning bouts were found to be strongly correlated (Fig. 1e-i, Supplementary Figure 1, Movie
105 1). We observed that over 85 % of the tail-beats that could be unequivocally classified as an
106 attempted turning bout were oriented in the direction of the gaze. Moreover, a large fraction
107 (60.2 %) of these bouts occurred within the first second following the onset of an ipsiversive
108 saccade. This coordination mechanism was true for both large-amplitude reorienting saccades that
109 drove the right-left alternation of gaze direction, and for low-amplitude secondary saccades that
110 maintained the gaze to the right or to the left by compensating for slow ocular drift (Extended
111 Data Fig 1d-g).

112 These observations suggest that a unique command circuit may drive ocular saccades and set
113 the direction of successive tail-beats, such that the gaze sequence may be viewed as a proxy for
114 fish reorienting dynamics. We thus posited that phototaxis should manifest as a bias in the animal
115 gaze-angle distribution towards illuminated regions. We tested this hypothesis by replicating, in
116 agarose-restrained animals, two visual stimulation protocols known to evoke phototaxis in freely

117 swimming larvae while monitoring gaze dynamics^{12,13}. Visual stimulation was obtained by
118 projecting two LEDs onto a screen below the animal, each delivering uniform illumination to one
119 eye's field of view (see Supplementary Methods).

120 We first submitted the larva to a 3 min period of whole-field (bilateral) illumination followed
121 by a step decrement of the intensity to one eye, while illumination to the other eye was held
122 constant (Fig. 1j, Supplementary Figure 2). The unilateral illumination period was maintained for
123 30 s, and the sequence was then repeated. In 67 % of the fish (18 of 27), we observed that the gaze
124 orientation was significantly biased towards the more illuminated side during unilateral
125 illumination periods (Fig. 1k). This process was reflected in the trial-averaged post-extinction gaze
126 sequence, which exhibited a transient drift toward the illuminated region (Supplementary Figure
127 2f). This bias was associated with a $27\pm 3.4\%$ (mean \pm std) increase in fixation time towards the
128 illuminated area. In total, a significant phototactic behaviour was observed in 77 % of the fish, yet
129 10 % displayed negative phototaxis, in accord with experiments performed in freely swimming
130 configurations¹². We confirmed that, owing to gaze–tail coordination, this light-induced gaze bias
131 resulted in a turning bias of the animal toward the light by performing similar experiments while
132 simultaneously monitoring both the eyes and tail movements (Extended Data 2k-m).

133 In a second approach, we developed a virtual-reality phototaxis assay in which the animal had
134 access to spatial cues through spatio-temporal probing only. Both eyes were exposed to the same
135 whole-field illumination at an intensity that was locked in real-time to the gaze orientation (Fig. 1l,
136 Supplementary Figure 2i-j). The illumination was thus at its maximum when the gaze was oriented
137 to one side, and at its minimum for the other side. A significant light-induced bias of the gaze
138 orientation was observed in 85 % of the fish ($p<0.05$, N=11 of 13). All responsive larvae showed
139 an increased fixation time towards the brighter direction, consistent with a positive phototactic
140 behaviour (Fig 1m).

141 In both assays, the imposed spatial light gradient did not trigger a systematic and immediate
142 gaze shift. Instead, it induced a statistical bias of the spontaneous saccadic dynamics whose net
143 result was to increase the relative duration of gaze fixations towards the brightest region.

144

145 **Functional mapping of gaze-tuned neuronal populations**

146

147 These observations suggested that the saccadic dynamics play a central role in phototaxis by
148 enabling a sequential sampling of illumination gradients through spontaneous gaze shifts, while
149 driving the reorienting dynamics via gaze–tail coordination. We thus sought to identify the
150 saccade command circuit. Ocular saccades in zebrafish have been studied mostly as a model of
151 neural integration^{14,15,16}. The accessibility of this vertebrate model to optogenetic techniques
152 allows one to examine with unmatched precision how a transient neural command that rapidly
153 brings the eyes into a desired position can be transformed into a sustained signal to maintain a
154 fixed eye position¹⁷. However, in contrast with mammals¹⁸, the upstream command circuit that
155 drives the rhythmic alternation between leftward and rightward saccades in zebrafish remains
156 elusive¹⁹.

157 Our approach to identify the saccade command neuronal population consisted of recording
158 large fractions of the brain using light-sheet functional imaging in animals expressing calcium
159 reporter in nearly every neuron (*Tg(elavl3:GCaMP6f)*) while monitoring eye dynamics (Fig. 2a,
160 Supplementary Movie 2). We restricted our analysis to the hindbrain and the caudal midbrain,
161 where saccade-induced distortions of the brain tissues remained small enough to enable consistent
162 signal extraction. We implemented a multilinear regression approach to classify individual voxels
163 based on their tuning with respect to the angular position and velocity signals of the eyes²⁰
164 (Supplementary Methods). We then applied a non-rigid registration method to align these
165 functional maps onto a single reference brain obtained by averaging four different samples imaged
166 using the one-photon light-sheet microscope at high spatial resolution²¹. A zebrafish brain atlas²²
167 was finally used to anatomically localize the various neuronal clusters that displayed robust tuning
168 with the gaze position and velocity (Fig. 2b-c, Supplementary Movie 3).

169 The most prominent velocity-tuned neuronal assemblies were located in two bilaterally
170 symmetric clusters in rhombomeres 4-6 (rh 4-6, Fig. 2d-f, region 1). These populations correspond

171 to the previously identified saccade generator burst neurons²³ (SGBN). Each lateral cluster triggers
172 ipsiversive saccades through direct activation of two oculomotor nuclei (abducens and oculomotor
173 nucleus III). Position-tuned neurons were found in the caudal hindbrain in a region consistent with
174 the previously described velocity-position neural integrator²⁰ (VPNI, Fig. 2d-f, region 2). These
175 analysis allowed us to further discover the existence of position-tuned clusters in the rostral
176 hindbrain (rh 2-3) in the form of four stripes bilaterally distributed on each side of the midline
177 (Fig. 2d-f, region 3)²⁴. These clusters systematically displayed increased and prolonged activity
178 after every ipsiversive saccade, whether reorienting or secondary (Supplementary Figure 6). We
179 also found two symmetric clusters, lying at the rostral border of the hindbrain (rh 1) ventral to the
180 cerebellum, that were strongly correlated with contraversive gaze orientation (Fig. 2d-f, region 4).

181 182 **Identifying a putative Saccade Command Circuit**

183
184 The morphology and anatomical location of this newly identified gaze-tuned ensemble in the
185 rostral hindbrain (the four stripes located in rh2-3) appeared very similar to the self-oscillating
186 circuit identified by Ahrens *et al.* in eyes-fixed experiments based on activity correlation analysis²⁵
187 (the so-called *hindbrain oscillator*, or HBO). Consistent with these findings, we observed that this
188 particular neuronal population displayed sustained anti-phasic dynamics, with each side activated
189 in alternation, in recordings where the saccades were abolished through eye fixation in agar (Fig.
190 3a-g). To properly delineate the neuronal population engaged in these self-generated oscillations,
191 which we refer to as the HBO, we first approximated the oscillatory signal using a small subset of
192 neurons and then computed the tuning of each voxel to this reference trace (Supplementary
193 Methods, Supplementary Figure 3). This functional criterion yields a neuronal map that essentially
194 encompasses the gaze-tuned circuit in rh-1-3 as formerly identified through regression with the
195 gaze signal (Fig. 3a-b and Extended Data Fig 3c). In more caudal regions of the hindbrain (SGBN
196 and VPNI areas, rh4-7), a small number of neurons also participated in these self-oscillatory
197 dynamics. We analysed the temporal structure of the HBO's endogenous oscillations in eye-fixed

198 conditions by running the Hilbert transform on the differential signal (left minus right circuit
199 activity, Fig. 3e-g). We found the period distribution to be peaked at ~ 20 s (19.9 ± 4.8 s mean \pm std,
200 N=8 fish), *i.e.* close to the spontaneous saccadic period.

201 The quasi-periodic nature of the saccadic dynamics suggests the existence of a circuit, akin to a
202 central pattern generator, capable of maintaining oscillations with a period on the order of 20 s in
203 the absence of rhythmic sensory or proprioceptive inputs. The HBO constitutes the best candidate
204 for this saccade command circuit. This putative role was found to be consistent with optogenetic
205 assays using larvae expressing ChR2 pan-neurally (Fig. 3h-l, Supplementary Figure 4). We
206 delivered series of 2.75 s-long light pulses over $47 \times 57 \mu\text{m}^2$ brain areas, alternately on either side
207 of the midline with a 18 s period (one pulse every 9 s), while monitoring saccades (Fig. 3j). Each
208 pair of bilaterally symmetric regions was tested 5 times before the targeted regions were relocated
209 to eventually probe a large fraction of the hindbrain encompassing both the HBO and the SGBN.
210 As previously reported²³, activation of the SGBN (rh 4-6) consistently entrained the saccadic
211 dynamics (8 fish of 19, see Supplementary Methods for details on the quantification of the
212 response). For these responsive fish, activation of the hindbrain in the rh 2-3 region evoked
213 ipsiversive saccades with comparable efficiency (Fig. 3i). These responses could not result from
214 direct activation of the oculo-motor nuclei, which lie immediately rostral to rh 1 but drive
215 contraversive saccades. In contrast, optogenetic activation of the two most rostral regions of the
216 oscillator, located in rh1, failed to evoke conjugated saccades, which might indicate that these two
217 assemblies lie downstream of the HBO's gaze-driving neurons. Finally, a small area in the caudal
218 midbrain was found to trigger ipsiversive saccades in two larvae.

219 Careful examination of the functional imaging data in eyes-free preparations offers hints
220 regarding a putative connectivity map between the HBO and the SGBN. We identified two small
221 clusters in rh 7 systematically activated 2-3 s prior to the saccade onset (Supplementary Figure 6a-
222 c), which are thus analogous to the so-called long-lead burst neurons in the mammalian saccadic
223 circuit²⁶. Such a functional trait can be understood within the assumption that they receive
224 inhibitory inputs from the contralateral HBO circuit, whose spike-rate consistently decays before

225 the saccade onset. In contrast, the ipsilateral HBO circuit remained silent until the saccade onset,
226 which precludes the possibility that it drives, *via* excitatory inputs, these long-lead burst neurons.
227 Our observations further indicate that the HBO may receive ascending ipsilateral signals from
228 saccadic pre-motor centres (efference copy). When two successive saccades occurred in the same
229 direction, the second one was systematically followed by a rebound of the HBO active module
230 (Supplementary Figure 6d-e). This process cannot result from the reciprocal inhibitory coupling
231 with the contralateral HBO module²⁵, as the latter remains silent during such phases. Although
232 more work will be needed to definitely establish that the HBO drives spontaneous saccades, these
233 various observations suggest a neural architecture of the saccadic command circuit as sketched in
234 Supplementary Figure 6f.

235 236 **The Hindbrain Oscillator responds to visual stimuli**

237
238 Dunn *et al.* recently reported that the HBO left and right activity biased the orientation of
239 fictive turning bouts to the right and the left, respectively²⁷. This finding is in line with our
240 hypothesis that a unique command circuit controls both turning bout orientation and spontaneous
241 ocular saccades. The resulting gaze–tail coordination process, analogous to the well-documented
242 head-eye coordination in vertebrates^{28,29}, explains why the orientation of successive turning bouts
243 exhibits a ~10 s autocorrelation decay in freely-swimming larvae¹³, as this value corresponds to
244 the typical period between successive reorienting saccades.

245 To evaluate the HBO's putative role in driving the phototactic behaviour, we sought to
246 investigate whether its endogenous dynamics could be visually biased. We thus successively
247 probed its response to asymmetric (unilateral illumination of one eye) and symmetric (similar
248 illumination on both eyes) visual stimuli (Fig. 4). In order to prevent visual perturbations by the
249 light-sheet, these experiments were carried out using two-photon excitation, *i.e.* with an infrared
250 source that is invisible to the fish³⁰. In a first series of experiments, we alternately illuminated each
251 eye for 15 s while performing brain-wide functional imaging. The associated response maps

252 indicated that the most prominent visually sensitive clusters in the hindbrain corresponded to the
253 HBO (Fig. 4b-f and Supplementary Figure 3b). The right HBO, whose activity is associated with a
254 rightward reorienting bias, was activated when the right eye was stimulated, and vice-versa. These
255 unilateral visual responses are consistent with a stereo-visual positive phototaxis mechanism. In 1
256 of 11 fish, however, we found a reverse response, *i.e.* the visual stimulation elicited activity in the
257 contralateral HBO. This observation parallels, and may explain, the 10 % of fish found to display
258 negative phototaxis in the behavioural assays.

259 Phototaxis has been shown to implicate OFF retinal ganglion cells, *i.e.* neurons activated upon
260 light decrement¹². We thus asked whether the visually evoked transient of the left or right HBO
261 was driven by the stimulus onset (light-on) on the ipsilateral eye, the stimulus offset (light-off) on
262 the contralateral eye, or both. To answer this question, we monitored the HBO dynamics while
263 exposing one eye to alternating on-off illumination, the other being maintained at constant
264 illumination. We found that light-on and light-off stimuli induced a sharp increase in activity in
265 the ipsilateral and contralateral subpopulations, respectively. This indicates that the ON and OFF
266 pathways both contribute to driving the HBO (Supplementary Figure 7, N=8 fish).

267 In a second experiment, we investigated the HBO response to bilateral illumination by
268 delivering a series of 100 ms-long flashes simultaneously to both eyes with a 10 s inter-flash
269 period (Fig. 4g-h). Both left and right HBO displayed a significant response as evidenced by the
270 trial-averaged peri-stimulus signal (Fig. 4i, n=1311 flashes, N=12 fish, Supplementary Figure 7d-
271 e), but the across-trials dispersion appeared surprisingly large (coefficient of variation 170 %). The
272 visual responses of the left and right HBO were strongly anti-correlated ($r=-0.5$) such that a given
273 flash seemed to stochastically evoke a response in either one of them (Fig. 4j). To evaluate
274 whether this apparent stochasticity may reflect a state-dependent sensitivity of the HBO, we
275 examined how the stimulus-induced transient in its activity depended on the particular phase of the
276 oscillation at which it was delivered. We used the Hilbert transform to extract the phase $\varphi(t)$ of
277 the HBO oscillation. We then computed the derivative of the left and right HBO signals at all
278 times corresponding to a given phase, separating those at which a stimulus had been delivered

279 from the times when the oscillation was running free. We then subtracted the means of both
280 groups in order to extract the sole contribution of the stimulus to the HBO transient dynamics.
281 This analysis yielded a phase-dependent response curve for each left and right HBO (Fig. 4k). It
282 revealed that each subpopulation is responsive to the visual stimulus within a particular phase
283 range and is essentially unresponsive for the rest of the cycle. More specifically, each flash
284 selectively reinforces the cluster that is already active or about to become active after a period of
285 rest. The transition between left–right HBO activity being associated with gaze shift events, such a
286 phase-dependent response curve can be interpreted as a motor-related gating mechanism. In this
287 view, each subpopulation selectively integrates light increments generated by ipsiversive saccades
288 as expected during spatio-temporal sampling.

289

290 **HBO entrainment by periodic uniform visual stimuli**

291

292 In biological and physical oscillators, phase-dependent responses can be revealed through
293 phase-locking and frequency entrainment by periodic forcing^{31,32,33}. Consistently, we observed that
294 the HBO oscillation exhibited a mean period of 20 s in the symmetric stimulation experiments, *i.e.*
295 precisely twice the stimulation period $T_{stim}=10$ s (Fig. 4l, $T_{osc}= 20.5 \pm 1.4$ s, $N=12$ fish).
296 Furthermore, the phase-offset between the HBO and the stimulus signal, defined as $\delta\varphi(t) =$
297 $\varphi(t) - \pi * t/T_{stim}$, displayed a marked bimodality, with two peaks located at 0 and π (Fig. 4m,
298 Rayleigh test, $p<0.01$, Supplementary Figure 8a). This indicates that visual stimuli induce a phase-
299 shift in the HBO oscillations such that the flashes tend to coincide with successive right-to-left and
300 left-to-right transitions (Fig. 4m-inset).

301 We suspected that this period-doubling mechanism ensued from the particular choice of the
302 stimulation period, which is close to half the HBO endogenous period T_{endo} . We sought to explore
303 how this synchronization process varied with the stimulation T_{stim} . To guarantee that the mean
304 illumination was independent of the stimulation period, we exposed the fish to a series of
305 alternating ON-OFF illuminations at 6 frequencies (20 periods each, $10 \text{ s} < T_{stim} < 60 \text{ s}$) separated

306 by 100 s-long periods of constant illumination (Fig. 5a). For each sequence, we extracted the mean
307 oscillation period T_{osc} and the phase-offset distribution (Fig. 5b-c). In all tested visually
308 responsive fish (N=5 of 7), this analysis revealed the existence of an entrainment plateau at
309 intermediate stimulation periods ($20\text{ s} < T_{stim} < 40\text{ s}$) for which the HBO frequency was controlled
310 by the stimulation period ($T_{osc}/T_{stim} \cong 1$) and the phase offset distribution was strongly non-uniform
311 (Fig. 5d-f, Rayleigh test, $p < 0.01$). At higher and lower frequencies, the entrainment ratio T_{osc}/T_{stim}
312 was close to 2 and 0.5, respectively. The same experiments were replicated for asymmetric stimuli
313 and yielded qualitatively similar results, albeit with a more pronounced phase-locking and a more
314 extended entrainment plateau (Fig. 5g-i, N=11, Supplementary Figure 8).

315

316 **A stochastic neural model of phototaxis**

317

318 A rate model approach³⁴ was used to model the oscillatory dynamics of the HBO and its
319 visually evoked responses based on the connectivity architecture suggested by our experimental
320 observations (Fig. 6a). We described the HBO as a half-centred oscillator consisting of two
321 symmetric modules with recurrent excitation, reciprocal inhibition, and adaptation currents (see
322 Supplementary Methods). Such a simple model, derived from a spiking, conductance-based
323 model, has been proposed for cortical circuits to account for the phenomenology of perceptual bi-
324 stability^{35,36}. This description is consistent with the neurotransmitter identity of the different
325 clusters that participate in the self-oscillatory dynamics.²⁵ The medial clusters of the HBO were
326 identified as glutamatergic and the lateral clusters as primarily GABAergic, reflecting the
327 hindbrain columnar organization of the neurotransmitter classes.³⁷

328 The model parameters were adjusted in order to best reproduce the self-sustained quasi-
329 periodic oscillations observed in the absence of visual input (Fig. 6c, Supplementary Figure 9).
330 Visual inputs were assumed to be relayed to the HBO in the simplest way consistent with the
331 proposed connectivity (Fig. 6b). A step increase in the illumination of the right eye was associated
332 with a burst of current in the right circuit, followed by a plateau, whereas a step decrease in the

333 illumination induced a transient current in the left circuit to account for the OFF pathway
334 contribution. We then numerically implemented the stimulation protocols used in the functional
335 imaging experiments. The left and right circuit responded to ipsilateral asymmetric visual stimuli
336 (Supplementary Figure 10). We further obtained a phase-dependent intensity response curve to
337 symmetric flashes in qualitative agreement with its experimental counterpart (Fig. 6d-e and Fig.
338 4k). The model allowed us to reinterpret the latter result in terms of a phase-response curve (PRC).
339 Within this scheme, the effect of a stimulus is to evoke a phase offset, *i.e.* a transient slowing
340 down or speeding up of the oscillatory dynamics. For each phase, we thus computed the visually
341 induced phase delay $\Delta\varphi$ by comparing the phase evolution after stimulation and in the free-
342 running (without stimulation) regime (Fig. 6f). The resulting π -periodic PRC provides a direct
343 interpretation of the phase-locking mechanism around the phases $\pi/2$ and $3\pi/2$, where the PRC
344 displays a negative slope³². Consistently, a phase-locking mechanism was observed with an
345 entrainment plateau around the endogenous oscillation frequency (Fig. 6g). However, for this
346 process to quantitatively compare with the experimental data, the current noise had to be set at a
347 relatively low value (Supplementary Figure 10).

348 We sought to evaluate whether this minimal neural model could account for the orientational
349 phototactic behaviour under the assumption that an imbalance in the HBO left-versus-right activity
350 distribution may be viewed as a proxy for the statistical orientational bias in the animal
351 locomotion²⁷. We considered configurations in which a distant light source was oriented at an
352 angle θ_s with respect to the animal's rostro-caudal axis. The total illumination impinging on each
353 eye was taken as a slowly varying function of θ_s , reflecting the large visual field of view of the
354 zebrafish, with a maximum at $\theta_s = 80^\circ$ for the right eye (Fig. 6h, Supplementary Methods). We
355 successively considered the stereo-visual comparison and spatio-temporal sampling phototactic
356 strategies. In the first case, we examined the sole effect of a continuous unbalanced bilateral
357 illumination. For each angle θ_s , the illumination on each eye was converted into a constant input
358 current on the ipsilateral subcircuit. We then numerically computed the HBO dynamics and
359 compared the mean left-versus-right activity. We found the HBO oscillations to be statistically

360 biased towards the subnetwork ipsilateral to the light source. This was assessed by comparing both
361 the time fraction during which one circuit was more active than the other (Fig. 6h) and the mean
362 activities of the two circuits (Supplementary Figure 11). Within the assumption that such an
363 imbalance reflects a reorienting bias²⁷, this result appears consistent with a positive phototactic
364 mechanism.

365 In a second approach, we focused on the spatio-temporal sampling strategy (Fig. 6i). We
366 imposed identical illumination on both eyes at all times so as to provide no explicit spatial cue to
367 the circuit. The stimulus intensity was assumed to be a slowly decreasing function of the gaze
368 orientation relative to the light source. We posited that each left-to-right or right-to-left transition
369 of the HBO corresponded to a rightward or leftward gaze shift of amplitude 30°, respectively. This
370 $\pm 15^\circ$ gaze oscillation in turn elicited a series of abrupt changes in the perceived stimulus. This
371 procedure yielded a left-versus-right activity bias that depended on the light source azimuth
372 (Fig. 6i, Extended Fig. 11) and was again consistent with a positive phototactic behaviour.

373

374 **Discussion**

375

376 A central goal in neuroscience is to decipher the neural computation underlying the execution
377 of natural tasks. In this respect, whole-brain functional imaging constitutes a game-changing
378 technique because it allows one to systematically map entire neuronal populations that respond to
379 a given sensory stimulus^{30,7,38} or correlate with a particular motor pattern^{27,20}. Here, this strategy
380 was taken one step further: we used three distinct functional properties as joint criteria to identify a
381 sensorimotor hub likely to play a key role for phototaxis. Based on behavioural assays, we
382 reasoned that there should exist a circuit that both sets the pace of spontaneous saccades and
383 integrates visual stimuli. We thus successively delineated three neuronal populations that *(i)*
384 correlated with the gaze signal during spontaneous saccades, *(ii)* displayed self-sustained
385 oscillating activity in eye-fixed configurations, and *(iii)* responded to unilateral visual stimulation.
386 We then used a morphological registration algorithm to demonstrate the existence of a well-

387 defined intersecting neuronal ensemble in the rostral hindbrain, identified as the HBO, that
388 combines all three functionalities (Supplementary Movie 4).

389 Using a rate model, we showed that the HBO's phase-dependent visual sensitivity suffices to
390 explain the tendency of larvae to reorient towards illuminated areas using both stereo-visual
391 comparison and spatio-temporal sampling. The proposed sensorimotor processing leading to
392 phototaxis can be summarized as follows: *(i)* the HBO self-sustained oscillations drive a quasi-
393 periodic sequence of gaze shifts that allow the animal to actively explore the light angular
394 gradient; *(ii)* asymmetric visual stimuli enhance the activity of the HBO clusters ipsilateral to the
395 eye that receives the larger illumination, which in turn biases the fish reorientation towards the
396 light source; and *(iii)* a gaze shift-induced light increment reinforces the active HBO
397 subpopulation (ipsilateral to the new gaze direction), thus delaying further left–right transition.
398 Over multiple cycles, this process yields a statistical bias of the fish turning probability towards
399 the brightest region.

400 In foveate species, ocular saccades enable detailed visual exploration by sequentially bringing
401 different regions of the visual scene onto a small area of the retina (the fovea) where the resolving
402 power is maximal³⁹. The present study suggests that saccades in afoveate species such as zebrafish
403 may subserve a non-image forming visual function by allowing the animal to sequentially sample
404 the light level at two distinct angles without the need to execute a whole-body reorientation.
405 Within this scheme, the large stereotyped gaze shifts that characterize spontaneous saccades in
406 zebrafish might be understood as a way to maximize the detected contrast in the context of weak
407 illumination gradients.

408 The HBO presents striking similarities with central pattern generators (CPG). These specialized
409 networks drive cyclic motor patterns underlying rhythmic behaviours such as locomotion,
410 chewing, or breathing⁴⁰. Although they can operate in the absence of external sensory or
411 proprioceptive inputs, CPGs play an important role in regulating the circuit dynamics in order to
412 produce behaviourally relevant motor output⁴¹. Their action generally varies with the particular
413 phase within the cycle at which they occur⁴². The HBO differs from standard CPGs in the sense

414 that it drives a pseudo-periodic motor pattern— the saccadic period displays significant variations
415 from cycle to cycle—but also controls the sequence of discrete turning-bout orientations. By
416 modulating the rhythmic HBO oscillations, the visual inputs thus modulate the temporal pattern of
417 reorienting movements, effectively biasing the animal’s trajectory towards brightest areas over
418 multiple cycles. It has been recently demonstrated, in *Drosophila* larvae, that sensorimotor
419 neurons can be engaged in distinct goal-directed behaviours⁴³. It will thus be interesting to see
420 whether other sensory information—chemical cues, water flow, temperature gradients, etc. —may
421 also be relayed to the HBO, and how these multi-sensory cues are weighted in order for the larva
422 to navigate towards the most favourable environments.

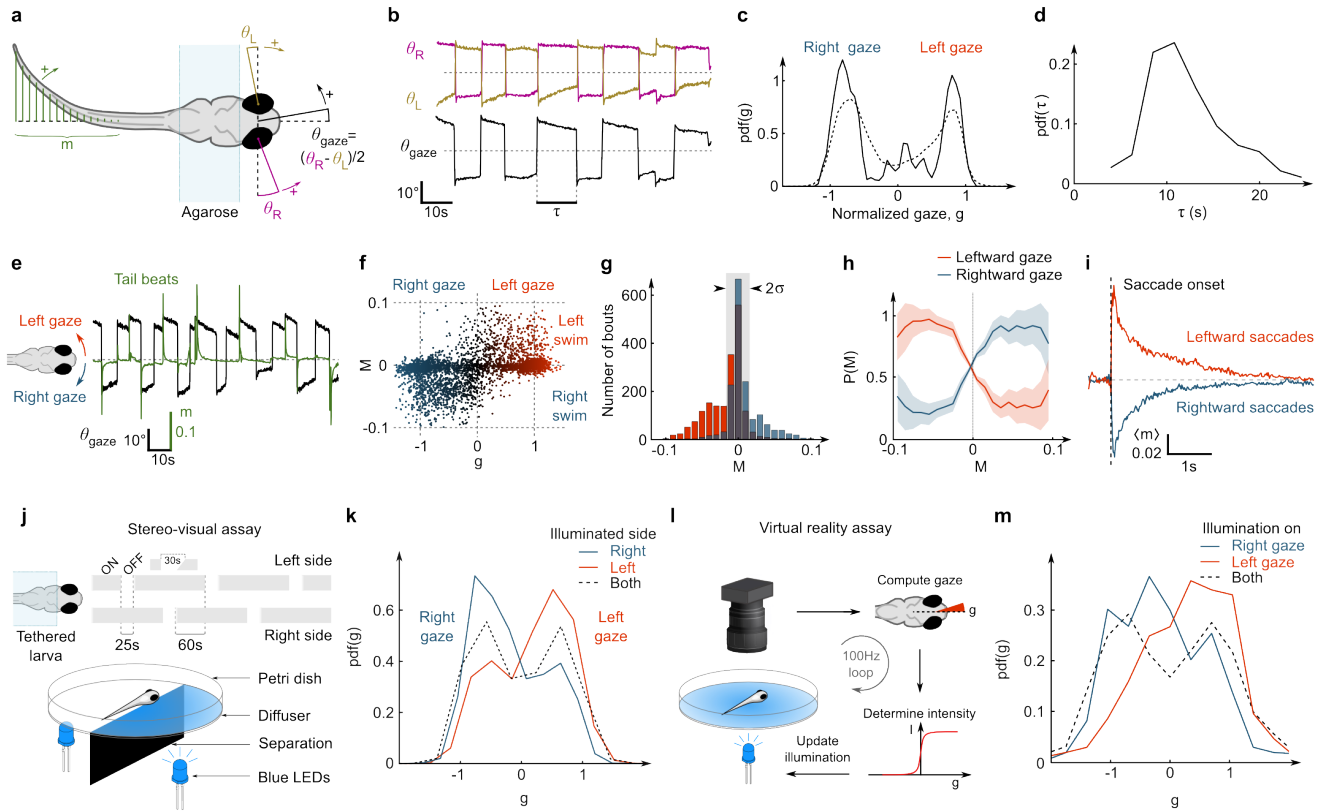
423 Beyond phototaxis, the sensorimotor processing operated by the HBO may also be examined in
424 the broader context of active sensing. In vertebrates, including mammals, sensory perception—
425 olfaction, touch, vision, etc. —generally rely on conjugated motor routines^{44,45} such as sniffing,
426 whisking, eye saccades, etc. The rhythms of these motor patterns have been shown to entrain low-
427 frequency neuronal oscillations in primary sensory cortices, which in turn modulate their
428 sensitivity according to specific motor phases⁴⁶. This sensorimotor coordination plays a key role in
429 sensory processing. Given the generic nature of this neural mechanism, it will be exciting to
430 further investigate whether the HBO oscillation may similarly drive, through afferent projections,
431 rhythmic changes in sensitivity in sensory centres such that the olfactory bulb or the optic tectum.

432

433

434
435

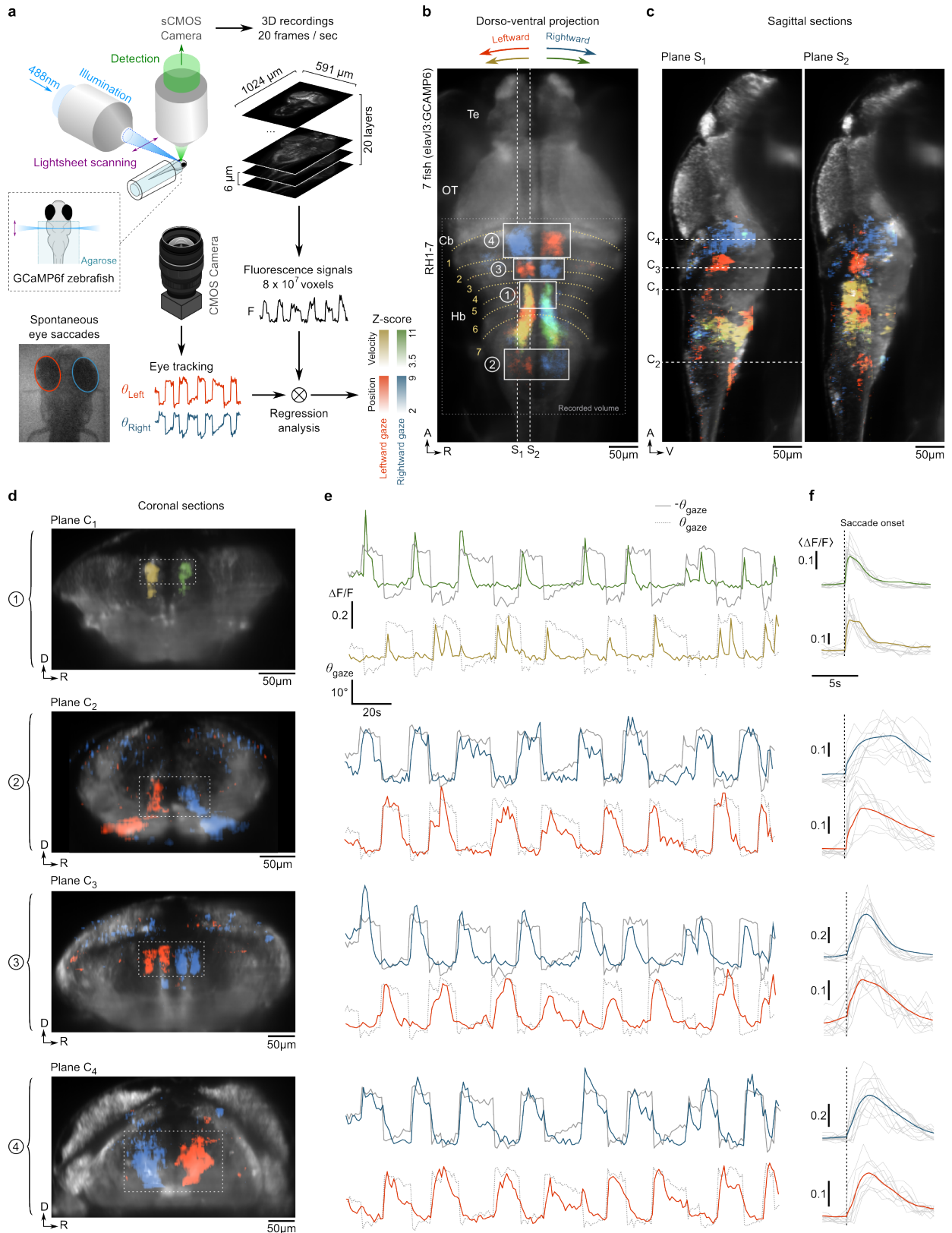
Figure 1 | Behavioural assays of ocular-saccade–turning-bout coordination and light-induced gaze bias.



436
437

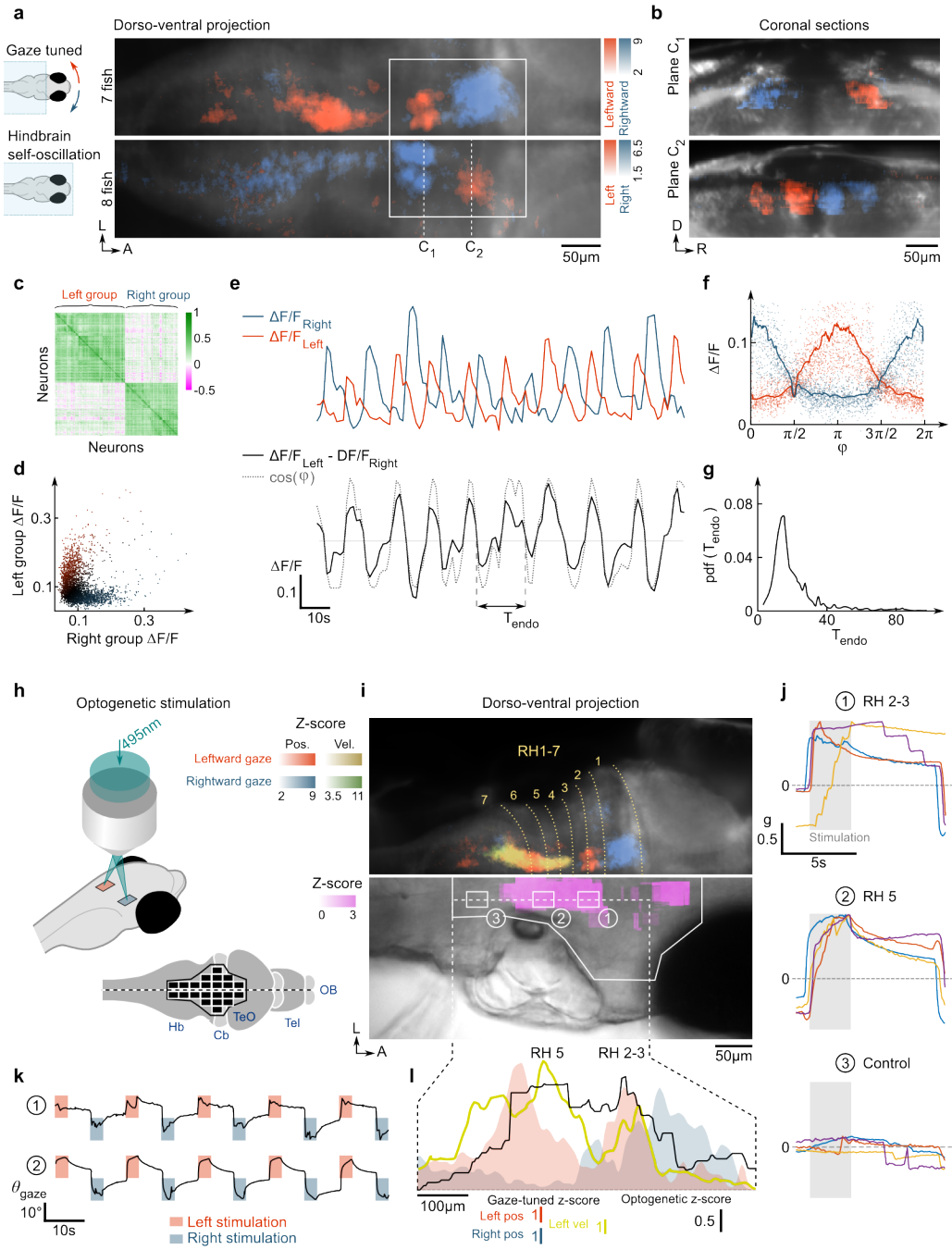
438 **Figure 1 | Behavioural assays of ocular-saccade–turning-bout coordination and light-induced**
439 **gaze bias.** **a**, Definition of the eye and tail kinematic parameters. The larva’s tail and eyes are free.
440 The gaze angle, θ_{gaze} , is defined as the mean orientation of both eyes. The parameter m characterizes
441 the instantaneous tail deflection (Supplementary Methods). **b-d**, Gaze dynamics. **b**, Example time-
442 traces of the eye and gaze angles. **c**, Probability distribution function (PDF) of the gaze angle,
443 normalized by its characteristic range (see Supplementary Methods), for one fish (solid line) and for
444 $N=29$ fish (dashed line). **d**, PDF of the delay τ between successive reorienting saccades for one fish. **e-**
445 **i**, Ocular-saccade–tail-beat coordination. **e**, Gaze angle and tail deflection signals. **f**, Individual tail-
446 beats turning score M , defined as the integral of $m(t)$ over the swim-bout (Supplementary Methods),
447 versus the normalized gaze angle g (3681 tail-beats, $N=11$ fish). **g**, Histograms of M for leftward (red)
448 and rightward (blue) gaze orientation. The central part of the distribution (standard deviation σ) is used
449 to assess the significance of the tail-bout orientational bias. **h**, Conditional probability of the gaze to be
450 orientated to the left (red) or right (blue) given the tail-beat turning score M (3681 tail-beats, $N=11$
451 fish). The shaded region corresponds to the standard error. **i**, Mean peri-saccadic tail deflection signal
452 averaged over leftward (blue) and rightward (red) saccades. **j-k**, Stereo-visual phototaxis. **j**, Scheme of
453 the experimental assay. **k**, PDF of the normalized gaze during periods of unilateral stimulation for
454 animals displaying positive phototaxis ($N=18$ fish). Red and blue curves correspond to illumination on
455 the left and right eye, respectively. Dashed curve indicates bilaterally symmetric illumination. **l-m**,
456 Spatio-temporal gaze phototaxis. **l**, Scheme of the virtual-reality assay. The fish is submitted to a
457 uniform illumination whose intensity is driven in real-time by the animal’s gaze angle. **m**, PDF of the
458 normalized gaze angle for virtual leftward (red) and rightward (blue) illumination ($N=13$ fish). The
459 dashed curve corresponds to the neutral runs (constant illumination).

Figure 2 | Regression-based identification of gaze-tuned neuronal populations.



462 **Figure 2 | Regression-based identification of gaze-tuned neuronal populations.** **a,**
463 Schematic of the experimental setup and regression analysis. Volumetric recordings on GCaMP6f-
464 expressing larvae were performed using one-photon light-sheet imaging (20 slices per stack, 1
465 stack per s) while monitoring saccadic dynamics. Voxel-by-voxel regression with the eye
466 orientation signals were used to produce position-tuned and velocity-tuned 3D maps. Notice that
467 the two maps overlap in a small subset of voxels (the two 3D maps are displayed separately in
468 Supplementary Movie 3). **b-c,** Dorso-ventral projection view and sagittal sections along two
469 planes of the 3D functional map (mean over 7 fish) showing neuronal populations whose activity
470 is tuned to the gaze orientation (blue and red) and to the gaze angular velocity (green and yellow).
471 The voxel colour encodes the Z-score values obtained through multi-linear regression
472 (Supplementary Methods). Te: telencephalon, OT: optic tectum, Cb: cerebellum, Hb : hindbrain,
473 RH: rhombomere. The grey dotted rectangle indicates the effective recorded volume. **d,** Coronal
474 sections along the dotted lines shown in (c) for one sample of the four regions delineated in (b).
475 Region 1 encompasses the saccade generator burst neurons (SGBN); region 2 is the velocity-
476 position neural integrator (VPNI); region 3 and 4 constitute the newly identified gaze-tuned rostral
477 hindbrain population. It consists of 4 bilaterally symmetric clusters tuned to the ipsiversive gaze
478 orientation (region 3) and 2 more rostral clusters tuned to the contraversive gaze angle (region4).
479 **e,** Example $\Delta F/F$ time-traces for these 4 regions. The red and yellow (respectively blue and
480 green) traces correspond to the sub-populations tuned to leftward (respectively rightward) gaze
481 orientation. The grey lines are the gaze angle traces ($-\theta_{gaze}$: solid line, θ_{gaze} : dashed line). **f,**
482 Corresponding mean peri-saccade $\Delta F/F$ signals, computed over the leftward (red) and rightward
483 (blue) saccades. Grey lines are peri-saccadic signals for individual saccades.

Figure 3 | Self-oscillatory dynamics and optogenetically evoked saccades.

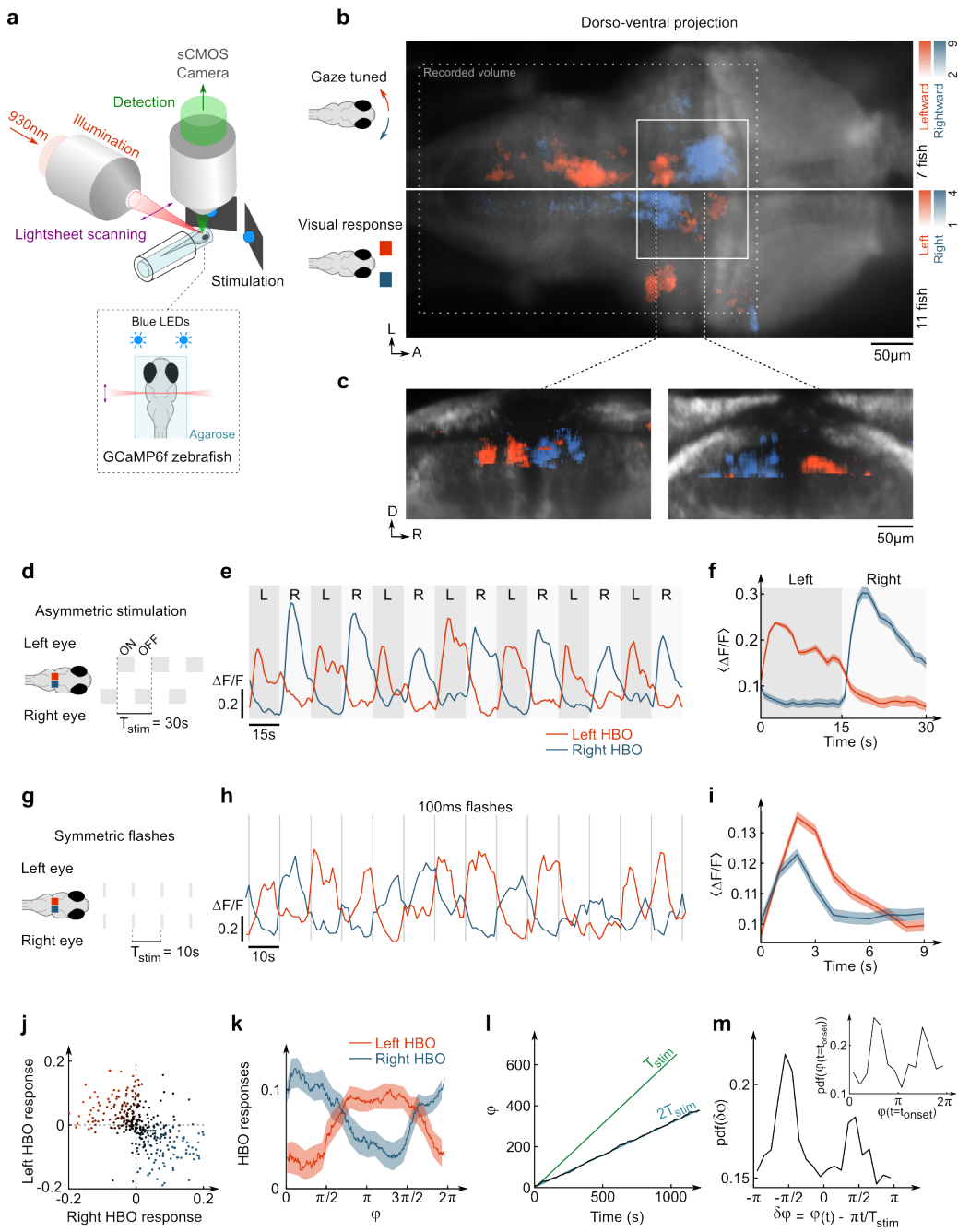


487 **Figure 3 | Self-oscillatory dynamics and optogenetically evoked saccades.** **a**, Dorso-ventral
488 projection of the gaze-tuned (top-half, N=7 fish) and self-oscillatory hindbrain population
489 (bottom-half, N=8 eye-fixed fish). In the latter, the colour encodes tuning to the left (red) and right
490 (blue) pre-selected neuronal clusters, revealing strong antiphasic activity (see Supplementary
491 Methods). The two functional maps were registered on the same reference brain to enable side-by-
492 side comparison. The rectangle indicates the region of the rostral hindbrain gaze-tuned population.
493 **b**, Coronal sections of the self-oscillatory population along the dotted lines in the projected view.
494 **c**, Pearson correlation matrix of the neurons engaged in the self-oscillatory dynamics (616
495 neurons). The matrix was reordered to reveal two highly correlated (and reciprocally anti-
496 correlated) clusters. **d**, Activity of the left versus right populations ($r=-0.43$). **e**, Example $\Delta F/F$
497 traces of the left and right groups (top), and of the differential signal (bottom). The grey dotted
498 line shows $\cos(\varphi(t))$, where $\varphi(t)$ is the oscillatory phase extracted using Hilbert's transform. **f**,
499 $\Delta F/F$ of the right (blue) and left (red) circuits as a function of the oscillatory phase. The blue and
500 red lines correspond to the mean values. **g**, PDF of the instantaneous oscillation period. **h-k**,
501 Optogenetic activation of ocular saccades. **h**, Schematic of the optogenetic stimulation protocol. **i**,
502 Top: projective view of the previously mapped gaze-tuned regions. Bottom: Z-score map of
503 saccadic entrainment averaged over 8 fish (see Supplementary Methods). **j**, Mean peri-stimulation
504 normalized gaze signal for 3 regions: the rostral HBO (rh 2-3), the SGBN (rh 5), a control region
505 (rh 7). The responses of 4 different fish are shown, and the associated targeted areas are indicated
506 in (i). The 2.75 s-long stimulation periods are indicated by the grey area. **k**, Example gaze signals
507 upon periodic left or right optogenetic stimulation for 2 region pairs in rh 2-3 and rh 5. **l**, Profile
508 plot of the mean optogenetic Z-score along the rostro-caudal axis (black), overlaid on the
509 ipsiversive (red) and contraversive (blue) gaze-tuned Z-score. Yellow curve indicates the
510 ipsiversive velocity-tuned Z-score. Ipsiversive saccades are evoked with comparable efficiency by
511 targeting the SGBN (rh 5) or the rostral HBO (rh 2-3).

512

513

514

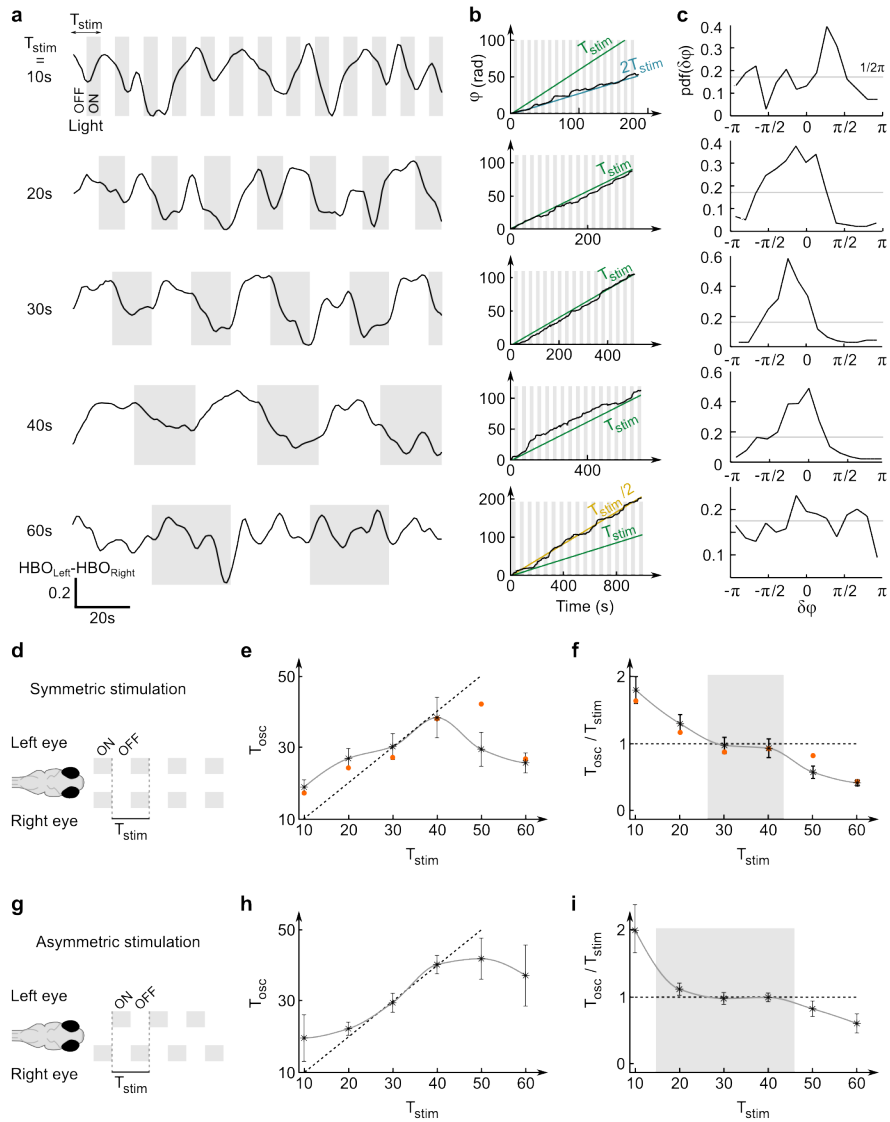
Figure 4 | Response of the HBO to asymmetric and symmetric visual stimuli.

518 **Figure 4 | Response of the HBO to asymmetric and symmetric visual stimuli.** **a**, Schematic
519 of the two-photon light-sheet imaging setup with stereo-visual stimulation. **b**, Comparison of the
520 gaze-tuned and visual response projection maps. Top: the red and blue colours encode leftward
521 and rightward gaze-tuning Z-score, respectively (N=7 fish). Bottom: the red and blue colours
522 encode the visual response Z-score (see Supplementary Methods) to unilateral stimulation on the
523 left and right eye, respectively (N=11 fish). The HBO circuit (white rectangle) is engaged in both
524 sensory and motor processing. **c**, Coronal sections of the visual response map along the two dotted
525 lines shown in (a). In (b) the dotted rectangle delineates the recorded volume. **d**, Alternated
526 unilateral visual stimulation. **e**, Example traces of left and right HBO. **f**, Trial-averaged response
527 of the HBO over 20 stimulation periods. Shaded regions correspond to left (dark grey) and right
528 (pale grey) illumination. **g**, Bilaterally symmetric 100 ms-long flashes. **h**, Example traces of the
529 right and left HBO. The grey lines indicate the flashes. **i**, Trial-averaged flash-induced responses
530 of each subpopulation (100 flashes). **j**, Left versus right HBO responses (1311 flashes, N=12 fish,
531 $r=-0.5$). **k**, Phase-dependent response of each subpopulation to symmetric flashes. **l**, Time-
532 evolution of the HBO oscillatory phase $\varphi(t)$. The slope of the green line corresponds to the
533 stimulation frequency (period $T_{stim}=10$ s). The HBO is entrained at half the frequency of the
534 stimulation (period $2T_{stim}$). **m**, PDF of the HBO stimulation phase-offset $\delta\varphi$. The inset shows the
535 PDF of the HBO phase at times where the flashes were delivered. Notice that in panels f, i and k,
536 the error bars indicate the standard error.

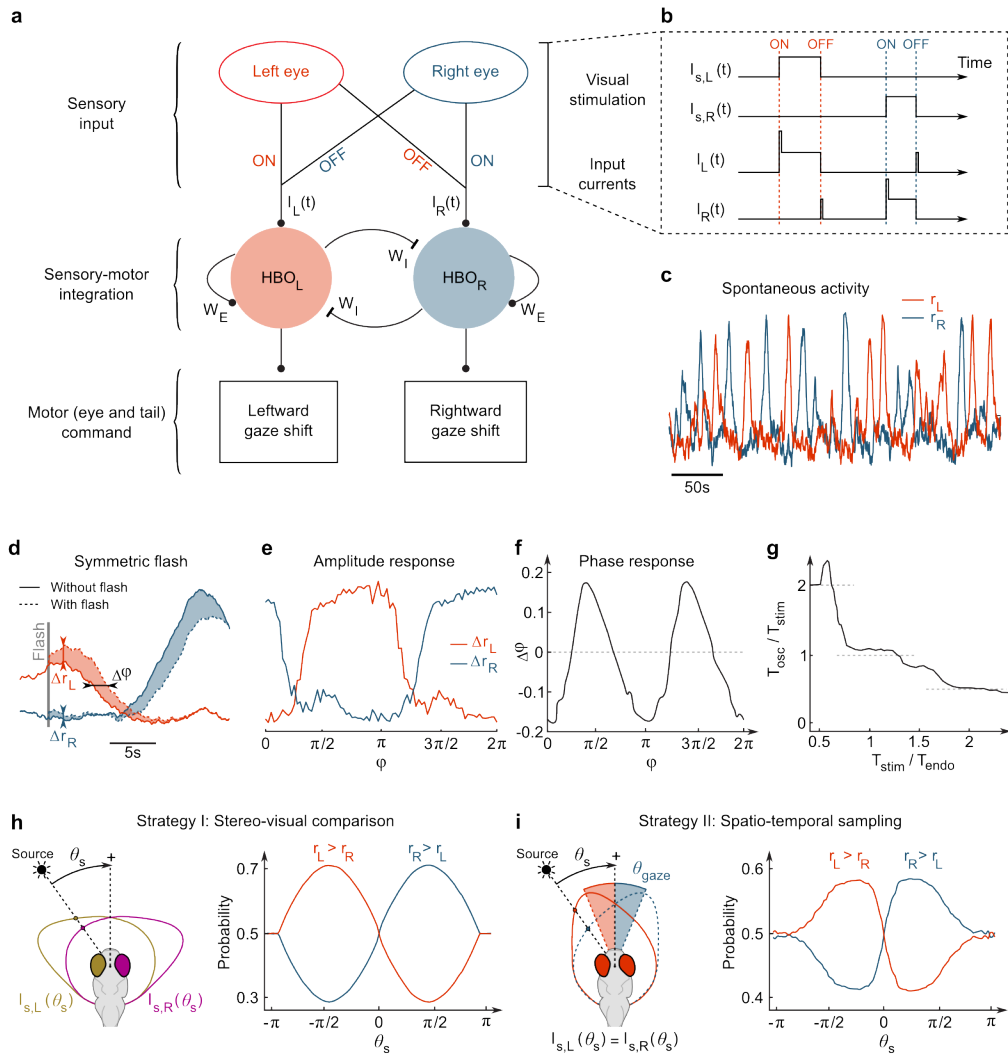
537

538

stimuli.



542 **Figure 5 | Phase-locking and frequency entrainment of the HBO by periodic visual**
543 **stimuli. a**, Example HBO signals during symmetric visual stimulus presentation consisting of
544 alternating light-ON and light-OFF periods of similar duration. Difference of the left and right
545 HBO signals for 5 stimulation frequencies. Light-ON periods are indicated by the shaded areas. **b**,
546 Time-evolution of the HBO phase signal demonstrating frequency entrainment by periodic visual
547 stimuli. The green line indicates the phase evolution of the stimulation. The HBO is entrained at
548 half the frequency for $T_{stim}=10s$, and twice the frequency for $T_{stim}=60s$. **c**, The HBO stimulation
549 phase-offset displays a non-uniform distribution, revealing phase-locking (Rayleigh test, $p<0.01$).
550 **d-f**, Frequency entrainment by symmetric stimulation. **d**, Symmetric stimulation schematic. **e**,
551 HBO oscillatory period T_{osc} as a function of the stimulation period T_{stim} ($N=5$ fish, red points show
552 the data presented in a-c). The dotted line shows the $T_{osc}=T_{stim}$ entrainment curve. **f**, Entrainment
553 ratio T_{osc}/T_{stim} as a function of T_{stim} ($N=5$ fish). **g-i**, Frequency entrainment by asymmetric
554 stimulation ($N=11$ fish). The shaded areas in (f) and (i) are guides to the eye showing the
555 approximate domain of one-to-one frequency entrainment in each configuration. In panels e-f and
556 h-i, the error bars represent the standard error.

Figure 6 | A rate model of the HBO's visually entrained dynamics leading to phototaxis.

559 **Figure 6 | A rate model of visually entrained HBO dynamics leading to phototaxis. a-b,**
560 Schematic of HBO network connectivity. Visual stimuli are relayed to the HBO via the ON and
561 OFF pathways, as detailed in (b). The HBO activity controls gaze shifts via ocular saccades and
562 turning bouts. Self-oscillatory dynamics result from the recurrent excitation (W_E), reciprocal
563 inhibition (W_I), and adaptation currents (see Supplementary Methods). c, Example traces of the
564 endogenous antiphase oscillations of the left and right HBO in the absence of varying visual
565 stimulation (arbitrary units). d, Response of the HBO to a symmetric flash. The shaded areas
566 display the difference in activity induced by the flash, from which we extract an amplitude
567 response for each circuit and a flash-induced phase offset. e-f, Mean amplitude and phase response
568 to symmetric flashes as a function of the HBO phase at stimulation. g, Frequency entrainment
569 curve for symmetric periodic stimulations (light-ON–light-OFF alternation). The ratio of the
570 oscillatory over the stimulation periods (T_{osc}/T_{stim}) is plotted as a function of T_{stim} normalized by
571 the endogenous period T_{endo} . h, Numerical implementation of a stereo-visual comparison strategy
572 for phototaxis. Each eye receives a different intensity ($I_L(\theta_s)$ and $I_R(\theta_s)$) set by the light source
573 azimuth θ_s . The red and blue curves show, as a function of θ_s , the time fraction for which $r_L > r_R$
574 and $r_R > r_L$, respectively. The light source reinforces the ipsilateral circuit leading to orientational
575 positive phototaxis. i, Spatio-temporal sampling strategy. Both eyes receive a similar intensity
576 which depends on the relative orientation of the gaze θ_{gaze} and the light source azimuth θ_s . The
577 gaze orientation oscillates between two values according to $\theta_{gaze} = \text{sign}(r_L - r_R) * 15^\circ$. As in (h), the
578 left-versus-right bias of the HBO as a function of θ_s is consistent with positive phototaxis.

579
580
581
582
583
584
585
586
587
588
589
590
591
592
593
594
595
596
597
598
599
600
601
602
603
604
605
606
607
608
609
610
611
612
613
614
615
616

References :

1. Berg, H. C. and Brown, D. A. Chemotaxis in *Escherichia coli* analysed by three-dimensional tracking. *Nature*, **239**, 500–504 (1972).
2. Chalasani, S. H. et al. Dissecting a circuit for olfactory behaviour in *Caenorhabditis elegans*. *Nature*, **450**, 63–70 (2007).
3. Ward, A., Liu, J., Feng, Z. and Xu, X. Z. S. Light-sensitive neurons and channels mediate phototaxis in *C. elegans*. *Nat Neurosci*, **11**, 916–922 (2008).
4. Gomez-Marin, A., Stephens, G. J., and Louis, M., Active sampling and decision making in *Drosophila* chemotaxis. *Nat Commun*, **2**, 441 (2011).
5. Gepner, R. et al. Computations underlying *Drosophila* photo-taxis, odor-taxis, and multi-sensory integration. *Elife*, **4**, e06229 (2015).
6. Porter, J. et al. Mechanisms of scent-tracking in humans. *Nat Neuroscience*, **10**, 27–29 (2007).
7. Ahrens, M. B. et al. Brain-wide neuronal dynamics during motor adaptation in zebrafish. *Nature*, **485**, 471–477 (2012).
8. Panier, T., et al. Fast functional imaging of multiple brain regions in intact zebrafish larvae using Selective Plane Illumination Microscopy. *Front Neural Circuits*, **7**, 65 (2013).
9. Feierstein, C. E., Portugues, R. and Orger, M. B. Seeing the whole picture: A comprehensive imaging approach to functional mapping of circuits in behaving zebrafish. *Neuroscience*, **296**, 26–38, (2015).
10. Brockerhoff, S. E. et al. A behavioral screen for isolating zebrafish mutants with visual system defects. *Proc Natl Acad Sci U S A*, **92**, 10545–10549 (1995).
11. Orger, M. B., & Baier, H. Channeling of red and green cone inputs to the zebrafish optomotor response. *Visual neuroscience*, **22**, 275–281 (2005).
12. Burgess, H. A., Schoch, H. and Granato, M. Distinct retinal pathways drive spatial orientation behaviors in zebrafish navigation. *Curr Biol*, **20**, 381–386 (2010).
13. Chen, X. and Engert, F. Navigational strategies underlying phototaxis in larval zebrafish. *Front Syst Neurosci*, **8**, 39 (2014).
14. Miri, A. et al. Spatial gradients and multidimensional dynamics in a neural integrator circuit. *Nat Neurosci*, **14**, 1150–1159 (2011).
15. Daie, K., Goldman, M. S. and Aksay, E. R. F. Spatial patterns of persistent neural activity vary with the behavioral context of short-term memory. *Neuron*, **85**, 847–860 (2015).
16. Lee, M. M., Arrenberg, A. B. and Aksay, E. R. F. A structural and genotypic scaffold underlying temporal integration. *J Neuroscience*, **35**, 7903–7920 (2015).
17. Joshua, M. and Lisberger, S. G. A tale of two species: Neural integration in zebrafish and monkeys. *Neuroscience*, **296**, 80–91 (2015).
18. Sparks, D. L. The brainstem control of saccadic eye movements. *Nat Rev Neurosci*, **3**, 952–964 (2002).

- 657 19. Gonçalves, P. J., Arrenberg, A. B., Hablitzel, B., Baier, H. and Machens, C. K. Optogenetic
658 perturbations reveal the dynamics of an oculomotor integrator. *Front Neural Circuits*, **8**, 10
659 (2014).
- 660 20. Miri, A., Daie, K., Burdine, R. D., Aksay, E. and Tank, D. W. Regression-based identification
661 of behavior-encoding neurons during large-scale optical imaging of neural activity at cellular
662 resolution. *J Neurophysiol*, **105**, 964–980 (2011).
- 663 21. <http://www.nitrc.org/projects/cmtk/>
- 664 22. Randlett, O. *et al.* Whole-brain activity mapping onto a zebrafish brain atlas. *Nat Methods*, **12**,
665 1039-1046 (2015).
- 666 23. Schoonheim, P. J., Arrenberg, A. B., Del Bene, F., and Baier, H. Optogenetic localization and
667 genetic perturbation of saccade-generating neurons in zebrafish. *J Neuroscience*, **30**, 7111–
668 7120, (2010).
- 669 24. The gaze-tuned property of this bilaterally symmetric region in the rostral hindbrain was
670 independently evidenced by the Emre Aksay’s group in a yet unpublished experiment (private
671 communication)
- 672 25. Ahrens, M. B. *et al.* Whole-brain functional imaging at cellular resolution using light-sheet
673 microscopy. *Nat Methods*, **10**, 413–420 (2013).
- 674 26. Scudder, C. A., Kaneko, C. S. and Fuchs, A. F. The brainstem burst generator for saccadic eye
675 movements: a modern synthesis. *Exp Brain Res*, **142**, 439–462 (2002).
- 676 27. Dunn, T. W. *et al.* Brain-wide mapping of neural activity controlling zebrafish exploratory
677 locomotion. *Elife*, **5**, e12741 (2016).
- 678 28. Berthoz, A. and Grantyn, A. Neuronal mechanisms underlying eye-head coordination. *Prog*
679 *Brain Res*, **64**, 325–343 (1986).
- 680 29. Einhäuser, W. *et al.* Eye-head coordination during free exploration in human and cat. *Ann NY*
681 *Acad Sci*, **1164**, 353–366 (2009).
- 682 30. Wolf, S. *et al.* Whole-brain functional imaging with two-photon light-sheet microscopy. *Nat*
683 *Methods*, **12**, 379–380 (2015).
- 684 31. Brown, T. G. On the nature of the fundamental activity of the nervous centres; together with an
685 analysis of the conditioning of rhythmic activity in progression, and a theory of the evolution of
686 function in the nervous system. *The Journal of physiology*, **48**, 18-46 (1914).
- 687 32. Winfree, A. T. Biological rhythms and the behavior of populations of coupled oscillators. *J*
688 *Theor Biol*, **16**, 15–42 (1967).
- 689 33. Roenneberg, T., Dragovic, Z. and Merrow, M. Demasking biological oscillators: properties and
690 principles of entrainment exemplified by the *Neurospora* circadian clock. *Proc Natl Acad Sci U*
691 *S A*, **102**, 7742–7747, (2005).
- 692 34. Dayan, P. and Abbott, L. F., Theoretical Neuroscience. *Cambridge MA: MIT Press*, 2001.
- 693 35. Laing, C. R. and Chow, C. C. A spiking neuron model for binocular rivalry. *J Comp Neuro*, **12**,
694 39-53 (2002).
- 695 36. Vattikuti, S. *et al.* Canonical Cortical Circuit Model Explains Rivalry, Intermittent Rivalry, and
696 Rivalry Memory. *PLoS Comput Biol*, **12**, e1004903 (2016).

- 697 37. Kinkhabwala, A. *et al.* A structural and functional ground plan for neurons in the hindbrain of
698 zebrafish. *Proceedings of the National Academy of Sciences*, **108**, 1164-1169 (2011)
- 699 38. Portugues, R., Feierstein, C. E., Engert, F., Orger, M. B. Whole-brain activity maps reveal
700 stereotyped, distributed networks for visuomotor behavior. *Neuron*, **81**, 6 (2014)
- 701 39. Martinez-Conde, S. and Macknik, S. L. Fixational eye movements across vertebrates:
702 comparative dynamics, physiology, and perception. *J Vis*, **8**, 28.1–2816 (2008).
- 703 40. Marder E. and Calabrese, R. L. Principles of rhythmic motor pattern generation. *Physiol Rev*,
704 **76**, 687–717 (1996).
- 705 41. Blitz D. M. and Nusbaum, M. P. Neural circuit flexibility in a small sensorimotor system. *Curr*
706 *Opin Neurobiol*, **21**, 544–552 (2011).
- 707 42. Pearson, K. G. Generating the walking gait: role of sensory feedback. *Prog Brain Res*, **143**,
708 123–129 (2004).
- 709 43. Tastekin, I. *et al.* Role of the subesophageal zone in sensorimotor control of orientation in
710 *Drosophila* larva. *Curr Biol*, **25**, 1448–1460 (2015).
- 711 44. Schroeder, C. E., Wilson, D. A., Radman, T., Scharfman, H. and Lakatos, P. Dynamics of
712 Active Sensing and perceptual selection. *Curr Opin Neurobiol*, **20**, 172–176 (2010).
- 713 45. Ranade, S., Hangya, B. and Kepecs, A. Multiple modes of phase locking between sniffing and
714 whisking during active exploration. *J Neurosci*, **33**, 8250–8256 (2013).
- 715 46. Ito, J., Maldonado, P., Singer, W. and Grün, S. Saccade-related modulations of neuronal
716 excitability support synchrony of visually elicited spikes. *Cereb Cortex*, **21**, 2482–2497 (2011).
- 717 47. Chen, T.-W. *et al.* Ultrasensitive fluorescent proteins for imaging neuronal activity. *Nature*,
718 **499**, 295–300 (2013).
- 719 48. Higashijima, S.-I. *et al.* Imaging neuronal activity during zebrafish behavior with a genetically
720 encoded calcium indicator. *Journal of neurophysiology*, **90**, 3986–3997 (2003).
- 721 49. Kimura, Y., Satou, C. and Higashijima, S.-I. V2a and V2b neurons are generated by the final
722 divisions of pair-producing progenitors in the zebrafish spinal cord. *Development*, **135**, 3001–
723 3005 (2008).
- 724 50. Quiñero, R., Kraskov, A., Kreuz, T. and Grassberger, P. Performance of different
725 synchronization measures in real data: a case study on electroencephalographic signals. *Phys*
726 *Rev E*, **65**, 041903 (2002).
- 727 51. Fisher, N. I. Statistical analysis of circular data. *Cambridge University Press*, (1995).
- 728 52. Arrenberg, A. B., Del Bene, F., & Baier, H. Optical control of zebrafish behavior with
729 halorhodopsin. *Proceedings of the National Academy of Sciences*, **106**, 17968-17973 (2009).
- 730 53. Easter Jr, S. and Nicola, G. N. The development of vision in the zebrafish. *Dev Biol*, **180**, 646–
731 663 (1996).
- 732
- 733

734 **Acknowledgements :**

735 We are very grateful to Claire Wyart for allowing us to use her optogenetic setup. We would
736 like to thank the IBPS fish facility staff, and in particular Stéphane Tronche and Alex Bois for
737 their invaluable help. We are also grateful to Carounagarane Dore for his important
738 contribution to the design of the light-sheet microscope. This work was supported by C’Nano
739 Ile de France, École des Neurosciences de Paris Ile-de-France (ENP), Fondation pour la
740 Recherche Médicale (FRM : FDT20160435670 and FDT20150532639), Fondation Pierre-Gilles
741 de Gennes (FPGG).

742

743 **Author Contributions:** S.W., A.D., V.B., R.C., R.M. and G.D. designed the project. S.W.,
744 T.B., V.B., R.C., S.K. and G.D. carried out the behavioural and neuroimaging experiments and
745 analysis. D.G.C.H. and I.H.B. generated the *elavl3:GCaMP6f* transgenic zebrafish line. A.D. and
746 R.M. developed the model and performed data analysis. S.W. and U.L.B. performed the
747 optogenetic assays. All the authors contributed to writing the manuscript.

748

749 **Author Information:** The authors declare no competing financial interests. Correspondence
750 should be addressed to G.D. (georges.debregeas@upmc.fr).

751

Supplementary Methods

Zebrafish lines and maintenance

All experiments were performed on zebrafish nacre mutants, aged 5 to 7 days post-fertilization (dpf). For functional imaging, embryos were exposed to 1-phenyl-2-thiourea at 0.2 mM (PTU, Sigma-Aldrich), from 12 to 24 hpf, in order to further reduce skin pigmentation. Larvae were reared in Petri dishes in E3 solution on a 14/10h light/dark cycle at 28°C, and were fed powdered nursery food every day from 6 dpf. Calcium imaging experiments were carried out on larvae expressing the calcium indicator GCaMP6f under the control of the nearly pan-neuronal promoter *elavl3*. This *Tg(elavl3:GCaMP6f)a12200* line was generated by PCR amplification of the GCaMP6f open reading frame (from pGP-CMV-GCaMP6f, Addgene plasmid 40755, ref. 47) with forward primer ataACTAGTgccaccATGGGTTCTCATCATCAT and reverse ataCCGCGGcTCACTTCGCTGTCATCATTTGTAC (restriction site and coding sequences in upper case, respectively). This fragment was cloned into a plasmid with Tol2 arms flanking an upstream attR1-R2 cassette and the insertion site using restriction enzymes SpeI and SacII. Previously described *elavl3 (HuC) cis*-regulatory elements⁴⁸ were placed upstream via LR recombination (Invitrogen) with an attL flanked *elavl3* entry clone. The resulting plasmid was then co-injected into 1-cell stage embryos at a concentration of 30 ng/μL with Tol2 transposase mRNA at a concentration of 30 ng/μL. A single founder was selected based on high and spatially broad expression. Outcrossing this founder generated ~50% GCaMP6f-positive embryos, which were selected to establish the line.

Optogenetic experiments were performed with double transgenic fish *Tg(elavl3:GAL4-VP16)*⁴⁹ X *Tg(UAS:ChR2-H134R-mCherry)*²³. All experiments were approved by *Le Comité d'Éthique pour l'Expérimentation Animale Charles Darwin* (02601.01).

Behavioural assays

778 Zebrafish larvae were embedded in a drop of 2 % low melting point agarose (UltraPure LMP
779 Agarose, Invitrogen) deposited on a petri dish. Agarose was removed from regions around the
780 eyes for phototaxis assays, and from the eyes and tail for assessing saccades/swim turns
781 coordination. The petri dish was then filled with E3 medium. We visually checked for robust
782 saccadic dynamics using a dissection microscope before placing the larvae at the center of a 5 cm
783 in diameter frosted glass disk lit from below with an infra-red LED and positioned inside a dark
784 chamber at 28 °C. Eye and/or tail movements were recorded using an infrared sensitive Flea3
785 USB3 Camera (FL3-U3-13Y3M-C, Point Grey Research, Richmond, BC, Canada) with an
786 adjustable macro lens (Zoom 7000, Navitar, USA) with pixel-encoded timestamps.

787 All visual assays reported in the manuscript were performed using stimuli in the blue domain in
788 order to prevent the fluorescence signal from being polluted by visual stimuli during neuro-
789 imaging experiments. Controlled stereo-visual stimulation was obtained using two LEDs
790 (LED465E - Thorlabs) separated by a partition and projected onto the frosted screen, so that each
791 LED delivered a uniform illumination to one side of the animal's visual field of view. Analog
792 outputs of a DAQ device (USB6000 - National Instrument) were used to control the intensity of
793 the visual stimulation in the range $0 < I < I_{max}$, with $I_{max}=60 \mu\text{W}/\text{cm}^2$. We used MATLAB
794 (MathWorks) for image analysis and on-line control of the visual stimuli.

795
796 Saccades/swim-turns coordination experiments were performed under whole-field constant
797 illumination. We recorded the eyes and tail kinetics over periods of ~2h at 200 frames/s. Image
798 analysis was performed offline. We extracted the orientation of each eye by computing the angle
799 between the equivalent-ellipse minor axis (i.e. the eye optical axis) and the medial-lateral axis of
800 the fish (right: θ_r , left: θ_l), from which we computed the gaze angle defined as $\theta_{gaze} = (\theta_r - \theta_l)/$
801 2. The mean post-saccadic gaze angles $\langle \theta_{gaze\ right} \rangle$ and $\langle \theta_{gaze\ left} \rangle$ were used to define a
802 characteristic gaze range (Supplementary Figure 1a) from which we computed the normalized
803 gaze angle:

$$804 \quad g = (2 * \theta_{gaze} - \langle \theta_{gaze\ right} \rangle - \langle \theta_{gaze\ left} \rangle) / (\langle \theta_{gaze\ left} \rangle - \langle \theta_{gaze\ right} \rangle) \quad (1)$$

805 The onset of each saccade was further extracted with a time resolution of ~ 5 ms based on the
 806 time-derivative of the gaze signal. Reorienting saccades were defined such that $g * \Delta g < 0$ where
 807 Δg is the saccade induced gaze shift and g is the gaze value prior to the saccade. Secondary
 808 saccades are in turn defined such as $g * \Delta g > 0$.

809 To evaluate swim bout orientation, we binarized the image of the tail region (from the caudal
 810 border of the swim bladder to the tip of the tail) and computed at each time the moment of area
 811 with respect to the animal rostro-caudal axis, *i.e.* the mean distance to the axis computed over the
 812 tail pixels. To allow for across-samples comparison, this quantity was normalized by the tail
 813 length yielding an adimensional parameter $m(t)$ characterizing the instantaneous lateral excursion
 814 of the tail. The time derivative of this signal was used to identify and separate discrete tail bouts
 815 (Supplementary Figure 1c). We computed for each event the onset and offset times τ_{on} and τ_{off} as
 816 well as a turning score defined as $M = \int_{\tau_{on}}^{\tau_{off}} m(t).dt$. Large positive (negative) M values
 817 corresponded to strong leftward (rightward) attempted turns. The normalized gaze angle
 818 associated with a given tail-bout was defined as its value evaluated in the middle of the bout,
 819 $g((\tau_{on} + \tau_{off})/2)$.

820
 821 To assess stereo-visually driven gaze bias, the fish were first submitted to a period of 10
 822 minutes of habituation (whole-field illumination at maximum intensity) followed by 100 cycles
 823 comprising, (1) 1 min of whole-field illumination, (2) 25 s of extinction of one (either left or right)
 824 LED, (3) 5 s during which the LED intensity was linearly increased up to the its initial value. This
 825 sequence was repeated 50 times for each eye, either alternately or sequentially. The gaze
 826 orientation signal was extracted offline. To evaluate light-induced bias in gaze orientation, we
 827 computed the trial-averaged gaze shift towards the illuminated eye during periods of unilateral
 828 stimulation. We thus calculated, for each fish :

$$\Delta\theta = \langle \int_{t_{on}}^{t_{on}+30s} (g(t) - g(t_{on})) . dt \rangle_{right\ extinction} - \langle \int_{t_{on}}^{t_{on}+30s} (g(t) - g(t_{on})) . dt \rangle_{left\ extinction}$$

829 where the first (resp. second) term is averaged over the 50 left (resp. right) extinction periods, t_{on}
830 being the onset times of the extinction. To assess the significance of the light-induced bias for
831 each fish, we calculated the same quantity for 100 randomly distributed times t_{on} . This procedure
832 was replicated 1000 times, yielding a distribution of $\Delta\theta_{null}$ centered on zero (standard deviation
833 σ) that characterized the expected probability distribution under the null hypothesis. A two-tailed
834 test with $\alpha = 0.05$ was applied to assess visual-induced gaze bias: $\Delta\theta > 2 * \sigma$ (resp. $\Delta\theta < 2 * \sigma$)
835 was interpreted as a positive (resp. negative) phototactic behaviour (Supplementary Figure 2g).

836

837 To check that the light-induced gaze bias resulted in a consistent swim bias, we ran a series of
838 experiments using the same stimulation protocols on fish whose both eyes and tail were freed.
839 Both the gaze and tail-deflection signals were extracted offline. We then computed the trial-
840 averaged swim bias during periods of unilateral stimulation by calculating, for each fish :

$$\Delta m = \left\langle \int_{t_{on}}^{t_{on}+30s} m(t) \cdot dt \right\rangle_{right\ extinction} - \left\langle \int_{t_{on}}^{t_{on}+30s} m(t) \cdot dt \right\rangle_{left\ extinction}$$

841 The significance of the light-induced swim bias for each fish was quantified as described above
842 for the gaze-bias ($\Delta m > 2 * \sigma$). With this criterium, the fish that exhibited a light-induced gaze
843 bias towards the light source, systematically showed a significant swim-bias towards the light
844 (N=5).

845

846 Virtual-reality assays of spatio-temporal gaze bias were performed as follows. Larvae were first
847 subjected to a minimum of 30 min of visual habituation at maximum illumination intensity. A
848 20 min-long recording was acquired during this initial period. The 5th and 95th percentile of the
849 gaze distribution during this neutral run - noted $\langle \theta_{gaze\ right} \rangle$ and $\langle \theta_{gaze\ left} \rangle$, respectively -
850 characterized the typical gaze range, from which we computed the normalized gaze angle $g(t)$ as in
851 equation (1) for all subsequent runs. The whole-field illumination intensity was then modulated in
852 real-time according to the extracted gaze angle with a refresh rate of 100 Hz. The intensity
853 delivered to the fish was a sigmoid function of the normalized gaze: $I(g) = \alpha + 0.5 \beta (1 +$

854 $erf(2g)$), where erf is the error function. Notice that the gaze signal $g(t)$ was dynamically
855 smoothed with a non-linear filter to eliminate fluctuations due to image analysis, which would
856 otherwise result in flickering visual stimulation, while preserving the rapid transitions associated
857 with saccades. We successively imposed a rightward-biased ($\alpha = 0, \beta = I_{max}$) and a leftward-
858 biased ($\alpha = I_{max}, \beta = -I$) intensity profile. We extracted from these runs the time fraction f_{light}
859 during which the gaze was oriented towards the light ($I > I_{max}/2$). To assess the significance of the
860 light-induced bias, we implemented a bootstrap approach. The neutral run (constant illumination)
861 was randomly split into 100 segments, which were distributed into two packets. The segments
862 were 10 s-long in average, *i.e.* of the order of the gaze fixation duration such that they could be
863 considered as statistically independent. We computed the mean of the time-fraction for which
864 $g > 0$ for the first packet, and $g < 0$ for the second packet. We replicated this procedure for 1000
865 different segmentations of the neutral signal. The resulting distribution of the time-fractions was
866 gaussian-like (standard deviation σ) and centered on 0.5; it reflected the statistical distribution of
867 biases expected under the null hypothesis for a 1000 s long run. For an experiment of total
868 duration T_{bias} , the distribution was thus expected to have a standard deviation of $\sigma * \sqrt{1000/T_{bias}}$.
869 We used this latter value to perform a two-tailed test with $\alpha = 0.05$ (critical z-value of 2) on the
870 light-biased data to assess the significance of visually induced gaze bias (Supplementary Figure
871 2i-k).

872

873 Light-sheet functional imaging

874 Volumetric functional recordings were carried out using custom-made one-photon and two-
875 photon light-sheet microscopes whose optical characteristics have been detailed elsewhere³⁰.
876 Larvae were mounted in a 1 mm diameter cylinder of low melting point agarose at 2 %
877 concentration. The eyes region was systematically excluded from the scanned volume. One-
878 photon illumination was used for the eyes-free experiments as they require significant post-
879 processing to correct saccade-induced tissue deformation that proved difficult to implement in
880 two-photon recordings. However, four recordings under 2P light-sheet imaging were performed to

881 check the absence of any spurious effects associated with the background light level under 1P
882 imaging (Supplementary Figure 3a). Acquisition rate was set at 1 stack per second (20 brain
883 sections, 6 μm inter-slice separation), and typical recordings lasted for ~ 1 h. In the eyes-fixed
884 experiments (identification of the self-oscillatory circuit and characterization of the visual
885 response), the animal was fully embedded in the agarose gel, which entirely suppressed the
886 saccadic dynamics. In this configuration, the animal was weakly paralyzed by adding
887 Pancuronium bromide at 0.3 mg/mL in the agarose solution in order to further minimize
888 movement artifacts. These eyes-fixed experiments were performed in the two-photon regime to
889 mitigate perturbation of the visual system by the laser scanning³⁰. Recordings were performed at
890 1 stack per second (in general 10 brain sections, 9 μm inter-slice separation) and lasted for 1 to 2
891 h.

892
893 Image pre-processing, soma and neuropil regions segmentation as well as calcium transient
894 ($\Delta F/F$) extraction were performed offline using MATLAB, according to the workflow previously
895 reported^{8,30}. A non-rigid 2D registration was further implemented in eyes-free recording to correct
896 saccade-induced tissue deformations using the Matlab built-in functions *registration* and *imwarp*.

897
898 During neuro-imaging, eyes movements were recorded from below using an infrared sensitive
899 Flea3 USB3 Camera (FL3-U3-13Y3M-C, Point Grey Research, Richmond, BC, Canada) with an
900 adjustable macro lens (Zoom 7000, Navitar, USA) with pixel-encoded timestamps. The setup was
901 lit from below with an infra-red LED at 850 nm. Image acquisition, mirror scanning, objective
902 motion and eyes movements monitoring were synchronized using a D/A multifunction card (NI
903 USB-6259 NCS, National Instruments) and a custom-written program in LabVIEW (National
904 Instruments). Both the behaviour and neuroimaging cameras were operated at 20 Hz.

905
906 In order to map gaze-tuned neuronal populations, we performed a regression analysis on eyes
907 angular position and velocity. The regression was performed voxel by voxel, after binning the

908 images down to a pixel size of $0.8 \times 0.8 \mu\text{m}^2$. We manually selected the brain region, excluding the
909 areas rostral to the cerebellum in which the saccade-induced tissue deformation precluded
910 consistent signal extraction. The method used to compute the Z-score of every voxel essentially
911 followed the approach proposed by Miri *et al.*²⁰. We used for the eye velocity regressor a vector
912 consisting of $+(-)1$ at the onset times of a leftward (rightward) saccades, and zeros elsewhere (for
913 saccade onset detection, see paragraph *Saccades/swim-turns coordination*). This discrete signal
914 offered a noise-free proxy for the time-derivative of the eye angular position.

915
916 The mean peri-saccadic response of the key functional regions shown in Figure 2 and
917 Supplementary Figure 3 were calculated over a 10 s-long window. Averaging was performed over
918 ~ 150 saccades, excluding time-segments in which movements or another saccade occurred during
919 the 10 s window. Before averaging, fluorescence signals from individual voxels were over-
920 sampled to match the eye-tracking frame-rate (20 Hz). To prevent mixing pre- and post-saccadic
921 activities, this interpolation was performed independently on the pre- and post-saccadic phases.

922
923 The neuronal assembly engaged in the self-generated oscillations in eyes-fixed experiments
924 was delineated based on activity correlation analysis (Supplementary Figure 4). We first
925 performed a morphological segmentation that yielded a $\Delta F/F$ signal for all the neurons in the
926 recorded region^{8,30}. We then calculated the Pearson correlation matrix, corrected by the uniform
927 correlation noise³⁰, of all pairs of neurons within a $100 \times 60 \times 27 \mu\text{m}^3$ volume positioned relative to
928 morphological landmarks such as to encompass the 4 most posterior clusters of the rostral
929 hindbrain gaze-tuned population (see Supplementary Figure 4a). We then selected the 10 pairs of
930 neurons with the largest anti-correlation. These neurons were separated into two groups, based on
931 their position relative to the medial axis. The mean $\Delta F/F$ signals of the left and right clusters
932 provided us with two reference signals (Supplementary Figure 4d). We then performed a
933 regression analysis on a voxel basis, as described above, using these reference signals as
934 regressors to produce the self-oscillatory functional map shown in Figure 3b-c.

935 The left and right HBO signals shown in Figures 3-5 were computed as the mean signal of
936 individual HBO neurons selected on the basis of their correlation with the left-minus-right
937 reference signal (Pearson correlation coefficient threshold +0.2 and -0.2). This selection method
938 yielded a total of 348.4 ± 16.1 neurons (std 142.5, N=78 fish).

939
940 We used blue LEDs (LED465E - Thorlabs, 5 cd, 15° aperture angle) for visual stimulation. The
941 stimulus intensity was calibrated by measuring the radiance at a similar distance as a function of
942 the applied voltage. For asymmetrical visual stimulation, two LEDs were positioned
943 symmetrically outside of the chamber at 45° and 4.5 cm from the fish eyes. Each LED delivered a
944 visual intensity of $20 \mu\text{W}/\text{cm}^2$. The flash stimulation was performed using a single LED positioned
945 inside the chamber 4.5 cm in front of the fish eyes³⁰ and delivering $31 \mu\text{W}/\text{cm}^2$, while symmetric
946 alternating stimulation was obtained by projecting one LED, delivering $8 \mu\text{W}/\text{cm}^2$, onto a $2 \times 2 \text{ cm}^2$
947 diffusive screen positioned 0.55 cm below the fish. The blue photons were filtered out from the
948 imaging system using a bandpass filter (525/39 nm Brightline, Semrock). Image acquisition and
949 visual stimulation were synchronized using a D/A multifunction card (NI USB-6259 NCS,
950 National Instruments) and a custom-written program in LabVIEW (National Instruments).

951 The unilateral visual response map (Figure 4 and Supplementary Figure 3b) was obtained by
952 delivering alternating asymmetric ON-OFF stimuli. The intensity time-sequence of the stimulus
953 delivered to each eye were used as regressors, and a Z-score was computed for each individual
954 voxel, as detailed in section *Regression analysis*.

955
956 We used the Computational Morphometry ToolKit²¹ (CMTK) to align the various volumetric
957 functional maps (gaze-tuned, self-oscillatory, visual response) onto a single reference brain-stack.
958 The latter was obtained by averaging four different samples (Tg(*elavl3*:GCaMP6f), 6 dpf) imaged
959 with the one-photon light-sheet microscope at high spatial resolution (voxel size $0.4 \times 0.4 \times 2 \mu\text{m}$).
960 We further used CMTK to compute the morphing transformation from our reference brain to the
961 Tg(*elavl3*:GCaMP5G) stack of the Z-Brain atlas²². This allowed us to map the functional data onto

962 the Z-Brain Viewer and thus to position various clusters relative to labeled anatomical landmarks.

963
964 Phase and frequency analysis of the HBO oscillations was carried out using the Hilbert
965 transform. This method allows one to extract the phase signal, associated with the dominant
966 frequency, in a broadband time trace⁵⁰. We implemented this mathematical tool on the differential
967 HBO signal (left- minus right-circuit activity) to assign a phase $\varphi(t)$ to the HBO oscillatory
968 dynamics. The angular frequency was then computed as the mean derivative of $\varphi(t)$; the HBO
969 period distribution was obtained by performing the same operation over a sliding window of width
970 2π (Fig. 3g). To determine the phase-dependent response curve (Fig. 4k), the local phase $\varphi(t)$ was
971 obtained through linear extrapolation of the Hilbert transform calculated over ~ 1 period, *i.e.* from
972 $t-20$ s to $t-1$ s. This method guaranteed that the phase calculated at the instant of the flash was not
973 affected by the flash-induced response itself. Phase-locking was assessed by evaluating the non-
974 uniformity of the peri-stimulus phase distribution within a 10 s window centered on the stimulus,
975 using the Rayleigh test. Given the large number of stimuli delivered in each run ($n>50$), we
976 computed the p-value using Fisher's approximation⁵¹: $p = e^{-z}$, where z is the score given by
977 Rayleigh test. Under this approximation, the critical Z-score beyond which the phase follows a
978 non-uniform distribution with $p<0.01$ is 4.6 (Supplementary Figure 8).

979 980 Optogenetics

981 Six dpf Tg(*elavl3*:GAL4; *UAS*:ChR2-mCherry) fish were immobilized in a drop of 2 % low
982 melting point agarose deposited on a petri dish, and their eyes were freed. Larvae were imaged
983 with a 10X objective on an upright microscope (Zeiss Examiner D1, Zeiss, Germany). Images
984 were acquired at 10 Hz with a camera (ImageEM, Hamamatsu, Japan), allowing for subsequent
985 extraction of the gaze sequence. We used a digital mirror device (DLP D4100, Vialux, Germany)
986 to generate 2D illumination patterns for optogenetic stimulation. The DMD surface was relayed
987 *via* a telescope onto the back-focal plane of the epifluorescent light-path of the microscope
988 (Supplementary Figure 5a). We used a high power white LED (Prizmatix, Israel) and a TIR prism

989 (Lida optical and electronic, China) to illuminate the DMD surface. The white light was passed
990 through a filter set in the epifluorescence light-path to select the spectral band necessary for ChR2
991 activation (bandpass 495 nm). The DMD and the camera were controlled in LabView (National
992 Instruments, Austin, TX, USA) and Matlab (Mathworks, Natick, MA, USA). The light source,
993 camera recording and light-patterning were synchronized *via* pClamp (Digidata 1440A, Molecular
994 Devices, Fremont, CA, USA).

995 The stimulation protocol was the following: pairs of bilaterally symmetric $47 \times 57 \mu\text{m}^2$ regions
996 were illuminated alternately for 2.75 s with a period of 18 s. This alternation was repeated 5 times
997 before moving to a new regions pair. The order of the 20 targeted pairs was randomized before
998 each trial. As previously reported²³, activation of the rh4-6 region of the hindbrain evoked
999 conjugate ipsiversive saccades. In some animals however, activation of the hindbrain failed to
1000 evoke any significant oculomotor response. This reflects the random variegation in the
1001 Tg(*elavl3*:GAL4; *UAS*:ChR2-mCherry) line, which results in diminished hindbrain ChR2
1002 expression in a fraction of the animals. These non-responsive animals (Z -score < 1 in rh4-6 regions)
1003 were excluded from further analysis, yielding a total of 8 (out of 19) larvae from which the
1004 analysis was performed.

1005 To estimate the photostimulation volume, we implemented the same illumination protocol
1006 using a Tg(HuC:gal4; *UAS*:Kaede) line, in which the photoconvertible protein Kaede is expressed
1007 near pan-neuronally. This approach was previously shown to provide a close estimate of the
1008 illuminated volume⁵². Seven regions, selected at different locations on the checkerboard, were
1009 illuminated for 40s using a mercury arc lamp as the light source for the DMD using the whole
1010 spectrum < 515nm of the mercury arc lamp. After photoconversion, whole brain stacks of red and
1011 green Kaede fluorescence were acquired using a spinning-disk confocal microscope (Intelligent
1012 Imaging Innovations, Denver, CO, USA) and the ratio of red/green fluorescence was calculated
1013 for further analysis (see Supplementary Figure 5c).

1014

1015 In order to position optogenetically-targeted regions with respect to the formerly identified
1016 gaze-tuned circuit (Supplementary Figure 5b), we successively imaged a unique reference fish
1017 (Tg(*elavl3*:GCaMP6), 6 dpf), successively with one-photon light-sheet (3D stack) and bright-field
1018 (2D image, $z=160\ \mu\text{m}$ from the dorsal skin) illumination at similar 10X magnification. We
1019 performed a 2D registration of the 19 tested fish onto the bright field reference image using the
1020 Matlab built-in functions *imregtform*, *fitgeotrans* and *imwarp*. The gaze-tuned 3D functional map
1021 (shown in Figure 2) was further registered onto the reference brain-stack using *CMTK*. For each
1022 fish, we computed the optogenetically-induced gaze shift $\Delta\theta_{gaze}(t_{stim}) = \theta_{gaze}(t_{stim} + I) -$
1023 $\theta_{gaze}(t_{stim} - I)$ for all stimulation onset times t_{stim} . For each targeted pair of regions, we computed
1024 a Z-score $= \langle \Delta\theta_{gaze}(t_{stim}) \rangle_{all\ stim} / std(\Delta\theta_{gaze})$, where the standard deviation was calculated over
1025 the entire run. Averaging was done over all ten stimulations with ipsiversive gaze shifts counted
1026 positively and contraversive gaze shifts counted negatively.

1027 To estimate the illumination volume, we aligned the 35 photo-converted volumes extracted
1028 from 5 different ratiometric stacks (7 regions were illuminated in each sample). The mean volume,
1029 shown in Extended Fig 5d, appears to faithfully reflect the 2D rectangular shape imposed by the
1030 DMD, while being essentially invariant along the z-axis. This observation, which is consistent
1031 with the low NA of the illumination system, guarantees that the activation efficiency should be
1032 relatively insensitive to the axial location of the neurons within the brain. .

1033

1034 Neuronal model

1035 *Rate model equations of the HBO dynamics:*

1036 The mean firing rate of the left/right HBO subcircuits were described by 4 differential equations:

$$1037 \quad \tau \frac{dr_{L/R}}{dt} = -r_{L/R} + \Phi[W_E r_{L/R} - W_I r_{R/L} - \Gamma a_{L/R} + I_0 + I_{L/R}(t)] + \xi_{L/R}(t) \quad (2)$$

1038 with

$$1039 \quad \tau_A \frac{da_{L/R}}{dt} = -a_{L/R} + r_{L/R} \quad (3)$$

1040 where $W_{E^r_{L/R}}$ and $W_{I^r_{R/L}}$ denote the recurrent excitation and reciprocal inhibition, the terms
1041 $-\Gamma a_{L/R}$ account for adaptation current, I_0 and $\xi_{L/R}$ are constant and white noise (standard
1042 deviation σ) inputs originating from non-visual projections, $I_{L/R}(t)$ are visually-evoked currents.
1043 The function Φ was taken as the simplest form consistent with the non-negative spiking constraint:
1044 $\Phi(x > 0) = x$ and $\Phi(x < 0) = 0$ otherwise. Equations (2) and (3) were numerically integrated
1045 using Euler's method. In such a dynamic system, the self-excitation and adaptation currents
1046 produce the rise and fall of activity in one population, while inhibition ensures that only one
1047 population can be active at a time. Within a finite range of parameters, the system exhibited self-
1048 sustained anti-phasic oscillations in the absence of visual inputs ($I_{L/R} = 0$). We further adjusted
1049 the values of the relaxation times such that the endogenous oscillatory period matched the mean
1050 saccadic period ($T_{endo} = 25$ s). The corresponding parameters read:

$$1051 \quad W_E = 3.5 \text{ A} \cdot \text{s}; \quad W_I = 0.5 \text{ A} \cdot \text{s}; \quad \Gamma = 2.9; \quad \tau = 2 \text{ s}; \quad \tau_A = 1 \text{ s}; \quad I_0 = 20 \text{ A};$$

1052 The current noise amplitude σ directly controlled the temporal regularity of the oscillations,
1053 which could be characterized by the phase-noise amplitude σ_f (Supplementary Figure 8). This
1054 quantity, defined as the standard deviation of the distribution of phase increment over a 1s
1055 interval, was measured at $\sigma_f = 0.55 \pm 0.11$ in experiments (fixed-eyes conditions, no visual
1056 stimulation, N=8 fish). We set the phase-noise at a slightly smaller value ($\sigma_f \sim 0.2-0.4$) in order to
1057 quantitatively reproduce all synchronization processes.

1058
1059 A unilateral step-increase in illumination was assumed to elicit a 0.3 s-long positive pulse of
1060 current followed by a constant input current on the ipsilateral HBO circuit. The intensity A_t of the
1061 pulse was proportional to the illumination increment, and the plateau intensity A_c was proportional
1062 to the stimulus intensity. A unilateral step-decrease in illumination further elicited a similar 0.3 s-
1063 long positive pulse of current on the contralateral HBO circuit. Data shown for flash stimuli were
1064 obtained with $A_t = 100$ A. For alternated stimulation, we used $A_t = 100$ A and $A_c = 400$ A.

1065 To evaluate amplitude- and phase-response curves, we successively produced free-running and
1066 flash-evoked traces using identical noise signals (Supplementary Figure 10). The flash-induced

1067 response was then characterized by the difference in activity and the phase-offset between both
 1068 configurations measured 1.5 s after the stimulus. This operation was repeated for different noise
 1069 realizations and stimulation times.

1070

1071 We modelled the effective visual stimulus received from a distant light source by each eye as a
 1072 slowly varying function of its azimuth θ_s relative to the fish caudo-rostral axis. The perceived
 1073 stimulus was maximum when the source was aligned with the eye's optical axis, *i.e.* for $\theta_s = \pm 80^\circ$,
 1074 and was null beyond the monocular visual field⁵² (total angular range 163°). The value of the left
 1075 and right visually evoked current as a function of the light source azimuth thus reads:

$$I_L(\theta_s) = 100 * \cos((\theta_s - 80^\circ) \frac{180^\circ}{163^\circ}) \Theta(\frac{163^\circ}{2} - |\theta_s - 80^\circ|)$$

$$I_R(\theta_s) = 100 * \cos((\theta_s + 80^\circ) \frac{180^\circ}{163^\circ}) \Theta(\frac{163^\circ}{2} - |\theta_s + 80^\circ|) \quad (4)$$

1077 where Θ is the Heaviside step function.

1078

1079 In this second configuration, we assumed that the light source produced an identical stimulation
 1080 on both eyes (no stereo-visual cue), and that the associated input current was a slowly decaying
 1081 function of the angle between the gaze orientation θ_{gaze} and the source azimuth θ_s :

$$I_L(\theta_{gaze}, \theta_s) = I_R(\theta_{gaze}, \theta_s) = \exp(-((\theta_{gaze} - \theta_s)/\sigma_{source})^2/2)$$

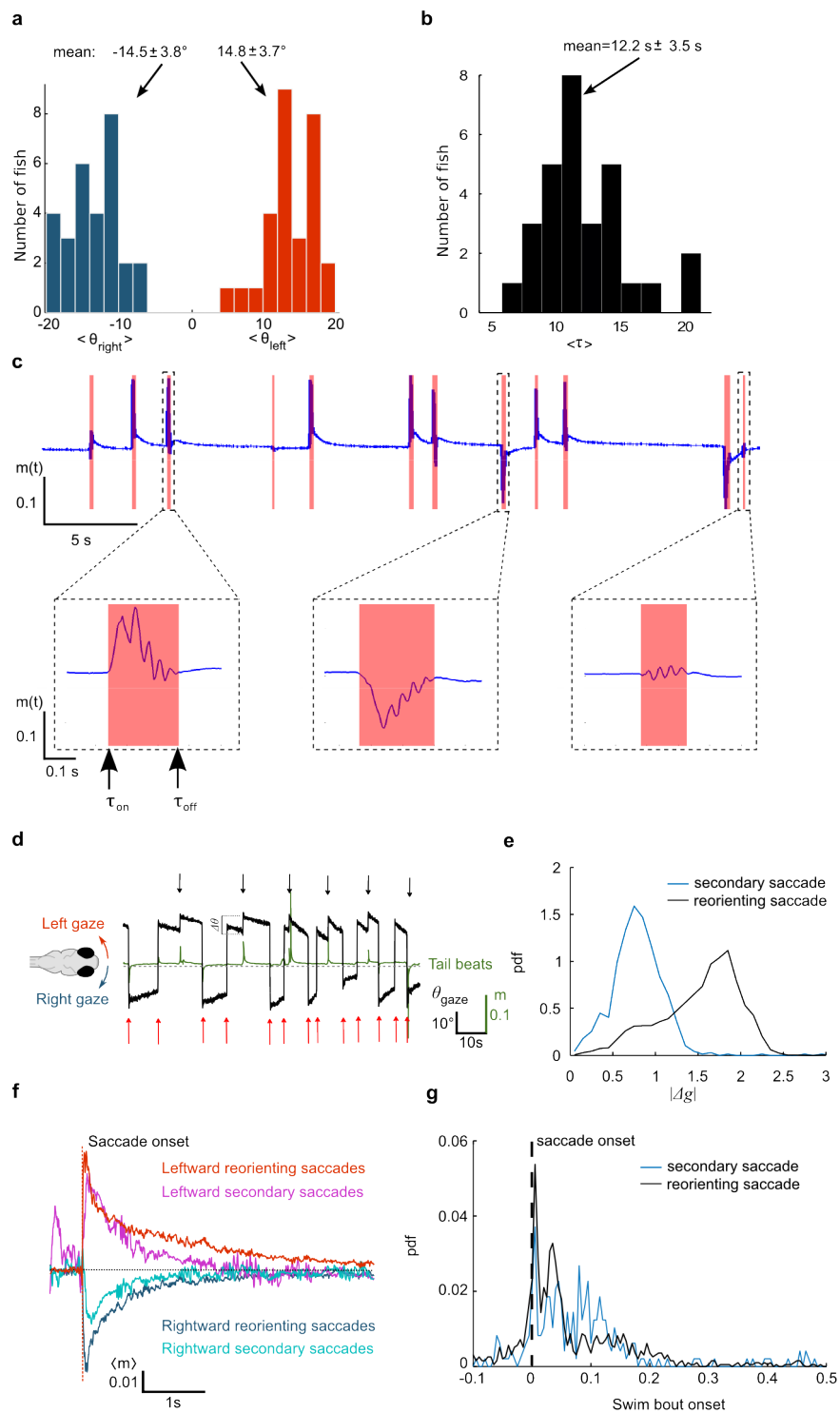
1083 with $\sigma_{source} = 45^\circ$. Saccade-induced gaze oscillations were accounted for by switching the
 1084 gaze orientation between $\theta_{gaze} = -15^\circ$ (when $r_L > r_R$, *i.e.* leftward gaze) and $\theta_{gaze} = +15^\circ$ (when $r_R > r_L$,
 1085 *i.e.* rightward gaze), which in turn elicited a rhythmic modulation of the received currents
 1086 (Supplementary Figure 11). In order to account for background adaptation, the input currents at
 1087 both angular positions were offset by the weaker one.

1088

1089 Data availability

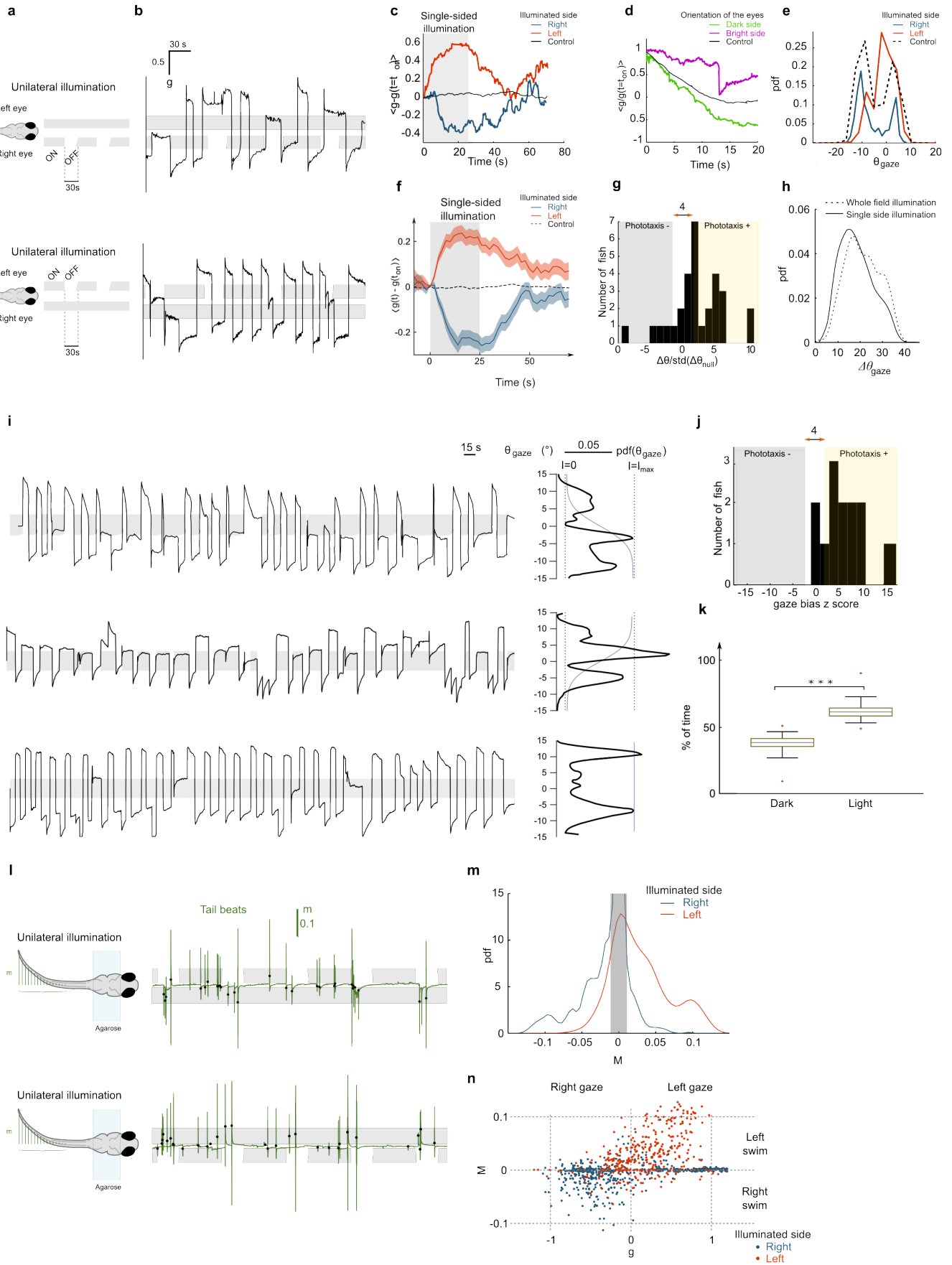
1090 All data and codes used for the analysis are available from the authors on request.

Supplementary Figure 1 | Behavioural assays: ocular saccades and eyes/tail coordination.



1094 **Supplementary Figure 1 | Behavioural assays: ocular saccades and eyes/tail coordination.**
1095 **a**, Histograms of the mean gaze angles measured immediately after rightward ($\langle \theta_{gaze\ right} \rangle$)
1096 and leftward ($\langle \theta_{gaze\ left} \rangle$) saccades (N = 29 fish). These angles are used to compute the
1097 normalized gaze angle g (see Supplementary Methods). **b**, Histogram of the mean gaze fixation
1098 times (N = 29 fish). **c**, Example tail-deflection signals (normalized area moment $m(t)$, see
1099 Supplementary Methods). Each red region corresponds to a discrete swim-bout from which the
1100 onset and offset times (τ_{on} and τ_{off}) are extracted, as well as a turning score M defined as the
1101 integral of $m(t)$ between τ_{on} and τ_{off} . **d-g**, Comparison between reorienting and secondary
1102 saccades. **d**, Example traces of the gaze angle and tail deflection signals. The arrows points to
1103 reorienting (red) or secondary (black) saccades. **e**, PDF of the absolute gaze shift amplitude $|\Delta g|$
1104 associated with reorienting (black) and a secondary (blue) saccades. **f**, Mean peri-saccadic tail
1105 deflection signal averaged over leftward reorienting (red) or secondary (magenta) saccades, and
1106 rightward reorienting (blue) or secondary (pale blue) saccades. **g**, Peri-saccade PSF of swim-bouts
1107 onset times ($\tau_{on} - t_{sac}$) for reorienting saccades (black) and secondary (blue) saccades. The
1108 saccade generally precedes the tail beat : 88% of the tail beats that occur within 0.3s of a saccade
1109 are triggered after the saccade onset.
1110

Supplementary Figure 2 | Behavioural assays: light-induced bias in gaze-dynamics.



1114 **Supplementary Figure 2 | Behavioural assays: light-induced bias in gaze-dynamics. a,**
1115 Scheme of the unilateral extinction experiment. **b,** Gaze signals during a series of unilateral light
1116 extinctions. The greyed areas indicate the stimulus sequence delivered to each eye. **c,**
1117 Corresponding trial-averaged normalized gaze signal $\langle g(t) - g(t = t_{on}) \rangle_{all\ stim}$ following of
1118 the light on the right (red) and left (blue) eye. The black line is the control, i.e. the mean gaze
1119 signal following 100 randomly distributed times t_{on} . **d,** Trial-averaged gaze decay $\langle g(t)/g(t =$
1120 $t_{on}) \rangle_{all\ stim}$ following unilateral extinction. In magenta, averaging was performed over trials for
1121 which the gaze is orientated towards the bright side at $t=t_{on}$. In green, the gaze is oriented towards
1122 the dark side at $t=t_{on}$. The black curve is the control (averaged over randomly distributed onset
1123 times). These data indicate that unilateral extinction both lengthens gaze fixation towards the
1124 bright side (slower decay) and shortens gaze fixation (faster decay) toward the dark side. **e,** PDF of
1125 the gaze during periods of unilateral visual stimulation for the same animal. In red (resp. blue), the
1126 light is ON on the left (resp. right) eye. The black dashed curve is the gaze distribution during
1127 bilaterally symmetric illumination. **f,** Trial-averaged gaze shift signal
1128 $\langle g(t) - g(t = t_{on}) \rangle_{all\ stim}$ following unilateral extinction on left (red) or right (blue) eye at
1129 $t = t_{on}$. The shaded region represents the standard error. **g,** Histogram of the mean gaze shift
1130 (normalized by the standard deviation of the control) during unilateral extinction phases (N=33
1131 fish). Gaze shifts are counted positively (resp. negatively) when oriented towards (away) from the
1132 bright side. Grey and yellow shaded areas correspond to animals displaying statistically significant
1133 gaze bias away and towards the illuminated side, respectively (two-tailed t-test, Z-score>2,
1134 $p<0.05$). **h,** PDF of the saccade-induced gaze variation during periods of unilateral illumination
1135 and whole field illumination (dotted line). **i,** Left : Example gaze signals for a virtual rightward
1136 (top), leftward (middle), uniform (bottom) illumination. Grey areas indicate bright illumination
1137 periods (intensity larger than half its maximal value). Right : corresponding gaze-angle PDFs. The
1138 blue curves show the imposed virtual illumination profile. **j,** Histogram of the gaze-biased Z-score
1139 (see Supplementary Methods). As in (g), the grey and yellow shaded areas correspond to animals
1140 displaying statistically significant gaze bias away and towards the illuminated side, respectively

1141 (two-tailed t-test, $Z\text{-score} > 2$, $p < 0.05$). **k**, Time fractions spent with the gaze oriented towards the
1142 dark and bright directions ($N=13$ fish). *** $p < 0.001$, paired-sample t-test. **l**, Tail-deflection signals
1143 (**m**) during a series of unilateral light extinctions. Greyed areas indicate the stimulus sequence
1144 delivered to each eye. **m**, PDF of the tail-beat turning index M during periods of unilateral visual
1145 stimulation for animals displaying light-induced gaze-bias ($N=5$). In red (resp. blue), the light is
1146 ON on the left (resp. right) eye. **n**, Individual tail-beats turning score M vs normalized gaze angle
1147 g during periods of unilateral visual stimulation.

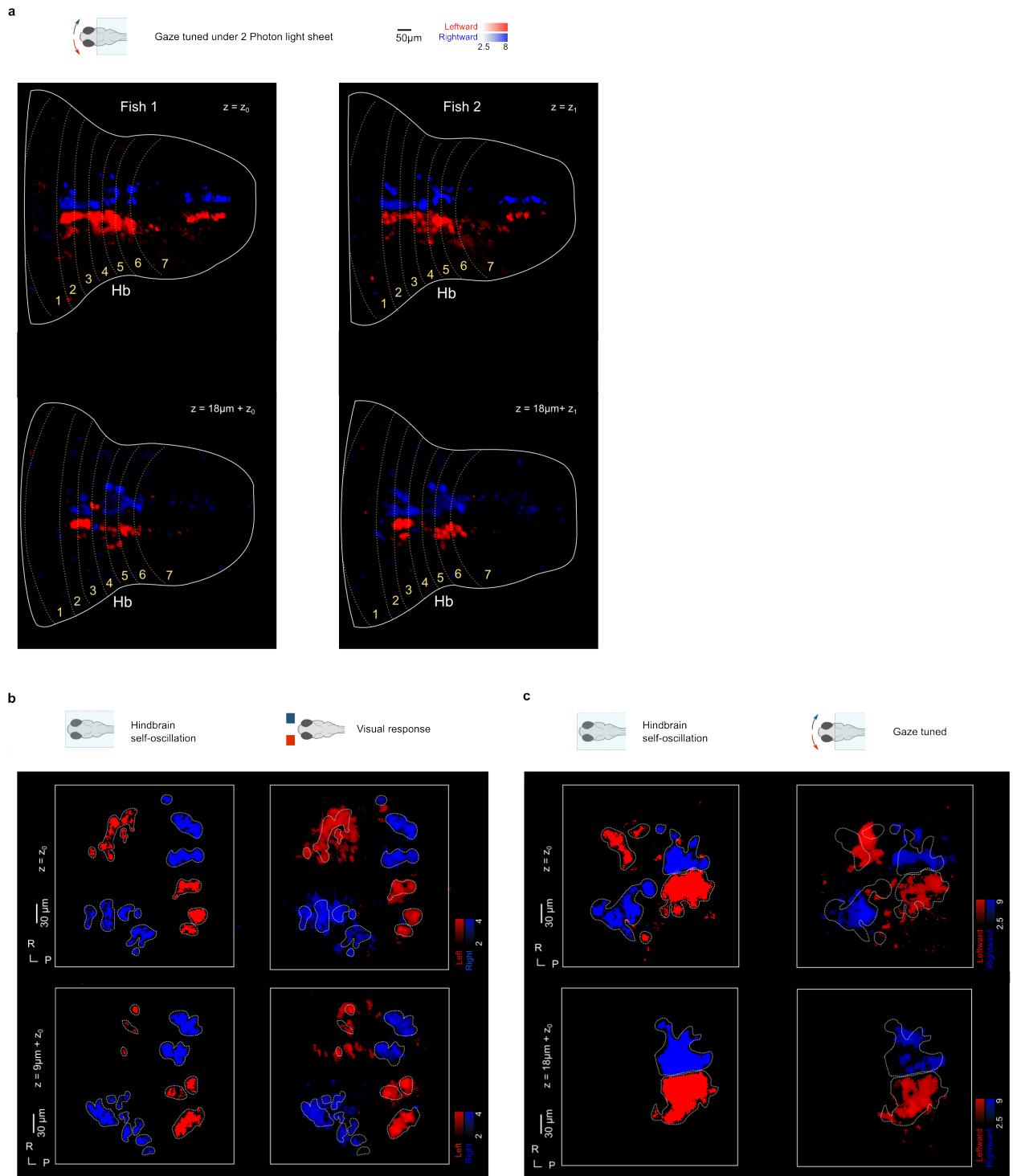
1148

1149

Supplementary Figure 3 | Gaze-tuned maps in the absence of visual stimulation and

1150

comparison between gaze-tuned, visually responsive and self-oscillatory maps.



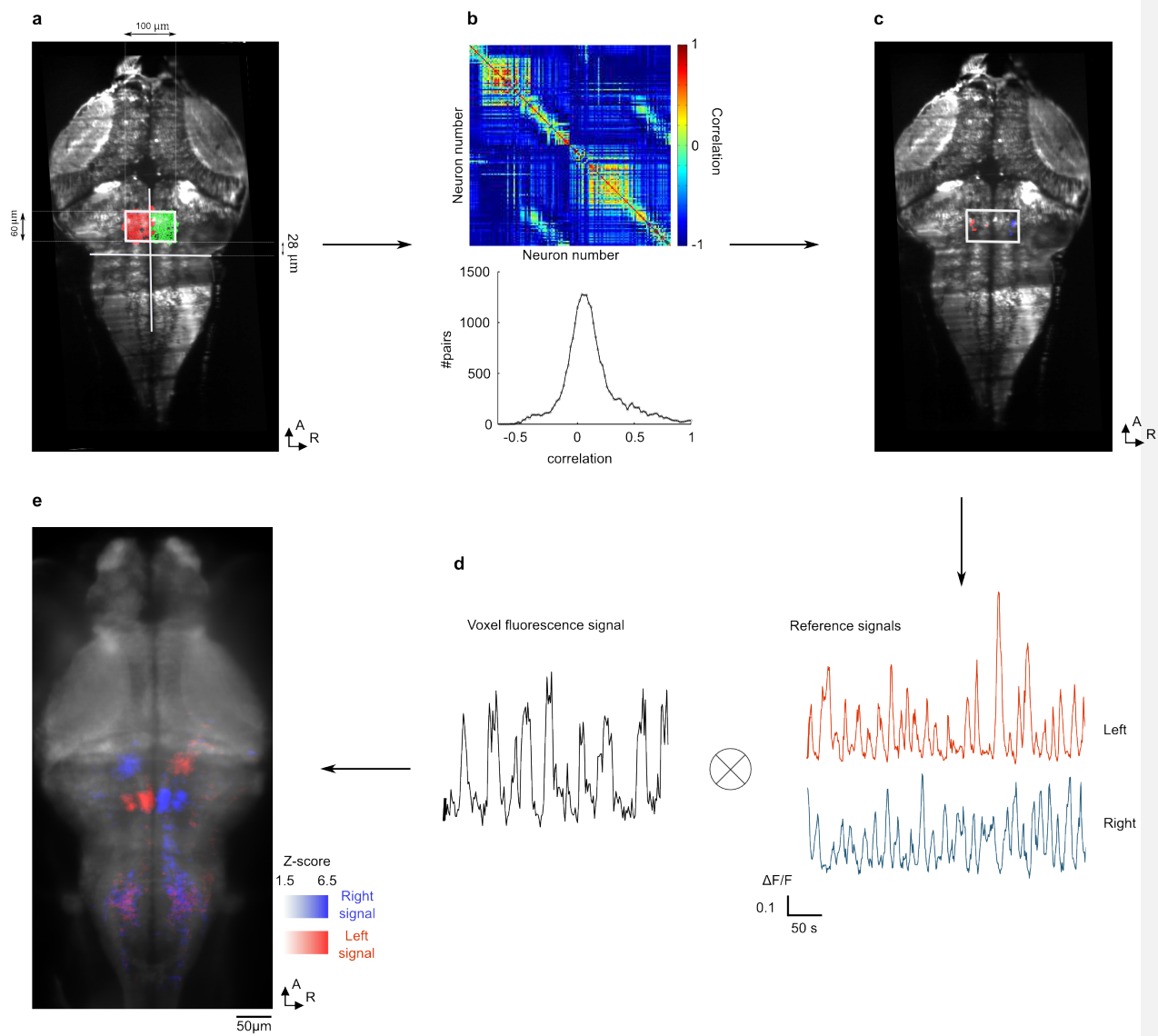
1151

1152 **Supplementary Figure 3 | Gaze-tuned maps in the absence of visual stimulation and**
1153 **comparison between gaze-tuned, visually responsive and self-oscillatory maps.**

1154 **a**, Two dorso ventral sections of gaze-tuned maps obtain on two different fish under 2-photon
1155 light-sheet imaging. Experiments were performed in the absence of visual stimulation. **b**,
1156 Comparison on the same fish, for two different brain sections, of the self-oscillatory hindbrain
1157 population (left) and the visually responsive neurons (right). The white contour line delineates the
1158 self-oscillatory region, *i.e.* the voxels that display a Z -score >3.5 when correlating with the
1159 reference oscillatory signal (see Supplementary Methods). **c**, Comparison on the same fish, for two
1160 different brain sections, of the self-oscillatory hindbrain population (left) and the gaze-tuned
1161 neurons (right). The white contour line is defined as in b. These data were obtained by performing
1162 experiments with a larva whose eyes were successively tethered then free.

1163

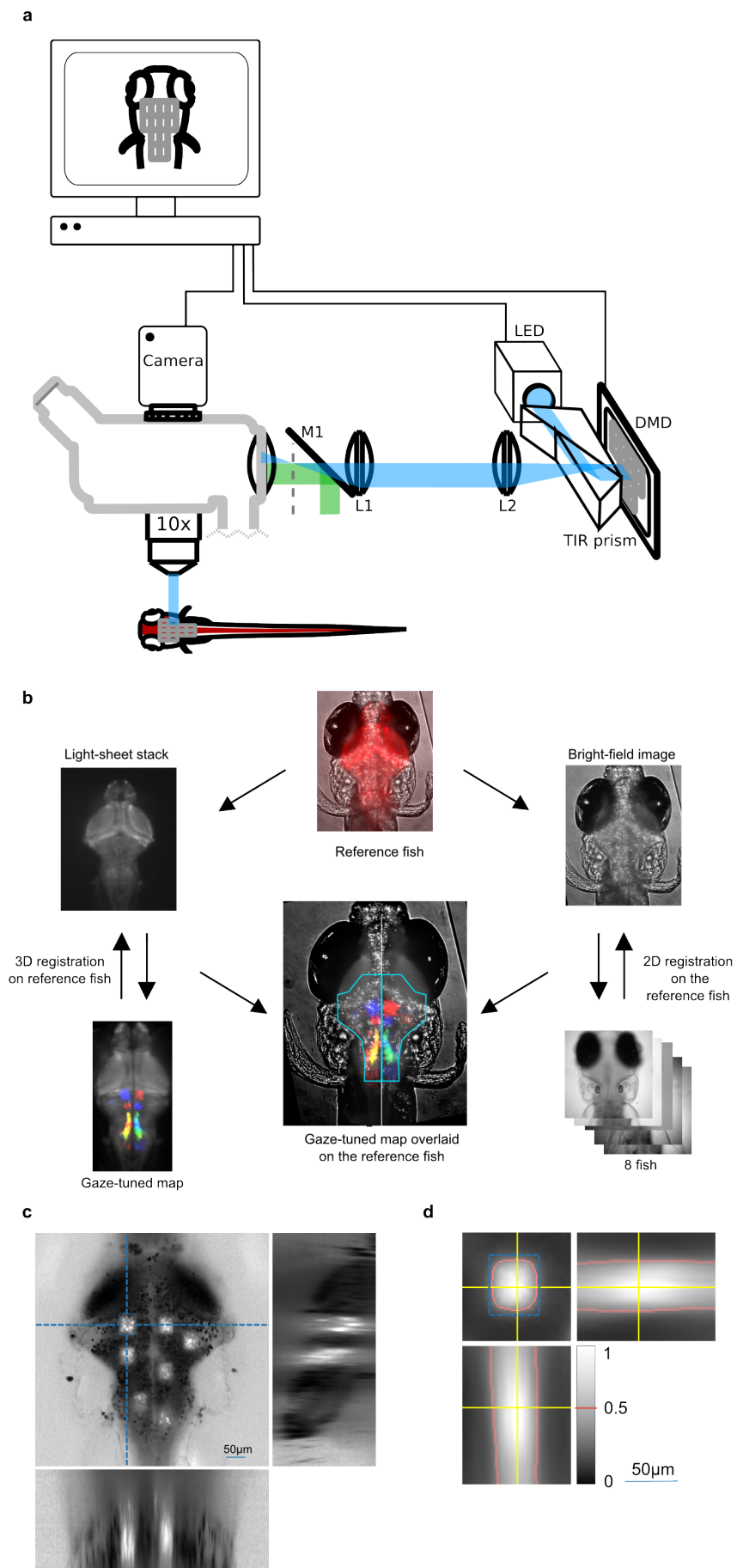
Supplementary Figure 4 | Delineating the self-oscillatory circuit in eyes-fixed experiments.



1167 **Supplementary Figure 4 | Delineating the self-oscillatory circuit in eyes-fixed experiments.**
1168 **a**, Pre-selected volume encompassing the gaze-tuned rostral hindbrain circuit. The rostral border
1169 of the 100x60x27 μ m volume is positioned 28 μ m from the hindbrain constriction axis. **b**, Pearson
1170 correlation matrix (top) and correlation histogram (bottom) of the neuron pairs within the pre-
1171 selected volume. **c**, Neurons engaged in the 10 most highly anti-correlated pairs. **d**, Reference
1172 signals are computed as the the mean $\Delta F/F$ of the left and right previously selected neurons, and
1173 then used as regressors to map the self-oscillatory network across the entire volume. **e**, Z-
1174 projection of the resulting self-oscillatory hindbrain network (N=8 fish). Color encodes tuning (Z-
1175 score) to the left (red) and right (blue) reference signals.

1176

1177



1180 **Supplementary Figure 5 | Optogenetic assay. a**, Schematic layout of the optogenetic
1181 experiment. A checkerboard pattern is drawn over the brain image and the rectangles are
1182 sequentially displayed on a digital mirror device (DMD). The pattern on the DMD is imaged *via*
1183 the lenses L1 ($f=40$ mm) and L2 ($f=80$ mm) onto a confocal plane (dashed line) of the
1184 epifluorescent light path and ultimately onto the targeted region of the fish brain. A total internal
1185 reflection prism (TIR) is used to illuminate the DMD with the stimulation light source (LED).
1186 The beam splitting mirror M1 (30% reflection, 70% transmission) allows one to simultaneously
1187 use a halogen light source for epifluorescence illumination and simultaneous eyes monitoring.
1188 Camera recording and optogenetic activation are synchronized by the computer. **b**, Schematic
1189 description of the morphological registration method used to merge different optogenetic
1190 experiments and to overlay the activated regions onto the gaze-tuned functional map. **c**, Sections
1191 of one photoconverted volume using a Tg(HuC:gal4; UAS:Kaede) larva. Pixel intensity represents
1192 the red/green fluorescence ratio. The larva was exposed to UV illumination using the same
1193 illumination pattern as in the optogenetic assay, but for 7 regions only. **d**, Sections of the average
1194 illumination volume, obtained by registering 5 larvae, *i.e.* 35 volumes in total. The pixel intensity
1195 denotes the red/green fluorescence ratio normalized between 0 (outside the volume) and 1 (at the
1196 center). The isovalue line corresponding to 0.5 is shown in red. In c and d, the dotted blue
1197 rectangle indicates the targeted area.

1198

1199

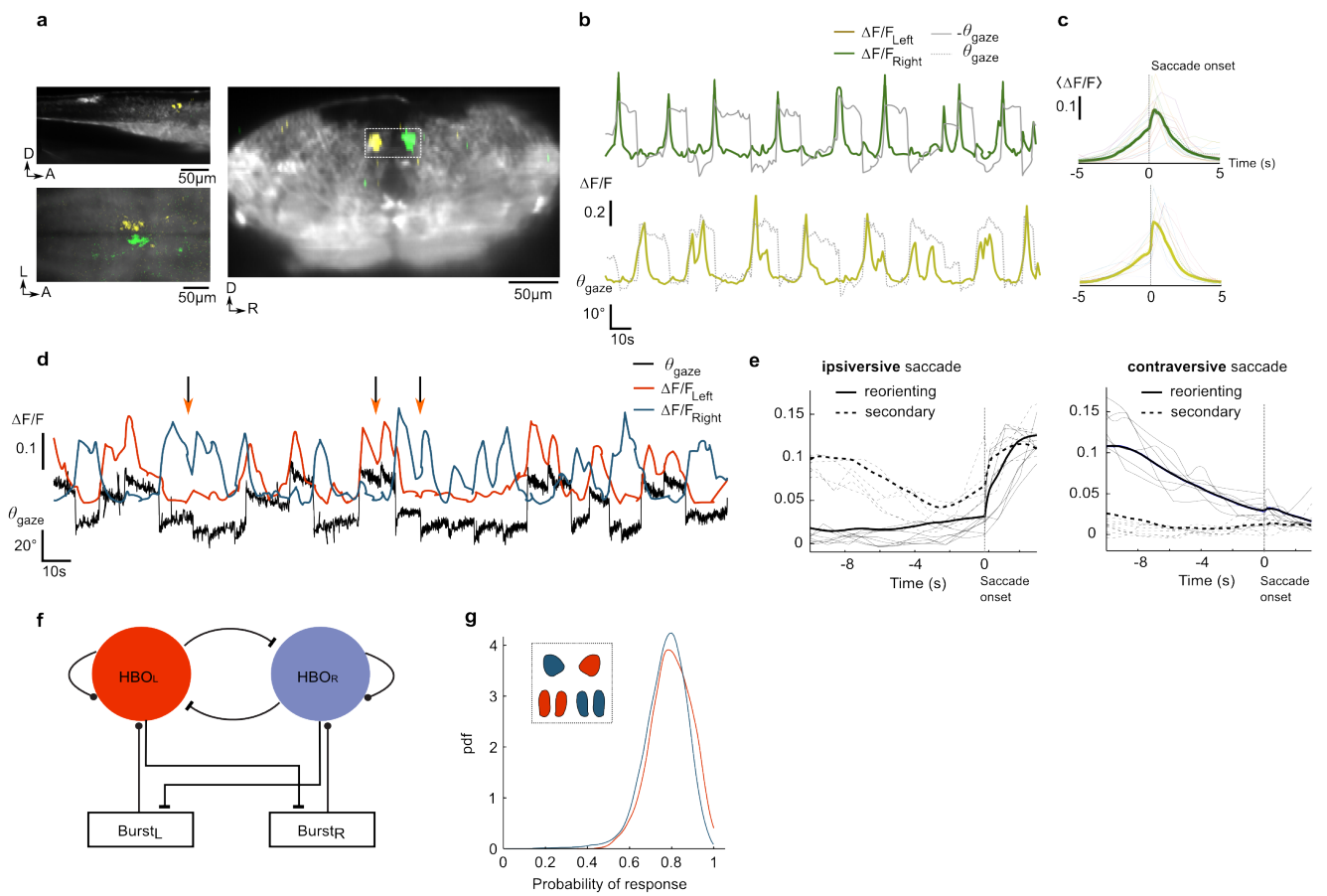
1200

1201

1202

Supplementary Figure 6 | Long-lead burst neurons, HBO activity during secondary saccades and putative circuit architecture.

1203



1204

1205

1206 **Supplementary Figure 6 | Long-lead burst neurons, HBO activity during secondary**
1207 **saccades and putative circuit architecture. a,** Sections of the velocity-tuned map (averaged
1208 over seven fish) showing the long-lead burst neurons located in two well-defined clusters in the
1209 dorsal region of rh 7. **b,** Example traces of these two clusters and associated gaze signals. **c,** Mean
1210 peri-saccadic signals. A systematic increase of activity is observed ~2-3 s before the ipsiversive
1211 saccade onset. **d-e,** Secondary saccades. **d,** Example traces of the left- and right-HBO activity and
1212 the gaze signal. When two successive saccades occur in the same direction (arrows), the active
1213 circuit displays a transient rebound. **e,** Mean peri-saccade signals of the HBO subnetworks for
1214 reorienting saccades (solid line) and secondary saccades (dashed line). The data are shown
1215 separately for ipsiversive (left) and contraversive (right) saccades. **f,** Scheme of a putative network
1216 architecture accounting for the HBO self-oscillatory dynamics and its interaction with the saccade
1217 generator circuit (burst cells). Each HBO subcircuit send inhibitory projections to the contralateral
1218 burst cells. It receives afferent excitatory inputs from ipsilateral burst neurons. **g,** Robustness of
1219 the HBO gaze-tuned characteristics. For each voxel of the right (blue) and left (red) HBO, we
1220 computed the fraction of ipsiversive saccades for which a significant post-saccadic increase in
1221 $\Delta F/F$ (larger than one standard deviation) is observed. The plot shows the PDF of this quantity for
1222 all the HBO voxels.

1223

1224

1225

1226

1227

1228

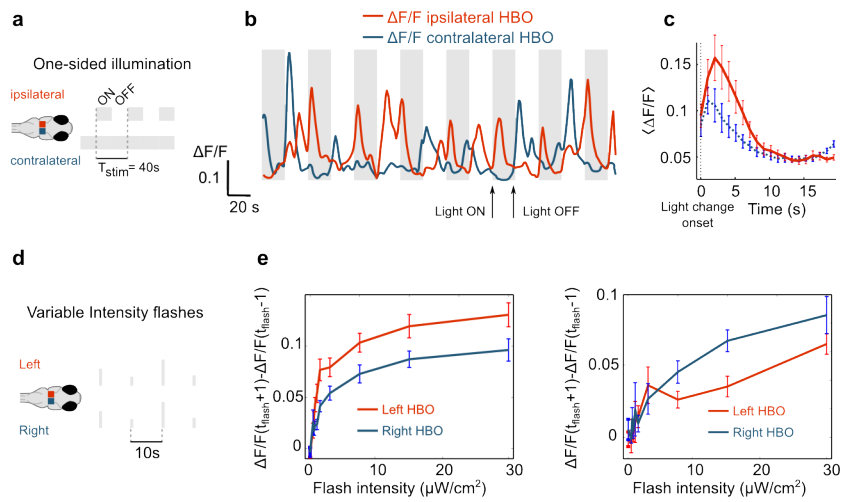
1229

1230

1231

1232

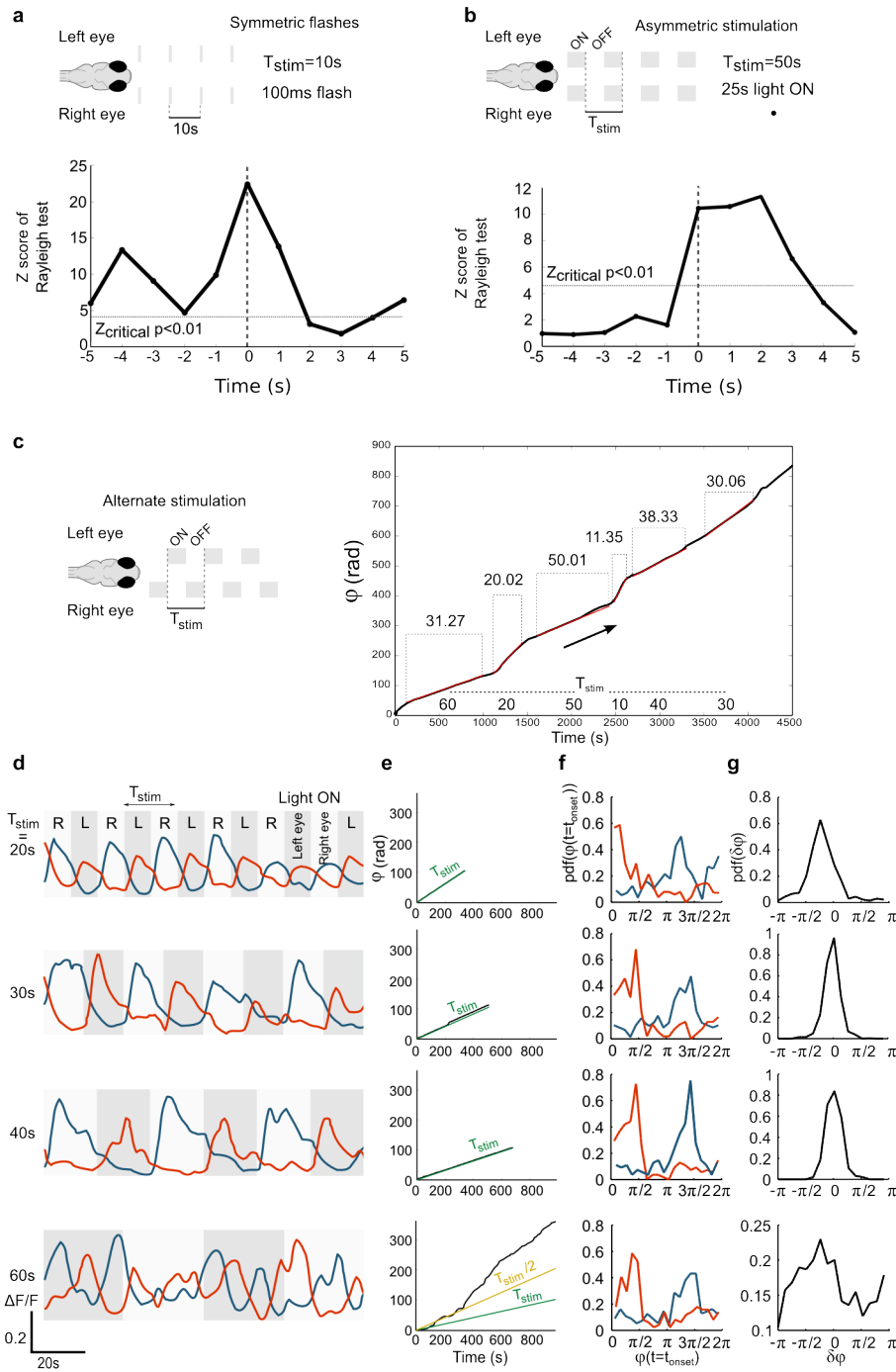
Supplementary Figure 7 | Visual stimulation on one eye and HBO intensity tuning curve.



1235 **Supplementary Figure 7 | Visual stimulation on one eye and intensity tuning curve. a,**
1236 One- sided stimulation experimental scheme. The illumination is maintained constant on one eye
1237 while it alternates between dark and bright every 20 s on the other eye. **b,** Response of the HBO
1238 populations to unilateral visual stimulation. The red (resp. blue) curve correspond to the ipsilateral
1239 (resp. contralateral) HBO with respect the eye exposed to the alternating stimuli. Greyed regions
1240 indicate the unilateral stimulation sequence. **c,** Red curve: trial-averaged response of the ipsilateral
1241 HBO to light-ON transitions. Blue curve: trial-averaged response of the contralateral HBO to
1242 light-OFF transitions. Data are averaged over N=8 fish. These response curves suggest that the
1243 HBO receive both ipsilateral projections from the ON visual pathway and contralateral projections
1244 from the OFF visual pathway. **d,** The fish is submitted to a series of 350 flashes of varying
1245 intensities with a 10 s inter-flash period. **e,** Mean intensity response defined as $\langle \Delta F/F(t =$
1246 $t_{flash} + 1) - \Delta F/F(t = t_{flash} - 1) \rangle$ as a function of the flash intensity. The tuning curve is
1247 computed for each subcircuit and is shown for two fish.

1248

Supplementary Figure 8 | Phase-locking and frequency entrainment of the HBO by periodic visual stimuli.



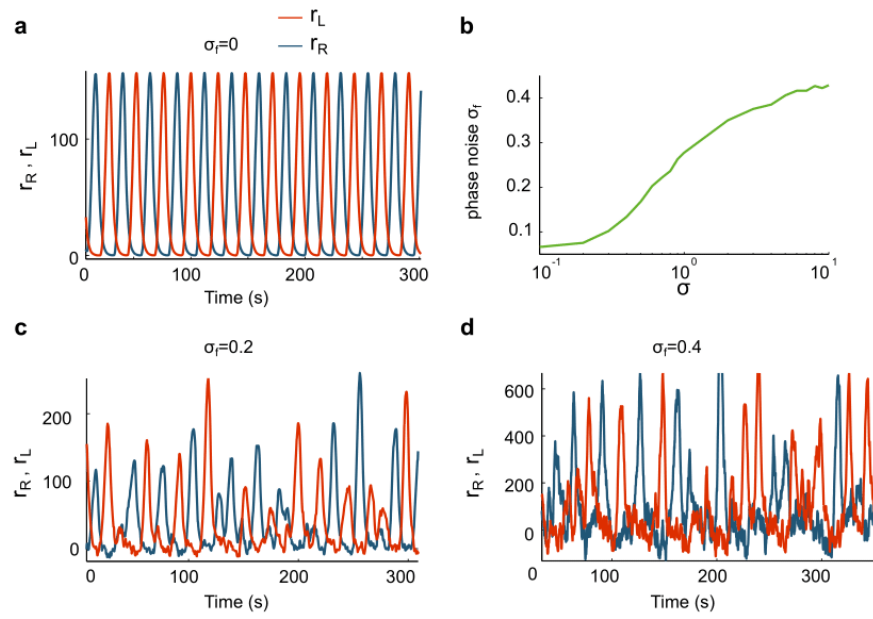
1252 **Supplementary Figure 8 | Phase-locking and frequency entrainment of the HBO by visual**
1253 **stimuli. a,** Bilateral 100 ms-flash are delivered every 10 s. The curve shows the Z-score,
1254 computed from Rayleigh statistics, of the oscillatory phase distribution at each time point in a 10 s
1255 window centered on the stimulus (n=500 flashes, N=12 fish). The dashed line shows the critical Z-
1256 score ($p < 0.01$) indicating threshold for significant phase concentration. This data indicates a
1257 strong visually induced phase concentration of the HBO oscillation. **b,** Same curve as (a) for
1258 bilateral light-ON/light-OFF stimulation (n=146 flashes, N=5 fish). Illumination onset induces a
1259 transient phase concentration. **c,** Evolution of the HBO phase signal during one run, upon
1260 antisymmetric alternated stimulation at different frequencies. Changes in the stimulation period
1261 (indicated above the x-axis) induce a change in the oscillatory dynamics (mean oscillatory periods
1262 are indicated above the curve), revealing frequency entrainment. **d,** Example signals of the two
1263 subpopulations for 4 stimulation frequencies. **e,** Evolution of the HBO phase (black curve). The
1264 phase of the stimulation $2\pi t/T_{stim}$ is shown in green. **f,** PDF of the HBO phase at light-ON (red)
1265 and light-OFF (blue) transitions. **g,** PDF of the HBO/stimulation phase-offset.
1266

1267

Supplementary Figure 9 | Effect of the current noise on the self-oscillatory signal in the

1268

neural model.



1269

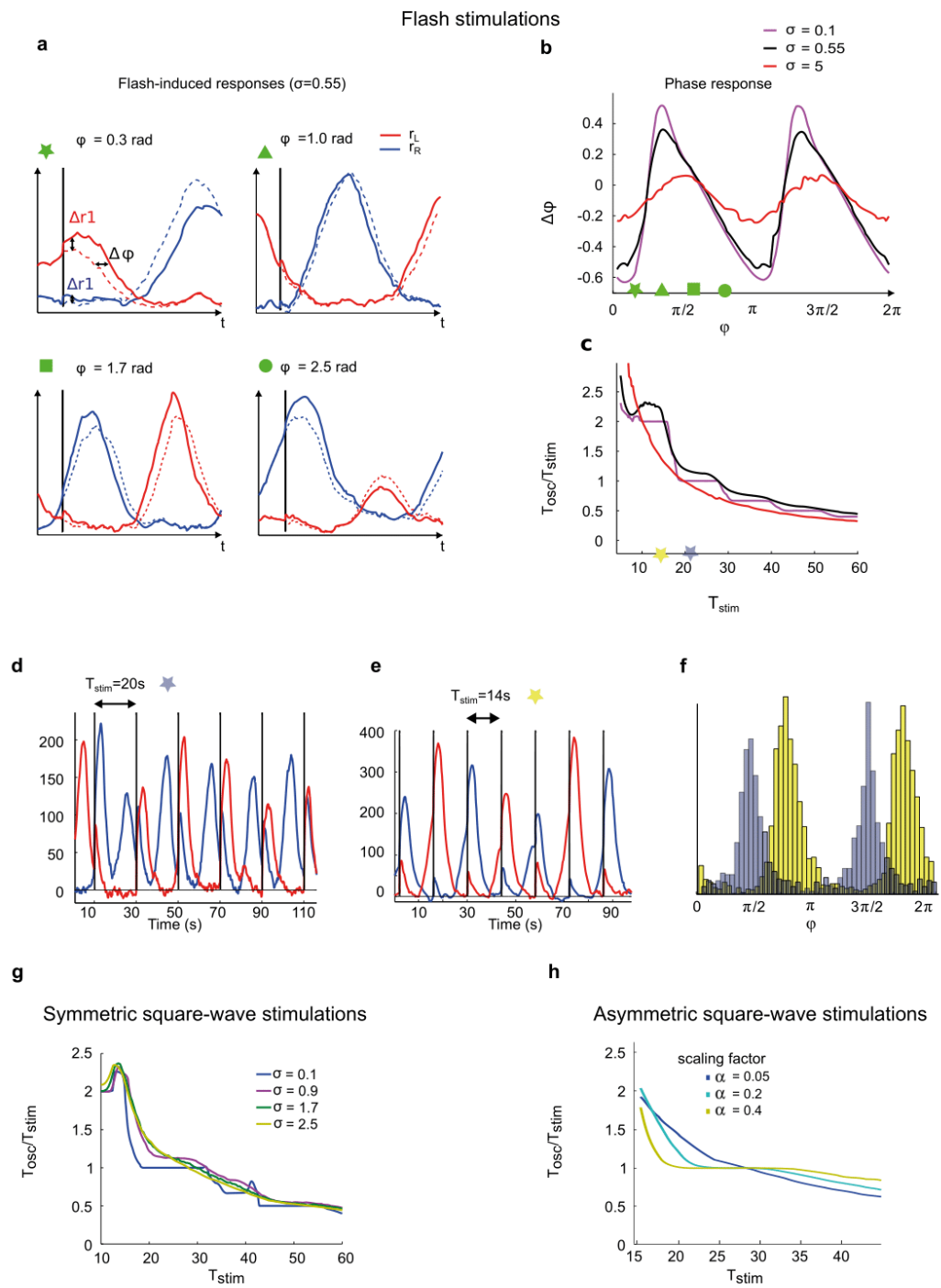
1270 **Supplementary Figure 9 | Effect of the current noise on the self-oscillatory signal in the**
1271 **neural model. a**, Activity of the left and right simulated networks in the absence of current noise
1272 ($\sigma = 0$). **b**, Phase noise σ_f as a function of the current noise σ . The phase noise is defined as the
1273 standard deviation of the distribution of phase increments measured over a 1 s interval. **c-d**, Self-
1274 oscillatory signals for a phase noise $\sigma_f = 0.2$ and 0.4 , *i.e.* for $\sigma_f = 0.55$ and 5 , respectively.

1275

Supplementary Figure 10 | Phase dependent responses and phase-locking in the network

1276

model.



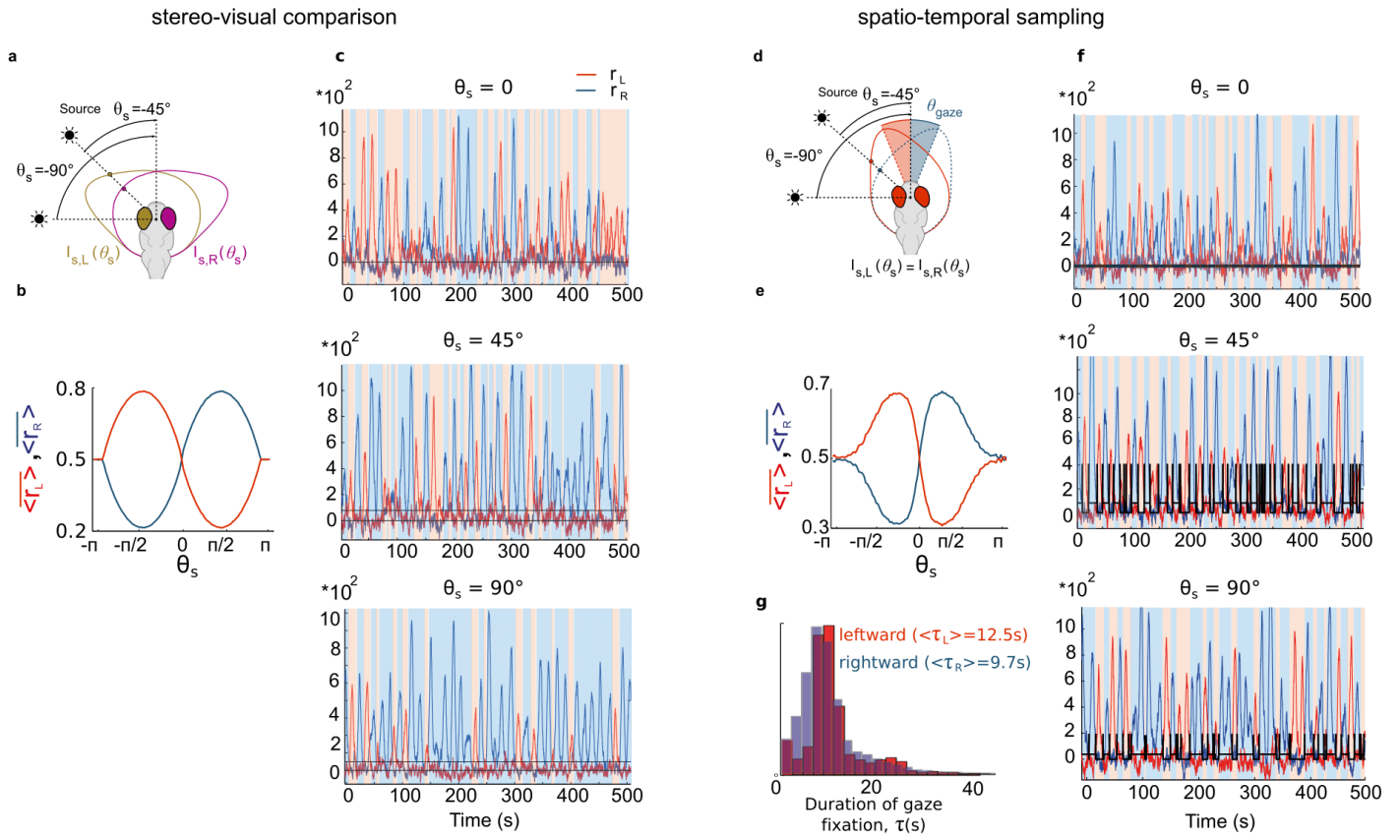
1277

1278

1279 **Supplementary Figure 10 | Phase-dependent visual responses and phase-locking in the**
1280 **network model. a**, Example HBO responses to flashes delivered at 4 different oscillatory phases
1281 (neuronal model). The dotted curve shows the HBO trace when no flash is delivered. **b**, Phase
1282 response curves (PRC) for different noise levels. The green symbols indicate the phases at flash
1283 delivery in (a). **c**, Ratio of the oscillatory and stimulation periods, as a function of the stimulation
1284 period, for different noise values. The “Devil’s Staircase” shape of the curve is a signature of the
1285 HBO synchronization at integer multiples or rational fractions of the stimulus period. **d-e**,
1286 Oscillatory HBO signals upon periodic flash stimulation for (d) $T_{stim} = 20$ s and (e) $T_{stim} = 14$ s. In
1287 the first case, the stimulus period is slightly below the endogenous period ($T_{endo} = 25$ s) and the
1288 HBO is entrained at the stimulus frequency. In the second case, T_{stim} is slightly larger than $T_{endo}/2$
1289 and the HBO oscillates at half the stimulus frequency (see corresponding symbols in (c)). **f**, Phase
1290 histograms at flash times for these two configurations. When $T_{stim}=20$ s (grey), the two peaks
1291 correspond to negative values in the phase-response curve ($\Delta\varphi>0$), indicating that the stimuli
1292 constantly speed up the HBO oscillation, allowing the one-to-one synchronization process to
1293 occur. When $T_{stim}=14$ s, the phase distribution at flash-times is peaked at phase values such that
1294 $\Delta\varphi<0$ (panel e, yellow histogram). The stimuli slow down the HBO oscillation, leading to the
1295 period-doubling synchronization. **g**, Entrainment curve for symmetric square-wave stimulation at
1296 different noise values. Compared to the flash stimuli, the addition of a continuous component
1297 during one-half of the cycle extends the entrainment plateau for which $T_{osc}\sim T_{stim}$. **h**, Entrainment
1298 curve for asymmetric periodic stimulation. The different curves are obtained for different
1299 intensities of the stimulus, $A_t=\alpha *400A$ and $A_c=\alpha *100A$ (Supplementary Methods). In the
1300 symmetric case, $\alpha = 1$.

1301

Supplementary Figure 11 | Phototactic behaviours in the rate model.



1305 **Supplementary Figure 11 | Phototactic behaviours in the rate model. a**, Stereo-visual
1306 comparison (see Figure 6). **b**, Normalized firing rates of the left and right HBO circuits
1307 ($\langle \overline{r_{L/R}} \rangle = \frac{\langle r_{L/R} \rangle}{\langle r_L \rangle + \langle r_R \rangle}$) as a function of the light source azimuth θ_s . The HBO mean activity is
1308 biased ipsilaterally to the light source. **c**, Example traces of the simulated left and right HBO
1309 activity for three light-source azimuthal angles. The orange (blue) shaded areas delineate the
1310 periods during which $r_L > r_R$ ($r_R > r_L$). The black curves indicate the constant currents delivered to the
1311 two subpopulations. **d**, Spatio-temporal sampling (see Figure 6). **e-f**, Same as a-b. Each left-to-
1312 right or right-to-left transition induces a change in the current delivered symmetrically to the two
1313 subpopulations (black line in (f)). **g**, Histogram of time durations during which $r_L > r_R$ ($r_R > r_L$)
1314 corresponding to leftward (rightward) gaze-fixation periods for a source located 45° to the left.
1315 When the gaze is oriented towards the light source, the mean fixation period is increased.
1316

1317 **Movies:**

1318

1319 **Movie 1 : Eye/tail coordination.**

1320 Sequence of spontaneous ocular saccades and swim-bouts in a partially restrained larva,
1321 showing eye/tail coordination. The blue and red curves show the tail deflection signal and the gaze
1322 angle, respectively. The animal is submitted to whole-field illumination.

1323

1324 **Movie 2 : Brain-scale peri-saccadic neural activity.**

1325 Images were obtained using one-photon light-sheet imaging (1h recording, 20 brain sections,
1326 one stack per second) with simultaneous monitoring of the eyes (bottom-left panel). Color encodes
1327 fluorescence transients of individual voxels: blue for rightward saccades, red for leftward
1328 saccades. The sequence was obtained by averaging over multiple saccades.

1329

1330 **Movie 3 : 3D functional maps of gaze-tuned neurons.**

1331 These maps were computed through regression between the gaze angle traces and individual
1332 voxel fluorescence activity. Colors encode the level of tuning (Z-score) to gaze position (left) and
1333 velocity (right). Seven fish were registered to produce these functional 3D maps.

1334

1335 **Movie 4 : Comparison of gaze-tuned, self-oscillatory, and visual response 3D maps.**

1336 Each 3D map was obtained through regression-based functional identification followed by 3D
1337 registration on a reference brain, as described in Supplementary Methods. From left to right :
1338 gaze-tuned populations, self-oscillatory hindbrain population, visually responsive neurons. This
1339 video shows that the HBO is engaged in all three processes.

1340

1341

1342

Chapter 4
Discussion on the neural basis of
saccadic eye movements
Followed by a discussion on
central pattern generator

4.1 Introduction

In Wolf *et al.* (2017), we mapped the hindbrain oculomotor circuit in zebrafish larva by identifying all neurons whose dynamics were correlated with the angular position of the larva's eyes (Figure 2 in Wolf *et al.*). In chapter 3 and in Wolf *et al.*, we showed that a sub region of this circuit – the so-called the hindbrain oscillator (HBO) - behaved like a central pattern generator (CPG). The HBO drives a rhythmic motor pattern (spontaneous saccades) and it can operate even in the absence of sensory and proprioceptive inputs. Dunn *et al.* (2016) had previously established that the HBO also drives the temporal pattern of zebrafish re-orientation. Finally we showed that the HBO is sensitive to visual stimulation in a state dependent manner, such that it should play a key role in phototaxis.

In the present chapter, I extend the discussion of the oculomotor circuit beyond what was presented in the paper. The chapter is divided in two main parts (4.1 to 4.3 and 4.4).

In the first part, I will focus on the (rest) of the oculomotor circuit, and I will present some of the new insights the eye-free whole brain recordings can bring to our understanding of the oculomotor system in the vertebrate brain. In vertebrates, visual exploration is characterized by an alternation of saccades and fixations. Saccades are rapid coherent eyes reorientation that redirect the gaze and thus change the field of vision in less than 100ms (Büttner and Büttner-Ennever 1988 ; Becker 1989). Saccades can target an object, a sound or even a memory (Scudder *et al.* 2002) but can also occur spontaneously without any obvious target. The muscle and neural mechanism responsible for saccade initiation and eye fixation have been widely studied in mammals during the last decades, particularly in non-human primates (Robinson 1972; Fuchs *et al.* 1985; Scudder 1988; Scudder *et al.* 2002; Sparks 2002; Kaneko 2006). Anatomical and electrophysiological studies offered a detailed description of the connectivity of the brainstem structure. Later, cell recordings and then theoretical models (Seung 1996; Dayan 1998; Seung *et al.* 2000; Dayan and Albright 2001; Goldman 2009) helped understanding of the oculomotor system dynamics.

Despite the numerous studies on mammals oculomotor system, a complete understanding of its functioning principle is still lacking, in large part due to the difficulty to simultaneously record the entire network dynamics. In all vertebrates, the pathways generating eye movements converge in a shared set of oculomotor neurons. Hence, the burst generator (Schoonheim *et al.* 2010) responsible for saccadic movements and the neural integrator responsible for eye fixation (Aksay *et al.* 2000, 2001, 2003, 2007; Koulakov *et al.* 2002; Miri *et al.* 2011) have found homologous regions in zebrafish larval brain. However, little is known in fish about the hindbrain circuitry for saccades generation and numerous elements of the brainstem oculomotor regions (OPN, LLBN, SLBN) still lack their homologues in zebrafish. To gain insight into this issue, we used light sheet fluorescence microscopy and recorded whole brain activity of zebrafish larva's brain with eyes free. We believe we may have found regions a homologous to OPN and LLBN neurons. Moreover, to our best knowledge it is the first study giving access to the entire "brainstem" oculomotor neural network. These extensive recordings may help testing the many existing models on persistent neural activity.

Here I will review the current knowledge on the brainstem burst generator in mammals, then I will present what has been done experimentally and theoretically on the neural integrator responsible for eye fixation. I will then focus on zebrafish and after briefly presenting the few works done on this animal I will show that with our eye free whole brain recordings, we have access to the dynamic of new neuronal ensembles in the zebrafish oculomotor circuit homologous to the mammalian system.

In the second part of the chapter, I will discuss some possible improvements that could be made to the HBO model reported in Wolf *et al.* (2017). As mentioned before, HBO presents striking similarities with central pattern generators. These networks are known to participate in almost all rhythmic motor pattern control. Numerous models have been proposed to account for their periodicity and to their ability to respond in a phase-dependent manner to external stimulus. After reviewing some of the major works of CPG's experts such as Marder's or Calabrese's team, I will discuss why the HBO may offer new opportunities to address some of the questions posed by the CPG's.

Note that this chapter is mostly a discussion chapter. Most of the results that are presented are still preliminary and will required confirmation.

4.2 Brainstem/Hindbrain

In this section of the chapter, I will focus on the brainstem circuit that generates saccades in mammals. Most of the properties described are shared among all vertebrates.

4.2.1 Motor command

Eye movements can be divided in three components: a “saccade” which is a rapid change in the eye position, a “step” that keeps the eyes in a fixed position and a “slide” between the step and the saccade where the position gradually changes (Fuchs *et al.* 1985; Scudder *et al.* 2002). The eyes can rotate horizontally, vertically or produce a torsion (we will see that this third mode of rotation is actually set by the vertical and horizontal rotation through the Listing’s law). Three pairs of muscle control the position of each eye and in turn six sets of oculomotor neurons control these muscles. They all exhibit pulse, step or slide type of discharge. The so-called medial and lateral rectus muscles produce the horizontal rotation. The contractions of the superior/inferior rectus muscle and the superior/inferior oblique muscle produce vertical and torsional rotation (Figure 4.1).

The oculomotor neurons that control these muscles are located in the oculomotor nucleus III, in the trochlear IV and in the abducens nucleus VI. The duration of a saccade is equal to the duration of the burst of spikes in these motor neurons. The saccade amplitude is proportional to the burst amplitude (discharge frequency) of the neurons. The oculomotor neurons can either produce a burst of spikes (“pulse”), discharge at a constant rate during steps or be silent. In the abducens nucleus, a specific population of neurons is recruited for a given range of saccade amplitude.

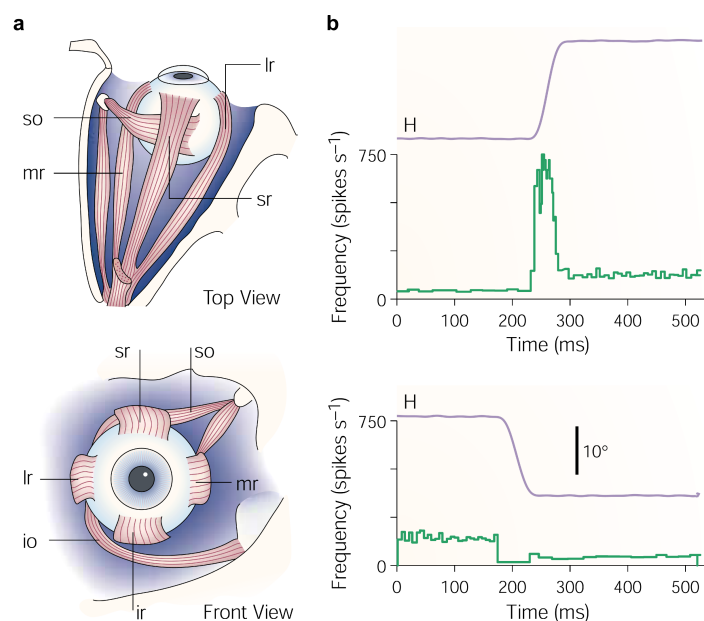


Figure 4.1: **a**, Drawings of the extraocular muscles showing top and front views

of the right eye. The horizontal components of eye rotations are generated by the medial rectus (mr) and lateral rectus (lr) muscles. Vertical and torsional movements are accomplished by the activation of combinations of the superior/inferior rectus (sr/ir) and superior/inferior oblique (so/io) pairs. **b**, The top panel shows horizontal eye position (H; up = right) and a plot of instantaneous spike frequency of an abducens motor neuron during a rightward saccade. The bottom panel shows the activity of the same cell during and after a leftward saccade. Taken from Sparks 2002.

4.2.2 Premotor command in the brainstem

The commands activating motor neurons originate from the brainstem regions: the pons and medulla for horizontal rotation and the rostral midbrain for vertical movements (Sparks 2002; Scudder *et al.* 2002). In the following we focus on the horizontal movements (the one we studied on zebrafish larva). The horizontal saccades are produced by premotor neurons located in three sub-regions of the pons and medulla: the paramedian pontine reticular formation (PPRF), a large region rostral to the abducens nucleus (Cohen *et al.* 1968; cit. Fuchs *et al.* 1985), the medullary reticular formation (med. RF) ventral to the abducens, the nucleus prepositus hypoglossi (NPH) and the medial vestibular nuclei (MVN) (Becker 1989; Scudder *et al.* 2002). Electrophysiology recording in eye free primates revealed that four main types of saccadic neurons can be found in these regions: 1) excitatory or inhibitory burst neurons (EBN or IBN) which fire just before (10ms) and during the saccade, sometimes called short-lead burst neurons (SLBN), 2) pause neurons which continuously discharge but display brief pauses during and just before the saccadic movements, 3) long lead burst neuron (LLBN) whose activity increases more than 100ms before the saccade onset, 4) step neurons which discharge constantly for a given position of the eyes, and are referred to as neural integrators (NI).

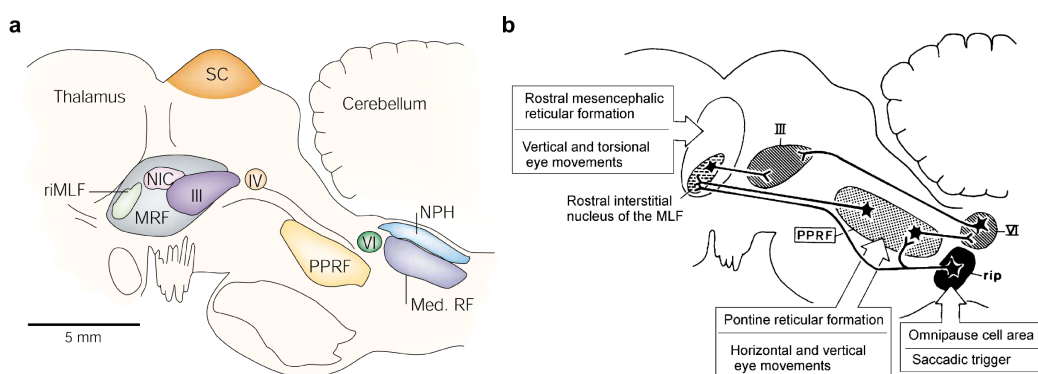


Figure 4.2: **a**, Drawing of the brainstem of a monkey, showing the locations of areas. III, oculomotor nucleus; IV, trochlear nucleus; VI, abducens nucleus; Med. RF, medullary reticular formation; MRF, midbrain reticular formation; NIC, interstitial nucleus of Cajal; NPH, nucleus prepositus hypoglossi; PPRF, paramedian pontine reticular formation; riMLF, rostral interstitial nucleus of the medial longitudinal fasciculus; SC, superior colliculus. Adapted from cit. Sparks 2002 and Becker 1989. **b**, Summary diagram of major pathways involved in

horizontal and vertical saccade generation. The abbreviations are the same in a. RIP Raphe interpositus. Taken from Büttner and Büttner-Ennever 1988.

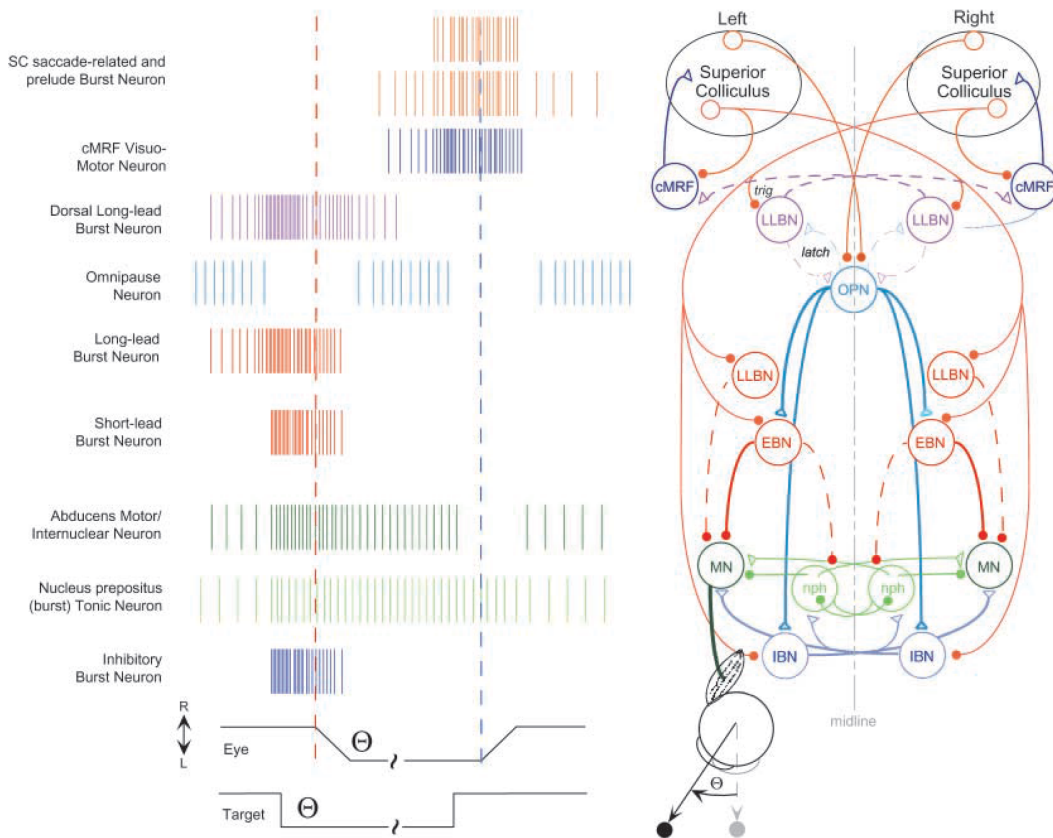


Figure 4.3: Schematic discharge patterns and anatomical connections of neurons of the brainstem burst generator for horizontal saccades (after Fuchs *et al.* 1985). Left: Firing patterns for a leftward (first vertical dashed line) and rightward (second dashed line) horizontal saccade of size Θ to a target step of the same size (depicted in the cartoon to the right). Right: Excitatory (filled circles) and inhibitory (open triangles) connections. The confidence in the connection is indicated by line thickness ranging from heavy solid (confirmed) to thin dashed (hypothesized). (cMRF central mesencephalic reticular formation, EBN excitatory burst neuron, IBN inhibitory burst neuron, latch reciprocal inhibitory circuit to prevent OPN discharge during saccades, LLBN long lead burst neuron, MN motoneuron, nph nucleus prepositus hypoglossi that provides eye position step, OPN omnipause neuron, trig trigger LLBN that converts excitatory trigger signal to inhibit OPNs). Taken from Scudder *et al.* 2002.

The burst neurons

1) The *excitatory burst neurons* (EBN), located in the PPRF, have an activity tightly coupled to saccade onset: they are generally silent, but generate a high frequency burst of spikes just before (10-12ms) and during an ipsiversive saccade. These neurons have monosynaptic excitatory connections with the oculomotor neurons located in the ipsilateral abducens (VI) (Strassman *et al.* 1986). The amplitude, duration and velocity of saccades are set by the number of spikes, the duration of the burst and frequency of the spikes of EBNs,

respectively.

The *inhibitory burst neurons* (IBN), located in the med. RF also generate a high frequency burst of spikes just before (10-12ms) and during an ipsiversive saccade. They send monosynaptic inhibitory connections to the contralateral abducens and the contralateral IBNs.

Note that for vertical rotations, EBNs and IBNs are located in the rostral midbrain, precisely in the rostral interstitial nucleus of the medial longitudinal fasciculus (riMLF) and in the interstitial nucleus of Cajal. They have the same properties as in the horizontal case.

The Pause neurons

2) Pause neurons discharge continuously in the absence of saccades and cease to discharge just before and during a saccade. A sub-class of pause neurons is constituted by the *omnidirectional pause neurons* or *omnipause neurons* (OPN) which discharge at a constant rate of 100 spikes per second when the eyes are fixed in a position and become transiently silent during saccades in all directions. Note that the pause begins before the saccade onset and terminates before the end of the saccade (Fuchs *et al.* 1985). Büttner and Büttner-Ennever (1988) showed that OPNs are located within the special midline structure called nucleus raphe interpositus (Figure 4.2b). OPNs have inhibitory projection to EBN and IBN and are in turn inhibited during a saccade. The inhibitory pathway leading to a suppression of OPN discharge remains controversial. It has been proposed that, since IBN do not project directly onto OPNs (Strassman *et al.* 1986) and OPNs have a decrease of activity before the saccade, OPNs must be inhibited by another set of neurons activated before the saccade onset (maybe LLBN, see below).

The long lead burst neurons

3) The *long lead burst neurons* (LLBN) have an increase in discharge rate that starts 20ms to over 100ms prior to the saccade onset. This prelude burst of activity generally ends in a saccade movement. Known since the earliest description of the brainstem saccadic system, LLBNs constitute a heterogeneous group of neurons overlapping EBN and IBN. They are also present in the rostral part of the PPRF (Scudder *et al.* 1996; Kaneko 2006).

The few works on LLBN tend to distinguish three neuronal classes:

(i) the excitatory and inhibitory LLBN (*eLLBN* and *iLLBN*) have an activity that resembles that of EBN and IBN. One sub-group is excitatory, mainly located nearby the abducens, and the other is inhibitory. They discharge during ipsilateral saccades and, as for the EBNs, the amplitude, duration and velocity of saccades correlate with the number of spikes, the duration of the burst and spiking frequency of the spikes of the neurons, respectively (Figure 4.4a and b and Kaneko 2006).

(ii) the LLBNs located in the nucleus reticularis tegmenti pontis (*nrtpt LLBN*) are directionally tuned for a given set of directions. They have a maximum discharge rate associated with specific direction of eyes movements. The burst characteristics are not correlated with the saccade amplitude, duration or velocity

(Figure 4.4c).

(iii) the *dorsal LLBN* are located dorsally to the nntp LLBN and rostrally to the eLLBN. They discharge for all ipsilateral saccades. Their burst intensity is tuned for small amplitudes and their activity is prolonged after the end of the saccade (Figure 4.4d).

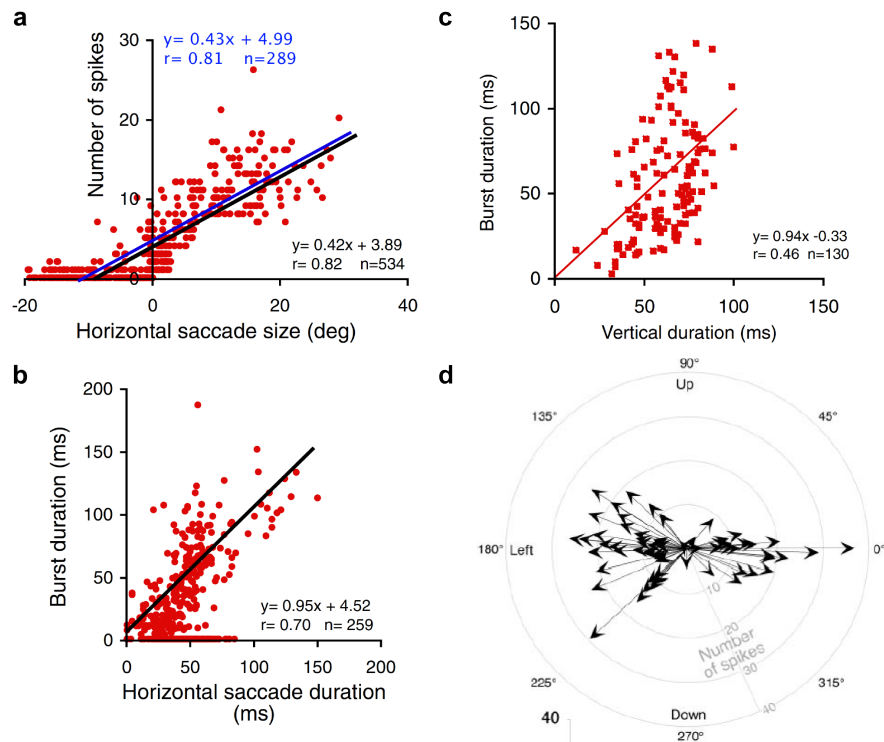


Figure 4.4: Long lead burst neurons. **a**, For eLLBN, number of spikes for each saccade of the indicated horizontal component amplitude for all saccades elicited while recording this neuron. The line is the least-squares linear regression (inset). The blue line is linear regression. Regression metrics in blue. **b**, For eLLBN, burst duration for each saccade of the indicated saccade duration. **c**, For nntp LLBN, burst duration for each saccade of the indicated saccade duration. **d**, For dLLBN, number of spikes in function of the angular size of the saccade. Adapted from Kaneko 2006.

The functional role of LLBN is still unknown but three main roles have been hypothesized in the literature, as detailed below: a relay from the cortex and superior colliculus to the saccadic circuit, a trigger function to suppress OPN discharge and a precerebellar function.

A relay

Still in debate, the question of the relay-role of LLBN seems to be confirmed by Kaneko (Kaneko 2006). Indeed, eLLBN and nntp LLBN receive inputs from the superior colliculus. They also have a lot of projections to the PPRF. Scudder *et al.* (1996 and 2002) proposed that these nntp LLBN could constitute the displacement integrator necessary to correct and hold the eyes in the right position (see Neural integrator section).

A trigger

Several studies suggest that LLBNs could trigger the suppression of OPN's

activity during saccadic events. In Kamogawa *et al.* (1996) the authors showed that stimulation in LLBN region inhibits OPNs in cats: “*The most effective region for producing inhibition of pause neurons corresponded to the area where long lead burst neurons were predominantly located*”. Kaneko *et al.* confirmed this hypothesis showing that dorsal LLBN can cease OPN discharge for small saccades. However this trigger/latch function of LLBN still needs confirmation since the early decrease in OPNs activity before a saccade is not gradual as is the ramping activity of LLBN.

A cerebellum relay

Scudder *et al.* (1996) and Kaneko (2006) showed that nrtp LLBNs relay activity from the superior colliculus to the cerebellum. Neurons in nrtp have been found to project mainly in the cerebellum (Hepp and Henn 1983; Kaneko 2006)

The oculomotor integrator

4) To keep the eyes position fixed between successive saccades, a subset of neurons located in the nucleus prepositus hypoglossi (NPH) and the medial vestibular nucleus (MVN) display a tonic discharge proportional to horizontal or vertical eye position. These neurons provide an excitation required for the step oculomotor neuron activity. Robinson suggested the existence of these “step” neurons in 1975 (Robinson 1975), claiming that a step signal proportional to the eyes position could be produced by “integration”, in the mathematical sense, of the EBN activity (Robinson 1989). This subset of neurons is thus called the *oculomotor integrator* or the *velocity to position neural integrator* (VPNI). More details on these neurons are provided in the section 4.3 of this chapter.

4.2.3 Other regions involved in the saccade-command signal

Superior Colliculus

Saccades can either bring the eyes to a well defined target or occur spontaneously. In the first case, saccades are mainly triggered by visual information coming from the frontal eye field (FEF) and passing by the superior colliculus (SC). The SC receives signals from many cortical areas and project to the premotor saccade generator circuit (Sparks *et al.* 1989). The SC is known to have seven interacting layers, the dorsal and medial layers being visual, auditory and somatosensory sensitive, the deeper layers being “motor” related (Büttner and Büttner-Ennever 1988). Stimulating the motor layers of the SC evokes a contralateral saccade whose amplitude and direction varies with the location of the electrode in the SC (Robinson 1972). Furthermore, many cells in the deep and intermediate layers of the SC generate a burst of activity just before (18-20ms) and during the saccade. One fascinating property of SC is that each saccade-related neuron discharges for a given saccade amplitude: “*the discharge is related to changes in eye position, not to movements to a particular position*”. In the SC, saccade-related neurons are topographically arranged given their discharge properties (preferred amplitude and direction). Studies on eyes and head-free animals recently showed that SC encodes the gaze, defined in the

laboratory referential. Thus SC sends combined command for eyes and head to produce a change of the vision field the animals toward a pre-defined target (Figure 4.5).

Encoding a target position

The inputs received by the burst generator from the SC encodes the target of the forthcoming saccade. As mentioned above, in the SC, the position of the target is topographically coded or “place” coded. The burst generator in turn encodes the kinetic of the eye movement during the saccade: the number of spikes and the burst duration give the amplitude, velocity and duration of an eye movement. The question is then: how is this place-coded position of the target converted in a temporal code in the saccade burst generator? Current studies suggest that the weighing of synaptic connection from the SC to the burst generator could allow for this transformation (Van Gisbergen *et al.* 1987): “*the total number of spikes coming from all cells in the SC multiplied by the synaptic weight of each cell could encode saccadic size*”. As we will see later, this idea is however not sufficient to explain the impressive ability of the oculomotor system to precisely aim at a target.

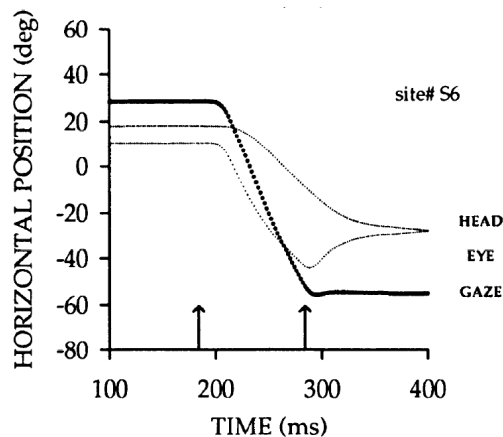


Figure 4.5: Stimulation induced movement evoked at a collicular site. Head, gaze and eye position as a function of time. Stimulation frequency, 500Hz; current=50 μ A. Left vertical arrow: stimulation onset; right vertical arrow: stimulation offset. Downward deflection indicates leftward movement. Taken from Freedman *et al.* 1996.

Cerebellum

The role of cerebellum inputs to the burst saccadic neurons of the brainstem is still unclear. The SC and the FEF projects to the nrtp area as we saw for the LLBN. The nrtp area constitutes a relay to the cerebellum. In Scudder and McGee (2003), the authors showed that cerebellum inputs must subserve a modulatory role in the PPRF. A small ensemble of neurons, the so-called fastigial oculomotor region, is able to increase the ongoing discharge of EBN or IBN (Robinson and Fuchs 2001) during a saccadic movement. Notice also that Purkinje cells appear to exhibit saccade-related bursts.

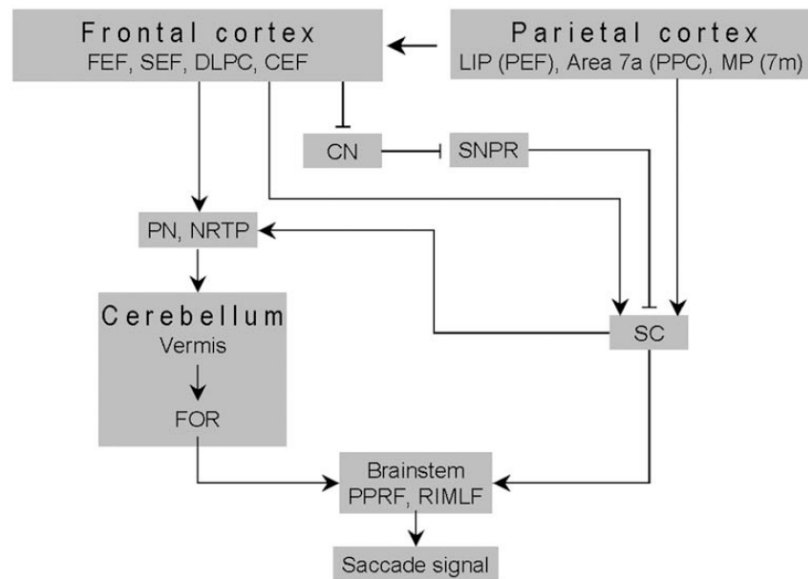


Figure 4.6: Some major structures for saccade control and their main connections to the brainstem. FEF frontal eye field, SEF supplementary eye field, CEF cingulate eye field, DLPC dorsolateral prefrontal cortex, PN pontine nuclei, NRTP nucleus reticularis tegmenti pontis, FOR fastigial oculomotor region, PPRF paramedian pontine reticular formation, RIMLF rostral interstitial nucleus of the MLF, SC superior colliculus, CN caudate nucleus, LIP lateral intraparietal area, PEF parietal eye field, PPC posterior parietal cortex, MP medial parietal area, SNR substantia nigra pars reticulata. The pathways from CN to SNR and from SNR to SC are inhibitory. Adapted from Büttner and Büttner-Ennever 2006.

The feedback control of eyes trajectory

Despite the considerable variability of saccades duration and velocity, eye movements are extremely accurate in aiming at a given target. To account for this accuracy, it has been proposed that saccades are under feedback control. Because the delays in the visual system are so large (100-200ms) that a saccade ends before any signal from the retina could reach the brainstem, the feedback control is unlikely to integrate visual cues. In 1975, Robinson proposed the first feedback control model (Robinson 1975):

“The brain constructs a neural representation of the target position in head coordinates by summing the retinal eccentricity of the target with eye position. This representation of target position is stored and compared with an efferent copy of eye position during the saccade. As long as the two disagree, there is a net excitation of the EBNs and IBNs, and the eye continues to be driven toward the target.”

Scudder, Kaneko, Fuchs (2002)

In this model, Robinson suggested that the eye position was obtained from the oculomotor integrator that produces steps and drives oculomotor neurons, and that the so-called “motor error” (the difference between the eye position and the desired target-position) could be computed in the EBNs.

An important limitation of this model resides in its position dependence: Robinson needs an absolute position of the target whereas, as we saw before, the SC encodes for the displacement from the initial position of the eye to the target. In 1988, Scudder (Scudder 1988) proposed a modified version of the model wherein a second integrator receives the burst generator output and calculates the eye displacement, which in turn can be compared with the target displacement signal. After each saccade this second integrator is reset to zero. (figure 4.7a)

Many experimental results confirmed the existence of such a feedback pathway but the exact location of the comparator and the second resettable integrator is still under investigations. Also, some studies suggested that it could be the gaze (the direction of the line of sight) rather than the position that could be under feedback, requiring a feedback control from the head.

SC and cerebellum in debate

What is the source of the “motor error”? This question is still under investigations but two regions have been proposed to hold this error signal and to encompass the resettable integrator: the SC and the cerebellum.

Many studies showed that SC could be the source of motor error using the argument that the same SC neurons are active before the saccade (to send the target command) and during the saccade itself (Waitzman *et al.* 1991, 2000; Soetedjo *et al.* 2002). The mechanism could be described as follows: the SC sends the target command position, the burst generator moves the eyes and, during the saccade, sends back the displacement of the eyes to the SC neurons, whose decaying activity reflects the decrease in motor error.

The role of the cerebellum may be crucial in the feedback loop (Scudder *et al.* 2002; Quaia *et al.* 1999). Neurophysiologists have proposed that it could be the place of the resettable integrator and the location at which the motor error is computed since it can receive a copy of SC’s command. The cerebellum could then send back the new command to the burst neurons.

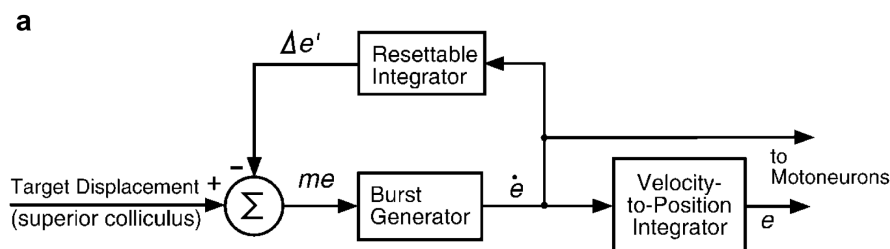


Figure 4.7: **a**, A Generic feedback model of the saccadic dynamics. The output of the burst generator is an eye velocity command (de/dt), which is sent directly to the motoneurons and also integrated (to produce eye position e before being conveyed to the motoneurons). A copy of the velocity command is also conveyed to the resettable integrator, which produces a neural replica of current eye displacement ($\Delta e'$). This signal is compared to the neural replica of the target displacement to produce motor error (me), the input to the burst generator. The target displacement signal is usually thought to be located in the SC, where it is encoded topographically; however, different models assign various locations

to other elements of the local feedback circuit. For instance, some models place the comparator (Σ) in the SC. Taken from Scudder et al 2002.

4.2.4 Eye-head coordination and gaze shift

All the neurophysiological models presented earlier were based on head-fixed experiments. However, in natural settings, it is common to see a coordinated shift of eyes and head during a gaze reorientation (Figure 4.8a). But as some experts in the domain wrote (Scudder, Fuchs and Kaneko): the understanding of the brainstem control of head-free gaze shifts is still stammering. Here we mention five of the main insights the literature can tell us regarding this coordinated motion.

1) It is now accepted that a unique target command given by the SC is fed to both the saccadic system and the head movement's circuitry (Freedman *et al.* 1996). This target signal goes from the SC to the cervical spinal cord directly and *via* the midbrain, the pons and the medulla. (Figure 4.8b).

2) In Philips *et al.* (2001), the authors claim that some LLBN in the PPRF discharging well before the gaze-shift and continuing after the end of the saccade could be the analogs of LLBN for head movements.

3) Head and eye movements are under the same target command but must have separate circuitry. However, the head system like the saccadic system should be under a feedback control since the head can target very precise positions in tens of milliseconds. This feedback control of head movements is still unknown.

4) As shown in Figure 4.8b, the contribution to gaze shift from head or eye movement can vary a lot. The relative contribution of each movement seems to depend on the initial position of the eyes.

5) EBN and IBN activities are modulated by the gaze shift and not by the eye displacement. The compensatory eye movement (Figure 4.8b) can be explained by the modulation of saccade-related burst neurons by the head position and velocity. Re-analyzing the data on EBN and IBN, neuroscientists found that the number of spikes in these neurons is better correlated with the gaze shift than the eye displacement (Figure 4.8c, Ling *et al.* 1999). Moreover the gain of EBNs is strongly modulated by head velocity during head and eye movements.

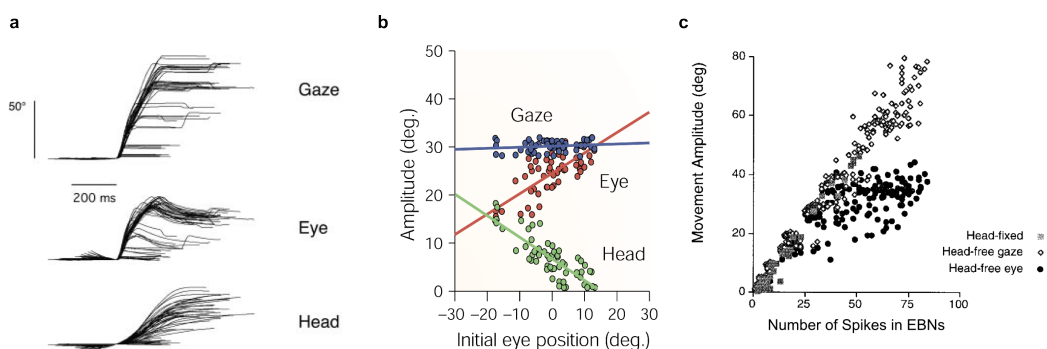


Figure 4.8: **a**, Head free experiments on monkeys. Traces from top to bottom show horizontal gaze shifts and their horizontal eye and head components, respectively. Taken from Fuchs *et al.* 2005. **b**, Gaze, eyes, head-shifts after an SC stimulation. This plot shows 57 gaze shifts evoked by stimulation of the same collicular site with the same stimulation parameters. The position of the eyes in the orbits at the time of stimulation onset varied from 20° left to 14° right, but a gaze shift of about 30° was always evoked. This 30° gaze shift was sometimes accomplished with a 15° head movement and a 15° eye movement; at other times, it was seen with a 5° head movement and a 25° eye movement. Stimulation of a particular collicular site using constant stimulation parameters produces gaze shifts that have relatively constant amplitudes and directions, but does not produce a particular eye movement coupled with a particular head movement. Taken from Sparks 2002. **c**, Discharge characteristics of the EBN when the head is unrestrained. Relation between movement amplitude and the number of action potentials (spikes) in the burst. Taken from Ling *et al.* 1999.

4.3 The neural integrator

As we saw earlier in the chapter, the maintenance of stable eyes positions relies on a subset of neurons called the oculomotor integrator that transforms the pulse of activity originating from burst neurons into a ramp and hold sequence of activity driving the position of the eyes. This ensemble of neurons - often called the *velocity to position neural integrator* (VPNI) - has been found in all vertebrates. In primates (Fuchs *et al.* 1985; Robinson 1972) or in cats (Delgado Garcia *et al.* 1986) the horizontal VPNI (hVPNI), responsible for horizontal eye stability, is located in the nucleus prepositus hypoglossi (NPH) and the medial vestibular nucleus (MVN). Experiments in goldfish (Aksay *et al.* 2000, 2001) showed that the hVPNI is localised in a region of the medulla analogous to NPH of mammals called the area I. In zebrafish, hVPNI has been discovered in the rostral part of the hindbrain (Miri *et al.* 2011, Gonçalves *et al.* 2014, Wolf *et al.* 2017).

In the following, we will see why the VPNI is an essential region from a theoretical perspective and how the numerous studies on this region could provide guidelines to analyse our own data sets.

4.3.1 Persistent activity and STM

To begin, let's take a look at why the VPNI might be so interesting. Memory is one of the key functional feature of the brain. In neuroscience, memory could be roughly defined as "*the panoply of changes in the activity or connectivity of neural systems that are triggered by stimuli or brain states and then persist over a duration longer than the triggering events*" (Chaudhuri and Fiete 2016). Memory is often classified into two categories depending on the associated persistence time: short-term memory (STM) or "working memory" lasting for seconds to tens of seconds and long-term memory lasting for hours to decades. To store a memory, a system should possess states that can persist over time. Most models differentiate STM and LTM as they rely on distinct strategies to maintain a persistent state: STM relies on some form of persistent neural activity whereas LTM relies on persistent synaptic changes.

Persistent neural activity is a signature of STM that manifests in a sustained discharge of action potentials that lasts after a stimulus. It is thus a long-lasting neural representation of the stimulus. Sustained discharges have been observed in many areas of the brain: in the thalamus (Komura *et al.* 2001), the superior colliculus or the brainstem (Major and Tank, 2004). Neural integrators are circuits that are able to "mathematically" integrate a stimulus over time and exhibit such persistent activity. The VPNI was the first neural integrator discovered in the brain, after Robinson hypothesized its existence in the 1960's. The VPNI converts the velocity signal into a position signal through mathematical integration.

4.3.2 Modeling neural integrators: recurrent network models

Two general mechanisms have been proposed to account for the integration ability of the VPNI: one relies on the circuit-level property of recurrent neural network models using feedback activation. (Seung 1996, Seung *et al.* 2000), while the second one is based on properties of individual neurons (Kiehn and Eken, 1998). During the last two decades these two approaches have been highly debated, although the true mechanism may in fact combine both mechanisms (Goldman 2009; Gonçalves *et al.* 20014).

How can a single neuron or a population of neurons integrate?

The relaxation time constant of membrane potential of individual neuron is of the order of a few ms to tens of ms; it thus can not store inputs for long because of the leakage of the neuronal current. This is why numerous models incorporate tuned *positive feedback* in order to offset the intrinsic leakage of membrane currents (Goldamn *et al.* 2008; Seung 1996). This feedback can be synaptic, *i.e.* originates from recurrent excitatory or dis-inhibitory neurons, or it can result from an intracellular biochemical loop.

To understand how the integration can result from a positive feedback mechanism, let consider a given neuron numbered i out of N neurons. The mean firing rate r_i can be written as:

$$\tau_r \frac{dr_i}{dt} = -r_i + \sum_{j=1}^N w_{i,j} v_j + B_i$$

Where τ_r is the time constant of the intrinsic cellular dynamics, $w_{i,j}$ is the synaptic weight from neuron j to neuron i , v_j is the presynaptic firing rate and B_i is the net burst input to the neuron i from the saccade generator (or other external inputs). Note that experiments tell us that $v_i \propto r_i$ (Seung *et al.* 2000).

Let us assume for now that there is only one neuron in the VPNI circuit, then the equation becomes

$$\tau_r \frac{dr}{dt} = -r + wr + B$$

Provided that the synaptic (or autaptic) weight is “fine tuned” such that $w = 1$, then $r(t)$ is exactly the integral of the input:

$$r(t) = \frac{1}{\tau_r} \int B(t) dt$$

Depending on the exact value of w , the neuron can achieve perfect integration ($w = 1$), leaky integration ($w < 1$) or unstable integration ($w > 1$), see Figure 4.9.

With the preceding reasoning, it is easy to understand how a positive feedback can give rise to the integration property. The problem is then to identify the origin of this positive feedback? Two mechanisms have been proposed: it is an intrinsic property of each cell in the neural integrator, where each cell sends a positive feedback to itself (single-cell approach); it is a collective property of the ensemble of neurons (recurrent network approach).

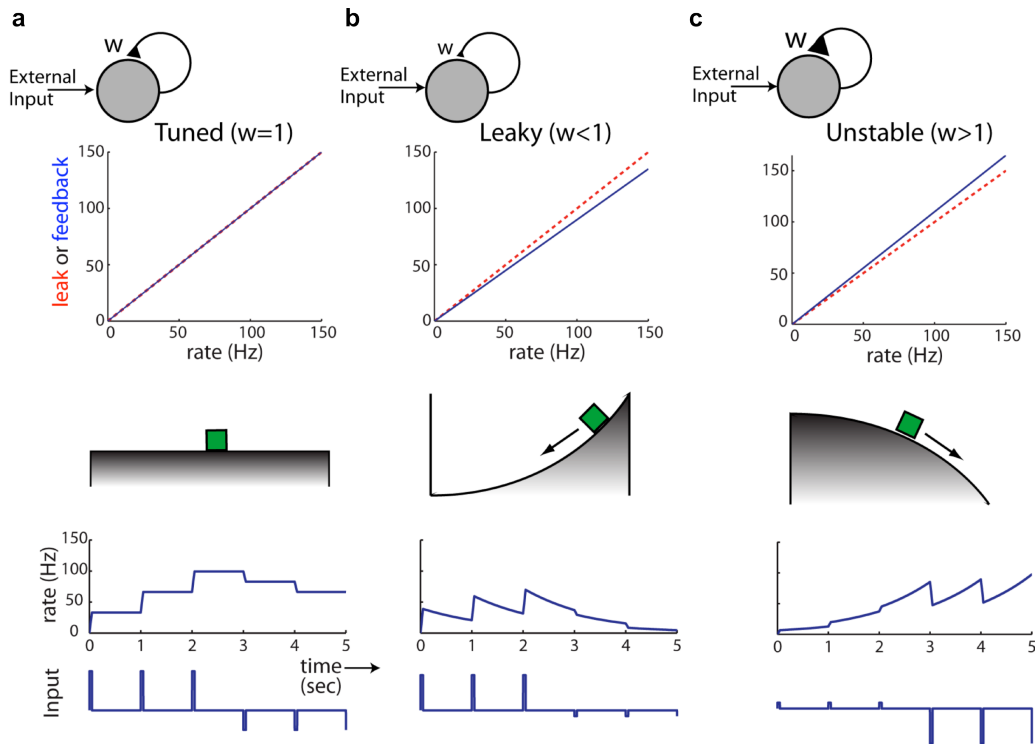


Figure 4.9: Positive feedback as a mechanism for neural integration. **a**, Simple model of a neuronal population with positive recurrent feedback carried by a synaptic connection of weight w . Top, When properly tuned, the feedback at any firing rate offsets the intrinsic leak processes that pull the firing rate back towards zero (dashed red line, intrinsic leak; solid blue line, synaptic feedback). Middle, The integrated total of external inputs can be conceptually represented by the location of a block along a surface. External inputs that are accumulated by the integrator move the block along the surface. When well-tuned, the integrator can stably maintain any accumulated value, corresponding to the block not slipping along the flat surface. Bottom, Accumulation of pulsed excitatory or inhibitory inputs into sustained firing rates. **b**, Top, Model in which the synaptic weight is decreased so that the positive feedback is less than the intrinsic leak at all firing rates. Firing rate drift is proportional to the difference between the feedback and leak traces. Middle, The model firing rate behavior can be represented by the location of a block on a curved surface, where the curvature is proportional to the firing rate drift in the absence of input. Bottom, Decrease in the synaptic weight leads to exponential decay of firing rates in the absence of input. **c**, A model in which feedback is too large leads to exponential growth of firing rates. Taken from Goldman *et al.* 2007.

How can a recurrent network of neurons integrate?

If we go back to the general case of N neurons, we can write the dynamical equation of a firing rate vector $\vec{r} = (r_1 \dots r_N)$ as:

$$\tau_r \frac{d\vec{r}}{dt} = -\vec{r} + T\vec{v} + \vec{B}$$

With $\vec{v} = (v_1 \dots v_N)$ and $T = (w_{i,j})_{i,j \in [1:N]}$

Using $v_i \propto r_i$ (Seung *et al.* 2000), we can rewrite this equation a matrix of weights W

$$\tau_r \frac{d\vec{r}}{dt} = -\vec{r} + W\vec{r} + \vec{B}$$

If \vec{u}_{λ_i} is an eigenvector of W associated with the eigenvalue λ_i , we can write $\vec{r} = \sum_{i=1}^N c_i \vec{u}_{\lambda_i}$ and thus rewrite the preceding equation in the eigenvector base:

$$\tau_r \frac{dc_i}{dt} = -c_i + \lambda_i c_i + \vec{B} \cdot \vec{u}_{\lambda_i}$$

For such a network to behave as an integrator, the matrix W needs to possess an eigenvalue equal to unity such that $\lambda_1 = 1$ and thus

$$\tau_r \frac{dc_1}{dt} = \vec{B} \cdot \vec{u}_{\lambda_1}$$

Then

$$c_1 = \vec{r} \cdot \vec{u}_{\lambda_1} = \frac{1}{\tau_r} \int \vec{B} \cdot \vec{u}_{\lambda_1} dt$$

The projection of the activity of the network on the vector \vec{u}_{λ_1} represents the accumulated total of inputs being stored by the network.

As one can read from the equations, for a recurrent network to behave as a neural integrator, a precise tuning of the coefficients of the matrix W is needed such that one of the eigenvalue is close to unity. This “fine-tuning” requirement of the synaptic weights instigated many debates in the community, some groups claiming that it is unlikely to be implemented in the brain.

The source of the feedback in recurrent networks: the goldfish model

In the field of persistent activity, two mechanisms have been struggling to explain the integration process: a single-cell mechanism where the positive feedback comes from an intracellular mechanism, an a circuit mechanism where the feedback comes from recurrent interactions of the neurons in the network. Among the advocates of the recurrent network mechanism, two hypotheses have been proposed for the positive feedback: (i) it could arise from recurrent

excitation between excitatory neurons in the network, or (ii) it could come from an inhibitory feedback loop involving a second population of neurons.

During the last two decades, goldfish has been used as a model animal to solve these two debates (single-cell/recurrent network, self-excitatory/inhibitory feedback) using the VPNI as a model integrator. Thanks to David Tank's group, the question of the source of the *positive feedback* has been clarified.

Recurrent excitation within each population

In a first approach, Seung *et al.* (2000) proposed a realistic conductance-based model with excitatory feedback within the population of neurons: active neurons exchange feedback through recurrent synaptic excitation and are sequentially recruited as the network global activity increases. Seung *et al.* introduced some non-linearities in the model: a threshold on eye position for action potential discharge and a synaptic saturation as presynaptic firing rates increase: “in a properly tuned network, a balance between recruitment and saturation keeps the amount of synaptic feedback sufficient to maintain persistent neural activity” (Seung *et al.* 2000).

Anatomy and mutual inhibition

However, in several integrators like the prefrontal cortex circuit for tactile vibrations, the intraparietal area of primates, the connection between the left/right side of the integrator have been shown to be primarily inhibitory. Hence in the goldfish's medulla, the VPNI has been located in a region called area I, encompassing two populations (left and right) neurons. Aksay *et al.* (2003) showed that the inputs to these populations are typically arranged in a “push-pull” manner such that: when one population is excited (“pushed”) by the external input, the other population is inhibited (“pulled”) (Aksay *et al.* 2003, 2007). Moreover anatomical studies (Aksay *et al.* 2000) revealed a commissural connection between the two sides of the integrator in goldfish.

These anatomical results have suggested that positive feedback in recurrent models of integrator could be mediated by mutual inhibition between both populations (Figure 4.10a and b).

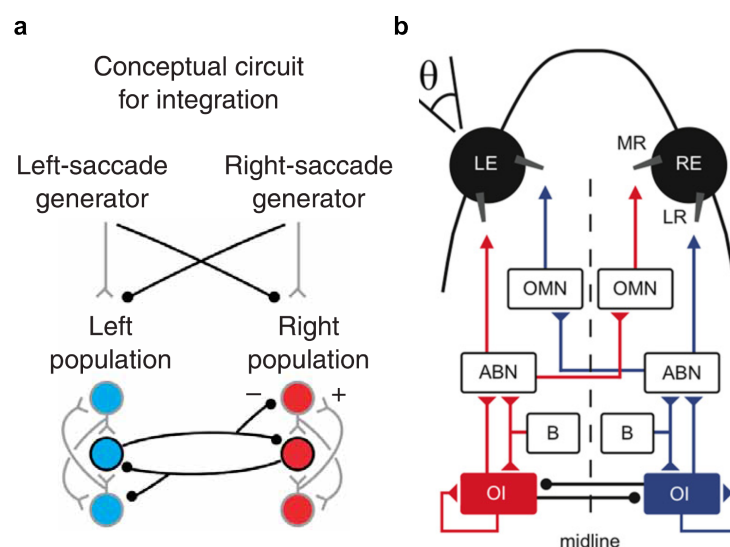


Figure 4.10: Traditional model of feedback for opposing populations. **a**, Conceptual circuit for an integrator with opposing left and right populations

which transforms brief eye velocity commands from saccade generators into sustained eye position commands (black, inhibitory interactions; gray, excitatory). Taken from Aksay *et al.* 2007. **b**, Schematic of the oculomotor system for horizontal eye movements. The neurons carrying a position signal are located in the oculomotor integrator (OI) and are thought to integrate (in the mathematical sense) the velocity signal from the burst nucleus (B). Studies of pairwise neural correlations suggest recurrent excitatory connections within each side of the OI and mutual-inhibition between opposite sides. The burst nucleus (B) generates the saccadic eye movements. Position and velocity signals are provided to the muscles (LR: lateral rectus; MR: medial rectus) *via* excitation of the motoneurons in the abducens nucleus (ABN) and the contralateral oculomotor nucleus (OMN). Taken from Gonçalves *et al.* 2014.

Aksay 2007: mutual inhibition or auto-excitation

In 2007, David Tank's group (Aksay *et al.* 2007) aimed to close the debate between a recurrent excitation in the same population *versus* mutual inhibition between two symmetric clusters. They ended showing that integration in goldfish's VPNI cannot be generated through cross inhibition between populations but with recurrent excitation within each population of the integrator. Using electrophysiology and pharmacological to silence a subset of neurons in the VPNI, they found that 1) above equilibrium (the equilibrium being defined as the firing rate when a given eye is at an orientation of 0°) the firing rates could be maintained after an inactivation of the opposite (contralateral) neuronal population; 2) below equilibrium, firing rates could be maintained after an inactivation of the ipsi population. They concluded that mutual inhibition between populations of neurons, rather than providing positive feedback, is necessary for the coordination between both populations. They proposed a new model for integration based on their observations, which states that the firing rates of a neuron must exceed a threshold level before affecting the others.

Note that in order to test these recurrent network models, the strategies are always to find an experimental way to disrupt or inactivate some parts of the network while probing the neuronal activity and behavioral consequences, and then to confront them to the predicted outcomes of the various models.

Arguments for recurrent network models

In the debate between recurrent network models and single-cell models, the work of David Tank's group on goldfish provided many arguments favoring a recurrent network model:

- In Aksay *et al.* 2000 and 2001, the authors performed intracellular current injections in neurons of the VPNI (area I). They did not observe a plateau potential as would be expected for a single-cell integration mechanism (see next section).
- In Aksay *et al.* 2001, the authors showed that a persistent firing increase is associated with an increase in post-synaptic potentials, which is consistent with recurrent network models.

- In Major *et al.* 2004, the authors showed that goldfish's VPNI (area I) could be trained to instability or to leaking using visual feedback. This property fits naturally with recurrent networks models (Major and Tank 2004).
- In Aksay *et al.* 2003, the authors evaluated the cross-correlation functions of neurons in the VPNI. An absence of correlation would have indicated that neurons discharge independently as in a single-cell paradigm, but the results show spike-time cross-correlogram peaks, often with zero lag, consistent with common inputs including recurrent feedback.

4.3.3 Modeling neural integrators: single-cell approach

Neural integrators can nevertheless reside in the internal biochemical machinery of a single neuron. Many *in vitro* experiments (Egorov *et al.* 2002; Alaburda *et al.* 2002; Kiehn and Eken 1998; Viana *et al.* 1997) reported that intrinsic cellular mechanisms could produce multi-stability (Figure 4.11). These persistent firing rates are driven by plateau potentials. Neural integrators models can be built using these intracellular feedback properties. Today neuroscientists claim that neural integrators may combine recurrent network and cellular persistence mechanisms (Major and Tank 2004, Goldman 2009).

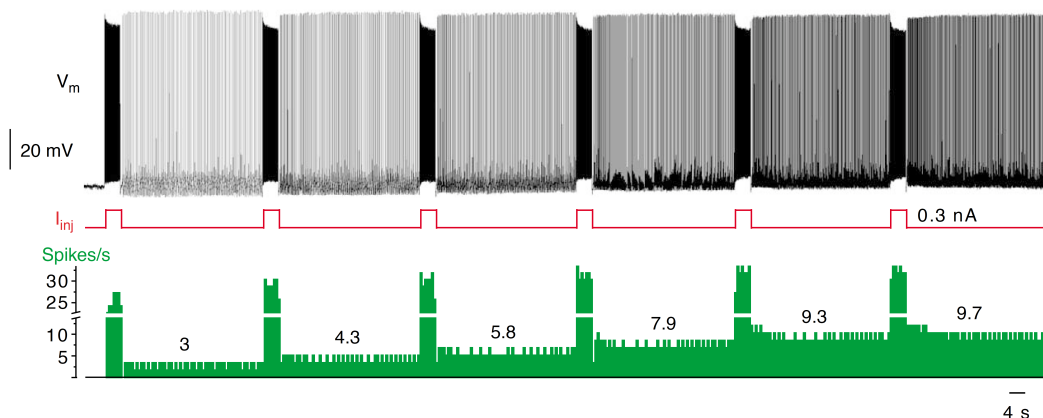


Figure 4.11: Entorhinal cortex layer 5 pyramidal neurons *in vitro*. When activated cholinergically, synaptically-isolated neurons of the entorhinal cortex integrate successive, brief 4s pulses of current injection (I_{inj} , red trace) into stable graded firing rates levels (top and bottom traces). Adapted from Egorov *et al.* 2002.

4.3.4 Zebrafish: new insights in the VPNI

More recently, calcium imaging in behaving zebrafish and optogenetics perturbation of the VPNI offered new insights in the mechanisms of neural integration (Miri *et al.* 2011, Gonçalves *et al.* 2014).

Multidimensional dynamics in the VPNI

Calcium imaging with 2-photon microscopy in awake behaving larval zebrafish allowed to probe in details the functional properties of VPNI neurons.

Miri *et al.* (2011) reported a high variability of the firing-rate persistence: some neurons have a rapid decrease in activity during the drift of the eye toward the central position whereas others maintain a high and relatively stable firing-rate (Figure 4.12a and b). The topographical organization of cells in function of their persistence time suggest that nearby neurons are more interconnected than distant ones (Figure 4.12d-g). Building on these observations, Miri *et al.* proposed three possible descriptions of the VPNI that differ in the associated synaptic weight distribution: a proximity-biased feedback model, an asymmetric connectivity feedforward model and a mix of recurrent network and cell-intrinsic model. These models could capture the spatially graded persistence activity seen in the experiments.

Note that the same time-varying firing rate of neurons has been observed in the primate neural integrator by Joshua and Lisberger 2015.

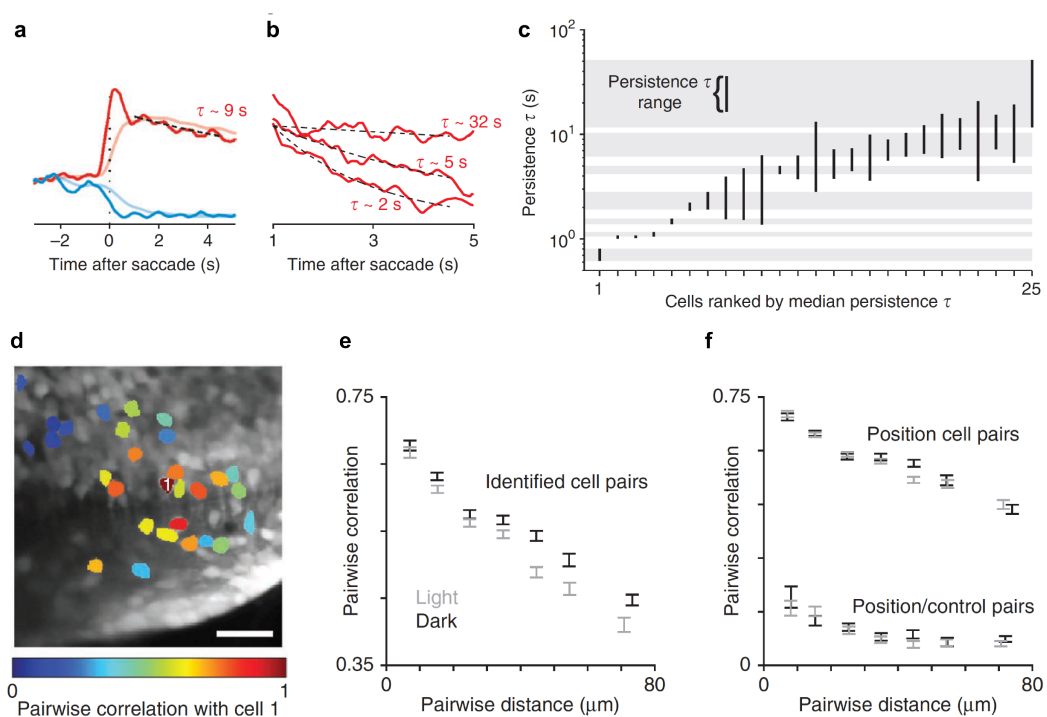


Figure 4.12: **(a-c)** Distribution of persistence time ranges in individual larvae. **a**, Representative ipsiversive (red) and contraversive (blue) saccade-averaged fluorescence responses, before (translucent) and after (opaque) deconvolution. The mean of the first 1.5 s of each trace is subtracted off. The black dashed line is the fit to an exponential decay function. **b**, Ipsiversive saccade-averaged fluorescence responses from three cells in one fish from 1–5 s after saccade onset. Black dashed lines show exponential fits with time constants indicated. Traces are normalized to the value of the fit at $t=1$ s after the saccade onset. **c**, Persistence time ranges for 25 cells imaged in one fish in the dark. The vertical extent of each bar spans the persistence time range for each cell. The gray bars span the ranges for seven cells for which the ranges do not overlap. Cells are ordered according to their rank in terms of the median of their persistence time distribution. **(d-f)** Activity correlations between cells depend on their pairwise distance. **d**, Time projection of an image time series with 29 identified neurons color-coded according to the Pearson correlation of their fluorescence time series with that of the cell labeled '1'. Scale bar represents 20 μ m. **e**, Pairwise

correlation of fluorescence time series for pairs of identified cells versus pairwise distance for data collected in the light (gray) and in the dark (black). **f**, Pairwise correlation of fluorescence time series for position cell pairs and position/control cell pairs versus pairwise distance for data collected in the light (gray) and in the dark (black). Adapted from Miri *et al.* 2011.

Optogenetic perturbations of the VPNI

The recurrent network models introduced above for the VPNI can be distinguished by the specific ratio of excitatory and inhibitory inputs to the neurons. These recurrent models, despite their different ratio of excitatory and inhibitory inputs, can have the same fixed points (line). However they differ when the system is perturbed and then relax toward the persistent activity state. The work of Aksay *et al.* (2007) used inactivation by lidocaine to show the superior relevance of excitatory positive feedback. More recently Gonçalves *et al.* (2014) used optogenetic stimulation to address the question of relaxation in the VPNI. They first confirmed the model from Aksay *et al.* 2007: a dominance of unilateral self-excitation concurrent with a weak mutual inhibition between both sides. Second, they showed that the dynamics around the line attractor state (persistent activity state) is organized around the null position of the eyes.

4.4 Light-sheet imaging of the oculomotor system in zebrafish

During my PhD, I used whole brain light-sheet imaging to monitor the neuronal activity of larval zebrafish during spontaneous saccadic behaviour. Among the gaze-tuned hindbrain population, we identified a bi-laterally distributed cluster that self-oscillates and is involved in light seeking processes. In the following, we speculate in the light of what the literature provides on primates, cat and goldfish, on possible new insights that these experiments could offer to better understand the functioning of the oculomotor system in the vertebrate.

Note that the following results are still preliminary. More experiments will be needed to confirm them.

4.4.1. Long lead burst neuron in zebrafish

Since the earliest studies on the brainstem saccadic system, primate's studies described a subset of burst neurons with the ability to increase their activity before the saccade onset (20-100ms before). Excitatory as well as inhibitory (EBN or IBN), this population of neurons has been named *long lead burst neurons* (LLBN), yet their functional role remains elusive. Using whole-brain activity recordings in freely eyes moving experiments, we identified two small clusters in the hindbrain in the rhombomere 7 that systematically activated 2-3 s prior to the saccade onset. This subset of burst neurons could therefore be analogous to the primate's LLBN.

In Figure 4.13, we show the anatomical location of these LLBN for two different fish (yellow and purple voxels) and some traces showing their ramping activity prior to the saccade onset. As shown below, the LLBN activity is in fact strongly predictive of a forthcoming saccade event.

LLBNs are predictive of saccade events

Spontaneous saccadic dynamics in zebrafish larvae consists of quasi-periodic alternation of leftward and rightward saccades. When the HBO activity is about to switch from the left to the right side, the right LLBN's activity starts rising, and their burst of activity coincides with the transition of the network from one side to the other, and with an ocular saccade (see Figure 4.13b and c). The process keeps repeating in both direction in a quasi-periodic fashion. Nonetheless, with a frequency that varies strongly across individuals, successive saccades in the same direction can also be observed (see Supplementary Figure 3d in Wolf *et al.*). When this happens, the ipsilateral part of the HBO exhibits a sudden increase of activity, then it starts decreasing again (Figure 4.13d). This process can be observed several times until a reorienting saccade takes place, and the other part of the HBO becomes active. The state of the HBO alone is not sufficient to predict the occurrence of forthcoming saccade: when one of the two subcircuits is active, the only certainty is that a saccade on the other direction is

very unlikely (see OPN). Although the state of the HBO seems to control the orientation of the saccades, its activity does not provide a deterministic indication of the saccadic time itself.

Our hypothesis is that the LLBN is the region that initiates the saccadic event. We thus looked at the perisaccadic signals of both the HBO and the LLBN, separating the cases in which the saccade was preceded by a saccade in the opposite direction (simple saccade) and the case in which the saccade was preceded by a saccade in the same direction (multiple saccade). The ipsilateral LLBN was found to have the same anticipating behavior in both simple and multiple saccades, while the ipsilateral HBO showed two different behaviors (Figure 4.13d and e). In simple saccades, it remained silent until the saccade onset, and showed an abrupt activation immediately after the saccade, while in multiple saccades it showed the typical rebound previously described.

To evaluate if LLBNs activity is predictive of saccadic events, we computed the conditional probability of observing a saccade event within the next second ($t \in [T, T + 1s]$) given the level of activity of LLBN at time T ($\Delta F/F(T)$). This probability has a peak for a non zero value for ipsiversive saccades (Figure 4.13a). As soon as LLBN's activity starts to increase, there is a high probability to see a saccade event in the next second or so. This analysis is thus consistent with the proposed hypothesis.

We also computed the cumulative probability to have a saccade event within the next second ($t \in [T, T + 1s]$) given the level of activity of LLBN at T ($\Delta F/F(T)$). If $N(T)$ is the number of saccade occurring during $[T, T + 1s]$, the number of saccade cumulated at A is $\sum_i N(\forall t_i \setminus \Delta F/F_{LLBN}(t_i) < A)$, where A varies from 0 to $\max(\Delta F/F_{LLBN})$. The plot presented in Figure 4.14b confirms the predictive nature of LLBN activity for ipsiversive saccades. The fact that the cumulative probability reaches the plateau value 1 for $\Delta F/F_{LLBN}$ values slightly greater than zero demonstrates that as soon as ipsiversive LLBN has a non-zero activity, it is very likely that an ipsiversive saccade will be triggered in the next second.

LLBNs receive inhibitory projections from the HBO

In summary, the state of the HBO appears to control the direction of saccadic events, whereas the activity of the LLBN is predictive of the probability that a saccade is actually triggered. Such a mechanism can be understood if each left/right LLBN population is under inhibitory control from the contralateral HBO sub-region. Consistently, we show in Figure 4.13c that LLBN activity is anticorrelated with the contralateral HBO. This hypothetical architecture needs to be confirmed by tracing the projections from the GABAergic lateral cluster of the HBO.

LLBNs are excitatory neurons

In Figure 4.13f, we applied a non-rigid registration method (CMTK) to align our functional maps and then used the Z-brain atlas (Randlett *et al.* 2015) to localize the position of the LLBNs. This morphological analysis indicates that LLBN are located with the glutamatergic stripe 3, such that LLBNs are likely to

be excitatory neurons. This result should be confirmed by using double transgenic lines that expressing GCaMP pan-neurally, to functionally identify the LLBN, and for which glutamatergic neurons are separately tagged (Vglut promoter).

When two successive saccades occur in the same direction, the second one is systematically followed by a rebound of the HBO active module. This process cannot result from the reciprocal inhibitory coupling with the contralateral HBO module, as the latter remains silent during such phases. Such a functional trait can be understood within the assumption that LLBN receives inhibitory inputs from the contralateral HBO circuit and the ipsilateral HBO receives ascending ipsilateral signals from LLBNs. In Figure 4.13g, we propose an improved (see Figure 6 of Wolf *et al.* 2017) connectivity diagram of the saccadic system that for these interactions between the LLBN and HBO populations.

The functional role of the LLBN is still poorly understood in primate:., some studies suggest that LLBN acts as a relay from the cortex and superior colliculus to the saccade circuit, others as a trigger function to suppress OPN discharge. These two possibilities could be studied in the case of zebrafish combining whole-brain recordings with optogenetic activation of the LLBN in eye-free animals.

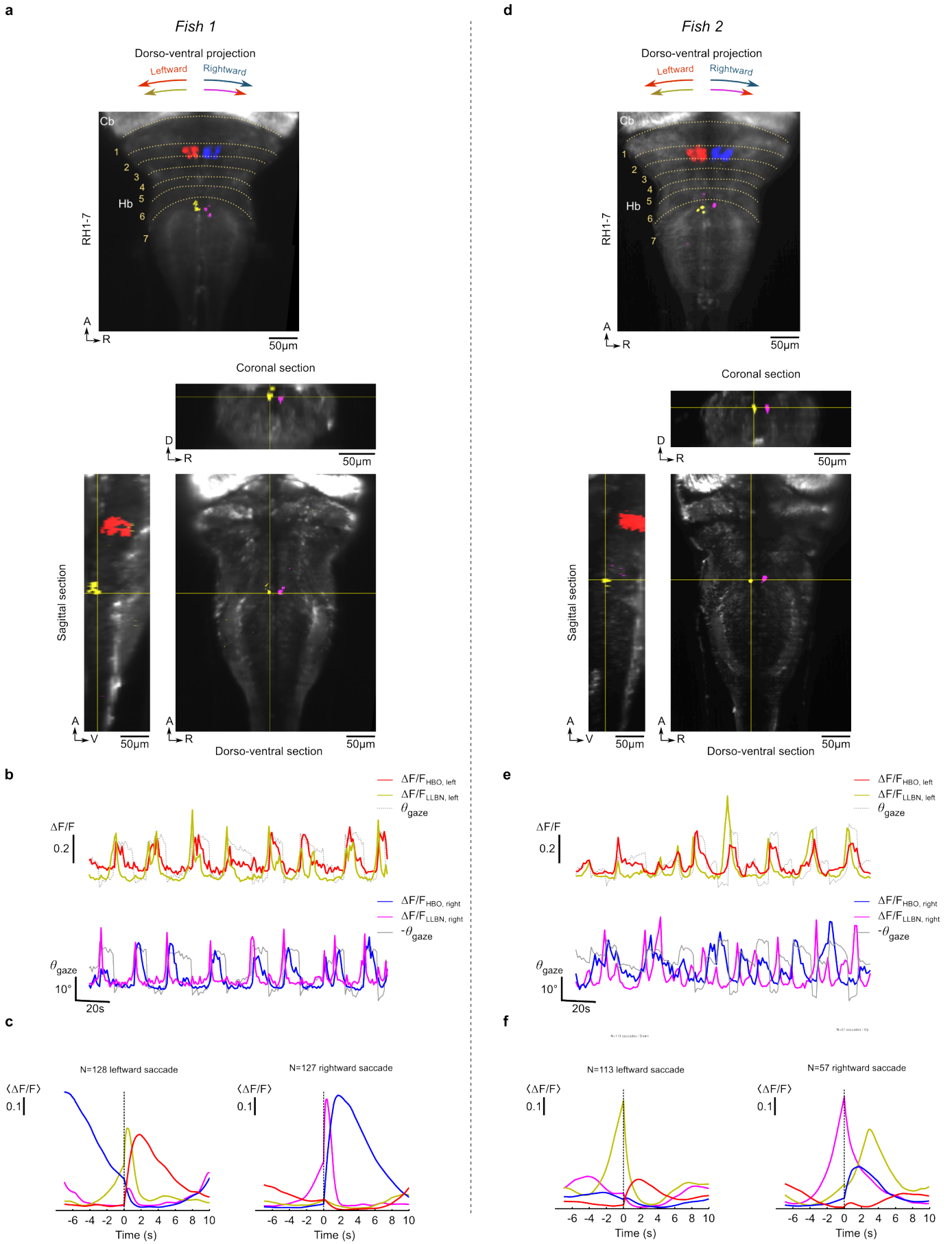


Figure 4.13: **a**, Up: Dorso-ventral projection of zebrafish brain showing the rh2-3 HBO region (red and blue voxels) and the long-lead burst neurons located in two well-defined clusters in the dorsal region of rh 7 (yellow and purple). Down: Coronal, sagittal and dorso-ventral sections showing in more detail the location of the LLBNs. **b**, Example traces of these two clusters (yellow and purple), associated gaze signals (grey), and ipsilateral HBO signal (red and blue). **c**, Mean peri-saccadic signals. A systematic increase of activity is observed ~2-3 s in the LLBN (yellow and purple line) before the ipsiversive saccade onset. **d-f**, same analysis obtained with another fish.

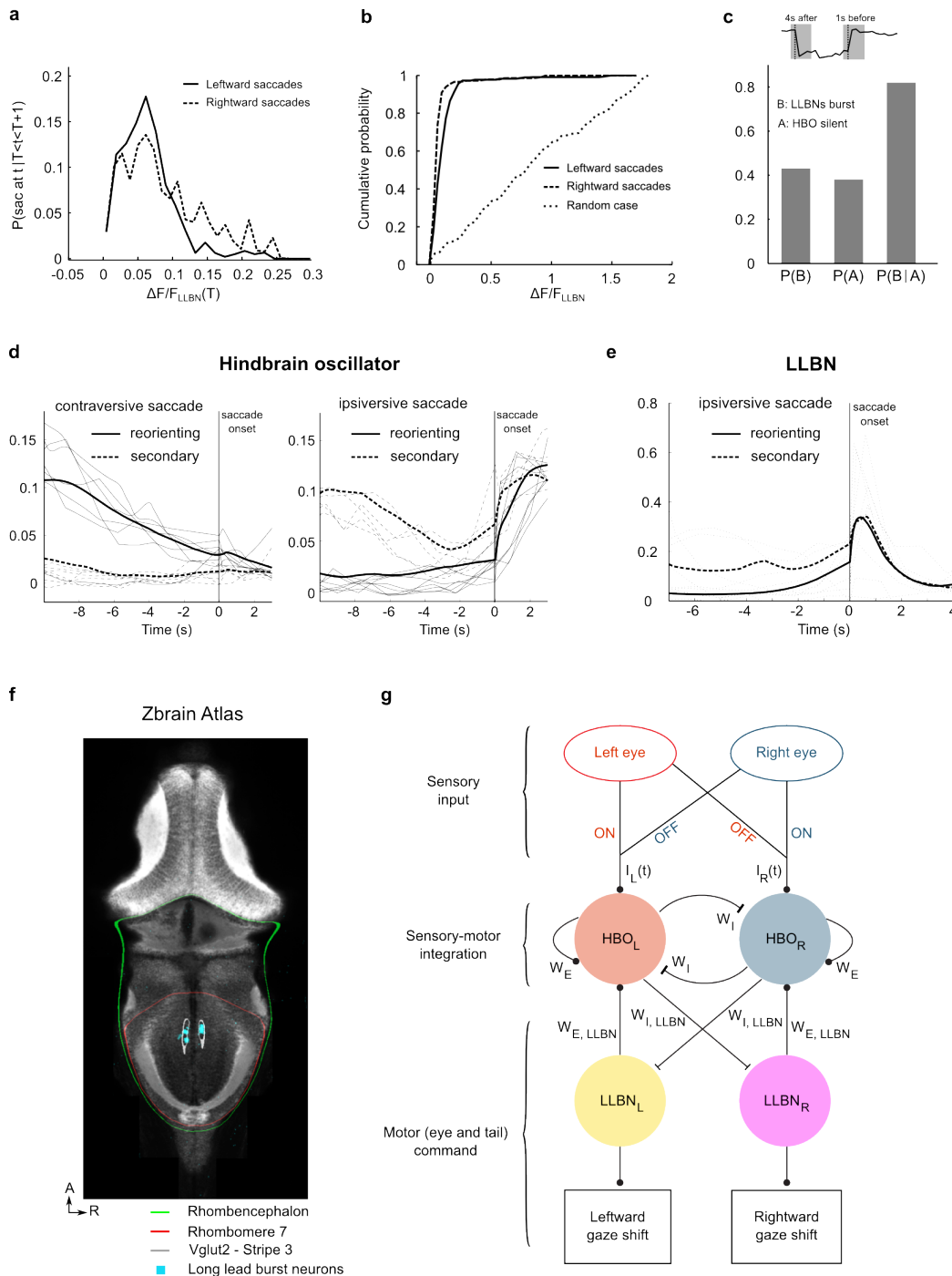


Figure 4.14: **a**, Probability to have a saccade within one second after T given the activity of the ipsilateral LLBN at T for leftward and rightward saccades. **b**, Cumulative probability to have a saccade within one second after T given the activity of the ipsilateral LLBN at T for leftward and rightward saccades. If the level of activity of the LLBN at T was unrelated to the saccade onset, the cumulative probability should follow the dotted line. **c**, Probability of A (HBO is silent), B (LLBN active) and A/B (LLBN active when HBO is silent). The probabilities are calculated for time points more than 4s after a saccade and less than 1s before a saccade. **d**, Mean peri-saccade signals of the HBO subnetworks for reorienting saccades (solid line) and secondary saccades (dashed line). The data are shown separately for ipsiversive (right) and contraversive (left)

saccades. **e**, Mean peri-saccade signals of the LLBN subnetworks for reorienting saccades (solid line) and secondary saccades (dashed line). The data are shown for ipsiversive. **f**, Dorso-ventral view of zebrafish brain showing the LLBN (cyan voxels) and the glut2 Stripe 3 location (grey line) location given by Zbrain atlas. **g**, Connectivity diagram of the saccadic generation system including LLBN.

4.4.2. Discussion on HBO

An omnipause-like network in zebrafish?

Omnipause neurons are inhibitory neurons that discharge constantly and inhibit the burst neurons while the eyes are fixed, then transiently stop spiking during a saccadic movement. We were unable to identify such neurons (see part 4.1) in our data sets. We can propose two possible explanations for this fact:

The first possibility is that we failed to identify omnipause neurons because our functional imaging configuration does not allow us to detect them. In primates, omnipause neurons stop firing for only ~100ms. Such brief pauses might be hard to detect with GCaMP6 (whose decay time is ~800ms) in particular at low acquisition rate (1Hz). We might be able to reveal omnipause neurons by carrying out experiments at faster frame rate (e.g. 5-10Hz per brain) and/or using calcium-indicators with faster dynamics.

The second possibility is that omnipause neurons do not exist in zebrafish. In this case, we propose that the hindbrain oscillator could play the role of such omnipause neurons. More precisely, each sub-region (right/left) of the HBO could be the equivalent of lateralized omnipause neuron ensembles. Two arguments may be put forward in favor of this hypothesis.

The first argument comes from anatomy. In primates studies, it has been shown that OPNs are located within a special structure called the nucleus raphe interpositus (Büttner and Büttner-Ennever 2006). We applied a non-rigid registration method (CMTK) to align our functional maps and then used the Zbrain atlas (Randlett *et al.* 2015) to localize the position of the HBO. This analysis reveals that the most ventral part of the HBO is located at the interior border of zebrafish's superior raphe interpositus (Figure 4.15a).

The second argument comes from the dynamic of the HBO. As reported in Wolf *et al.* (2017), when examining each HBO's sub region (right/left) activity traces, we observed that there are no saccades in the left (resp. right) direction when the right (resp. left) HBO is active. Thus we can interpret the role of the HBO as a lateralized inhibitory network: each part (left/right) of the HBO inhibits the onset of contraversive saccades (right/left). When one HBO sub-region ceases to discharge, it releases this inhibition and enables the triggering of a contraversive saccadic event. One simple way to illustrate this process is to plot the probability distribution of the derivative of each sub network activity at all time points, during ipsiversive saccades and contraversive saccades (Figure 4.15b). A contraversive saccade event systematically corresponds to a decrease of the sub-network activity, which can be seen as a brief cessation of the sub-network activity given the slow decrease of the GCaMP6 fluorescence signal. Examining the sum of each sub HBO region activity is also consistent with this mechanisms, as this quantity is systematically around zero when a saccade occurs (Figure 4.15c).

Other experiments will be necessary to confirm the possible lateralized pause neuron role of the HBO (Figure 4.15d). In Dunn *et al.* (2016), the authors identified the lateral clusters of the HBO as primarily GABAergic. To confirm this putative role, it should be important to show that the GABAergic clusters project onto the contralateral burst neurons. Furthermore, an ablation of these GABAergic neurons should lead to contralateral saccades occurring even when

the ipsilateral network is active.

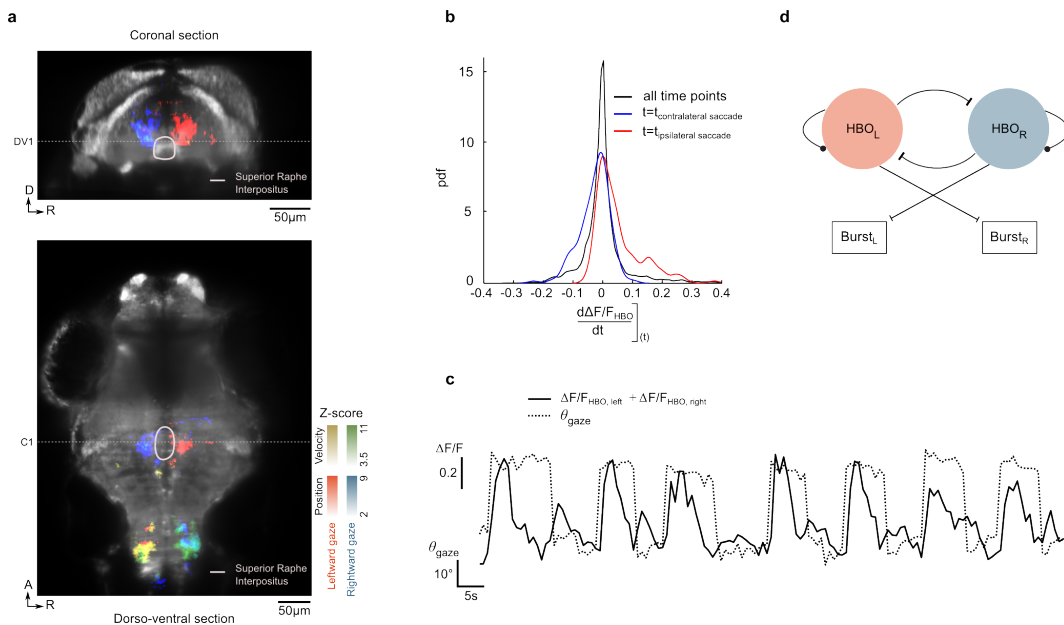


Figure 4.15: **a**, Dorso-ventral and coronal sections along planes of the 3D functional map (mean over 7 fish) showing neuronal populations whose activity is tuned to the gaze orientation (blue and red) and to the gaze angular velocity (green and yellow). The voxel color encodes the Z-score values obtained through multi-linear regression (see Wolf et al 2017 for details). The grey circle indicates the position of the superior raphe interpositus region localized thanks to Zbrain atlas (Randlett *et al.* 2015). **b**, PDF of the derivation of HBO's sub-network fluorescence activity. In black, the PDF is calculated for all time points. In blue (resp. red), the PDF is calculated only at the times of ipsilateral (resp. contralateral) saccadic events. **c**, Sum of the HBO's sub-regions $\Delta F/F$ traces. The dotted line is the gaze angle trace. **d**, Scheme of a network architecture accounting for the lateralized pause neuron role of the HBO and its interaction with the saccade generator circuit (burst cells).

A common eye-head/eye-swim orientation?

As detailed in part 4.1, eyes/head coordination in primates is still poorly understood. However it is now accepted that both the saccadic system and the head movement circuitry receive a common command.

In zebrafish, head reorientation is driven by turning bouts. We demonstrated in Wolf et al 2017 that the HBO drives eyes orientation, while in Dunn *et al.* (2016), the authors showed that the HBO controls the swim bout orientation. HBO could thus constitute this common command, controlling the coordination of eyes and swim bouts orientations.

Several works have demonstrated that primates saccadic system is modulated by the gaze position, encompassing eye and head position. Moreover, studies in primates showed that eye and head movement contribution to a reorientation of the sight depends on the initial position of the sight. It would be interesting to determine in zebrafish what is the “zero” of the HBO: is the

left/right orientation absolute or is it a function of the position of the eyes before the reorientation? To begin, on our behavioral data set, we could plot eyes angle displacement, swim bout angle and gaze as a function of the initial position of the eyes. We could also examine in our data set what are the relative contribution of eyes displacement and swim bout angle for a given gaze reorientation. Then the next step should be to record the hindbrain activity while monitoring both eye and tail movements.

4.4.3. Discussions on what we could get

In this section, we discuss some of the information we could extract from whole brain activity recordings of zebrafish in eye-free configuration.

EBN and IBN studies

In Schoonheim *et al.* (2010), the authors used optogenetics to localize a saccade-generating ensemble of neurons in the zebrafish hindbrain. In Wolf *et al.* (2017) we identified a velocity-tuned neuronal assembly located in rhombomeres 4-6 that most likely corresponds to this saccade-generating population (see Figure 2 from Wolf *et al.* 2017).

In primates, two populations of burst neurons in the brainstem have been identified: one is excitatory (EBN) located in the paramedian pontine reticular formation (PPRF) and the other one is inhibitory (IBN) located in the medullary reticular formation (RF). It would be interesting to characterize the neurotransmitter class of the velocity-tuned neuronal assembly in rhombomeres 4-6 in zebrafish's hindbrain to see if we similarly identify two distinct (excitatory and inhibitory) populations.

Moreover, in primates it has been shown that the amplitude, duration and velocity of saccades is given by the number of spikes, the duration of the burst and frequency of the spikes of EBNs. It would be interesting to analyze the activity of the velocity-tuned neuronal assembly in zebrafish hindbrain and try to characterize the encoding mechanisms of the saccadic movement.

Finally, it is well known in primate that EBN and IBN project respectively to the ipsilateral and the contralateral abducens motor neurons. We need to trace the projections of the velocity-tuned neuronal assembly in zebrafish hindbrain and see if they project to the abducens nuclei.

More data for the VPNI in zebrafish

A large effort has focused on the persistent activity of the VPNI when eyes are fixed in a given position. Aksay *et al.* (2007) concluded a series of studies demonstrating that the VPNI's activity in goldfish can be understood within the scope of a network model of neural integrator where each sub-population (left/right) recurrent excitation provides a positive feedback mechanism required for temporal integration. Later, Miri *et al.* (2011) observed that the individual neuronal dynamics leading to the persistent activity of the VPNI are spatially organized in zebrafish's hindbrain rh7. The authors used

these observations to build a functional model for the VPNI.

Using our whole brain light-sheet recordings in eye-free configurations, we could build an improved model of the VPNI including all the position-tuned neurons in zebrafish brain since this technique gives access to the dynamics of the entire oculomotor circuit.

Moreover Major and Tank (2004) proved that the goldfish oculomotor system makes use of visual feedback to tune the stability of its neural integrator. The authors imposed trajectories to the goldfish eyes using the optokinetic response (OKR). After training in a leaky or an unstable environment, VPNI neurons' stability is differently tuned. Such experiments could be replicated on zebrafish under 2P light-sheet imaging.

The main advantage of zebrafish experiments is to enable the simultaneous recording of the entire network activity. This may allow us to compute correlation matrix of the entire neuronal population engaged in the saccadic process. Using inverse modeling of neural activity (Cocco *et al.* 2017), we could infer the connectivity between the neurons in the network and thus build a precise model of the VPNI.

Other opened question: inputs from the tectum, a parallel with the SC in primates

In primates, numerous works on the superior colliculus (SC) demonstrated that this region encodes the target characteristics for a saccadic movement and send this command to the brainstem (see part 4.1). Could we also find in the zebrafish tectum some “target command” neurons? Could we find in the tectum cells whose discharge rate encode the direction and amplitude of a saccadic movement?

4.5 Discussion on the HBO model: considerations on CPG for the future

The HBO presents striking similarities with central pattern generators (CPG). These specialized networks display periodic activity (for a review, see Marder and Calabrese 1996; Marder and Bucher 2001; Ijspeert 2008) driving rhythmic movements of animals such as walking, swimming, breathing, chewing, etc.. Although these circuits can maintain rhythmic activity in the absence of external sensory or proprioceptive inputs, CPGs must be able to adjust their dynamics and respond appropriately to inputs from higher centers and sensory inputs by shifting their phase or adjusting their oscillatory frequency. Here are some examples of well studied CPGs: the pyloric and gastric networks of crustacea (Selverston and Moulins 1987), the leech heartbeat network (Albas and Calabrese 1987), the reticulospinal neurons CPG of lamprey (Grillner *et al.* 1991), the swimming networks marine molluscs and vertebrate embryos (Arshavsky *et al.* 1993; Satterlie 1985), and the escape swim response in sea slugs (Getting, 1989b).

In the end, fundamental questions on CPG are always, as Eve Marder put it:

- 1) *Why is the circuit rhythmic/periodic?*
- 2) *What sets the timing of the circuit oscillation?*

To answer the first question, as in the VPNI modeling debate, two possible mechanisms have been identified: a single-cell process with “pacemaker” neurons and a network-based mechanism where rhythmicity emerges from the concerted dynamics between many interacting units.

4.5.1 Why is the circuit rhythmic/periodic?

Single-cell properties

In a “pacemaker driven network”, a neuron or several neurons play the role of a seeding oscillator, driving neurons that are not themselves self-oscillating. Three of the main models of pacemaker neurons are the pyloric dilator (PD) neurons involved in the pyloric rhythm of the crustacean stomatogastric ganglion crustacean (Prinz *et al.* 2003), the reticulospinal neurons in the locomotor CPG of lamprey (Grillner *et al.* 1995) and the pre-Bötzinger complex neuron of the vertebrate respiratory rhythm (Smith *et al.* 1991). These neurons oscillate on their own without any other interaction. Despite the existence of this single-cell oscillatory property, strong intrinsically oscillatory neurons are relatively rare (Marder and Bucher 2001). The majority of CPG rhythmic activity thus relies on neuronal inhibitory interactions.

Before going into the network modeling of CPGs, let us list the single-cell properties that can be encountered in CPG’s neurons:

- Bistable neurons are able to generate plateau potentials (Egorov *et al.* 2002; Alaburda *et al.* 2002; Kiehn and Eken 1998), as we already mentioned in the

section on VPNI. Following a depolarization input, these plateau neurons produce a discharge pattern that long outlasts the duration of the depolarization signal.

- Many of the synaptic interactions in central pattern generators are inhibitory, and some CPG neurons are able to fire after inhibition (postinhibitory rebound).
- Some neurons display a spike-frequency adaptation: “a decrease in the frequency of firing during a constant depolarization” (Marder and Bucher 2001).

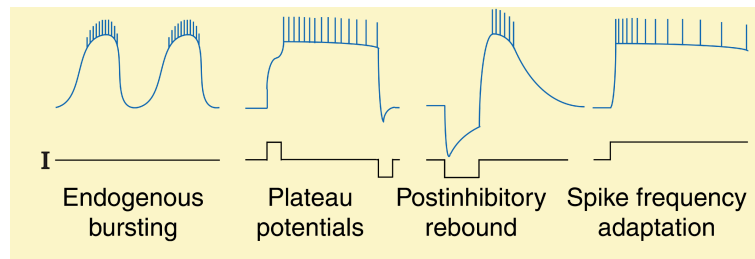


Figure 4.16: CPG neurons can have different intrinsic properties. Some neurons fire bursts of action potentials endogenously (panel 1). In some neurons depolarizing current pulses trigger plateau potentials that outlast the duration of the depolarization signal. The plateau potential can be terminated by hyperpolarizing current pulses (panel 2). Some neurons respond to inhibition with rebound firing (panel 3), others show spike frequency adaptation (panel 4). Taken from Marder and Bucher 2001.

Half-center oscillator

The rhythmicity of a CPG can also result from interaction of several cells that are not rhythmically active when isolated. In particular, reciprocal inhibition can result in rhythmic alternations between functional antagonists. These circuits are often called half-center oscillators (HCO). Since the existence of HCO was first suggested by Brown (1914) to explain the muscle dynamics during cats' locomotion, many versions of HCOs have been proposed with different intrinsic and network mechanisms (Wang and Rinzel 1992; Calabrese 1995; Marder and Calabrese 1996; Skinner *et al.* 1993, 1994). Furthermore, numerous experiments demonstrated that reciprocal inhibition is crucial in the oscillatory behavior of CPGs (Arbas and Calabrese 1987).

To understand the dynamics of alternation between half-centers, it is essential to understand what triggers the transitions between activated and inhibited states. Different mechanisms for these transitions have been discovered in the last two decades. For example, the activity of each half-center can undergo some form of spike-frequency adaptation. The active HC slows down or even stops firing, allowing the previously silent HC to escape from inhibition at a particular moment in time thus inhibiting the currently active HC (Skinner *et al.* 1994). In another mechanism, each HC exhibits a hyperpolarization rebound activity after inhibition (post-inhibitory rebound) and thus becomes active after a period of silence (Skinner *et al.* 1994). Alternatively, each HC may be able to generate an intrinsic bursting activity on their own, which then becomes

alternating and antiphase because of reciprocal inhibition between the HCs. All these models consist of two neurons with mutually inhibitory synaptic connections. The unique ingredients of these reduced models are, respectively, a persistent (slowly inactivating) current coming from recurrent positive feedback, neural adaptation, and postinhibitory rebound.

Morris-Lecar/Skinner equations for half-center oscillators

In 1994, Skinner *et al.*, following the work of Wang and Rinzel (1992), built an HCO model for the neural control of rhythmic motor pattern based on the standard current balance given by the Morris-Lecar equations (Morris and Lecar 1981):

$$C \frac{dV_i}{dt} = I_{ext,i}(t) - g_L(V_i - E_L) - g_{Ca}m_\infty(V_i)(V_i - E_{Ca}) - g_K n_i(V_i - E_K) + g_{syn}s_\infty(V_j)(V_i - E_{syn})$$

$$\frac{dn_i}{dt} = \frac{\epsilon_n}{\tau_n(V_i)}(n_\infty(V_i) - n_i)$$

where,

V_i is the membrane potential for cell i ,

n_i is the fraction of opened potassium ions channel with a rate constant of $\frac{\epsilon_n}{\tau_n(V_i)}$

C is the membrane capacitance;

g_{Ca} , g_K and g_L are the maximal conductances leak for the calcium, potassium and leakage currents, respectively,

E_{Ca} , E_K and E_L are the reversal potentials leak for the calcium, potassium and leakage currents, respectively.

$I_{ext,i}(t)$ is an external current injected into cell i .

The functions $m_\infty(V_i)$ and $n_\infty(V_i)$ describe the voltage-dependent steady state activation curves for the calcium and potassium conductance. This dependency is modeled by monotonically increasing sigmoid functions:

$$m_\infty(V_i) = \frac{1}{2} \left[1 + th\left(\frac{V - V_a}{V_b}\right) \right]$$

$$n_\infty(V_i) = \frac{1}{2} \left[1 + th\left(\frac{V - V_c}{V_d}\right) \right]$$

where,

V_a is the voltage at which half of the calcium ions channels are open at steady state,

$1/V_b$ is the slope of the voltage dependence of the fraction of open calcium ions channels at steady state,

V_c is the voltage at which half of the potassium ions channels are open at steady state,

$1/V_d$ is the slope of the voltage dependence of the fraction of open potassium ions channels at steady state,

$\frac{\tau_n(V_i)}{\epsilon_n}$ is the time constant for potassium conductance where
 $\tau_n(V_i) = ch^{-1}\left(\frac{V-V_c}{2V_d}\right)$.

The level of activation of the potassium conductance n_i is modeled as a dynamic variable to capture its relatively slow response to changes in the membrane potential, which can be controlled by scaling the factor ϵ_n .

g_{syn} and E_{syn} are, respectively, the maximal synaptic conductance and the reversal potential for the synaptic currents. The synaptic conductances are assumed to have fast dynamics and are taken to be instantaneous functions of the membrane potential of the presynaptic neuron (V_j). Specifically, the level of activation of the synapses is given by the monotonically increasing sigmoid function,

$$s_{\infty}(V_j) = \frac{1}{2} \left[1 + th\left(\frac{V_j - V_{thres,syn}}{k_{syn}}\right) \right]$$

Where $V_{thres,syn}$ is the membrane potential at which the synaptic conductance is half-maximal, and k_{syn} determines the steepness of the synaptic activation curve $s_{\infty}(V_j)$. In these models, k_{syn} is assumed to be small and the synaptic activation curve to be steep. Thus, we interpret $V_{thres,syn}$ as the ‘‘synaptic threshold’’. Also, for small values of $\frac{\epsilon_n}{\tau_n(V_i)}$ the oscillatory behaviour exists in the relaxation mode.

Parameters used in Skinner *et al.*

$g_K=20\mu\text{S}/\text{cm}^2$, $g_{Ca}=15\mu\text{S}/\text{cm}^2$, $g_L=5\mu\text{S}/\text{cm}^2$, $E_{Ca}=100\text{mV}$, $E_K=-80\text{mV}$,
 $E_L=-50\text{mV}$, $E_{syn}=-80\text{mV}$, $C=1\mu\text{F}/\text{cm}^2$, $V_a=0\text{mV}$, $V_b=15\text{mV}$, $V_c=0\text{mV}$, $V_d=15\text{mV}$
 $\epsilon_n=0.000002\text{msec}^{-1}$, $k_{syn}=0.001\text{mV}$, $g_{syn}=10\mu\text{S}/\text{cm}^2$

4.5.2 What does determine the timings of the circuit?

The intrinsic properties of the neurons and the synaptic weights in a CPG set the timing of the entire circuit. Experiments (Sharp *et al.* 1993, 1996, Figure 4.18) and theoretical analysis (Skinner *et al.* 1993 1994, Figure 4.17) have shown that ‘‘*At any moment in time the dynamics of a network depend on both synaptic properties and the intrinsic electrical properties of the constituent neurons*’’ (Marder 1998).

Theoretical models proved efficient to predict the synaptic and intrinsic neuronal properties that govern oscillations in CPG. Wang and Rinzel (1992) proposed two mechanisms to produce oscillations in a coupled reciprocal inhibitory network: *release* and *escape*. Later Skinner *et al.* (1994) built a refined HCO model not limited to the postinhibitory rebound mechanism and renamed *release* and *escape* as *intrinsic* and *synaptic*. The authors found that four different mechanisms may lead to oscillations in a network comprising two reciprocally inhibitory cells under Morris-Lecar equations. In the case of an

intrinsic mechanism, the active and the inhibited cells must be “*endogenous bursters*” (*i.e.* able to display persistent activity) or silent, whereas for a synaptic mechanism the active or the inhibited cells must be “tonic” or endogenous bursters, not silent. Skinner *et al.* (1994) and later Izhikevich (2007) summarized these four mechanisms as follows:

- Intrinsic release: if $V_{thres,syn}$ is less than the voltage at which the free cell’s burst terminates or if $V_{thres,syn}$ is larger than the voltage of free cell’s silent state, then the transition occurs when the active cell reaches the end of a bursting period, terminates inhibition and thus allows the inhibited cell to fire
- Intrinsic escape: if $V_{thres,syn}$ is larger than the voltage at which the inhibited cell starts to burst or $V_{thres,syn}$ is less than the voltage of the inhibited cell’s tonic state, then the transition occurs when the inhibited cell recovers, starts to fire and shuts off the active cell.
- Synaptic release: if $V_{thres,syn}$ is larger than the voltage at which the free cell’s burst terminates and $V_{thres,syn}$ is larger than the voltage of the free cell’s tonic state, then the transition occurs when the inhibition weakens, *e.g.*, due to spike frequency adaptation or short-term synaptic depression, and allows the inhibited cell to fire.
- Synaptic escape: if $V_{thres,syn}$ is less than the voltage at which the inhibited cell starts to burst or $V_{thres,syn}$ is less than the voltage of the inhibited cell’s silent state, then the transition occurs when the inhibited cell depolarizes above a certain threshold and starts to inhibit the active cell.

These four mechanisms arise from slow variables of the dynamical system that are responsible for slowing down or termination of spiking, recovery, or synaptic depression. These dynamical systems are fast-slow system with two times scales. As their name suggests, two of these mechanisms are determined by the intrinsic properties of the neurons, and the other two are determined by the properties of the synapses.

Control of network frequency

One other interesting result provided by the authors is that for mechanisms involving the synapses, the period of oscillation of the network depends critically on the synaptic threshold voltage (Figure 4.17). Experiments done in Marder’s group confirmed this prediction (Sharp *et al.* 1993, 1996, Figure 4.18). Using dynamic clamp methods, Sharp *et al.* (1996) constructed from neurons in the crab stomatogastric ganglion, a simple two-cell reciprocally inhibitory circuit with controlled connectivity. They showed that changing the synaptic threshold or increasing the time constant and the conductance of the inhibitory synaptic current strongly alter the half-center period (Figure 4.18A-D). They also demonstrated that the intrinsic conductance of the neuron modulates the half-center period (Figure 4.18E-H).

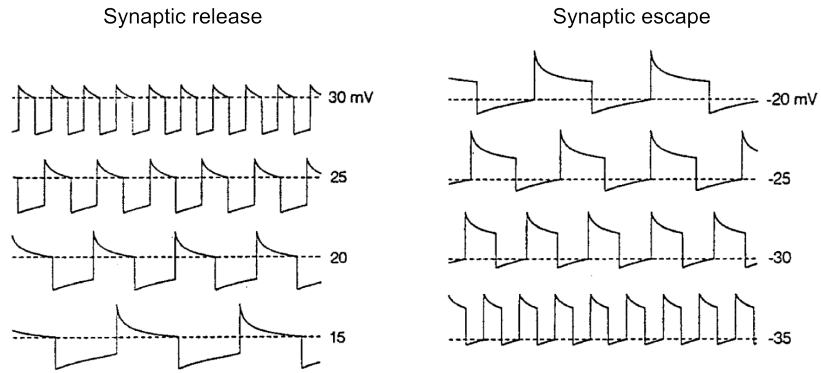


Figure 4.17: Left panel: Synaptic Release Mechanism. Voltage *versus* time for one cell using synaptic threshold voltages of 15, 20, 25, 30 mV. The dashed line represents the synaptic threshold voltage. Right panel: Synaptic Escape Mechanism. Voltage *versus* time for one cell using synaptic threshold voltages of -35, -30, -25, -20 mV. The dashed line represents the synaptic threshold voltage. Adapted from Skinner *et al.* 1994

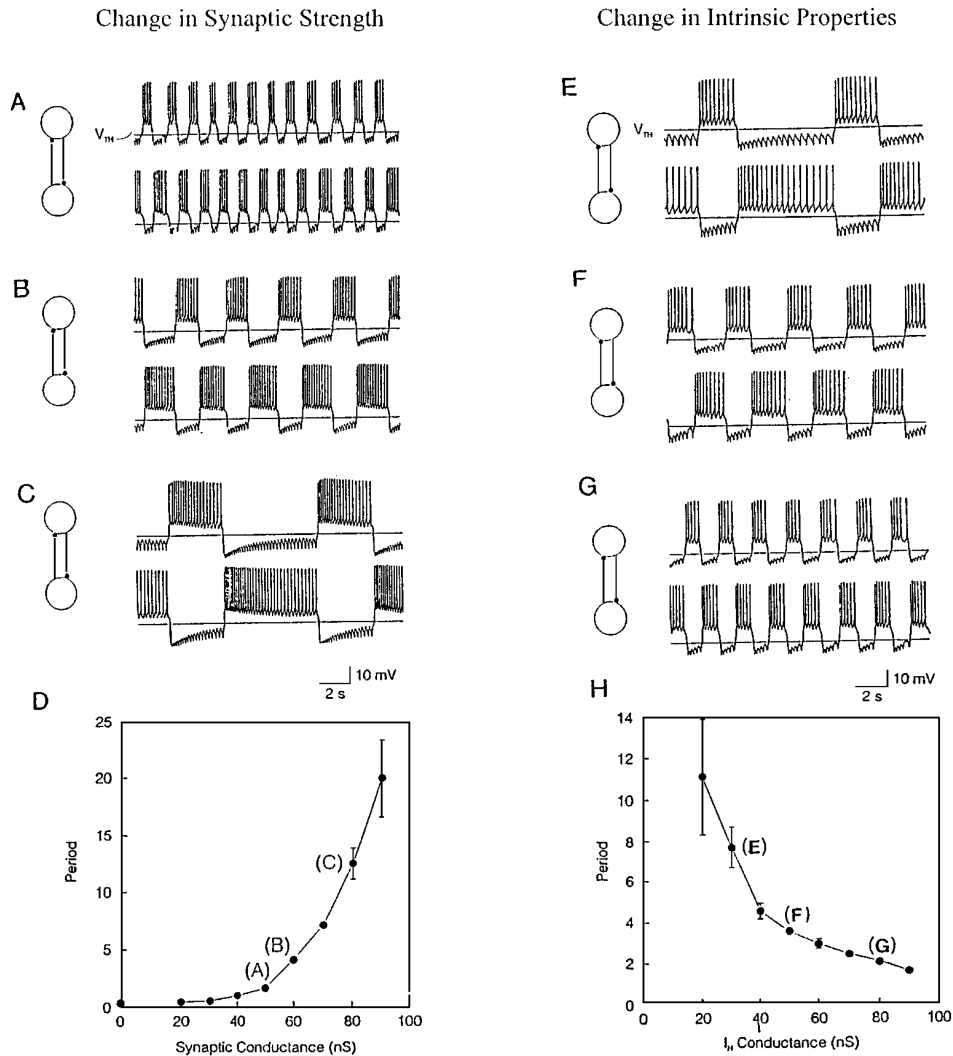


Figure 4.18: Network dynamics depend on the interaction of synaptic and intrinsic properties. Intracellular recordings were made from two Gastric Mill neurons of the stomatogastric ganglion of the crab *Cancer borealis*. These

neurons are not biologically coupled. The dynamic clamp was used to construct artificial reciprocally inhibitory connections between the two neurons. The left-hand panel shows that as the synaptic conductance is varied from 20 to 80 nS, the network period increases. The right-hand panel shows that as the Ih conductance is increased from 20 to 80 nS, the network period decreases. Taken from Marder 1998.

Consequences on the response to inputs

These two modeling approaches (Skinner *et al.* 1994; Wang and Rinzel 1992) have been used and analyzed subsequently (Daun *et al.* 2009; Zhang and Lewis 2013). One interesting outcome of these studies is that response properties of these oscillatory networks are sensitive to the mechanisms producing oscillations (intrinsic release or escape, synaptic release or escape). To characterize how oscillators respond to external inputs, one common method consists in evaluating their phase response curves (PRCs). PRCs measure the phase shift of an oscillator in response to a brief perturbation as a function of the timing of the input within the cycle. In Zhang and Lewis (2013), the authors show that PRCs are extremely sensitive to the mechanism producing oscillations (Figure 4.19)

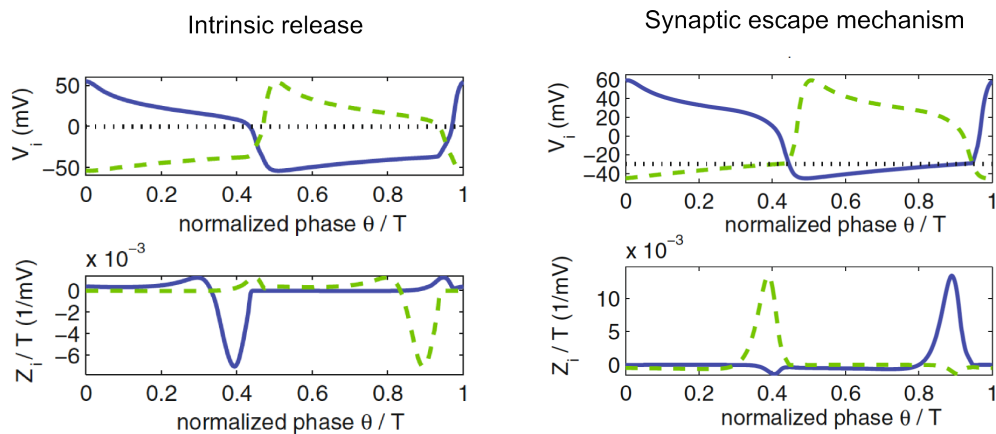


Figure 4.19: Left panel: Dynamics and PRC of a Morris-Lecar-based HCO under the intrinsic release mechanism. $g_{syn} = 0.006$ mS/cm², $V_{thres,syn} = 0$ mV. V_i is the voltage response of the half-center i to an external input. Z_i/T is the normalized variation of the phase of the half-center i evoked by an external input. Half-center 1 corresponds to the solid curve and 2 to the dashed curve. In the intrinsic release mechanism, the active cell's membrane potential is always above the synaptic threshold. The transition between the active and the suppressed states is triggered by the active cell's intrinsic properties. Right panel: Dynamics and PRC of a Morris-Lecar-based HCO under the synaptic escape mechanism. $V_{thres,syn} = -30$ mV. Same notations as in the left panel. In the synaptic escape mechanism, the transition between the active and the suppressed states is triggered by the suppressed cell's membrane potential rising above the synaptic threshold, and hence turning on the inhibition to the active cell. Taken from Zhang and Lewis 2013.

Phase models

Besides characterizing the response to inputs of a HCO, as we reported in Wolf *et al.* (Figure 6f and g in Wolf *et al.* 2017), PRCs can be used to understand the phase locking dynamics of HCOs in response to a periodic stimulus. HCO model can be reduced to a phase dynamical model. The phase for a T -periodic HCO can be written as: $\varphi(t) = t + \Delta\varphi(t) \bmod (T)$. If the effect of the periodic external input is small, *i.e.* the phase-shift is small over one period, one can write a 1st order differential equation of the phase shift to compute the effect of the periodic external input (Zhang and Lewis 2013):

$$\frac{d\Delta\varphi}{dt} = F_1(\Delta\varphi) + F_2(\Delta\varphi)$$

Where $F_i(\varphi)$ quantifies the effect of the periodic external input on the half-center i . $F_i(\varphi)$ can be written with the above notations (Morris-Lecar/Skinner equations for half-center oscillators):

$$F_i(\varphi) = \frac{1}{T} \int_0^T Z_i(t' + \Delta\varphi) * \frac{I_{ext,i}(t')}{C} dt'$$

where $Z_i(\varphi)$ is the PRC for cell i and C is a normalization constant of (Schwemmer and Lewis 2012).

Neuromodulation

Theoretical (Skinner *et al.* 1994) and experimental (Sharp *et al.* 1996) results presented above demonstrate that synaptic properties and intrinsic electrical properties of neurons can change drastically the frequency of CPGs. Moreover, these modulations of CPG's frequency are common in natural behaviors, altering breath speed (mammals) or swim velocity (lamprey). How can synaptic and neuronal intrinsic properties be altered? One possibility has been explored in the last two decades: neuromodulation. Neuromodulators are able to change the output of neural networks by altering the intrinsic properties of the neurons or by changing the synaptic properties in the circuit (Harris-Warrick and Marder 1991; Marder and Weimann 1992; Marder 1998). Generally, neuromodulators bind to a receptor and alter membrane conductance either to modulate synaptic processing or voltage current in the cell (Marder *et al.* 1987). Even if a lot of work needs to be done to understand in details the modulatory control of central pattern generating circuits, it is now clear that neuromodulators can strongly affect the motor patterns produced by a given circuit in terms of frequency and phasing (Figure 4.20).

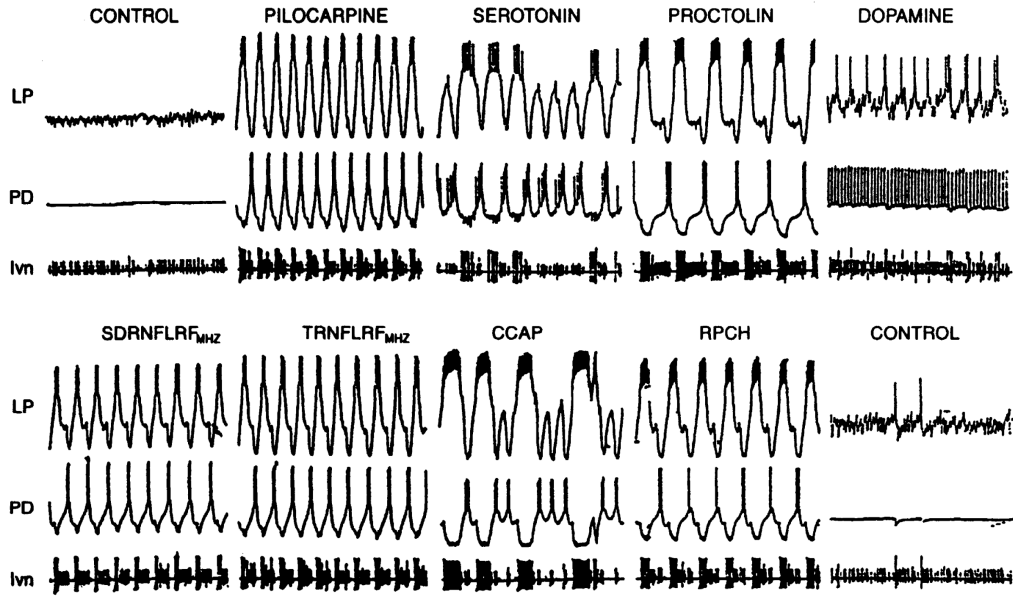


Figure 4.20: Pyloric rhythm of crustacean stomatogastric ganglion. Modulators produce characteristic and different forms of pyloric rhythm. Each panel shows simultaneous intracellular recordings from Lateral Pyloric (LP) and pyloric dilator (PD) neurons and an extracellular recording from lateral ventricular nerve. Taken from Marder and Calabrese 1996.

4.5.3 Comments on possible improvement of HBO model

In modeling the HBO oscillatory dynamics, we chose the network strategy rather than the single-cell properties model. HBO is reduced to two equivalent neurons forming a minimal “half centered oscillator”. In the proposed model, two left/right “neurons” mutually inhibit each other, excite themselves and exhibit a long habituation time constant. We simplified the Morris-Lecar equations into a firing-rate equation. The mean firing rate of the left/right HBO subcircuits was described by 4 differential equations:

$$\tau \frac{dr_{L/R}}{dt} = -r_{L/R} + \Phi[W_E r_{L/R} - W_I r_{R/L} - \Gamma a_{L/R} + I_0 + I_{L/R}(t)] + \xi_{L/R}(t)$$

with

$$\tau_A \frac{da_{L/R}}{dt} = -a_{L/R} + r_{L/R}$$

where $W_E r_{L/R}$ and $W_I r_{R/L}$ denote the recurrent excitation and reciprocal inhibition, the terms $-\Gamma a_{L/R}$ account for adaptation current, I_0 and $\xi_{L/R}$ are constant and white noise (standard deviation σ) inputs originating from non visual projections, $I_{L/R}(t)$ are visually-evoked currents. The function Φ is a linear function thresholded at zero. In this dynamic system, the self-excitation and adaptation currents produce the rise and fall of activity in one population, while inhibition ensures that only one population can be active at a time. We adjusted the values of the relaxation times such that the endogenous oscillatory

period matched the observed mean saccadic period of the HBO ($T_{endo}=25$ s). The corresponding parameters were: $W_E = 3.5 A.s$; $W_I = 0.5 A.s$; $\Gamma = 2.9$; $\tau = 2$ s; $\tau_A = 1$ s; $I_0 = 20 A$.

In Wolf et al (2017), we reported that this half-center oscillator model of the HBO accounts for the phase-dependent visual response of the circuit and accounts for the phototactic behavior. However, some aspects of this ad-hoc description appear unrealistic. For example, the time of habituation is set at a value (2s) that is way larger than commonly observed habituation time constants (typically in the range 10-500ms). To go beyond this minimal model would require understanding the actual origin of the timings of the hindbrain oscillator. Could we model HBO as a recurrent network of cells? Can we explain the unusually long effective time of habituation in our model using a population approach? Is there a way to understand the oscillation period by modeling the synaptic interaction within this population?

The first step could be to build a “four” neurons model. Dunn *et al.* (2016) reported that the medial clusters of the HBO were identified as glutamatergic whereas the lateral clusters as primarily GABAergic. In each part of the network a subpopulation is then excitatory and the other one inhibitory.

A second step would be to build a population model with $N \approx 200$ neurons and predict some of the consequences of the activation/inactivation of cells and/or ablation of a subset of cell, following the experimental approach developed in Aksay *et al.* (2007) for the VPNI. These effects could be a modification of the network frequency and a drifting firing rate of some part of the network. We could then test these predictions with optogenetics and ablation experiments.

Response to inputs

Another interesting question raised by our study on HBO is concerned with this network’s response to stimuli. As for other CPGs, the HBO responds to stimuli in a phase-dependent manner, leading to phase locking when the stimulus is periodic. The work from Marder’s team, showing that neuromodulators can alter the frequency of a CPG is suggestive of a possible mechanism: rather than resulting from direct electrical inputs to the network, the HBO’s visual response may arise from a modulation of synaptic and intrinsic neuronal properties through visually-driven neuromodulation. The close proximity of the HBO and the raphe interpositus, largely comprised of serotonergic neurons, renders this hypothesis rather tempting. Moreover, a recent publication (Cheng *et al.* 2016) showed that a disruption of serotonergic raphe neurons’ activities impairs light preference of zebrafish. The raphe being light-sensitive (cit. Cheng *et al.* 2016), this region constitutes a good candidate for a possible neuromodulatory drive of the HBO.

Chapter 5

Thermotaxis

5.1 Introduction

Temperature is a variable that affects biological systems. From chemical reactions occurring in cells to behavior at the macroscopic level, changes in environmental temperatures have a drastic impact on numerous biological mechanisms. Exposure to extreme thermal conditions such as excessive heat or cold can permanently damage tissues. Organisms are constantly seeking for the best environment with a specific temperature, corresponding to its thermal comfort. Two groups of organisms exist: (i) endotherms which developed a mixed of internal physiological process and behavioral strategies to adapt their temperature and (ii) ectotherms, such as invertebrates, fish or unicellular organisms, which do not possess any intrinsic mechanisms to regulate their internal temperature.

Endotherms like mammals, and more particularly humans, have been able to adapt to a great diversity of climates. Still, exposure to excessive warm or cold environment may place the organism in possible hypo- or hyperthermia, leading to possible death. To avoid such homeostasis disruption mammals developed physiological and behavioral strategies (Leonard 1974; Terrien *et al.* 2011) such as collective behaviors like “huddling strategy “ which consists in the aggregation of numerous individuals to limit energy dissipation and thus decrease the energetic needs for body heat production (Gilbert *et al.* 2010) to hibernation. For neo-natal hamster and rats, behavioral strategies are fundamental since at 1-10dpf they are ectotherms because they have not yet developed a thermoregulatory body mechanism (Leonard 1974).

Ectotherms such as invertebrates, fish or unicellular organisms depend directly on their environmental temperature. In particular *Caenorhabditis elegans*, *Drosophila melanogaster* or *Danio rerio* are constantly in equilibrium with their environment. Because of their small size and mass, the time scale of the temperature equilibration goes from 0.1s for *C. elegans* to a few seconds for adult zebrafish (Garrity *et al.* 2010). So these organisms need to rely upon locomotor mechanisms to regulate their internal temperature (Huey *et al.* 2003).

This chapter is specifically focused on thermotaxis - i.e. the locomotor strategy to sense temperature and to migrate up a gradient of temperature - of ectotherms. First, we will review recent articles (Luo *et al.* 2006, 201; Garrity *et al.* 2010; Barbagallo and Garrity 2015; Robson 2013; Klein *et al.* 2015) on thermal navigation and neuronal modeling of invertebrates thermotaxis, particularly *C. elegans* and *D. melanogaster* larva. Second, we will focus on vertebrates, specifically zebrafish. Third, I will present preliminary data that suggest that the HBO circuit, which we extensively studies in the context of phototaxis, may also be implicated in zebrafish thermotaxis.

5.2 Thermotaxis in Invertebrates

5.2.1 *Caenorhabditis elegans*

Worms, like *C. elegans*, are able to navigate toward a preferred temperature T_c , which, interestingly is in part controlled by the temperature at which the animal was raised. In their seminal work on *C. elegans* by Hedgecock and Russell (Figure 5.1) (1975) described 3 modes of thermotaxis: an isothermal tracking (around T_c), a positive and a negative thermotaxis (respectively exhibited below or above T_c).

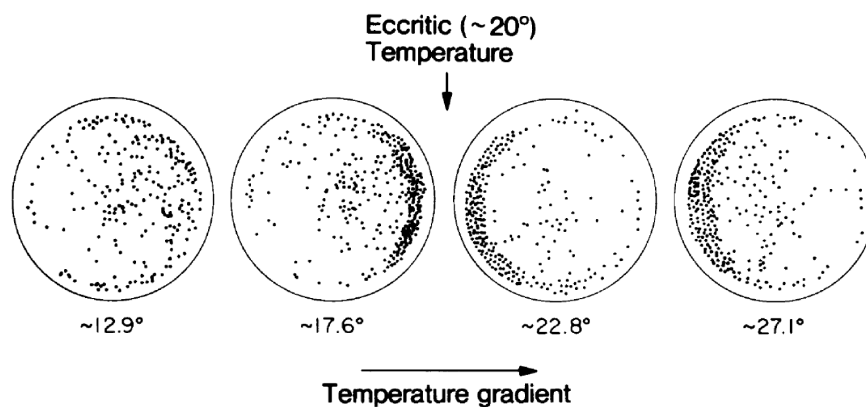


Figure 5.1: Position distribution of 20°C raised worms in a temperature gradient. Animals were deposited at the plate centers and allowed to run for one hour, chloroformed and their final positions were recorded by dots. Taken from Hedgecock and Russell 1975.

Thermosensory neurons

In 1995, Mori and Ohshima published an article where they identified the most important neurons for thermotaxis. By ablating individual cells, they showed that bilateral amphid sensory neurons (AFD) are extremely thermosensitive. They further found two groups of interneurons named AIY and AIZ, which are responsible for “thermophilic” behavior (moving toward warm region) and “cryophilic” behavior (moving toward cold region), respectively. They built a qualitative neuronal model, claiming that thermotaxis results from the interaction between thermophilic and the cryophilic drives, engaging the AFD, AIY and AIZ neurons, and a downstream comparator of the two drives involving RIA neurons.

Thermosensors

The molecular pathway engaged in thermosensation is still poorly understood in *C. elegans*. The TRP, a cation channel family, well studied in thermosensation in vertebrates, may be conserved in *C. elegans* (Garrity *et al.*

2010). The thermal sensitivity of AFD neurons relies on a recently identified cGMP-dependent signaling pathway (Ramot *et al.* 2008).

Isothermal tracking is a process in which worms align along and actively follow an isotherm. With this process they can minimize temperature fluctuations within 2°C of T_c (Luo *et al.* 2006). In order to do so, *C. elegans* continuously swings its head left and right during forward swimming (Figure 5.2b). The thermosensory neurons located on its head are thus alternatively exposed to a decreasing and increasing temperature. This periodic variation in temperature is used by the worm to correct its curvature and then stabilize its position on the isotherm. In Luo *et al.*, this dynamic mechanism is modeled such that the curvature is proportional to the temporal derivation of the temperature sensed by the head of the worm.

Negative thermotaxis

If the temperature is $>2^\circ\text{C}$ above T_c , *C. elegans* display a negative thermotactic behaviour, navigating down the thermal gradient toward T_c (Hedgecock and Russell 1975; Mori and Ohshima 1995). When *C. elegans* navigates in an homogenous environment its trajectory is an unbiased random walk alternating forward runs and large reorientations in the form of omega turns. The absolute heading angle after a given reorientation is random if the environment is isotropic. If a thermal gradient is present in the environment, the statistics of omega turns varies with the worm direction (Ryu and Samuel 2002). A worm moving toward colder temperatures will have a lower rate of abrupt turns thus a lengthening of the forward runs. Conversely, a worm moving toward warmer temperatures will have a higher rate of turns and thus a shortening of the forward runs. In Clark *et al.* (2007), the authors submitted *C. elegans* to time-varying gradient and show that the temporal information is sufficient to modulate the probability of reorientation. Negative thermotaxis is thus a biased random walk process relying on temporal information.

Positive thermotaxis

The behavior at low temperature ($>2^\circ\text{C}$ below T_c) is less clear. The original papers of Hedgecock and Russell (1975) and Mori and Ohshima (1995) reported a positive thermotactic behavior for worms raised at 25°C. However more recent publications (Ryu and Samuel 2002) show an atactic behavior and thus an unbiased random walk at temperature below T_c .

Plasticity

The preferred temperature T_c depend on environmental factors such as humidity, food concentration or cultivation temperature. Several articles show that *C. elegans* raised at a given temperature exhibit thermotactic behavior toward regions at the same temperature (Mori and Ohshima 1995; Hedgecock and Russell 1975; Kimura *et al.* 2004; Clark *et al.* 2007).

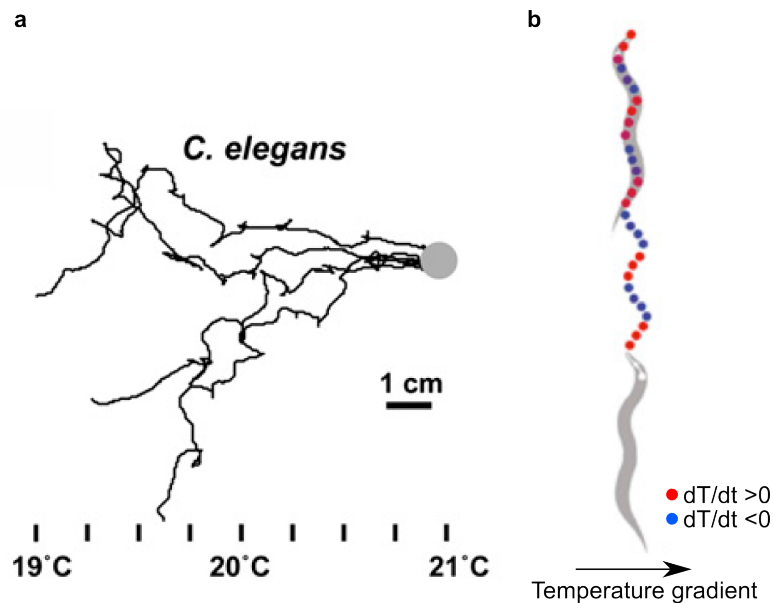


Figure 5.2: **a.** *C. elegans* negative thermotaxis is a biased random walk. Four *C. elegans* animals performing negative thermotaxis after being placed on a thermal gradient above their cultivation temperature (15 °C). Gray circle indicates starting point. Trajectories are stochastic, but show a clear tendency to drift down the thermal gradient toward the cultivation temperature. **b.** During isothermal tracking, *C. elegans* actively maintains its alignment to isotherms near its T_c . Schematic depiction of isothermal tracking. A pair of bilateral thermosensory neurons nears the nose of the animal phase-lock to the subtle temperature changes encountered during undulatory forward motion. This oscillatory signal drives directed gentle bending to maintain isothermal alignment. Adapted from Garrity *et al.* 2010.

Modeling the circuit

Using genetic tools and physiological studies, several groups have tried to dissect the neural circuit underlying thermotaxis in *C. elegans*.

The AFD neurons are central to this circuitry. Using genetically encoded calcium sensors and *in vivo* patch clamp recordings, Kimura *et al.* (2004) and later Clark *et al.* (2007) showed that AFD neurons respond to warming (Figure 5.4) and cooling, and can track temperature variation of 0.003-0.03°C/s. For steps stimuli, AFD follow changes in temperature with a delay $< 2s$. Moreover these neurons (Figure 5.4) have the ability to modulate intracellular calcium concentration only at temperature above T_c and this threshold can be modified by shifting animals to other growth temperature. Finally, Clark *et al.* (2007) described another amazing property of AFD neurons. Investigating calcium response in AFD neurons in freely moving worms under a spatial gradient of temperature, they found that AFD phase lock to the oscillations in temperature induced by left-right head swings.

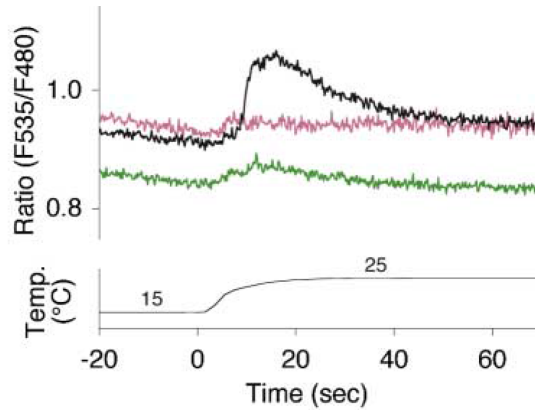


Figure 5.3: AFD neurons respond to warming. Taken from Clark *et al.* 2007.

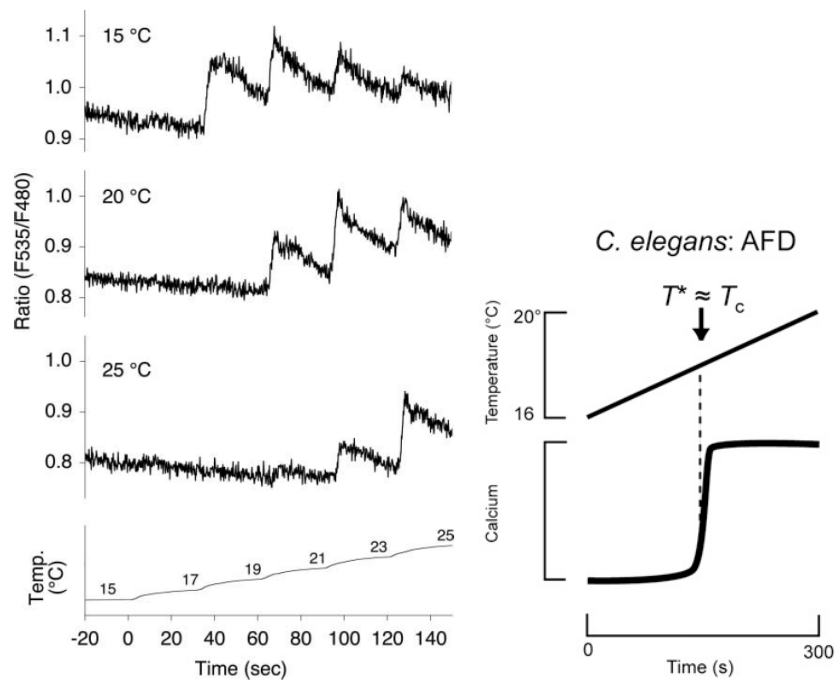


Figure 5.4: Left panel: The AFD Neurons responds to step-like warming above threshold temperature. *C. elegans* were grown at 20°C until the day before imaging and then cultivated at 15°C (top), 20°C (middle), or 25°C (bottom) overnight. The average ratio change during step-like warming is shown, displaying a variety of threshold correlated with the cultivation temperature. Taken from Clark *et al.* 2007. Right panel: Schematic calcium signal. Warming above a threshold, T^* , increases intracellular calcium in wild-type AFD neurons. T^* is variable and is approximately equal to the cultivation temperature, T_c . Taken from Garrity *et al.* 2010.

Despite the remarkable properties of the AFD neurons, their response are not sufficient to explain the multiples regimes of thermotaxis in *C. elegans* since they are able to encode sinusoidal stimuli near T_c and ramping a stimulus above T_c . Kuhara *et al.* (2008) showed that AWC olfactory neuron pair could be specifically responsible for the negative thermotactic behavior. AWC respond to

temperature above T_c and in the temperature range of negative thermotaxis, these neurons display higher levels of activity than around T_c (the isothermal tracking range) (Biron *et al.* 2008). AWC could be the distinguishing pathway between isothermal tracking and negative thermotaxis. Moreover it has been shown (Gray *et al.* 2005; Chalasani *et al.* 2007) that AIB and AIZ interneurons promote turns whereas AIA and AIY interneurons inhibit turns. All these results suggest a basic circuit architecture generating thermotactic behavior.

For *isothermal tracking*, *C. elegans* needs to suppress large or reversal turns. During this regime, AFD neurons have an increased activity and AWC neurons have a decreased activity. These activities are integrated by AIY and AIB interneurons to promote tracking.

For *negative thermotaxis*, if $T > T_c$, AFD and AWC neurons have an increased activity. The downstream interneurons AIY, AIZ, AIA, AIB integrate this activity which increases turn probability when the worms move up the gradient. If the temperature decreases, AFD and AWC have a decreased activity, which decreases the turn probability.

5.2.2 *Drosophila melanogaster* larvae

When *D. melanogaster* larvae are exposed to a temperature gradient, they navigate away from both excessively hot (negative thermotaxis) and excessively cold regions (positive thermotaxis) to reach a well-defined range of temperatures (Liu *et al.* 2003; Luo *et al.* 2010; Klein *et al.* 2015; Barbagallo and Garrity 2015) (Figure 5.5). Typically, positive thermotaxis is observed when larvae are navigating below 20°C whereas negative thermotaxis takes place when the temperature is above 30°C.

The trajectory of *D. melanogaster* larvae consists of two alternative motor programs: runs and turns (Figure 5.5). During the first phase, the larva runs forward and its head is aligned with the rest of its body. During turns, the larva pauses its forward movement and sweeps its head left and right one or multiple times. At the end of a turning event, the head faces a new selected direction, which will be the direction of the next run. Thermotactic strategy is a behavior that modulates the statistics of runs and turns.

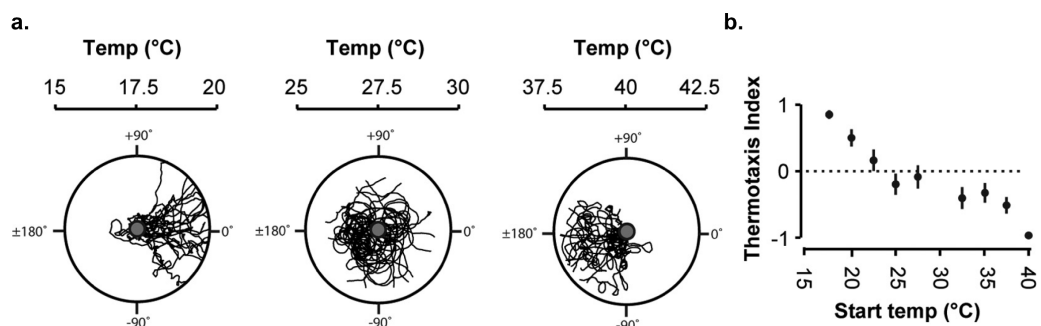


Figure 5.5: Thermotactic navigation in *Drosophila* larvae. **a.** Representative trajectories of wild-type larvae navigating in an environment exhibiting a linear thermal gradient (0.5°C/cm) on 9 cm diameter agar plates. Start temperatures were 17.5°C (left), 27.5°C (middle), and 40°C (right), respectively. **b.** Thermotaxis index of wild-type larvae navigating linear thermal gradients

($0.5^{\circ}\text{C}/\text{cm}$) after starting at different temperatures. The thermotactic index is defined as $(t_{\text{warm}} - t_{\text{cold}})/(t_{\text{warm}} + t_{\text{cold}})$ where t_{warm} and t_{cold} are the total time spent in the warmer and colder half of the gradient, respectively. Positive (resp. negative) indices thus reflect a preference for warmer (resp. colder) temperatures, while a null index indicates no temperature preference. Taken from Luo *et al.* 2010.

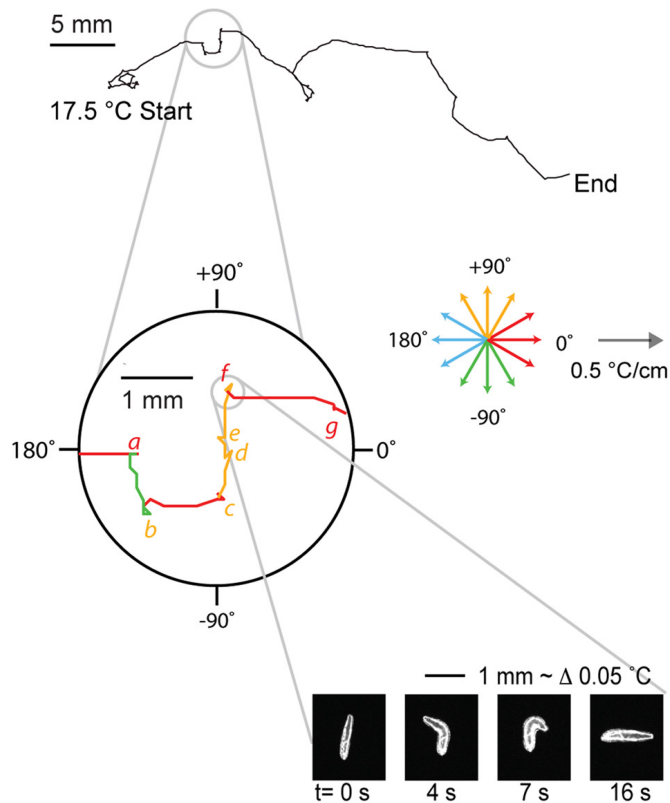


Figure 5.6: Representative trajectory of a wild-type larva crawling up a linear thermal gradient ($0.5^{\circ}\text{C}/\text{cm}$ steepness, 17.5°C start temperature) depicting the characteristic sequence of straight runs interrupted by turning events. The zoomed inset shows a portion of the trajectory, highlighting a series of distinct runs and seven turning events (indicated by letters a to g). For presentation purposes, a quadrant color code is presented to distinguish runs with different headings relative to 0° , the direction of the temperature gradient. Red, Runs pointed toward warmer temperatures with headings between -45° and $+45^{\circ}$. Orange, Transverse runs with headings between $+45$ and $+135^{\circ}$. Green, Transverse runs with headings between -45° and -135° . Blue, Runs pointed toward colder temperatures with headings $>135^{\circ}$ or $<-135^{\circ}$. For the representative turning event indicated by the letter f, a series of video frames reveal the details of the larva's head sweeps: the first head sweep is to the larva's left, the second head sweep is to the larva's right, and the new run is initiated with a heading change of -83.0° with respect to the previous run. Taken from Luo *et al.* 2010.

Positive thermotaxis

1. Similar to the biased random walk of *C. elegans*, *D. melanogaster* larvae modulate the rate of turning and thus the run duration during positive phototaxis. Note that run speed is insensitive to the temperature gradient.
2. As for negative phototaxis in *D. melanogaster* larva (chapter 3), turning events are used to correct the orientation of the body in the direction of warmer regions. In Luo *et al.* (2010), the authors show that the larva modulates the standard deviation of the distribution of heading direction changes to have “more options” when the larva is in a cold region and to maintain heading when the region is already warm. Moreover, they show that the range of head sweep during a turning event depends on the preceding run direction: the maximum amplitude of head sweeps is higher after runs toward colder temperatures (Figure 5.7).
3. When larvae pause and begin head sweep, the direction of the first head sweep is random (Luo *et al.* 2010) whereas the probability of terminating the turning events and run again is biased. If the head sweeps toward warmer region it is likely that the larva will interrupt the turn and run again.

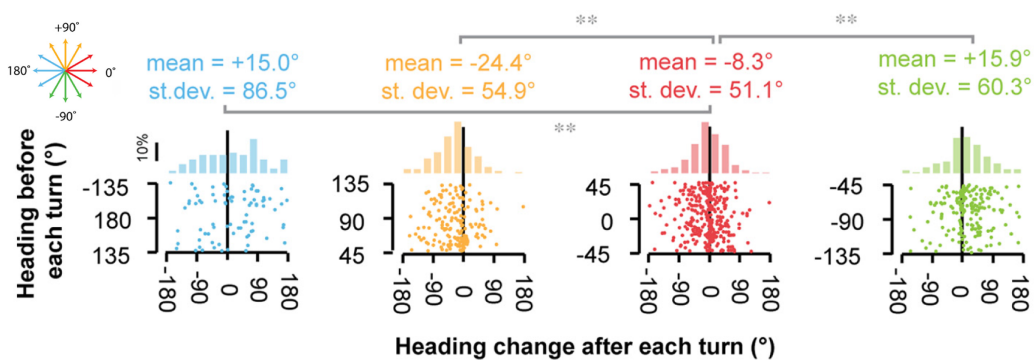


Figure 5.7: Statistics of heading changes generated by each turning event as a function of the run heading immediately before the turning event. Negative and positive heading changes correspond to rightward and leftward turns, respectively, from the larva’s point of view. Scatter plots (bottom) depict all measured turning events, separated into quadrants depending on the run heading immediately before each turning event. Histograms of these measurements (top) show the probability distributions of heading changes. The mean and standard deviation for each heading change distribution is shown above each histogram. On the left top part of the panel the color code corresponding to angles is provided. Taken from Luo *et al.* 2010.

Negative thermotaxis

Negative thermotaxis uses exactly the same elements as positive thermotaxis to crawl toward colder region.

A temporal strategy

In Luo *et al.* (2010) and Klein *et al.* (2015), the authors tried to decipher whether thermotactic behavior in larvae relies on a *tropotaxis* (the gradient of

the temperature is measured instantaneously by two sensors at different locations) or a *klinotaxis* (the gradient of the temperature is probed, using one unique sensor, at two different time points corresponding to two different locations) strategy. They developed a virtual-reality assay in which the larva can receive a laser heat pulse in function of its head orientation. In this assay, larvae only undergo temporal changes of temperature. They observed that the behavioral statistics of runs and turns are the same as observed during navigation in a spatial gradient of temperature. In the end, positive and negative thermotaxis is a response to temporal changes in temperature.

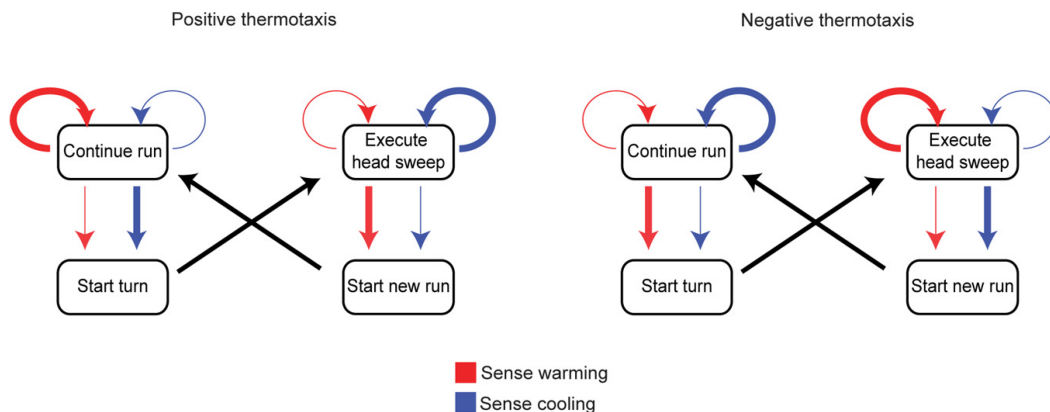


Figure 5.8: Schematic of transitions between the motor program for forward crawling during runs and the motor program for head sweeping during turns, and the dependence of these transitions on temporal variations in temperature. The dependence of these transitions on temperature yield two elements of navigational strategy during positive thermotaxis or negative thermotaxis, namely modulation of run duration and modulation of turn direction. When the larva detects warming or cooling during either runs or head sweeps, it raises (thickened arrows) or lowers (thinned arrows) the probability per unit time of transitions between the motor programs or the probability per unit time of remaining within a motor program. Adapted from Luo *et al.* 2010.

Thermosensory neurons

Although a detailed description of the sensory system underlying positive or negative thermotaxis is still lacking, some features are now well established (Liu *et al.* 2003; Rosenzweig *et al.* 2005; Klein *et al.* 2015). Thermosensory neurons activated by high or low temperature and connected to a shared downstream circuit have been identified. In *D. melanogaster* larva, two subsets of neurons are known to be implicated in thermotaxis: the terminal organ (a structure with about 30 neurons) and the chordotonal neurons (located on the larva body). Silencing of terminal organ neurons prohibits positive thermotaxis (Luo *et al.* 2010). Similarly chordotonal neurons respond to temperature variation. Transient Receptor Potential (TRP) A1 expressing neurons have been identified as sensors for negative thermotaxis (Rosenzweig *et al.* 2005) since these channels respond to positive changes of temperature. More recently Klein *et al.* used optogenetics activation to reveal thermosensory neurons in the dorsal organ ganglion that respond to both cooling and warming. These new thermosensory neurons are reminiscent of AFD neurons in *C. elegans*.

5.2.3 Conclusion

Comparisons of thermotactic behavioral strategies in D. Melanogaster larvae, C. elegans and E. Coli.

	Deterministic Steering	Random Walks		
	<i>C. elegans</i> isothermal tracking	<i>C. elegans</i> negative thermotaxis	<i>Drosophila larva</i> negative thermotaxis	<i>E. coli</i> chemotaxis
Overall trajectory	Long runs steered along isotherms, beginning and ending with abrupt turns	~straight runs punctuated at random by turns	~straight runs punctuated at random by turns	~straight runs punctuated at random by turns
Run speed	Unmodulated	Unbiased	Unbiased	Unbiased
Frequency of abrupt turns	Suppressed	Biased	Biased	Biased
Run orientation	Deterministic steering along isotherms	Unbiased	Biased	Unbiased
Direction of abrupt turns	Unbiased	Unbiased	Biased	Unbiased

Figure 5.9: Comparison of behavioral strategies that govern *C. elegans* thermotaxis, *D. melanogaster* larva thermotaxis, and *E. coli* chemotaxis. Both *C. elegans* thermotaxis and *E. coli* chemotaxis are a biased random walk, biased on the rate of reorientation events. *D. melanogaster* thermotactic behavior seems to be an improvement of these strategies, enriched for turning toward favorable headings. Taken from Garrity *et al.* 2010.

5.3 Thermotaxis in vertebrates

5.3.1 Structure of thermosensation

Despite the numerous studies on thermosensory neurons that have been published over the last decade (Moqrich *et al.* 2005; Dhaka *et al.* 2006), a holistic view from circuit to behavior is still lacking on thermotaxis and thermosensation in vertebrates. What is well established is the architecture of the circuit at the organ level: in rodents and teleost fish (Robson 2013), the thermal stimulation is detected by the trigeminal ganglion and the dorsal root ganglion. These two peripheral organs encompass somatosensory cells that respond to thermal, chemical or mechanical stimuli (Lumpkin and Caterina 2007).

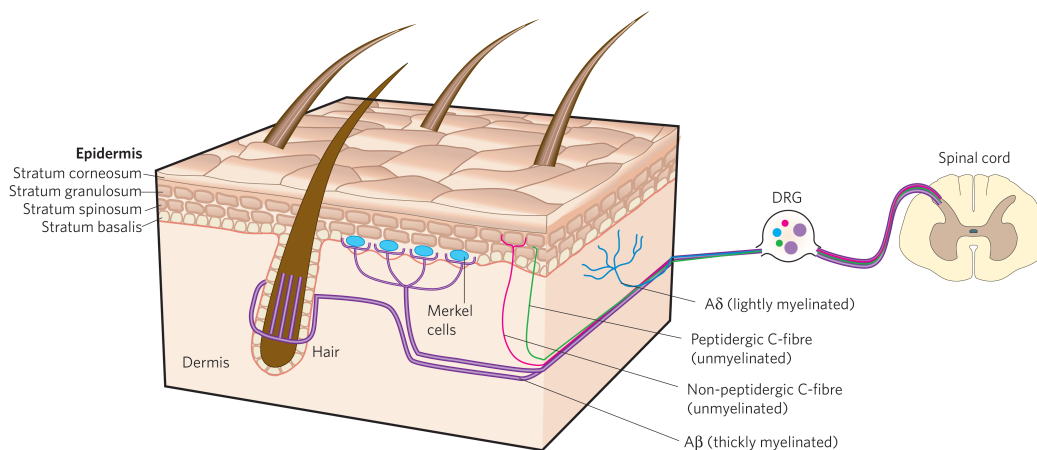


Figure 5.10: Diversity of somatosensory neurons in the skin in mammals? The skin is innervated by somatosensory neurons that project to the spinal cord through the dorsal root ganglion. A β -fibres, such as those that innervate Merkel cells and those around hair shafts, are thought to be touch receptors. A δ -fibres and C-fibres include thermoreceptors and nociceptors. Taken from Lumpkin and Caterina 2007.

In mammals, the transient receptor potential (TRP) superfamily composed of nine thermoTRPs (TRPV1, TRPV2, TRPV3, TRPV4, TRPM2, TRPM4, TRPM5, TRPM8, and TRPA1) has been identified as the thermosensors. Like other ion channels, thermoTRPs can be gated directly by sensory stimuli eliciting an action potential. Distinct temperature thresholds activate these ion channels (Dhaka *et al.* 2006; Saito and Shingai 2006). The work of Saito *et al.* suggests that thermosensation mechanisms have changed throughout vertebrate evolution. Fish lineage like *Danio rerio* (zebrafish) lacks some TRPs but possesses TRPV1 and TRPV2, which are very sensitive thermosensors (Gau *et al.* 2013).

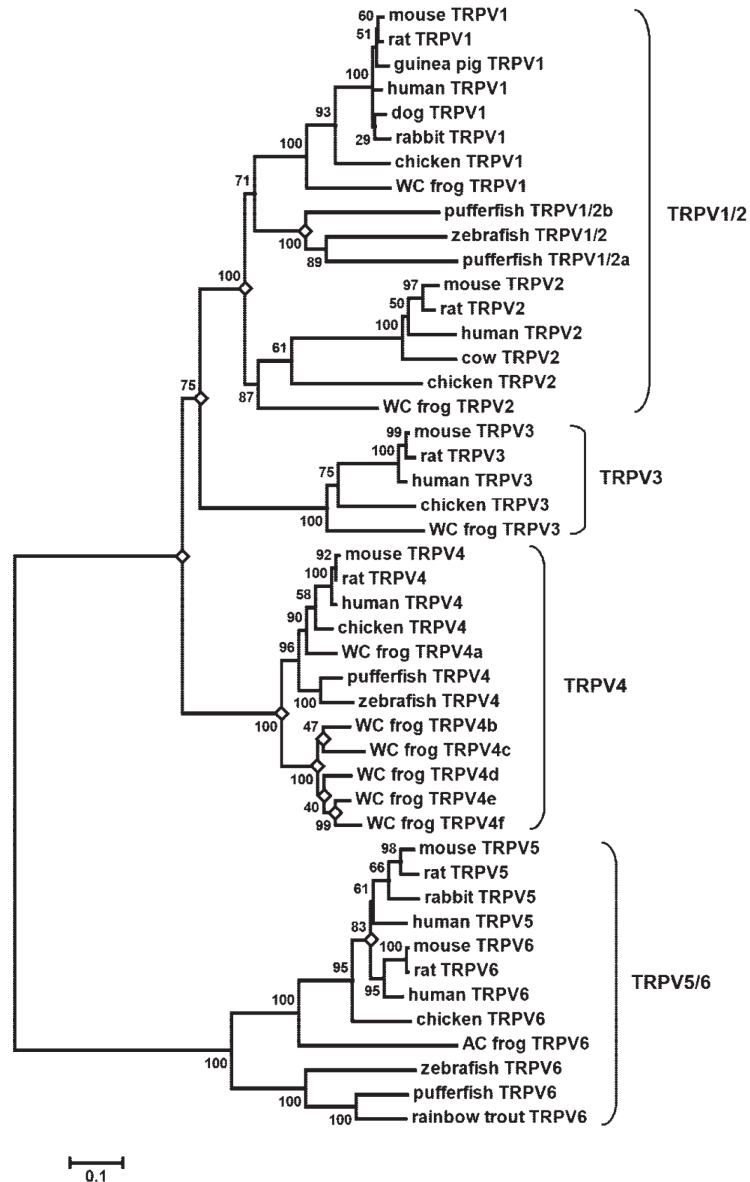


Figure 5.11: Phylogenetic tree of the vertebrate transient receptor potential-vanilloid (TRPV). Amino acid sequences from ankyrin (ANK) repeat 1 to TRP domains (392 residues) were used for estimating the numbers of substitutions by applying the Jones-Taylor-Thornton (JTT) model. The statistical confidence (bootstrap value) is indicated next to each interior branch. Gene duplication events are designated by open diamonds. Taken from Saito *et al.* 2006.

In zebrafish larvae, the trigeminal ganglion and the dorsal root ganglion exist, and are formed respectively at 1 and 5dpf (Robson 2013). According to Prober *et al.* (2008), zebrafish larvae respond robustly with increased locomotion to thermal, chemical, and mechanical stimuli. In the recent study of Gau *et al.* (2013), the authors show that TRPV1 and 2, expressed in the trigeminal ganglion, are activated by high temperatures above 25°C. Further studies using genetic mutants will be needed to confirm that TRPV1 and 2 are the unique thermosensors present in zebrafish.

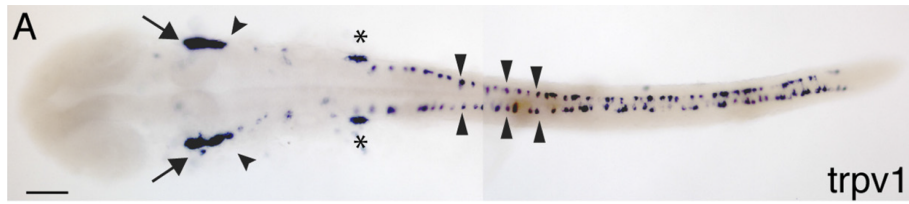


Figure 5.12: Zebrafish TRPV1 is expressed in different sensory neuron populations. The nociceptive ion channels *trpv1*, *trpa1b*, and *p2x3b* label neurons in zebrafish trigeminal ganglion. In situ hybridization of *trpv1* at 24 hpf shows that it is expressed in several sensory structures: the trigeminal (arrow) and anterior lateral line ganglion (arrowhead), the posterior lateral line ganglion (*), and Rohon Beard sensory neurons (flat arrowheads). Taken from Gau *et al.* 2013.

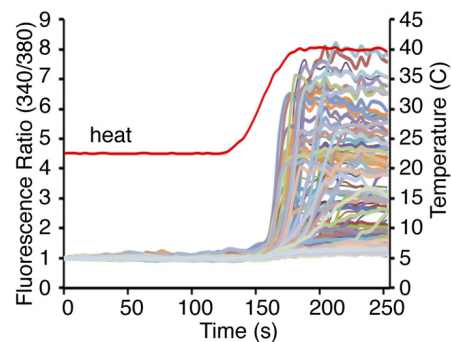


Figure 5.13: Zebrafish TRPV1 is activated by heat. Responses of zebrafish TRPV1 transfected HEK cells assessed by ratiometric calcium imaging. Temperature changes are shown by the red line and scale on the right. A large subset of TRPV1-expressing HEK cells respond to a heat ramp from 22°C to 40°C. Taken from Gau *et al.* 2013.

5.4 Thermotaxis in zebrafish

Compared to invertebrates, behavioral and neuronal coding of thermal navigation is still poorly understood in vertebrates. As indicated above, zebrafish larvae possess thermosensory neurons that are active from 3dpf on (Gau *et al.* 2013) and are thus able to sense external temperature at early larval stages. The publications on zebrafish heat sensation are scarce and it remains unknown how zebrafish thermosensory channels work, and how the brain integrates thermosensation to produce adequate motor behavior. However, the work of Drew Robson during his PhD (2013) is full of new insights on the thermotactic behavioral aspects of larval zebrafish. In the following I will summarize the results of Robson's dissertation which have motivated the development of a light sheet imaging set up to track the neuronal basis of thermotaxis as described in the next section.

Robson developed a set of behavioral assays to study thermotaxis of freely swimming larvae: a chamber to deliver tightly controlled and stable spatial thermal gradient and a thermal waveform chamber to deliver a time-varying thermal stimulation. Figure 5.14a-b compares trajectories of larvae navigating in a thermally uniform environment and in a chamber where the temperature increase radially from 25°C to 37°C. In the latter, The larvae stays in the central region of lower temperature, as quantified by the density function to find a larva swimming at a given temperature (Figure 5.14c). Notice that this density distribution falls to zero in the hot regions.

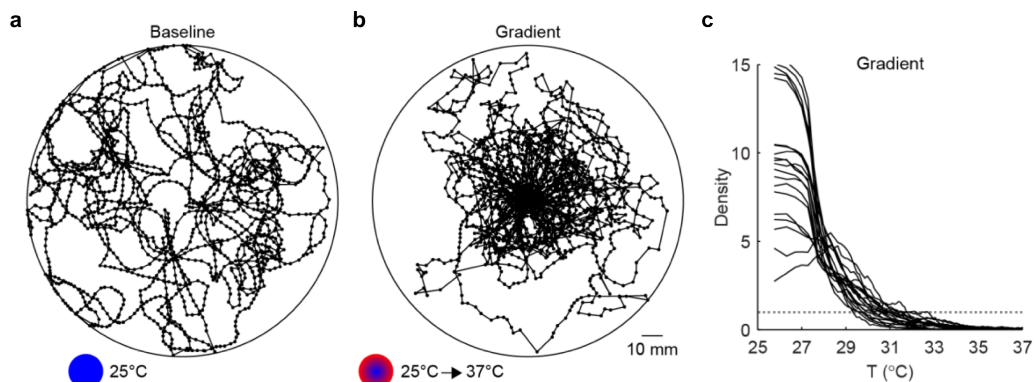


Figure 5.14: Representative behavior during the thermal navigation assay. **a**, Trajectory of a 7 dpf larval zebrafish during a 30 min baseline period in which the entire chamber is held at 25 °C. An acclimation period of 5 min precedes the baseline period, and is excluded to avoid handling artifacts introduced by loading the fish into the chamber. **b**, Trajectory of the same animal during a 30 min gradient period in which the chamber temperature increases radially from 25 °C in the center to 37 °C at the edges. A gradient formation period of 5 min precedes the gradient period, and is excluded from analysis since the stimulus is changing during this period. **c**, Comparison of radial distributions in thermal gradient. Individual distributions of 20 larval zebrafish along the radial axis of the chamber during the 30 min gradient period. Dotted gray line indicates expected density assuming uniform coverage of the chamber. Taken from Robson 2013.

Negative thermotaxis

Using high-speed imaging and tracking software, Robson was able to resolve individual movements and extract key parameters of fish navigation. From the series of discrete movements called swim bouts, he extracted four components: (i) the dwell time, which is the time between two swim bouts, (ii) the displacement, which is the distance between the beginning and the end of a swim bout, (iii) the turn magnitude, which is the absolute value of angle variation during a swim bout and (iv) the turn direction, which is the sign of angle variation during a swim bout. For each of these kinetic features, he analyzed whether its statistics was dependent on the absolute value of the temperature just before the swim bout or/and on the gradient of temperature experienced by the larvae during the preceding movement. Note that all the data provided in Robson's dissertation were obtained in a regime of negative thermotaxis conditions i.e. the temperature gradient ranges from a preferred temperature to a noxiously hot temperature (typically 25°C to 37°C).

The main results are summarized in figure 5.15. The displacement increases with the absolute temperature and depends on the gradient of temperature, such that the larvae will perform longer swim bout in warm region even if the gradient has just decreased. The dwell time is found to be a sole a function of the absolute temperature: it decreases with the temperature, i.e. swim bouts are more frequent in warm regions. The turn magnitude increases with both T and ΔT i.e. larvae will perform turns of larger amplitude in warm regions and if the temperature is increasing ($\Delta T > 0$). Finally, turn bias is controlled by the gradient of heat:

“When larvae move up the gradient, they tend to bias their turns so that they consistently turn toward the direction currently specified by their turn state. Once they start moving down the gradient, they cease to strongly bias their turns in the preferred turn direction”.

Negative thermotaxis in zebrafish larva can thus be summarized as follows: in warm regions, larvae move faster (by increasing the swim bouts frequency and distance travelled for each swim bout) and make bigger turns to maximize the probability to find a colder region; if the larvae swim down the gradient of temperature, then the larvae is less likely to change its orientation (since it is the “good” one) to keep descending down the thermal gradient.

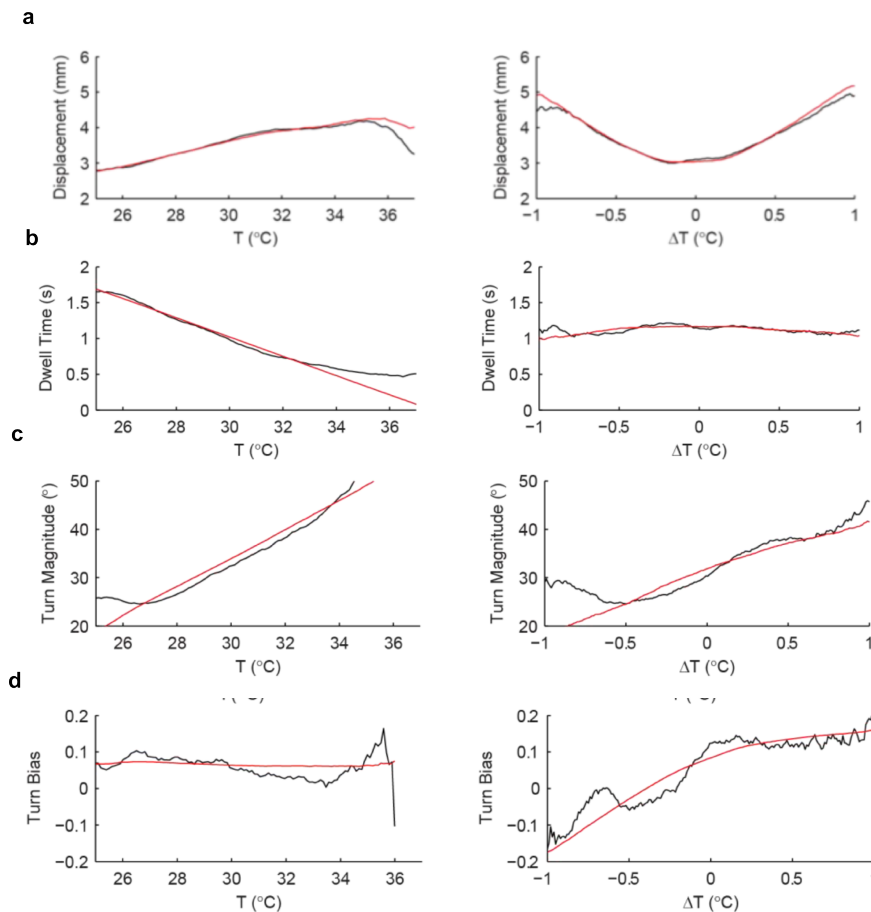


Figure 5.15: Relationship between T , ΔT , and displacement (a), dwell time (b), turn magnitude (c) and turn bias (d) in the gradient condition. Estimated component by KDE (black line) and regression (red line) as a function of T (left) and ΔT (right). Taken from Robson 2013.

A temporal strategy

To distinguish whether larvae directly probe the spatial gradient of temperature or infer it using spatio-temporal sampling, Robson used a thermal waveform chamber to deliver a time-varying thermal stimulation. A sinusoidal thermal stimulus was presented to larvae (Figure 5.16a). The relationship between locomotor components and absolute or gradient temperature are conserved. Turn magnitude increases in the rising phase of the sine wave of temperature (Figure 5.16c and e). Turn bias is high in rising phase of the stimulus and low or even negative in falling phase of the stimulus (Figure 5.16b and d).

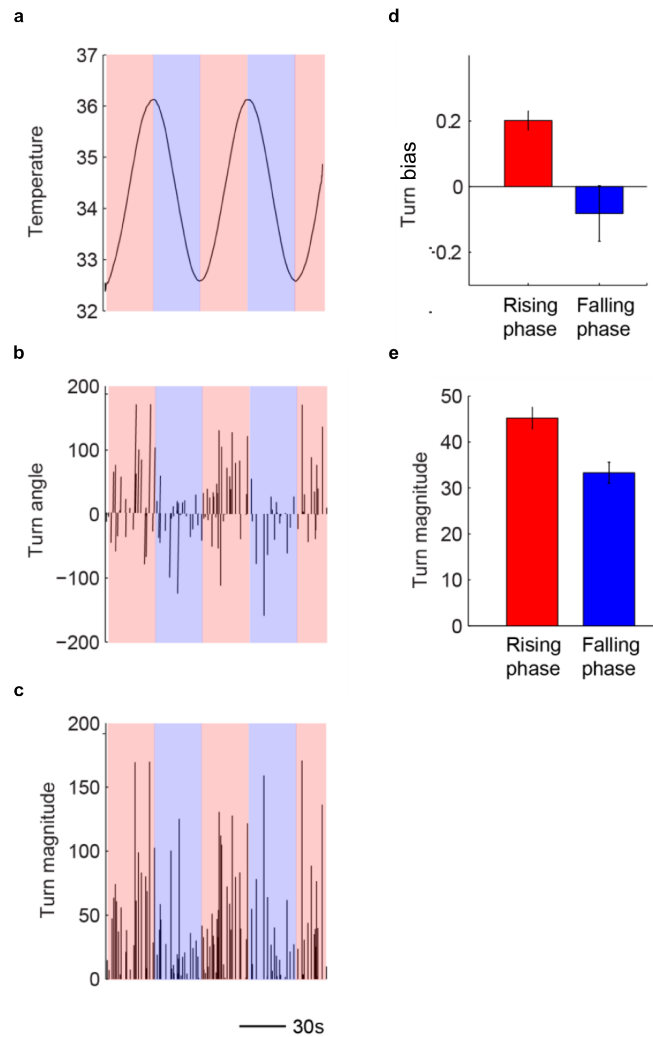


Figure 5.16: Example of a 7dpf zebrafish responding to sinusoidal thermal stimuli. **a**, Sinusoidal thermal stimulus was presented with a 2 °C peak to peak amplitude oscillation. **b**, Turn angles occurring during two cycles of the thermal stimulations. The animal favored positive turns during rising temperature, which would correspond to a turn state of +1. **c**, Turn magnitudes during two cycles of the thermal stimulus at a high baseline temperature. Turn magnitudes are higher during the rising phase than the falling phase. **d**, Turn bias is elevated during rising phase, but decreases and becomes negative during the falling phase. **e**, Average turn magnitude during the rising phase significantly exceeds the falling phase. Adapted from Robson 2013.

Comparing zebrafish with others

This thermotaxis strategy can be compared with that at play in invertebrates. As detailed in the preceding section, *C. elegans* negative thermotactic behavior is a biased random walk. *Worms* bias the rate of turning events (omega turns) such that the runs will be longer if they are following a decreasing gradient of temperature. During turning events the next direction is strictly random. It is difficult to compare zebrafish thermotaxis to *C. elegans* since there is no distinction between runs and turns in zebrafish locomotion.

However the lengthening of displacement that increases with temperature in zebrafish negative thermotaxis is reminiscent of *C. elegans* strategy. *Drosophila melanogaster* thermotaxis has more common points with the zebrafish thermotactic behavior. Indeed *D. melanogaster* larvae and zebrafish larvae modulate their turn magnitude upon temperature gradient. Unlike *D. melanogaster* larvae, which sense the temperature during the head sweep phase to find the preferred direction for the next run, zebrafish larvae do not use a sensing phase. As Robson showed in its work, zebrafish developed another strategy: “favoring a preferred turn direction in response to rising temperature and then suppressing the expression of this preference when temperature is flat or falling”.

5.5 Whole-brain imaging characterization of zebrafish heat sensation in zebrafish larva

5.5.1 Introduction

Zebrafish larva is an ideal vertebrate to investigate behavioral strategies and to understand neuronal coding. Taxis behaviors such as phototaxis (chapter 3) or thermotaxis always rely on the ability to probe the spatial gradient of a stimulus $\nabla\mathcal{S}$ (light for phototaxis or temperature for thermotaxis) to eventually infer the location of the source of the stimulus. Two strategies are then possible to probe this spatial distribution: a *tropotaxis* strategy where the animal evaluates $\nabla\mathcal{S}$ directly using two sensors at different locations like the two eyes, or a *klinotaxis* strategy where the animal evaluate $\nabla\mathcal{S}$ using a unique sensor that measure \mathcal{S} at two different time points after a displacement corresponding to two different locations.

In the case of phototaxis, we showed that zebrafish larvae use both tropotaxis and klinotaxis. In Wolf *et al.* (2017) we reported that self-oscillating hindbrain population (HBO) that acts as a pacemaker for ocular saccades and controls the orientation of successive swim-bouts is a key to this mixed tropo/klinotaxis leading to phototaxis. The HBO self-sustained oscillations allow the animal to actively explore the light angular gradient. The tropotaxis strategy is then the following: asymmetric visual stimuli enhance the activity of the HBO clusters ipsilateral to the eye that receives the larger illumination, which in turn biases the fish reorientation towards the light source; and a gaze shift-induced light increment reinforces the active HBO subpopulation (ipsilateral to the new gaze direction), thus delaying further left–right transition. Over multiple cycles, this process yields a statistical bias of the fish turning probability toward the brightest region. To explain the klinotaxis strategy, we showed that the HBO is sensitive to symmetric visual stimuli in a state-dependent manner such that an increase of light reinforces the active HBO subpopulation and thus keeps the orientation of the swimming in the current direction, leading statistically to brightest region.

The behavioral mechanism for photo-klinotaxis in zebrafish show strong analogy with what Robson established using behavioral assays in thermotaxis. It is thus tempting to suggest that the same neuronal circuit (notably the HBO) may be at play for both goal-directed navigation. In the case of thermotaxis a very simple scaling argument demonstrates that zebrafish larvae likely use a *klinotaxis* strategy: zebrafish larvae are small animals (in the mm range), such that a temperature gradient over the scale of the animal body is almost instantaneously smoothed out (in less than ~ 1 s). The results described by Drew Robson in his PhD dissertation (2013) corroborate this intuition. As we saw just before zebrafish strategy for negative thermotaxis is to favor a preferred turn direction in response to rising temperature and to suppress this preference if the temperature falls. In other word, when larvae are navigating up the gradient they bias their turns to keep turning in the direction they were already exploring as if saying: “I am still moving up the gradient, so keep turning and for sure you will finally find a descending gradient”. If the temperature begins to fall, then larvae

stop biasing the turns and so they descend the gradient stochastically. These behavioral results look a lot like the state-dependent response of HBO to illumination changes!

With that in mind, we decided to add a heat stimulation device onto the 1P light-sheet microscope. With Guillaume Le Goc (an undergraduate student, soon to start his PhD in the lab), we built a stimulation apparatus that allowed us to deliver hot or cold water pulses. We used it to map thermal responsive neurons zebrafish larvae, and then to specifically analyze how the HBO's oscillatory dynamics may be modulated by temperature changes.

Note that at the time of writing, these experiments are still preliminary.

5.5.2 A heat stimulation apparatus for light-sheet imaging microscope

In Haesemeyer *et al.* (2015), the authors developed a heat-stimulation system based on a fiber-coupled infrared laser that delivers precise heat-stimuli to a larval zebrafish. In this stimulation system, the heat stimulus arises from the absorption of infrared light by larvae pigments located on the skin and the eyes. Our approach was to develop a more naturalistic stimulation protocol since larvae sense heat at the contact with water and not via infrared light absorption.

The heat stimulation apparatus (Methods)

Our stimulation set-up aims at delivering puffs of hot or cold water to an embedded larva in agar (Figure 5.17a). Two separate water delivery paths were built for hot or cold water.

For hot water, a 50 mL Eppendorf tube is placed about 1.20m above the fish pool. A pipe leads the water to the pool. A computer-controlled microvalve allows us to instantaneously (within 1ms) turn on or off the flow. A heating wire is wrapped around the water pipe. The wire and the pipe are held together with thermoplastic coating. A type K thermocouple (National Instrument) is inserted within the water pipe and positioned in the middle of the heated segment in order to monitor the water temperature of the water inside the pipe. The thermocouple is connected to a temperature proportional-integral-derivative (PID) controller along with the heating wire. The measured temperature (control temperature, T_c) is enslaved on a user-set target temperature (temperature set point, T_{set}). A thinner pipe is inserted at the outlet of the water supply pipe over a length of ~25cm to fetch hot water, which is then delivered in the pool via a short metal hose (1cm). The latter is placed in front of the fish, tethered in agarose and held in a glass capillary.

For cold-water delivery, a Huber Ministat 240 apparatus is used. Then, like for the hot water apparatus, a thin pipe is inserted at the outlet of the water supply. This pipe delivers the water in the pool via the same metal hose.

(Figure 5.17a)

Calibration of the apparatus

To calibrate the heat stimulation apparatus and properly control the temperature experienced by zebrafish larvae, we replace the embedded fish by a thermocouple type K embedded in agar (Figure 5.17b). We deliver 17 puffs of water at a given T_{set} and we measure the temperature T_{calb} sensed by the thermocouple in agar. The puffs are first separated by 5s. This protocol is repeated after a 60s idle-time for a stimulation period of 10s and 15s. The peak value of the measured temperature is noted T_m , and the height of the peaks is noted ΔT (Figure 5.17c). We then plot the average T_m and the average height of the peaks ΔT as a function of the set temperature T_{set} . Both T_m and ΔT increase

linearly with T_{set} (Figure 5.16d and e). From a temporal point of view, our heat-stimulation set-up allows to deliver short pulses of water with a 1s transition time (the temperature ramps up to its peak value T_m in ~ 1 s). In order to precisely control the temperature experienced by the fish during an experiment, we chose to calibrate the apparatus after each imaging run.

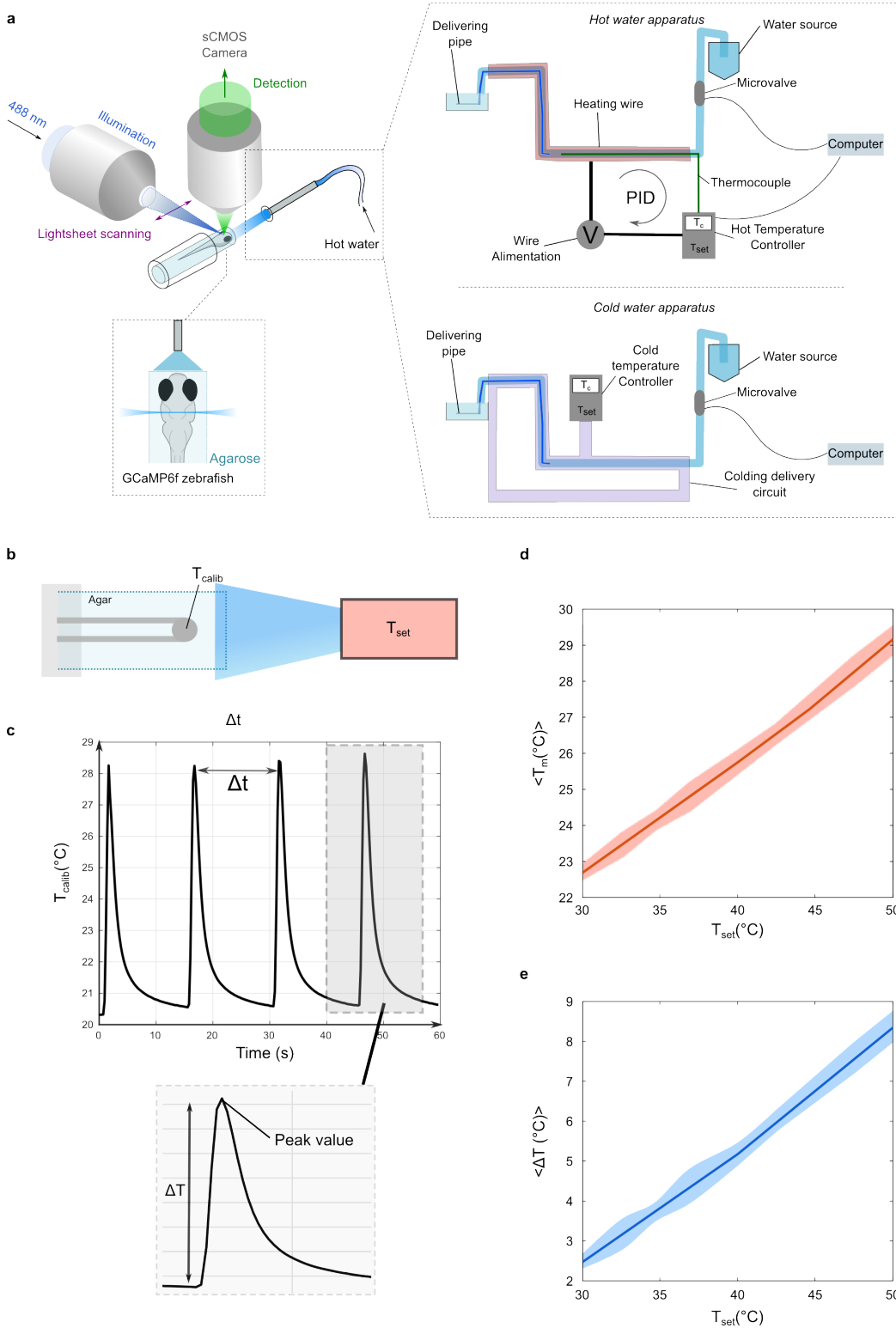


Figure 5.17: **a**, One-photon light-sheet functional imaging set-up with heat stimulation apparatus. **b**, Scheme of the calibration set-up: a thermocouple is embedded in agarose and set at the same distance the fish will be during the experiment. The experimentalist sets a temperature T_{set} to the apparatus. The thermocouple measures an absolute temperature T_{calb} . **c**, Typical trace recorded during the calibration of the set-up. **d**, Mean temperatures values measured with the calibration thermocouple as a function of the temperature set to the apparatus. Shaded region represents standard deviation. **e**, Mean peaks values (ΔT) as a function of the temperature set to the apparatus. Shaded region represents standard deviation.

5.5.3 Whole brain imaging of heat-perception in zebrafish larvae

Response map of heat stimulations

To evaluate the neuronal response of zebrafish larvae to heat stimulation, we successively submitted the animal to 6 different thermal stimuli, while recording the neural activity of the entire brain. In a first series of experiment, 40 heat pulses were delivered at random times. The associated dorsal projection of the trial-averaged response maps is presented in Figure 5.18. These maps were obtained by averaging data from four 6dpf fish using CMTK registration.

A large number of neurons were found to be responsive to heat stimulations in the telencephalon, habenula, optic tectum, cerebellum and hindbrain. As expected, these maps depend on the value of the temperature variation (ΔT) and display a graded activity as a function of $|\Delta T|$. The larger $|\Delta T|$, the more neurons are responsive.

Region 1: For positive values of ΔT , the hindbrain response is very sensitive to the value of ΔT . For $\Delta T=1.2^\circ\text{C}$, regions located in the posterior hindbrain, in rhombomeres 5 to 7 (region 1 in figure 5.18) are silent, but they display large responses to stimulation at $\Delta T=3^\circ\text{C}$ and 4.5°C .

Region 2: Similarly, more neurons in the rhombomere 1 (region 2) and the cerebellum respond to $\Delta T=3^\circ\text{C}$ and 4.5°C .

Interestingly, the sign of the temperature variation gives the largest difference between the response maps.

Region 1: The hot-responsive posterior hindbrain (rhombomeres 5 to 7 - region 1) is unresponsive to cold stimuli, as can be seen in the response map for $\Delta T < 0$.

Region 3: The ensemble of neurons in rhombomere 1 and cerebellum (region 3) display activity upon stimulations with $\Delta T < 0$, but remains silent for stimulations with $\Delta T > 0$.

Thus, it seems that distinct neuronal pathway are engaged during positive or negative variations of temperature.

These differences become more apparent when one analyzes in details some coronal, dorsal or sagittal sections of the response map (Figure 5.19 and 5.20).

Region 4: Left and right habenula are sensitive to stimulations with $\Delta T > 0$, whereas only left habenula is responsive to $\Delta T < 0$ (region 4 in left panels, Figure 5.19).

Region 5: In figure 5.19, one can notice that a ventral region in the “mesencephalon tegmentum”, is responsive to $\Delta T < 0$ and silent for $\Delta T > 0$ stimulations.

Region 6: An important difference between positive and negative ΔT is that the neuropil region 4 located in the lateral areas of the hindbrain (Figure 5.20) is very sensitive to $\Delta T < 0$ and silent for $\Delta T > 0$.

Region 7: the telencephalon seems sensitive to both $\Delta T > 0$ and $\Delta T < 0$ stimulations (Figure 5.19).

Region 8: In the cerebellum, two symmetric neuronal ensembles, in the form of oblique stripes, respond to negative temperature change ($\Delta T < 0$) but remain silent for $\Delta T > 0$. Conversely, a group of neuron in the most dorsal region of the cerebellum is sensitive to $\Delta T > 0$ stimuli.

Method

The red color of the response map encodes a coefficient R for each voxel, calculated using the $\Delta F/F$ signal. For each ΔT :

$$R = \left\langle \frac{1}{5} \int_{t_{stim}}^{t_{stim}+5} \left[\frac{\Delta F}{F}(t) - \frac{\Delta F}{F}(t_{stim}) \right] dt \right\rangle_{all\ stim}$$

Where t_{stim} is the stimulation onset time.

We chose to compute R as the time averaged response between t_{stim} to $t_{stim} + 5s$ to encompass all the neurons engaged in thermal perception, including those whose response may display a significant lag with respect to the stimulus onset.

Large diversity of neuronal responses

In figure 5.21, some typical traces of thermal responsive neurons in different brain regions are presented. These traces show the large diversity of responses to heat stimulation. Some neurons in the telencephalon or in the optic tectum display an increase in their activity at the onset of the heat stimulation and then remain active for several seconds, even after the fish temperature went back to its baseline value. Conversely, neurons in the hindbrain (rhombomere 1 and 7) seem to be solely activated during the heat pulse. Finally, a neuron in

rhombomere 6 displays a highly variable response to heat stimulation: it is activated by some of the heat pulses and silent for the rest of the stimuli.

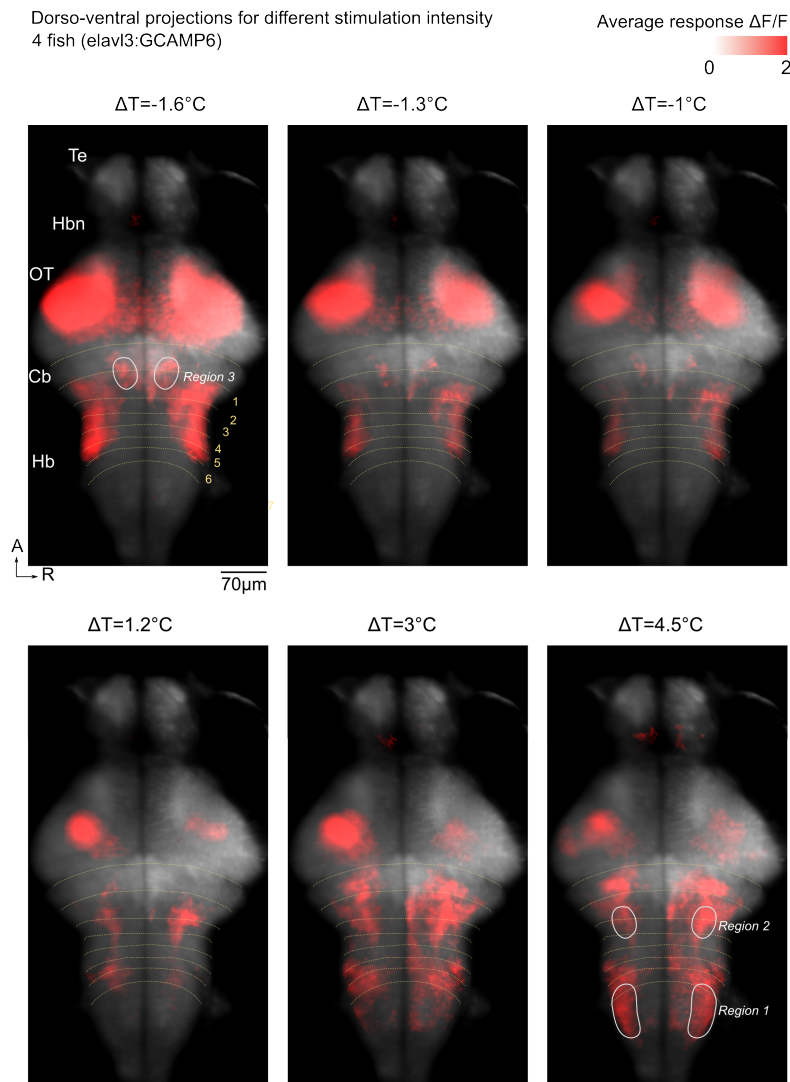


Figure 5.18: Thermal response projection maps for different stimulus intensity (ΔT). Each map is averaged on 4 different fish. The red color encodes the mean $\Delta F/F$ of each voxel for 40 heat stimuli on a temporal window going from the stimulus onset to 5 seconds after the stimulus.

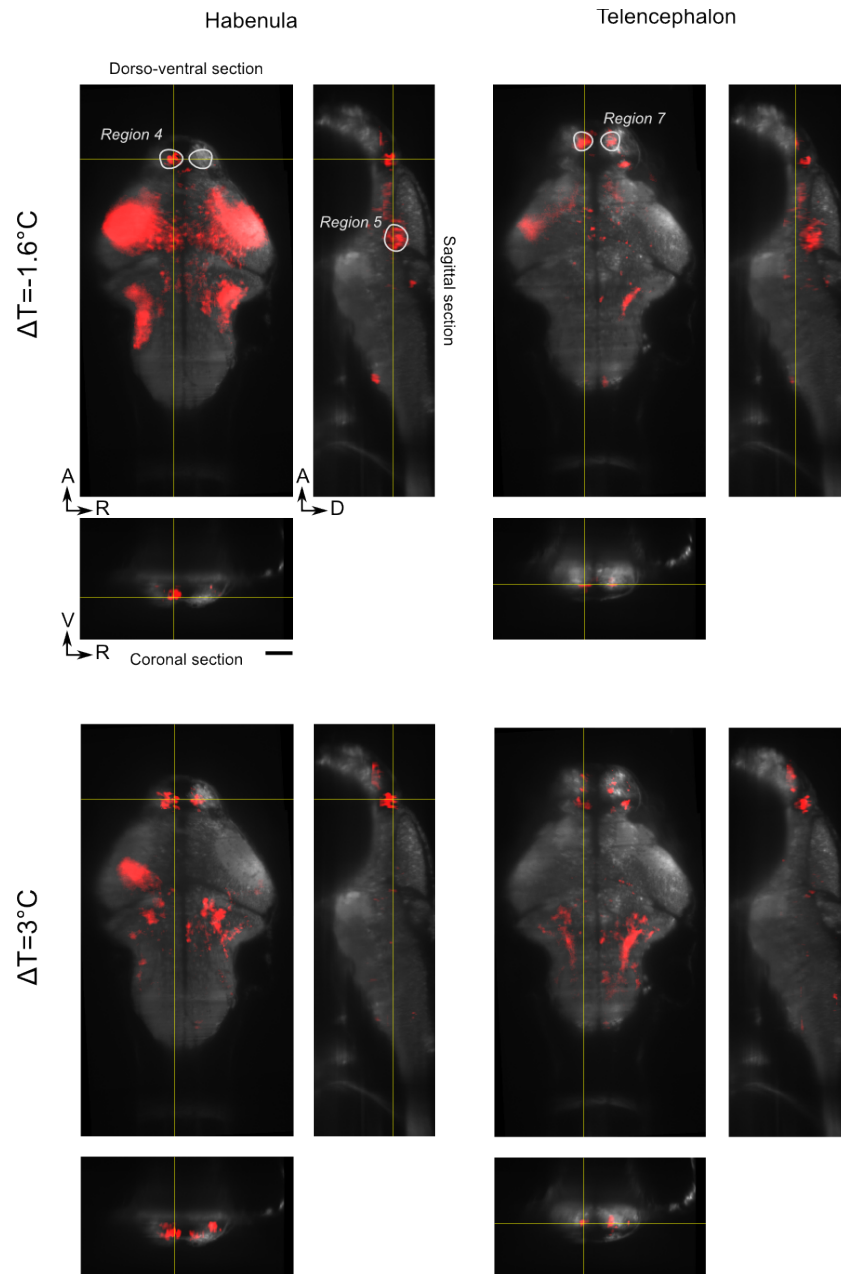


Figure 5.19: Coronal, dorsal and sagittal sections of heat response map for two different stimulus intensity. These sections illustrate the involvement of habenula and telencephalon in heat perception.

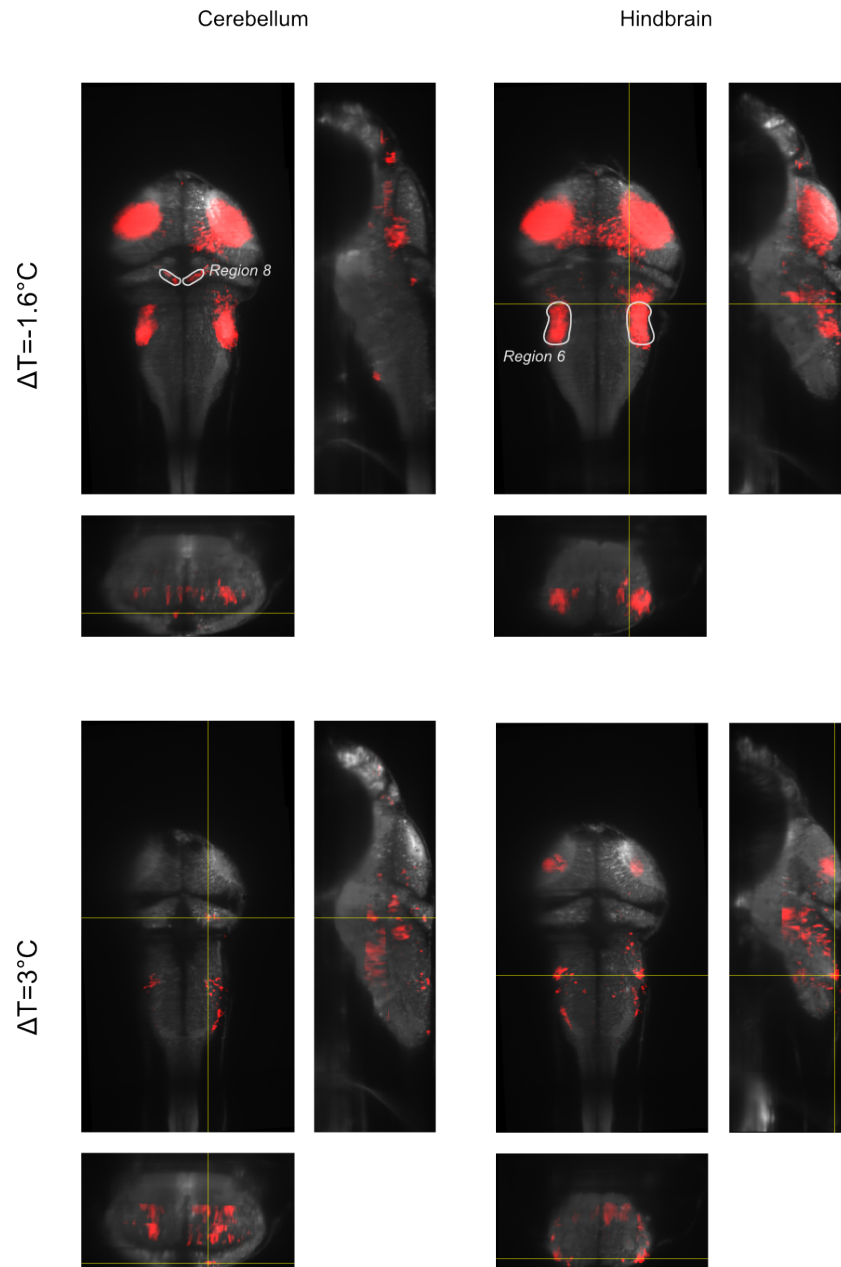


Figure 5.20: Coronal, dorsal and sagittal sections of the thermal response map for two different stimulus intensity. These sections illustrate the involvement of cerebellum and hindbrain in heat perception.

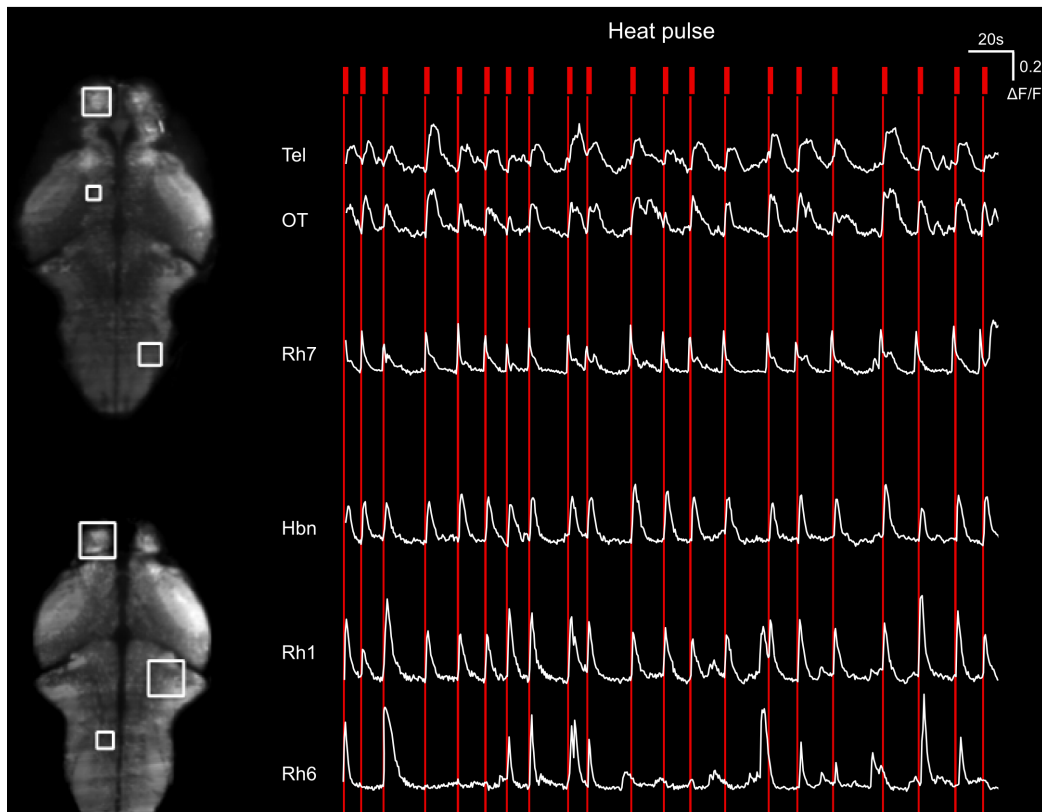


Figure 5.21: Typical signals of heat-responsive neurons in different brain regions (Tel, telencephalon; OT, optic tectum; Rh, rhombomere, Hbn, habenula) for heat stimulations with $\Delta T=3^{\circ}\text{C}$.

5.5.4 Hindbrain oscillator responds to heat stimulation in a phase-dependent manner

Reminder

As we already mentioned in the introduction of the chapter, we had the intuition that the hindbrain oscillator (HBO) could be involved in thermotaxis.

In Wolf *et al.*, we showed that the HBO dynamics enable to understand the tropo and klinotaxis strategy occurring in phototactic behavior of zebrafish larvae. HBO is a self-oscillatory network that drives the orientation of the navigation of zebrafish larvae; it responds in a state-dependent manner to visual stimulation. The currently activated region of the HBO is reinforced by a symmetric visual. Consequently a larva sensing an increase in light intensity during its navigation will tend to maintain its turning orientation unchanged for a longer time.

This klinotaxis mechanism could also account for thermotaxis. Thermotactic and phototactic behavior are very similar: as for phototaxis (see chapter 3), under a gradient of temperature, zebrafish larvae modulate its turning magnitude and bias their turning statistics to navigate for a longer time away from regions with a high temperature. Could the hindbrain oscillator dynamics similarly drive this sensory-driven modulation of the turning statistics?

HBO responds to heat stimulation...

To test this hypothesis, we used our heat-stimulation apparatus and one-photon light-sheet microscope to specifically probe the HBO's response to heat stimuli. We submitted larvae to series of 40 heat stimulations randomly distributed in time at $\Delta T=3^{\circ}\text{C}$. We recorded at 2Hz a brain volume of $100\mu\text{m}$ in thickness that encompassed the HBO. We extracted the activity of the HBO using a semi-automatic algorithm as described in chapter 3 (Supplementary method of Wolf *et al.*, 2017).

In Figure 5.22b, we show a typical trace of the left (red) and right (blue) regions of the HBO. The cross-bars denote the position of the onset of each heat pulse. We observed that for some stimuli it is the right part of the HBO that respond, for the other it is the left part of the HBO. This result is reminiscent of the stochastic response of the HBO to symmetric light flashes (see Figure 4 in Wolf *et al.*). We computed the trial-averaged signal from all heat stimulations (Figure 5.22c): both left and right network are responsive to heat-stimulation but the standard deviation is very high (70%). This high variability reflects the fact that each pulse stochastically evokes a response in either one of the two sub-networks, as shown in Figure 5.22b.

... in a phase-dependent manner

As we did in the phototaxis experiments, we tested whether this apparent variability in the HBO response could reflect a state-dependent. We thus

performed a similar analysis. To quantify the state of the HBO we extracted the phase of its oscillatory signal using a Hilbert transformation. We then computed the derivative of the left and right HBO signals at all times corresponding to a given phase, separating those at which a stimulus had been delivered from the times when the oscillation was running free. We then subtracted the means of both groups in order to extract the sole contribution of the stimulus to the HBO transient dynamics. We obtained the response curve of each network to heat stimulation as a function of the phase of the HBO (Figure 5.22d). This phase-dependent response curve demonstrates the state-dependent sensitivity of the HBO to heat stimulations. It shows that each subpopulation is responsive to heat stimulation within a particular phase range and is essentially unresponsive for the rest of the cycle. This phase-dependent response curve reveals that when a heat-stimulus is delivered, the currently active subpopulation of the HBO is more likely to respond than the currently silent sub-region. The phase-dependent response curve accounts for the following mechanism: when a zebrafish larva turns and enters in a region of higher temperature, navigating in a direction given by the currently active subpopulation of the HBO, the positive gradient of heat activate the currently active subpopulation which delays the forthcoming reversal of the fish turning state. Thus the following turning events will be directed to the same side until the larva senses a decreasing temperature gradient.

In conclusion, these results corroborate our intuition. The HBO responds to heat-stimulation in phase-dependent manner, allowing the fish to escape from hot region. Moreover the HBO reacts to a positive gradient of temperature such that it delays the next change in the orientation of turning events. This result is in line with the results of Robson's (2013) thermotaxis assays, which state that in a presence of a positive gradient of temperature, zebrafish larvae tend to "turn toward the direction currently specified by their turn state".

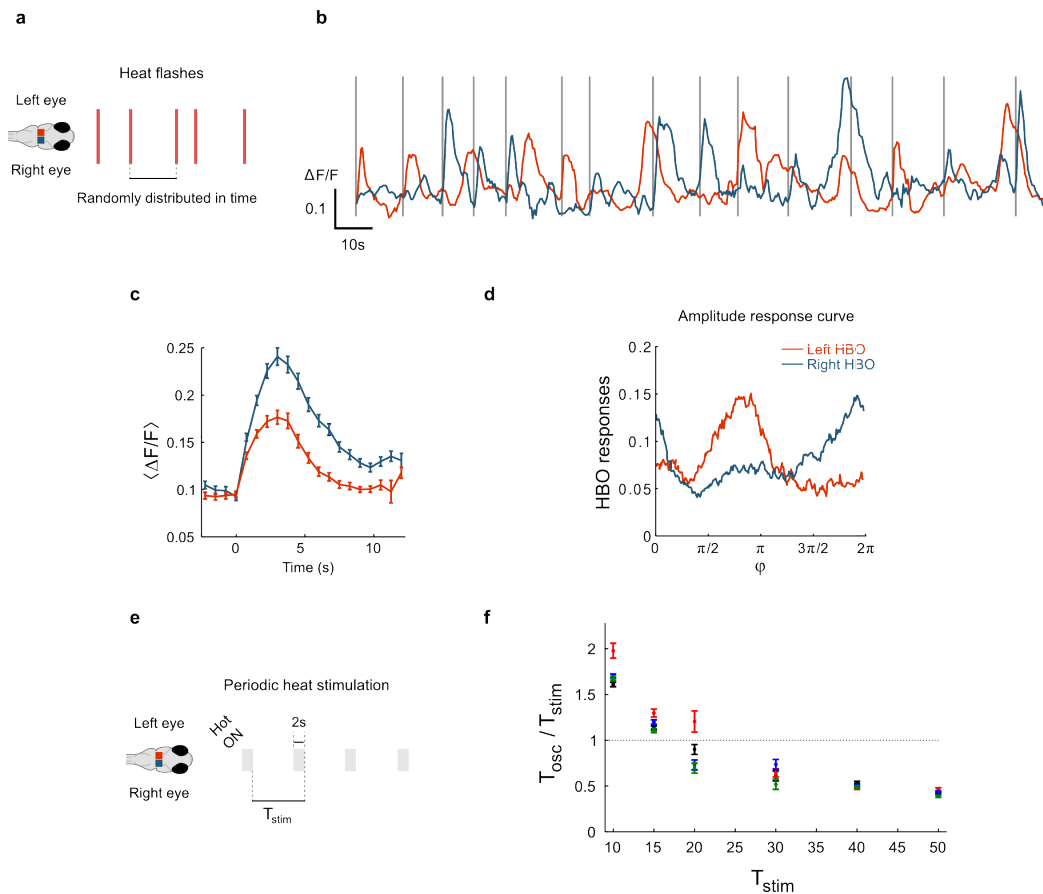


Figure 5.22: **a**, Randomly distributed in time heat stimulation. **b**, Example traces of the right and left HBO. The grey lines indicate the heat pulses. **c**, Trial-averaged heat-induced responses of each subpopulation of the HBO ($N=6$ fish, 220 heat-pulses). The bars correspond to SEM. **d**, Phase-dependent response of each subpopulation to heat stimuli ($N=6$ fish). **e**, Frequency entrainment by heat stimulation. **f**, Entrainment ratio T_{osc}/T_{stim} as a function of T_{stim} for 4 different fish (different colors). The dotted line shows the $T_{osc}=T_{stim}$.

5.5.5 HBO can be entrained by periodic heat stimuli?

In Wolf *et al.* (2017), we showed experimentally and theoretically that the phase-dependent sensitivity of the hindbrain oscillator has a funny consequence: the HBO oscillatory dynamics can be locked onto a periodic visual stimulus. In particular, the oscillatory period of the HBO can be controlled by a periodic visual stimulus such that for a certain range of stimulation period values, the HBO oscillates at the same period. This phase-locking process is a generic properties of CPG (chapter 4).

Since the HBO is sensitive to heat in a phase-dependent manner, we thought that it could be possible to reproduce the synchronization process we already obtained for periodic visual stimuli. To test this hypothesis, we exposed larvae to series of 20 regularly spaced heat stimulations with $\Delta T=3^{\circ}\text{C}$, at 6 different frequencies ($10\text{s}<T_{\text{stim}}<50\text{s}$) separated by 200s at constant baseline temperature (Figure 5.22e). As before, we recorded a volume of $100\mu\text{m}$ high at 2Hz and later extracted the HBO neuronal activity. Using Hilbert transformation, we obtained the phase of the oscillator and thus computed the mean oscillation period T_{osc} for each stimulation period.

For 4 different fish, we plotted the oscillation period as a function of the stimulation period. In these few fish, the data are rather inconclusive, as we did not observe a clear staircase-type graph, with plateaus at $T_{\text{osc}} / T_{\text{stim}} = 2, 1,$ and 0.5 as expected. More experiments under periodic heat stimulation will thus be needed, possibly using more intense heat pulses, to conclude on the possibility to entrain the HBO with periodic heat stimulation.

Conclusion

The work done during these years of PhD allowed us to answer some questions, asking also new ones.

I began my PhD with the purpose of building a two-photon light sheet microscope for whole-brain imaging of zebrafish brain. We succeeded in adapting two-photon light-sheet to whole-brain imaging in zebrafish larvae. Comparing recordings with one and two-photon light-sheet microscopes of zebrafish brain activity under visual stimulation, we demonstrated the large visual disturbance inherent to the one-photon system.

I then focused my work on deciphering the neural basis of phototaxis in zebrafish. Using virtual-reality behavioral assays, one- and two-photon light-sheet microscopy and optogenetics, we showed that a hindbrain circuit called the “hindbrain oscillator” acts as a pacemaker for zebrafish ocular saccades and controls the sequence of turns during animal’s navigation. This neural ensemble is sensitive to light in a state-dependent manner. Its response to light stimuli varies in function of the motor context such that the currently activated part of the circuit is reinforced by a stimulus allowing the fish to delay an orientation change. Over multiple cycles this process leads the fish toward brighter regions.

We anticipated that this hindbrain oscillator circuit could be involved in other goal-directed navigation mechanisms. Therefore, I initiated a project on thermotaxis demonstrating that the hindbrain oscillator displays a similar response to heat stimulation, thus confirming our original intuition.

Finally, the whole brain data sets recorded on eyes-free zebrafish provided new insights in the understanding of zebrafish saccadic circuit architecture. We identified neuronal ensembles in the hindbrain, whose activity increases prior to a saccade, which could be the analogs of the well-described Long Lead Burst neurons of the mammalian oculomotor system. Although more experiments with higher temporal resolution are still needed, several lines of evidence also suggest that the HBO could play the role of the so-called mammalian omnipause neurons.

In the dissertation, I already discussed several perspectives and future works that could be done to go further the present study. Just a reminder.

Two-photon light sheet microscopy is currently limited by the accessible power of the pulsed-infrared lasers and the sensitivity of calcium indicators. As a result, at a zebrafish whole brain scale it is still difficult to record at more than a full brain at 1.5Hz. More powerful laser might allow us to overcome this limitation.

A precise understanding of the neuronal pathway conveying visual inputs to the hindbrain oscillator is still needed. Inspired by several studies on central-pattern generator circuits, one hypothesis might be that the hindbrain oscillator is sensitive to light stimulus through neuromodulatory mechanisms coming from a region called raphe interpositus. This assumption is now on the verge of experimental tests in the lab.

Behavioral and neuronal study of thermotaxis is already on track and the preliminary results are very promising.

On the theoretical point of view, the data sets collected on the saccadic system could be used in the future to build models of the velocity to position neural integrator at larger scales. Moreover, it could be interesting to construct a neuronal model of the hindbrain oscillator inspired by the large literature on central-pattern generator circuits.

The method

Lastly, I wanted to have a short afterthought on the methodological pathway we used during this PhD. In the classical framework of David Marr, a cognitive task can be analyzed at three distinct levels: (1) the computational level, or the function, *i.e.* what the system tries to do; (2) the algorithmic level, or the strategy, *i.e.* how the system actually does it; (3) the physical level, or the implementation, *i.e.* how the brain physically/chemically performs the necessary operations. Consider, for instance, orientational phototaxis. The computational level would be: to orient the animal's body towards a light source. The algorithmic level could be: to perform a series of saccades and swim turns with a left/right statistical bias given by (i) the difference in light level between both two eyes, (ii) the change in total light level associated with the preceding gaze-shift. The physical level could comprise the hindbrain oscillator, *i.e.* a well-defined neuronal ensemble that self-oscillates, driving successive gaze-drifts and reorientations while integrating visual cues in a state-dependent manner, which allows over multiple cycles the system to evaluate the direction of the light source.

Our approach illustrates how whole-brain imaging offers a generic method to identify, in a systematic and unbiased way, the circuit engaged in a given cognitive task, once the behavioral strategy has been established. During our research on the neural mechanism underlying phototaxis in zebrafish we followed a path respecting Marr's advice. We asked how the system localizes a light source (2). Using results from the literature and behavioral experiments we ended in two mechanisms: (i) a tropotaxis strategy where the fish compares the light intensity between its two eyes and redirect its sight and its body orientation to minimize this difference; (ii) a klinotaxis strategy where the fish compares the intensity before and after a change of orientation of sight and body, then it needs to minimize this variation of intensities. We then asked to the system how this could be implemented "physically" (3). Thus, we thought to seek for a circuit that could explain the two strategies. And we found the hindbrain oscillator that controls sight and body orientation, and is responsive to light such that it accounts for both trop and klinotaxis. This methodology could be summarized as follows: take a behavior, dissect it and extract its key parameters; then, use a whole-brain imaging microscope to correlate these parameters to zebrafish brain activity and find the circuit involved in the behavioral. Maybe, this could be a standard method for system neuroscience now that whole brain imaging techniques exist.

Seeing the whole picture

Will whole-brain imaging propulse system neuroscience in a new age? For the first time, we are able to record the activity of an entire vertebrate brain at single-cell resolution. However, one question remains: what could we really hope from this technique in terms of new knowledge compared with older ones?

To characterize neuronal circuits involved in a sensory-driven behavior, standard approaches consist in sequentially recording activities of subsets of neurons in different regions of the brain, while stimulating the animal, and then mapping the different response types. This approach proved its efficiency as we

saw for example with the understanding of the brainstem saccadic circuitry (chapter 4). The main advantage of light-sheet microscopy is that it provides a simultaneous recording of all neurons' activity. What could this simultaneity of the recording tell? One may claim that for the moment light sheet has not demonstrated its interest: it is no more than an "fMRI single cell" technique that gives whole brain functional maps of zebrafish brain and sometimes lost the researchers in a too big amount of data. However the whole brain recordings provided by light sheet microscopy give a lot more than response maps to stimuli. With the development of new computational and theoretical methods, one may hope that in a near future, we could extract from these whole brain data sets the effective connectivity of large populations. Knowing where the links are and then what are the weights of these links may eventually enable neuroscientists to build microscopic models of neural computations at the brain scale. The development during the last decade of several techniques to infer the connectivity matrix from population recordings is very promising even if the size of whole brain activity recordings still limits the use of these inference methods.

Neuroscience is still waiting for the revolution expected by the technical revolution of fluorescence microscopy and particularly large-scale recording. Despite the doubts of some, we stay confident that seeing the whole picture will be a boon rather than a burden.

References

REFERENCES

- Abbe, E. (1874). A contribution to the theory of the microscope and the nature of microscopic vision. *Proc. Bristol Nat. Soc.*, 1, 200-261.
- Abbe, E. (1881). VII.—On the Estimation of Aperture in the Microscope. *Journal of Microscopy*, 1(3), 388-423.
- Abbe, E. (1883). XV.—The Relation of Aperture and Power in the Microscope (continued). *Journal of Microscopy*, 3(6), 790-812.
- Ahissar, E., & Assa, E. (2016). Perception as a closed-loop convergence process. *Elife*, 5, e12830.
- Ahrens, M. B., Li, J. M., Orger, M. B., Robson, D. N., Schier, A. F., Engert, F., & Portugues, R. (2012). Brain-wide neuronal dynamics during motor adaptation in zebrafish. *Nature*, 485(7399), 471-477.
- Ahrens, M. B., Orger, M. B., Robson, D. N., Li, J. M., & Keller, P. J. (2013). Whole-brain functional imaging at cellular resolution using light-sheet microscopy. *Nature methods*, 10(5), 413-420.
- Akerboom, J., Chen, T. W., Wardill, T. J., Tian, L., Marvin, J. S., Mutlu, S., ... & Gordus, A. (2012). Optimization of a GCaMP calcium indicator for neural activity imaging. *Journal of Neuroscience*, 32(40), 13819-13840.
- Aksay, E., Baker, R., Seung, H. S., & Tank, D. W. (2000). Anatomy and discharge properties of pre-motor neurons in the goldfish medulla that have eye-position signals during fixations. *Journal of Neurophysiology*, 84(2), 1035-1049.
- Aksay, E., Gamkrelidze, G., Seung, H. S., Baker, R., & Tank, D. W. (2001). In vivo intracellular recording and perturbation of persistent activity in a neural integrator. *Nature neuroscience*, 4(2), 184.
- Aksay, E., Baker, R., Seung, H. S., & Tank, D. W. (2003). Correlated discharge among cell pairs within the oculomotor horizontal velocity-to-position integrator. *Journal of Neuroscience*, 23(34), 10852-10858.
- Aksay, E., Olasagasti, I., Mensh, B. D., Baker, R., Goldman, M. S., & Tank, D. W. (2007). Functional dissection of circuitry in a neural integrator. *Nature neuroscience*, 10(4), 494.
- Alaburda, A., Perrier, J. F., & Hounsgaard, J. (2002). Mechanisms causing plateau potentials in spinal motoneurons. In *Sensorimotor Control of Movement and Posture* (pp. 219-226). Springer US.
- An, M., Luo, R., & Henion, P. D. (2002). Differentiation and maturation of zebrafish dorsal root and sympathetic ganglion neurons. *Journal of Comparative Neurology*, 446(3), 267-275.

- Arendt, D. (2003). Evolution of eyes and photoreceptor cell types. *International Journal of Developmental Biology*, 47(7-8), 563-571.
- Arrenberg, A. B., Del Bene, F., & Baier, H. (2009). Optical control of zebrafish behavior with halorhodopsin. *Proceedings of the National Academy of Sciences*, 106(42), 17968-17973.
- Arrenberg, A. B., Del Bene, F., & Baier, H. (2009). Optical control of zebrafish behavior with halorhodopsin. *Proceedings of the National Academy of Sciences*, 106(42), 17968-17973.
- Baker, M. D., Wolanin, P. M., & Stock, J. B. (2006). Signal transduction in bacterial chemotaxis. *Bioessays*, 28(1), 9-22.
- Barbagallo, B., & Garrity, P. A. (2015). Temperature sensation in Drosophila. *Current Opinion in Neurobiology*, 34, 8-13.
- Bargmann, C. I., & Horvitz, H. R. (1991). Chemosensory neurons with overlapping functions direct chemotaxis to multiple chemicals in *C. elegans*. *Neuron*, 7(5), 729-742.
- Becker, K., Jährling, N., Kramer, E. R., Schnorrer, F., & Dodt, H. U. (2008). Ultramicroscopy: 3D reconstruction of large microscopical specimens. *Journal of biophotonics*, 1(1), 36-42.
- Becker, W. (1989). The neurobiology of saccadic eye movements. *Metrics. Reviews of oculomotor research*, 3, 13.
- Behrenfeld, M. J., O'Malley, R. T., Siegel, D. A., McClain, C. R., Sarmiento, J. L., Feldman, G. C., ... & Boss, E. S. (2006). Climate-driven trends in contemporary ocean productivity. *Nature*, 444(7120), 752-755.
- Berg, H. C. (1993). *Random walks in biology*. Princeton University Press.
- Berg, H. C., & Brown, D. A. (1972). Chemotaxis in *Escherichia coli* analysed by three-dimensional tracking. *Nature*, 239(5374), 500-504.
- Berg, H. C., & Purcell, E. M. (1977). Physics of chemoreception. *Biophysical journal*, 20(2), 193-219.
- Berthoz, A., & Grantyn, A. (1986). Neuronal mechanisms underlying eye-head coordination. *Progress in brain research*, 64, 325-343.
- Biron, D., Wasserman, S., Thomas, J. H., Samuel, A. D., & Sengupta, P. (2008). An olfactory neuron responds stochastically to temperature and modulates *Caenorhabditis elegans* thermotactic behavior. *Proceedings of the National Academy of Sciences*, 105(31), 11002-11007.
- Blitz, D. M., & Nusbaum, M. P. (2011). Neural circuit flexibility in a small sensorimotor system. *Current opinion in neurobiology*, 21(4), 544-552.

- Bloembergen, N. (2000). Nonlinear optics: past, present, and future. *IEEE Journal of Selected Topics in Quantum Electronics*, 6(6), 876-880.
- Bouchard, M. B., Voleti, V., Mendes, C. S., Lacefield, C., Grueber, W. B., Mann, R. S., ... & Hillman, E. M. (2015). Swept confocally-aligned planar excitation (SCAPE) microscopy for high-speed volumetric imaging of behaving organisms. *Nature photonics*, 9(2), 113-119.
- Briggman, K. L., & Bock, D. D. (2012). Volume electron microscopy for neuronal circuit reconstruction. *Current opinion in neurobiology*, 22(1), 154-161.
- Brockerhoff, S. E., Hurley, J. B., Janssen-Bienhold, U., Neuhauss, S. C., Driever, W., & Dowling, J. E. (1995). A behavioral screen for isolating zebrafish mutants with visual system defects. *Proceedings of the National Academy of Sciences*, 92(23), 10545-10549.
- Brody, C. D., Romo, R., & Kepecs, A. (2003). Basic mechanisms for graded persistent activity: discrete attractors, continuous attractors, and dynamic representations. *Current opinion in neurobiology*, 13(2), 204-211.
- Brown, T. G. (1914). On the nature of the fundamental activity of the nervous centres; together with an analysis of the conditioning of rhythmic activity in progression, and a theory of the evolution of function in the nervous system. *The Journal of physiology*, 48(1), 18-46.
- Bucher, D., Prinz, A. A., & Marder, E. (2005). Animal-to-animal variability in motor pattern production in adults and during growth. *Journal of Neuroscience*, 25(7), 1611-1619.
- Burgess, H. A., & Granato, M. (2007). Modulation of locomotor activity in larval zebrafish during light adaptation. *Journal of Experimental Biology*, 210(14), 2526-2539.
- Burgess, H. A., Schoch, H., & Granato, M. (2010). Distinct retinal pathways drive spatial orientation behaviors in zebrafish navigation. *Current biology*, 20(4), 381-386.
- Büttner, U., & Büttner-Ennever, J. A. (1988). Present concepts of oculomotor organization. *Reviews of oculomotor research*, 2, 3-32.
- Büttner, U., & Büttner-Ennever, J. A. (2006). Present concepts of oculomotor organization. *Progress in brain research*, 151, 1-42.
- Calabrese, R. L. (1995). Half-center oscillators underlying rhythmic movements. *Nature*, 261, 146-148.

- Cao, G., Platisa, J., Pieribone, V. A., Raccuglia, D., Kunst, M., & Nitabach, M. N. (2013). Genetically targeted optical electrophysiology in intact neural circuits. *Cell*, *154*(4), 904-913.
- Chalasanani, S. H., Chronis, N., Tsunozaki, M., Gray, J. M., Ramot, D., Goodman, M. B., & Bargmann, C. I. (2007). Dissecting a circuit for olfactory behaviour in *Caenorhabditis elegans*. *Nature*, *450*(7166), 63.
- Chalfie, M., Tu, Y., Euskirchen, G., Ward, W. W., & Prasher, D. C. (1994). Green fluorescent protein as a marker for gene expression. *Science*, 802-805.
- Chaudhuri, R., & Fiete, I. (2016). Computational principles of memory. *Nature neuroscience*, *19*(3), 394.
- Chen, C. C., Bockisch, C. J., Straumann, D., & Huang, M. Y. Y. (2016). Saccadic and Postsaccadic Disconjugacy in Zebrafish Larvae Suggests Independent Eye Movement Control. *Frontiers in systems neuroscience*, *10*.
- Chen, T. W., Wardill, T. J., Sun, Y., Pulver, S. R., Renninger, S. L., Baohan, A., ... & Looger, L. L. (2013). Ultrasensitive fluorescent proteins for imaging neuronal activity. *Nature*, *499*(7458), 295-300.
- Chen, X., & Engert, F. (2014). Navigational strategies underlying phototaxis in larval zebrafish. *Frontiers in systems neuroscience*, *8*.
- Cheng, R.K., Krishnan, S., and Jesuthasan, S. (2016). Activation and inhibition of tph2 serotonergic neurons operate in tandem to influence larval zebrafish preference for light over darkness. *Sci. Rep.* *6*, 20788.
- Chhetri, R. K., Amat, F., Wan, Y., Höckendorf, B., Lemon, W. C., & Keller, P. J. (2015). Whole-animal functional and developmental imaging with isotropic spatial resolution. *Nature methods*.
- Clark, D. A., Biron, D., Sengupta, P., & Samuel, A. D. (2006). The AFD sensory neurons encode multiple functions underlying thermotactic behavior in *Caenorhabditis elegans*. *Journal of Neuroscience*, *26*(28), 7444-7451.
- Clark, D. A., Gabel, C. V., Gabel, H., & Samuel, A. D. (2007). Temporal activity patterns in thermosensory neurons of freely moving *Caenorhabditis elegans* encode spatial thermal gradients. *Journal of Neuroscience*, *27*(23), 6083-6090.
- Clark, D. A., Gabel, C. V., Lee, T. M., & Samuel, A. D. (2007). Short-term adaptation and temporal processing in the cryophilic response of *Caenorhabditis elegans*. *Journal of neurophysiology*, *97*(3), 1903-1910.
- Cocco, S., Monasson, R., Posani, L., & Tavoni, G. (2017). Functional networks from inverse modeling of neural population activity. *Current Opinion in Systems Biology*.

- Cohen, B., Komatsuzaki, A., & Bender, M. B. (1968). Electrooculographic syndrome in monkeys after pontine reticular formation lesions. *Archives of neurology*, *18*(1), 78-92.
- Conchello, J. A., & Lichtman, J. W. (2005). Optical sectioning microscopy. *Nature methods*, *2*(12), 920-931.
- Daie, K., Goldman, M. S., & Aksay, E. R. (2015). Spatial patterns of persistent neural activity vary with the behavioral context of short-term memory. *Neuron*, *85*(4), 847-860.
- Darwin, C. (1859). *On the Origin of Species by Means of Natural Selection, or the Preservation of Favoured Races in the Struggle for Life*. John Murray; London. . Vol. 186.
- Daun, S., Rubin, J. E., & Rybak, I. A. (2009). Control of oscillation periods and phase durations in half-center central pattern generators: a comparative mechanistic analysis. *Journal of computational neuroscience*, *27*(1), 3.
- Dayan, P. (1998). A hierarchical model of binocular rivalry. *Neural Computation*, *10*(5), 1119-1135.
- Dayan, P., & Abbott, L. F. (2001). *Theoretical neuroscience* (Vol. 806). Cambridge, MA: MIT Press.
- Delgado-Garcia, J. M., Del Pozo, F., & Baker, R. (1986). Behavior of neurons in the abducens nucleus of the alert cat—I. Motoneurons. *Neuroscience*, *17*(4), 929-952.
- Denk, W., & Svoboda, K. (1997). Photon upmanship: why multiphoton imaging is more than a gimmick. *Neuron*, *18*(3), 351-357.
- Denk, W., Strickler, J. H., & Webb, W. W. (1990). Two-photon laser scanning fluorescence microscopy. *Science*, *248*(4951), 73-76.
- Dhaka, A., Viswanath, V., & Patapoutian, A. (2006). Trp ion channels and temperature sensation. *Annu. Rev. Neurosci.*, *29*, 135-161.
- Di Prisco, G. V., Pearlstein, E., Robitaille, R., & Dubuc, R. (1997). Role of sensory-evoked NMDA plateau potentials in the initiation of locomotion. *Science*, *278*(5340), 1122-1125.
- Dirac, P. A. M. (1958). *Quantum mechanics* 4th Ed.
- Dodt, H. U., Leischner, U., Schierloh, A., Jährling, N., Mauch, C. P., Deininger, K., ... & Becker, K. (2007). Ultramicroscopy: three-dimensional visualization of neuronal networks in the whole mouse brain. *Nature methods*, *4*(4), 331-336.
- Drobizhev, M., Makarov, N. S., Tillo, S. E., Hughes, T. E., & Rebane, A. (2011). Two-photon absorption properties of fluorescent proteins. *Nature*

methods, 8(5), 393-399.

Dunn, T. W., Mu, Y., Narayan, S., Randlett, O., Naumann, E. A., Yang, C. T., ... & Ahrens, M. B. (2016). Brain-wide mapping of neural activity controlling zebrafish exploratory locomotion. *Elife*, 5, e12741.

Dunsby, C. (2008). Optically sectioned imaging by oblique plane microscopy. *Optics express*, 16(25), 20306-20316.

Easter Jr, S. S., & Nicola, G. N. (1996). The development of vision in the zebrafish (*Danio rerio*). *Developmental biology*, 180(2), 646-663.

Egorov, A. V., Hamam, B. N., Fransén, E., Hasselmo, M. E., & Alonso, A. A. (2002). Graded persistent activity in entorhinal cortex neurons. *Nature*, 420(6912), 173-179.

Einhäuser, W., Moeller, G. U., Schumann, F., Conradt, J., Vockeroth, J., Bartl, K., ... & König, P. (2009). Eye-head coordination during free exploration in human and cat. *Annals of the New York Academy of Sciences*, 1164(1), 353-366.

Erclik, T., Hartenstein, V., McInnes, R. R., & Lipshitz, H. D. (2009). Eye evolution at high resolution: the neuron as a unit of homology. *Developmental biology*, 332(1), 70-79.

Fahrbach, F. O., Simon, P., & Rohrbach, A. (2010). Microscopy with self-reconstructing beams. *Nature Photonics*, 4(11), 780-785.

Feierstein, C. E., Portugues, R., & Orger, M. B. (2015). Seeing the whole picture: A comprehensive imaging approach to functional mapping of circuits in behaving zebrafish. *Neuroscience*, 296, 26-38.

Fernandes, A. M., Fero, K., Arrenberg, A. B., Bergeron, S. A., Driever, W., & Burgess, H. A. (2012). Deep brain photoreceptors control light-seeking behavior in zebrafish larvae. *Current Biology*, 22(21), 2042-2047.

Fisher, N. I. (1995). *Statistical analysis of circular data*. Cambridge University Press.

Fraenkel, G. S., & Gunn, D. L. (1961). *The orientation of animals*. Dover Publications, Inc; New York.

Franken, E. P., Hill, A. E., Peters, C. E., & Weinreich, G. (1961). Generation of optical harmonics. *Physical Review Letters*, 7(4), 118.

Freedman, E. G., Stanford, T. R. & Sparks, D. L. (1996). Combined eye-head gaze shifts produced by electrical stimulation of the superior colliculus in rhesus monkeys. *J. Neurophysiol.* 76, 927-952.

- Fuchs, A. F., Kaneko, C. R. S., & Scudder, C. A. (1985). Brainstem control of saccadic eye movements. *Annual review of neuroscience*, *8*(1), 307-337.
- Fuchs, A. F., Ling, L., & Phillips, J. O. (2005). Behavior of the position vestibular pause (PVP) interneurons of the vestibuloocular reflex during head-free gaze shifts in the monkey. *Journal of neurophysiology*, *94*(6), 4481-4490.
- Fujishiro, A., Kaneko, H., Kawashima, T., Ishida, M., & Kawano, T. (2014). In vivo neuronal action potential recordings via three-dimensional microscale needle-electrode arrays. *Scientific reports*, *4*, 4868.
- Gannaway, J. N., & Sheppard, C. J. R. (1978). Second-harmonic imaging in the scanning optical microscope. *Optical and Quantum Electronics*, *10*(5), 435-439.
- Garrity, P. A., Goodman, M. B., Samuel, A. D., & Sengupta, P. (2010). Running hot and cold: behavioral strategies, neural circuits, and the molecular machinery for thermotaxis in *C. elegans* and *Drosophila*. *Genes & development*, *24*(21), 2365-2382.
- Gau, P., Poon, J., Ufret-Vincenty, C., Snelson, C. D., Gordon, S. E., Raible, D. W., & Dhaka, A. (2013). The zebrafish ortholog of TRPV1 is required for heat-induced locomotion. *Journal of Neuroscience*, *33*(12), 5249-5260.
- Gehring, W. J. (2004). Historical perspective on the development and evolution of eyes and photoreceptors. *International journal of developmental biology*, *48*(8-9), 707-717.
- Gepner, R., Skanata, M. M., Bernat, N. M., Kaplow, M., & Gershow, M. (2015). Computations underlying *Drosophila* photo-taxis, odor-taxis, and multi-sensory integration. *Elife*, *4*, e06229.
- Gerlai, R., Lahav, M., Guo, S., & Rosenthal, A. (2000). Drinks like a fish: zebra fish (*Danio rerio*) as a behavior genetic model to study alcohol effects. *Pharmacology biochemistry and behavior*, *67*(4), 773-782.
- Gershow, M., Berck, M., Mathew, D., Luo, L., Kane, E. A., Carlson, J. R., & Samuel, A. D. (2012). Controlling airborne cues to study small animal navigation. *Nature methods*, *9*(3), 290-296.
- Gilbert, C., McCafferty, D., Le Maho, Y., Martrette, J. M., Giroud, S., Blanc, S., & Ancel, A. (2010). One for all and all for one: the energetic benefits of huddling in endotherms. *Biological Reviews*, *85*(3), 545-569.
- Giometto, A., Altermatt, F., Maritan, A., Stocker, R., & Rinaldo, A. (2015). Generalized receptor law governs phototaxis in the phytoplankton *Euglena gracilis*. *Proceedings of the National Academy of Sciences*, *112*(22), 7045-7050.

- Göbel, W., & Helmchen, F. (2007). In vivo calcium imaging of neural network function. *Physiology*, 22(6), 358-365.
- Goldman, M. S., Levine, J. H., Major, G., Tank, D. W., & Seung, H. S. (2003). Robust persistent neural activity in a model integrator with multiple hysteretic dendrites per neuron. *Cerebral cortex*, 13(11), 1185-1195.
- Goldman, M. S. (2009). Memory without feedback in a neural network. *Neuron*, 61(4), 621-634.
- Goldman, M., Compte, A., & Wang, X. J. (2008). Theoretical and computational neuroscience: Neural integrators: recurrent mechanisms and models. *Squire, L.; Albright, T.; Bloom, F.*
- Golgi, C. Sulla struttura della sostanza grigia del cervello. *Gazz. Med. Ital. (Lombardia)* 33, 244–246 (1873) (in Italian).
- Gomez-Marin, A., & Louis, M. (2012). Active sensation during orientation behavior in the *Drosophila* larva: more sense than luck. *Current opinion in neurobiology*, 22(2), 208-215.
- Gomez-Marin, A., Stephens, G. J., & Louis, M. (2011). Active sampling and decision making in *Drosophila* chemotaxis. *Nature communications*, 2, 441.
- Gonçalves, P. J., Arrenberg, A. B., Hablitzel, B., Baier, H., & Machens, C. K. (2014). Optogenetic perturbations reveal the dynamics of an oculomotor integrator. *Frontiers in neural circuits*, 8.
- Gong, Z. (2009). Behavioral dissection of *Drosophila* larval phototaxis. *Biochemical and biophysical research communications*, 382(2), 395-399.
- Göppert-Mayer, M. (1931). Über elementarakte mit zwei quantensprüngen. *Annalen der Physik*, 401(3), 273-294.
- Göppert, M. (1929). Über die Wahrscheinlichkeit des Zusammenwirkens zweier Lichtquanten in einem Elementarakt. *Naturwissenschaften*, 17(48), 932-932.
- Gray, J. M., Hill, J. J., & Bargmann, C. I. (2005). A circuit for navigation in *Caenorhabditis elegans*. *Proceedings of the National Academy of Sciences of the United States of America*, 102(9), 3184-3191.
- Grewe, B. F., Langer, D., Kasper, H., Kampa, B. M., & Helmchen, F. (2010). High-speed in vivo calcium imaging reveals neuronal network activity with near-millisecond precision. *Nature methods*, 7(5), 399-405.
- Grewe, B. F., Langer, D., Kasper, H., Kampa, B. M., & Helmchen, F. (2010). High-speed in vivo calcium imaging reveals neuronal network activity with near-millisecond precision. *Nature methods*, 7(5), 399-405.
- Grienberger, C., & Konnerth, A. (2012). Imaging calcium in neurons. *Neuron*, 73(5), 862-885.

- Grillner S, Wallen P, Brodin L, Lansner (1991) A: Neuronal network generating locomotor behavior in lamprey: circuitry, transmitters, membrane properties, and simulation. *Annu Rev Neurosci* 14:169-199.
- Guggiana-Nilo, D. A., & Engert, F. (2016). Properties of the visible light phototaxis and UV avoidance behaviors in the larval zebrafish. *Frontiers in behavioral neuroscience*, 10.
- Haesemeyer, M., Robson, D. N., Li, J. M., Schier, A. F., & Engert, F. (2015). The structure and timescales of heat perception in larval zebrafish. *Cell systems*, 1(5), 338-348.
- Hays, G. C. (2003). A review of the adaptive significance and ecosystem consequences of zooplankton diel vertical migrations. In *Migrations and Dispersal of Marine Organisms* (pp. 163-170). Springer, Dordrecht.
- Hedgecock, E. M., & Russell, R. L. (1975). Normal and mutant thermotaxis in the nematode *Caenorhabditis elegans*. *Proceedings of the National Academy of Sciences*, 72(10), 4061-4065.
- Hellwarth, R., & Christensen, P. (1974). Nonlinear optical microscopic examination of structure in polycrystalline ZnSe. *Optics Communications*, 12(3), 318-322.
- Helmchen, F., & Denk, W. (2005). Deep tissue two-photon microscopy. *Nature methods*, 2(12), 932-940.
- Hepp, K., & Henn, V. (1983). Spatio-temporal recoding of rapid eye movement signals in the monkey paramedian pontine reticular formation (PPRF). *Experimental brain research*, 52(1), 105-120.
- Higashijima, S. I., Masino, M. A., Mandel, G., & Fetcho, J. R. (2003). Imaging neuronal activity during zebrafish behavior with a genetically encoded calcium indicator. *Journal of neurophysiology*, 90(6), 3986-3997.
- Hiraoka, Y., Sedat, J. W., & Agard, D. A. (1990). Determination of three-dimensional imaging properties of a light microscope system. Partial confocal behavior in epifluorescence microscopy. *Biophysical journal*, 57(2), 325-333.
- Holekamp, T. F., Turaga, D., & Holy, T. E. (2008). Fast three-dimensional fluorescence imaging of activity in neural populations by objective-coupled planar illumination microscopy. *Neuron*, 57(5), 661-672.
- <http://www.nitrc.org/projects/cmtk/>
- Huang, K. H., Ahrens, M. B., Dunn, T. W., & Engert, F. (2013). Spinal projection neurons control turning behaviors in zebrafish. *Current Biology*, 23(16), 1566-1573.

- Hubel, D. H. (1957). Tungsten microelectrode for recording from single units. *Science*, *125*(3247), 549-550.
- Huey, R. B., Hertz, P. E., & Sinervo, B. (2003). Behavioral drive versus behavioral inertia in evolution: a null model approach. *The American Naturalist*, *161*(3), 357-366.
- Huisken, J., & Stainier, D. Y. (2007). Even fluorescence excitation by multidirectional selective plane illumination microscopy (mSPIM). *Optics letters*, *32*(17), 2608-2610.
- Huisken, J., & Stainier, D. Y. (2009). Selective plane illumination microscopy techniques in developmental biology. *Development*, *136*(12), 1963-1975.
- Huisken, J., Swoger, J., Del Bene, F., Wittbrodt, J., & Stelzer, E. H. (2004). Optical sectioning deep inside live embryos by selective plane illumination microscopy. *Science*, *305*(5686), 1007-1009.
- Iino, Y., & Yoshida, K. (2009). Parallel use of two behavioral mechanisms for chemotaxis in *Caenorhabditis elegans*. *Journal of Neuroscience*, *29*(17), 5370-5380.
- Ijspeert, A. J. (2008). Central pattern generators for locomotion control in animals and robots: a review. *Neural networks*, *21*(4), 642-653.
- Ito, J., Maldonado, P., Singer, W., & Grün, S. (2011). Saccade-related modulations of neuronal excitability support synchrony of visually elicited spikes. *Cerebral Cortex*, *21*(11), 2482-2497.
- Izhikevich, E. M. (2007). *Dynamical systems in neuroscience*. MIT press.
- Jékely, G., Colombelli, J., Hausen, H., Guy, K., Stelzer, E., Nédélec, F., & Arendt, D. (2008). Mechanism of phototaxis in marine zooplankton. *Nature*, *456*(7220), 395-399.
- Jékely, G. (2009). Evolution of phototaxis. *Philosophical Transactions of the Royal Society of London B: Biological Sciences*, *364*(1531), 2795-2808.
- Ji, N., Milkie, D. E., & Betzig, E. (2010). Adaptive optics via pupil segmentation for high resolution imaging in biological tissues. *Nature methods*, *7*(2), 141-147.
- Joshua, M., & Lisberger, S. G. (2015). A tale of two species: neural integration in zebrafish and monkeys. *Neuroscience*, *296*, 80-91.
- Jutras, M. J., Fries, P., & Buffalo, E. A. (2013). Oscillatory activity in the monkey hippocampus during visual exploration and memory formation. *Proceedings of the National Academy of Sciences*, *110*(32), 13144-13149.
- Kaiser, W., & Garrett, C. G. B. (1961). Two-photon excitation in Ca F₂: Eu²⁺. *Physical review letters*, *7*(6), 229.

- Kalueff, A. V., Gebhardt, M., Stewart, A. M., Cachat, J. M., Brimmer, M., Chawla, J. S., ... & Gaikwad, S. (2013). Towards a comprehensive catalog of zebrafish behavior 1.0 and beyond. *Zebrafish*, *10*(1), 70-86.
- Kamogawa, H., Ohki, Y., Shimazu, H., Suzuki, I., & Yamashita, M. (1996). Inhibitory input to pause neurons from pontine burst neuron area in the cat. *Neuroscience letters*, *203*(3), 163-166.
- Kane, E. A., Gershow, M., Afonso, B., Larderet, I., Klein, M., Carter, A. R., ... & Samuel, A. D. (2013). Sensorimotor structure of *Drosophila* larva phototaxis. *Proceedings of the National Academy of Sciences*, *110*(40), E3868-E3877.
- Kaneko, C. R. (2006). Saccade-related, long-lead burst neurons in the monkey rostral pons. *Journal of neurophysiology*, *95*(2), 979-994.
- Katona, G., Szalay, G., Maák, P., Kaszás, A., Veress, M., Hillier, D., ... & Rózsa, B. (2012). Fast two-photon in vivo imaging with three-dimensional random-access scanning in large tissue volumes. *Nature methods*, *9*(2), 201-208.
- Keene, A. C., & Sprecher, S. G. (2012). Seeing the light: photobehavior in fruit fly larvae. *Trends in neurosciences*, *35*(2), 104-110.
- Keller, P. J., Schmidt, A. D., Santella, A., Khairy, K., Bao, Z., Wittbrodt, J., & Stelzer, E. H. (2010). Fast, high-contrast imaging of animal development with scanned light sheet-based structured-illumination microscopy. *Nature methods*, *7*(8), 637-642.
- Keller, P. J., Schmidt, A. D., Wittbrodt, J., & Stelzer, E. H. (2008). Reconstruction of zebrafish early embryonic development by scanned light sheet microscopy. *science*, *322*(5904), 1065-1069.
- Kiehn, O., & Eken, T. (1998). Functional role of plateau potentials in vertebrate motor neurons. *Current opinion in neurobiology*, *8*(6), 746-752.
- Kimura, K. D., Miyawaki, A., Matsumoto, K., & Mori, I. (2004). The *C. elegans* thermosensory neuron AFD responds to warming. *Current Biology*, *14*(14), 1291-1295.
- Kimura, Y., Satou, C., & Higashijima, S. I. (2008). V2a and V2b neurons are generated by the final divisions of pair-producing progenitors in the zebrafish spinal cord. *Development*, *135*(18), 3001-3005.
- Kinkhabwala, A., Riley, M., Koyama, M., Monen, J., Satou, C., Kimura, Y., ... & Fetcho, J. (2011). A structural and functional ground plan for neurons in the hindbrain of zebrafish. *Proceedings of the National Academy of Sciences*, *108*(3), 1164-1169.

- Klein, M., Afonso, B., Vonner, A. J., Hernandez-Nunez, L., Berck, M., Tabone, C. J., ... & Zlatic, M. (2015). Sensory determinants of behavioral dynamics in *Drosophila* thermotaxis. *Proceedings of the National Academy of Sciences*, *112*(2), E220-E229.
- Kobat, D., Durst, M. E., Nishimura, N., Wong, A. W., Schaffer, C. B., & Xu, C. (2009). Deep tissue multiphoton microscopy using longer wavelength excitation. *Optics express*, *17*(16), 13354-13364.
- Komura, Y., Tamura, R., Uwano, T., & Nishijo, H. (2001). Retrospective and prospective coding for predicted reward in the sensory thalamus. *Nature*, *412*(6846), 546.
- Koulakov, A. A., Raghavachari, S., Kepecs, A., & Lisman, J. E. (2002). Model for a robust neural integrator. *Nature neuroscience*, *5*(8), 775.
- Kuhara, A., Okumura, M., Kimata, T., Tanizawa, Y., Takano, R., Kimura, K. D., ... & Mori, I. (2008). Temperature sensing by an olfactory neuron in a circuit controlling behavior of *C. elegans*. *Science*, *320*(5877), 803-807.
- Lahiri, S., Shen, K., Klein, M., Tang, A., Kane, E., Gershow, M., ... & Samuel, A. D. (2011). Two alternating motor programs drive navigation in *Drosophila* larva. *PloS one*, *6*(8), e23180.
- Laing, C. R., & Chow, C. C. (2002). A spiking neuron model for binocular rivalry. *Journal of computational neuroscience*, *12*(1), 39-53.
- Lamb, T. D., Collin, S. P., & Pugh, E. N. (2007). Evolution of the vertebrate eye: opsins, photoreceptors, retina and eye cup. *Nature Reviews Neuroscience*, *8*(12), 960-976.
- Lee, M. M., Arrenberg, A. B., & Aksay, E. R. (2015). A structural and genotypic scaffold underlying temporal integration. *Journal of Neuroscience*, *35*(20), 7903-7920.
- Leonard, C. M. (1974). Thermotaxis in golden hamster pups. *Journal of Comparative and Physiological Psychology*, *86*(3), 458.
- Lichtman, J. W., & Conchello, J. A. (2005). Fluorescence microscopy. *Nature methods*, *2*(12), 910-919.
- Lim, D., Chu, K. K., & Mertz, J. (2008). Wide-field fluorescence sectioning with hybrid speckle and uniform-illumination microscopy. *Optics letters*, *33*(16), 1819-1821.
- Lindek, S., Pick, R., & Stelzer, E. H. (1994). Confocal theta microscope with three objective lenses. *Review of scientific instruments*, *65*(11), 3367-3372.
- Ling, L., Fuchs, A. F., Phillips, J. O., & Freedman, E. G. (1999). Apparent dissociation between saccadic eye movements and the firing patterns of

- premotor neurons and motoneurons. *Journal of neurophysiology*, 82(5), 2808-2811.
- Lister, J. A., Robertson, C. P., Lepage, T., Johnson, S. L., & Raible, D. W. (1999). Nacre encodes a zebrafish microphthalmia-related protein that regulates neural-crest-derived pigment cell fate. *Development*, 126(17), 3757-3767.
- Liu, L., Yermolaieva, O., Johnson, W. A., Abboud, F. M., & Welsh, M. J. (2003). Identification and function of thermosensory neurons in *Drosophila* larvae. *Nature neuroscience*, 6(3), 267-273.
- Louis, M., Huber, T., Benton, R., Sakmar, T. P., & Vosshall, L. B. (2008). Bilateral olfactory sensory input enhances chemotaxis behavior. *Nature neuroscience*, 11(2), 187-199.
- Lovely, P. S., & Dahlquist, F. W. (1975). Statistical measures of bacterial motility and chemotaxis. *Journal of theoretical biology*, 50(2), 477-496.
- Lumpkin, E. A., & Caterina, M. J. (2007). Mechanisms of sensory transduction in the skin. *Nature*, 445(7130), 858-865.
- Luo, L., Clark, D. A., Biron, D., Mahadevan, L., & Samuel, A. D. (2006). Sensorimotor control during isothermal tracking in *Caenorhabditis elegans*. *Journal of experimental biology*, 209(23), 4652-4662.
- Luo, L., Gershow, M., Rosenzweig, M., Kang, K., Fang-Yen, C., Garrity, P. A., & Samuel, A. D. (2010). Navigational decision making in *Drosophila* thermotaxis. *Journal of Neuroscience*, 30(12), 4261-4272.
- Luo, L., Wen, Q., Ren, J., Hendricks, M., Gershow, M., Qin, Y., ... & Calvo, A. C. (2014). Dynamic encoding of perception, memory, and movement in a *C. elegans* chemotaxis circuit. *Neuron*, 82(5), 1115-1128.
- Mahou, P. (2012). *Microscopie non linéaire de tissus biologiques: excitation multicolore, faisceaux de Bessel, et excitation en nappe de lumière* (Doctoral dissertation, Ecole Polytechnique X).
- Maiman, T. H. (1960). Stimulated optical radiation in ruby.
- Major, G., & Tank, D. (2004). Persistent neural activity: prevalence and mechanisms. *Current opinion in neurobiology*, 14(6), 675-684.
- Major, G., Baker, R., Aksay, E., Mensh, B., Seung, H. S., & Tank, D. W. (2004). Plasticity and tuning by visual feedback of the stability of a neural integrator. *Proceedings of the National Academy of Sciences of the United States of America*, 101(20), 7739-7744.
- Major, G., Baker, R., Aksay, E., Seung, H. S., & Tank, D. W. (2004). Plasticity and tuning of the time course of analog persistent firing in a neural integrator.

- Proceedings of the National Academy of Sciences of the United States of America*, 101(20), 7745-7750.
- Marder E: From biophysics to models of network function. *Annu Rev Neurosci* 1998, 21:25-45
- Marder, E., & Bucher, D. (2001). Central pattern generators and the control of rhythmic movements. *Current biology*, 11(23), R986-R996.
- Marder, E., & Calabrese, R. L. (1996). Principles of rhythmic motor pattern generation. *Physiological reviews*, 76(3), 687-717.
- Marder, E., & Calabrese, R. L. (1996). Principles of rhythmic motor pattern generation. *Physiological reviews*, 76(3), 687-717.
- Marder, E., & Goaillard, J. M. (2006). Variability, compensation and homeostasis in neuron and network function. *Nature reviews. Neuroscience*, 7(7), 563.
- Marder, E., & Weimann, J. M. (1992). Modulatory control of multiple task processing in the stomatogastric nervous system. *Neurobiology of motor programme selection*, 3-19.
- Martinez-Conde, S., & Macknik, S. L. (2008). Fixational eye movements across vertebrates: comparative dynamics, physiology, and perception. *Journal of Vision*, 8(14), 28-28.
- Mast, S. O. (1911). *Light and the Behavior of Organisms*. Wiley.
- McCain, D. A., Amici, L. A., & Spudich, J. L. (1987). Kinetically resolved states of the Halobacterium halobium flagellar motor switch and modulation of the switch by sensory rhodopsin I. *Journal of bacteriology*, 169(10), 4750-4758.
- McMahon, A., Supatto, W., Fraser, S. E., & Stathopoulos, A. (2008). Dynamic analyses of Drosophila gastrulation provide insights into collective cell migration. *Science*, 322(5907), 1546-1550.
- McNaughton, B. L., O'Keefe, J., & Barnes, C. A. (1983). The stereotrode: a new technique for simultaneous isolation of several single units in the central nervous system from multiple unit records. *Journal of neuroscience methods*, 8(4), 391-397.
- Mertz, J., & Kim, J. (2010). Scanning light-sheet microscopy in the whole mouse brain with HiLo background rejection. *Journal of biomedical optics*, 15(1), 016027-016027.
- Mesibov, R., Ordal, G. W., & Adler, J. (1973). The range of attractant concentrations for bacterial chemotaxis and the threshold and size of response over this range. *The Journal of general physiology*, 62(2), 203-223.

- Micali, G., & Endres, R. G. (2016). Bacterial chemotaxis: information processing, thermodynamics, and behavior. *Current opinion in microbiology*, *30*, 8-15.
- Minsky, M. (1955). Confocal scanning microscope. *Rapport technique, Patent*, *3*
- Minsky, M. (1961). *U.S. Patent No. 3,013,467*. Washington, DC: U.S. Patent and Trademark Office.
- Minsky, M. (1988). Memoir on inventing the confocal scanning microscope. *Scanning*, *10*(4), 128-138.
- Miri, A., Daie, K., Arrenberg, A. B., Baier, H., Aksay, E., & Tank, D. W. (2011). Spatial gradients and multidimensional dynamics in a neural integrator circuit. *Nature neuroscience*, *14*(9), 1150-1159.
- Miri, A., Daie, K., Burdine, R. D., Aksay, E., & Tank, D. W. (2011). Regression-based identification of behavior-encoding neurons during large-scale optical imaging of neural activity at cellular resolution. *Journal of neurophysiology*, *105*(2), 964-980.
- Miyawaki, A., Llopis, J., Heim, R., McCaffery, J. M., Adams, J. A., Ikura, M., & Tsien, R. Y. (1997). Fluorescent indicators for Ca²⁺ based on green fluorescent proteins and calmodulin. *Nature*, *388*(6645), 882-887.
- Moqrich, A., Hwang, S. W., Earley, T. J., Petrus, M. J., Murray, A. N., Spencer, K. S., ... & Patapoutian, A. (2005). Impaired thermosensation in mice lacking TRPV3, a heat and camphor sensor in the skin. *Science*, *307*(5714), 1468-1472.
- Mori, I., & Ohshima, Y. (1995). Neural regulation of thermotaxis in *Caenorhabditis elegans*. *Nature*, *376*(6538), 344.
- Morris, C., & Lecar, H. (1981). Voltage oscillations in the barnacle giant muscle fiber. *Biophysical journal*, *35*(1), 193-213.
- Mueller, K. P., & Neuhauss, S. C. (2010). Behavioral neurobiology: how larval fish orient towards the light. *Current Biology*, *20*(4), R159-R161.
- Muto, A., Lal, P., Ailani, D., Abe, G., Itoh, M., & Kawakami, K. (2017). Activation of the hypothalamic feeding centre upon visual prey detection. *bioRxiv*, 078527.
- Nakai, J., Ohkura, M., & Imoto, K. (2001). A high signal-to-noise Ca²⁺ probe composed of a single green fluorescent protein. *Nature biotechnology*, *19*(2), 137-141.
- Neil, M. A., Juškaitis, R., & Wilson, T. (1997). Method of obtaining optical sectioning by using structured light in a conventional microscope. *Optics letters*, *22*(24), 1905-1907.

- Nilsson, D. E. (2009). The evolution of eyes and visually guided behaviour. *Philosophical Transactions of the Royal Society of London B: Biological Sciences*, 364(1531), 2833-2847.
- Nilsson, D. E. (2013). Eye evolution and its functional basis. *Visual neuroscience*, 30(1-2), 5-20.
- Nultsch, W., & Häder, D. P. (1979). Photomovement of motile microorganisms. *Photochemistry and Photobiology*, 29(2), 423-437.
- Olivier, N., Luengo-Oroz, M. A., Duloquin, L., Faure, E., Savy, T., Veilleux, I., ... & Peyri ras, N. (2010). Cell lineage reconstruction of early zebrafish embryos using label-free nonlinear microscopy. *Science*, 329(5994), 967-971.
- Orger, M. B., & Baier, H. Channeling of red and green cone inputs to the zebrafish optomotor response. *Visual neuroscience*, 22, 275-281 (2005).
- Orger, M. B. (2016). The Cellular Organization of Zebrafish Visuomotor Circuits. *Current Biology*, 26(9), R377-R385.
- Otero-Millan, J., Troncoso, X. G., Macknik, S. L., Serrano-Pedraza, I., & Martinez-Conde, S. (2008). Saccades and microsaccades during visual fixation, exploration, and search: foundations for a common saccadic generator. *Journal of vision*, 8(14), 21-21.
- Panier, T., Romano, S. A., Olive, R., Pietri, T., Sumbre, G., Candelier, R., & Debr geas, G. (2013). Fast functional imaging of multiple brain regions in intact zebrafish larvae using selective plane illumination microscopy. *Frontiers in neural circuits*, 7.
- Paredes, R. M., Etzler, J. C., Watts, L. T., Zheng, W., & Lechleiter, J. D. (2008). Chemical calcium indicators. *Methods*, 46(3), 143-151.
- Pawley, J. B., & Masters, B. R. (1996). Handbook of biological confocal microscopy. *Optical Engineering*, 35(9), 2765-2766.
- Pearson, K. G. (2004). Generating the walking gait: role of sensory feedback. *Progress in brain research*, 143, 123-129.
- Perkel, D. H., & Mulloney, B. (1974). Motor pattern production in reciprocally inhibitory neurons exhibiting postinhibitory rebound. *Science*, 185(4146), 181-183.
- Phillips, J. O., Ling, L., Fuchs, A. F., Siebold, C., & Plorde, J. J. (1995). Rapid horizontal gaze movement in the monkey. *Journal of Neurophysiology*, 73(4), 1632-1652.

- Phillips, J. O., Ling, L., & Fuchs, A. F. (2001). A comparison of excitatory and inhibitory burst neuron activity during active head-unrestrained gaze shifts. In *Soc Neurosci Abstr* (Vol. 405).
- Piccolino, M. (1998). Animal electricity and the birth of electrophysiology: the legacy of Luigi Galvani. *Brain research bulletin*, *46*(5), 381-407.
- Pierce-Shimomura, J. T., Morse, T. M., & Lockery, S. R. (1999). The fundamental role of pirouettes in *Caenorhabditis elegans* chemotaxis. *Journal of Neuroscience*, *19*(21), 9557-9569.
- Pnevmatikakis, E. A., Soudry, D., Gao, Y., Machado, T. A., Merel, J., Pfau, D., ... & Ahrens, M. (2016). Simultaneous denoising, deconvolution, and demixing of calcium imaging data. *Neuron*, *89*(2), 285-299.
- Porter, J., Craven, B., Khan, R. M., Chang, S. J., Kang, I., Judkewitz, B., ... & Sobel, N. (2007). Mechanisms of scent-tracking in humans. *Nature neuroscience*, *10*(1), 27-29.
- Portugues, R., & Engert, F. (2009). The neural basis of visual behaviors in the larval zebrafish. *Current opinion in neurobiology*, *19*(6), 644-647.
- Portugues, R., Feierstein, C. E., Engert, F., & Orger, M. B. (2014). Whole-brain activity maps reveal stereotyped, distributed networks for visuomotor behavior. *Neuron*, *81*(6), 1328-1343.
- Power, R. M., & Huisken, J. (2017). A guide to light-sheet fluorescence microscopy for multiscale imaging. *Nature Methods*, *14*(4), 360-373.
- Prinz, A. A., Thirumalai, V., & Marder, E. (2003). The functional consequences of changes in the strength and duration of synaptic inputs to oscillatory neurons. *Journal of Neuroscience*, *23*(3), 943-954.
- Prober, D. A., Zimmerman, S., Myers, B. R., McDermott, B. M., Kim, S. H., Caron, S., ... & Schier, A. F. (2008). Zebrafish TRPA1 channels are required for chemosensation but not for thermosensation or mechanosensory hair cell function. *Journal of Neuroscience*, *28*(40), 10102-10110.
- Quaia, C., Lefèvre, P., & Optican, L. M. (1999). Model of the control of saccades by superior colliculus and cerebellum. *Journal of Neurophysiology*, *82*(2), 999-1018.
- Quirin, S., Jackson, J., Peterka, D. S., & Yuste, R. (2014). Simultaneous imaging of neural activity in three dimensions. *Frontiers in neural circuits*, *8*.
- Quiroga, R. Q., Kraskov, A., Kreuz, T., & Grassberger, P. (2002). Performance of different synchronization measures in real data: a case study on electroencephalographic signals. *Physical Review E*, *65*(4), 041903.

- Ramón y Cajal, S. Estructura de los centros nerviosos de las aves. *Rev. Trim. Histol. Norm. Pat.* **1**, 1–10 (1888) (in Spanish).
- Ramot, D., MacInnis, B. L., Lee, H. C., & Goodman, M. B. (2008). Thermotaxis is a robust mechanism for thermoregulation in *Caenorhabditis elegans* nematodes. *Journal of Neuroscience*, *28*(47), 12546-12557.
- Ranade, S., Hangya, B., & Kepecs, A. (2013). Multiple modes of phase locking between sniffing and whisking during active exploration. *Journal of Neuroscience*, *33*(19), 8250-8256.
- Randel, N., & Jékely, G. (2016). Phototaxis and the origin of visual eyes. *Phil. Trans. R. Soc. B*, *371*(1685), 20150042.
- Randlett, O., Wee, C. L., Naumann, E. A., Nnaemeka, O., Schoppik, D., Fitzgerald, J. E., ... & Schier, A. F. (2015). Whole-brain activity mapping onto a zebrafish brain atlas. *Nature methods*, *12*(11), 1039.
- Risner, M. L., Lemerise, E., Vukmanic, E. V., & Moore, A. (2006). Behavioral spectral sensitivity of the zebrafish (*Danio rerio*). *Vision research*, *46*(17), 2625-2635.
- Robinson, D. A. (1964). The mechanics of human saccadic eye movement. *The Journal of physiology*, *174*(2), 245-264.
- Robinson, D. A. (1972). Eye movements evoked by collicular stimulation in the alert monkey. *Vision Res.* *12*, 1795–1808.
- Robinson, D. A. (1975). Oculomotor control signals. *Basic mechanisms of ocular motility and their clinical implication*, 337-374.
- Robinson, D. A. (1989). Integrating with neurons. *Annual review of neuroscience*, *12*(1), 33-45.
- Robinson, F.R. and Fuchs, A.F. (2001). The role of the cerebellum in voluntary eye movements. *Ann. Rev. Neurosci.*, *24*: 981–1004.
- Robson, D. N. (2013). *Thermal navigation in larval zebrafish* (Doctoral dissertation).
- Roenneberg, T., Dragovic, Z., & Merrow, M. (2005). Demasking biological oscillators: properties and principles of entrainment exemplified by the *Neurospora* circadian clock. *Proceedings of the National Academy of Sciences of the United States of America*, *102*(21), 7742-7747.
- Roeser, T., & Baier, H. (2003). Visuomotor behaviors in larval zebrafish after GFP-guided laser ablation of the optic tectum. *Journal of Neuroscience*, *23*(9), 3726-3734.

- Rosenzweig, M., Brennan, K. M., Tayler, T. D., Phelps, P. O., Patapoutian, A., & Garrity, P. A. (2005). The *Drosophila* ortholog of vertebrate TRPA1 regulates thermotaxis. *Genes & development*, *19*(4), 419-424.
- Ryu, W. S., & Samuel, A. D. (2002). Thermotaxis in *Caenorhabditis elegans* analyzed by measuring responses to defined thermal stimuli. *Journal of Neuroscience*, *22*(13), 5727-5733.
- Saito, S., & Shingai, R. (2006). Evolution of thermoTRP ion channel homologs in vertebrates. *Physiological genomics*, *27*(3), 219-230.
- Salome, R., Kremer, Y., Dieudonne, S., Léger, J. F., Krichevsky, O., Wyart, C., ... & Bourdieu, L. (2006). Ultrafast random-access scanning in two-photon microscopy using acousto-optic deflectors. *Journal of neuroscience methods*, *154*(1), 161-174.
- Samuel, A. D., & Sengupta, P. (2005). Sensorimotor integration: locating locomotion in neural circuits. *Current Biology*, *15*(9), R341-R343.
- Santi, P. A. (2011). Light sheet fluorescence microscopy a review. *Journal of Histochemistry & Cytochemistry*, *59*(2), 129-138.
- Sawin, E. P., Harris, L. R., Campos, A. R., & Sokolowski, M. B. (1994). Sensorimotor transformation from light reception to phototactic behavior in *Drosophila* larvae (Diptera: Drosophilidae). *Journal of insect behavior*, *7*(4), 553.
- Schneidman, E., Berry, M. J., II, R. S., & Bialek, W. (2006). Weak pairwise correlations imply strongly correlated network states in a neural population. *Nature*, *440*(7087), 1007.
- Schoonheim, P. J., Arrenberg, A. B., Del Bene, F., & Baier, H. (2010). Optogenetic localization and genetic perturbation of saccade-generating neurons in zebrafish. *Journal of Neuroscience*, *30*(20), 7111-7120.
- Schroeder, C. E., Wilson, D. A., Radman, T., Scharfman, H., & Lakatos, P. (2010). Dynamics of active sensing and perceptual selection. *Current opinion in neurobiology*, *20*(2), 172-176.
- Schwemmer, M. A., & Lewis, T. J. (2012). The theory of weakly coupled oscillators. In *Phase response curves in neuroscience* (pp. 3-31). Springer New York.
- Schwickert, T. A., Lindquist, R. L., Shakhar, G., Livshits, G., Skokos, D., Kosco-Vilbois, M. H., ... & Nussenzweig, M. C. (2007). In vivo imaging of germinal centres reveals a dynamic open structure. *Nature*, *446*(7131), 83.
- Scudder CA, Moschovakis AK, Karabelas AB, and Highstein SM. (1996). Anatomy and physiology of saccadic long-lead burst neurons recorded in the alert squirrel monkey. II. Pontine neurons. *J Neurophysiol* 76: 353–370.

- Scudder, C. A. (1988). A new local feedback model of the saccadic burst generator. *Journal of Neurophysiology*, 59(5), 1455-1475.
- Scudder, C. A., Kaneko, C. S. and Fuchs, A. F. (2002). The brainstem burst generator for saccadic eye movements: a modern synthesis. *Exp Brain Res*, 142, 439–462.
- Scudder, C. A., & McGee, D. M. (2003). Adaptive modification of saccade size produces correlated changes in the discharges of fastigial nucleus neurons. *Journal of Neurophysiology*, 90(2), 1011-1026.
- Serra, E. L., Medalha, C. C., & Mattioli, R. (1999). Natural preference of zebrafish (*Danio rerio*) for a dark environment. *Brazilian journal of medical and biological research*, 32(12), 1551-1553.
- Seung, H. S. (1996). How the brain keeps the eyes still. *Proceedings of the National Academy of Sciences*, 93(23), 13339-13344.
- Seung, H. S., Lee, D. D., Reis, B. Y., & Tank, D. W. (2000). Stability of the memory of eye position in a recurrent network of conductance-based model neurons. *Neuron*, 26(1), 259-271.
- Scharf, B., & Wolff, E. K. (1994). Phototactic behaviour of the archaebacterial *Natronobacterium pharaonis*. *FEBS letters*, 340(1-2), 114-116.
- Sharp AA, O’Neil MB, Abbott LF, Marder E. (1993) The dynamic clamp: artificial conductances in biological neurons. *Trends Neurosci.* 16:389–94
- Sharp, A. A., Skinner, F. K., & Marder, E. (1996). Mechanisms of oscillation in dynamic clamp constructed two-cell half-center circuits. *Journal of neurophysiology*, 76(2), 867-883.
- Shen, C. H. (2015). *Dynamics of Neural Activity During Chemotaxis in Caenorhabditis Elegans* (Doctoral dissertation).
- Sheppard, C. J. R., & Kompfner, R. (1978). Resonant scanning optical microscope. *Applied optics*, 17(18), 2879-2882.
- Sheppard, C., Gannaway, J., Kompfner, R., & Walsh, D. (1977). The scanning harmonic optical microscope. *IEEE Journal of Quantum electronics*, 13(9), 912-912.
- Sherrington, C. S. (1906). Observations on the scratch-reflex in the spinal dog. *The Journal of physiology*, 34(1-2), 1.
- Shimomura, O., Johnson, F. H., & Saiga, Y. (1962). Extraction, purification and properties of aequorin, a bioluminescent protein from the luminous hydromedusa, *Aequorea*. *Journal of Cellular Physiology*, 59(3), 223-239.

- Siedentopf, H., & Zsigmondy, R. (1902). Visualisation and determination of size of ultra microscopic particles, with special use of Goldrubin glasses. *Annalen Der Physik*, 10(1), 1-39.
- Siegel, M. S., & Isacoff, E. Y. (1997). A genetically encoded optical probe of membrane voltage. *Neuron*, 19(4), 735-741.
- Skinner, F. K., Kopell, N., & Marder, E. (1994). Mechanisms for oscillation and frequency control in reciprocally inhibitory model neural networks. *Journal of computational neuroscience*, 1(1-2), 69-87.
- Smith JC, Ellenberger HH, Ballanyi K, Richter DW, Feldman JL. (1991). Pre-Bötzinger complex: a brainstem region that may generate respiratory rhythm in mammals. *Science*, 254:726-729.
- Soetedjo, R., Kaneko, C. R., & Fuchs, A. F. (2002). Evidence that the superior colliculus participates in the feedback control of saccadic eye movements. *Journal of neurophysiology*, 87(2), 679-695.
- Sparks, D. L. (2002). The brainstem control of saccadic eye movements. *Nature reviews. Neuroscience*, 3(12), 952.
- Sparks, D. L. & Hartwich-Young, R. in *The Neurobiology of Saccadic Eye Movements* (eds Wurtz, R. H. & Goldberg, M. E.) 213–255. *Elsevier, Amsterdam* (1989).
- Spence, D. E., Kean, P. N., & Sibbett, W. (1991). 60-fsec pulse generation from a self-mode-locked Ti: sapphire laser. *Optics letters*, 16(1), 42-44.
- Spudich, J. L. (2006). The multitasking microbial sensory rhodopsins. *Trends in microbiology*, 14(11), 480-487.
- Squirrell, J. M., Wokosin, D. L., White, J. G., & Bavister, B. D. (1999). Long-term two-photon fluorescence imaging of mammalian embryos without compromising viability. *Nature biotechnology*, 17(8), 763.
- Stelzer, E. H. (2015). Light-sheet fluorescence microscopy for quantitative biology. *Nature methods*, 12(1), 23-28.
- Stelzer, E. H. K., Lindek, S., Albrecht, S., Pick, R., Ritter, G., Salmon, N. J., & Stricker, R. (1995). A new tool for the observation of embryos and other large specimens: confocal theta fluorescence microscopy. *Journal of microscopy*, 179(1), 1-10.
- Stewart, A. M., Braubach, O., Spitsbergen, J., Gerlai, R., & Kalueff, A. V. (2014). Zebrafish models for translational neuroscience research: from tank to bedside. *Trends in neurosciences*, 37(5), 264-278.
- Stokes, G. G. (1852). On the change of refrangibility of light. *Philosophical Transactions of the Royal Society of London*, 142, 463-562.

- Strassman, A., Highstein, S. M. & McCrea, R. A. (1986). Anatomy and physiology of saccadic burst neurons in the alert squirrel monkey. I. Excitatory burst neurons. *J. Comp. Neurol.* 249, 337–357.
- Suzuki, H., Thiele, T. R., Faumont, S., Ezcurra, M., Lockery, S. R., & Schafer, W. R. (2008). Functional asymmetry in *C. elegans* taste neurons and its computational role in chemotaxis. *Nature*, 454(7200), 114.
- Svoboda, K., & Yasuda, R. (2006). Principles of two-photon excitation microscopy and its applications to neuroscience. *Neuron*, 50(6), 823-839.
- Svoboda, K., Tank, D. W., & Denk, W. (1996). Direct measurement of coupling between dendritic spines and shafts. *Science*, 272(5262), 716.
- Tastekin, I., Riedl, J., Schilling-Kurz, V., Gomez-Marin, A., Truman, J. W., & Louis, M. (2015). Role of the subesophageal zone in sensorimotor control of orientation in *Drosophila* larva. *Current Biology*, 25(11), 1448-1460.
- Terrien, J., Perret, M., & Aujard, F. (2011). Behavioral thermoregulation in mammals: a review. *Front Biosci*, 16, 1428-1444.
- Tian, L., Hires, S. A., Mao, T., Huber, D., Chiappe, M. E., Chalasani, S. H., ... & Bargmann, C. I. (2009). Imaging neural activity in worms, flies and mice with improved GCaMP calcium indicators. *Nature methods*, 6(12), 875-881.
- Togashi, T., & Cox, P. A. (2004). Phototaxis and the evolution of isogamy and 'slight anisogamy' in marine green algae: insights from laboratory observations and numerical experiments. *Botanical Journal of the Linnean Society*, 144(3), 321-327.
- Tokunaga, M., Imamoto, N., & Sakata-Sogawa, K. (2008). Highly inclined thin illumination enables clear single-molecule imaging in cells. *Nature methods*, 5(2), 159-161.
- Tomer, R., Khairy, K., Amat, F., & Keller, P. J. (2012). Quantitative high-speed imaging of entire developing embryos with simultaneous multiview light-sheet microscopy. *Nature methods*, 9(7), 755-763.
- Trachtenberg, J. T., Chen, B. E., Knott, G. W., Feng, G., Sanes, J. R., Welker, E., & Svoboda, K. (2002). Long-term in vivo imaging of experience-dependent synaptic plasticity in adult cortex. *Nature*, 420(6917), 788-794.
- Truong, T. V., Supatto, W., Koos, D. S., Choi, J. M., & Fraser, S. E. (2011). Deep and fast live imaging with two-photon scanned light-sheet microscopy. *Nature methods*, 8(9), 757-760.
- Tsien, R. Y. (1980). New calcium indicators and buffers with high selectivity against magnesium and protons: design, synthesis, and properties of prototype structures. *Biochemistry*, 19(11), 2396-2404.

- Tsien, R. Y., Pozzan, T., & Rink, T. J. (1982). Calcium homeostasis in intact lymphocytes: cytoplasmic free calcium monitored with a new, intracellularly trapped fluorescent indicator. *The Journal of Cell Biology*, *94*(2), 325-334.
- Tsien, R. Y. (1998). The green fluorescent protein. *Annual review of biochemistry*, *67*(1), 509-544.
- Tu, Y. (2013). Quantitative modeling of bacterial chemotaxis: signal amplification and accurate adaptation. *Annual review of biophysics*, *42*, 337-359.
- Turaga, D., & Holy, T. E. (2008). Miniaturization and defocus correction for objective-coupled planar illumination microscopy. *Optics letters*, *33*(20), 2302-2304.
- Valdmanis, J., & Fork, R. (1986). Design considerations for a femtosecond pulse laser balancing self phase modulation, group velocity dispersion, saturable absorption, and saturable gain. *IEEE journal of quantum electronics*, *22*(1), 112-118.
- Van Gisbergen, J. A. M., Van Opstal, A. J., & Tax, A. A. M. (1987). Collicular ensemble coding of saccades based on vector summation. *Neuroscience*, *21*(2), 541-555.
- Vattikuti, S., Thangaraj, P., Xie, H. W., Gotts, S. J., Martin, A., & Chow, C. C. (2016). Canonical Cortical Circuit Model Explains Rivalry, Intermittent Rivalry, and Rivalry Memory. *PLoS computational biology*, *12*(5), e1004903.
- Vergassola, M., Villermaux, E., & Shraiman, B. I. (2007). 'Infotaxis' as a strategy for searching without gradients. *Nature*, *445*(7126), 406-409.
- Vladimirov, N., Mu, Y., Kawashima, T., Bennett, D. V., Yang, C. T., Looger, L. L., ... & Ahrens, M. B. (2014). Light-sheet functional imaging in fictively behaving zebrafish. *Nature methods*.
- Vogelstein, J. T., Watson, B. O., Packer, A. M., Yuste, R., Jedynak, B., & Paninski, L. (2009). Spike inference from calcium imaging using sequential Monte Carlo methods. *Biophysical journal*, *97*(2), 636-655.
- Vogelstein, J. T., Packer, A. M., Machado, T. A., Sippy, T., Babadi, B., Yuste, R., & Paninski, L. (2010). Fast nonnegative deconvolution for spike train inference from population calcium imaging. *Journal of neurophysiology*, *104*(6), 3691-3704.
- Voie AH, Burns DH, Spelman FA. 1993. Orthogonal-plane fluorescence optical sectioning: three dimensional imaging of macroscopic biological specimens. *J Microsc*. 170:229-236.
- Voie AH. 1996. Three-dimensional reconstruction and quantitative analysis of

- the mammalian cochlea [dissertation]. [Seattle (WA)]: University of Washington.
- Voie, A. H. (2002). Imaging the intact guinea pig tympanic bulla by orthogonal-plane fluorescence optical sectioning microscopy. *Hearing research*, *171*(1), 119-128.
- Voie, A. H., & Spelman, F. A. (1995). Three-dimensional reconstruction of the cochlea from two-dimensional images of optical sections. *Computerized medical imaging and graphics*, *19*(5), 377-384.
- Wadhams, G. H., & Armitage, J. P. (2004). Making sense of it all: bacterial chemotaxis. *Nature reviews. Molecular cell biology*, *5*(12), 1024.
- Waitzman, D. M., Ma, T. P., Optican, L. M., & Wurtz, R. H. (1991). Superior colliculus neurons mediate the dynamic characteristics of saccades. *Journal of Neurophysiology*, *66*(5), 1716-1737.
- Waitzman, D. M., Silakov, V. L., DePalma-Bowles, S., & Ayers, A. S. (2000). Effects of reversible inactivation of the primate mesencephalic reticular formation. I. Hypermetric goal-directed saccades. *Journal of Neurophysiology*, *83*(4), 2260-2284.
- Wang, X. J., & Rinzel, J. (1992). Alternating and synchronous rhythms in reciprocally inhibitory model neurons. *Neural computation*, *4*(1), 84-97.
- Ward, A. (2010). *Phototaxis and phototransduction mechanisms in the model system C. elegans* (Doctoral dissertation, University of Michigan).
- Ward, A., Liu, J., Feng, Z., & Xu, X. S. (2008). Light-sensitive neurons and channels mediate phototaxis in *C. elegans*. *Nature neuroscience*, *11*(8), 916-922.
- Winfree, A. T. (1967). Biological rhythms and the behavior of populations of coupled oscillators. *Journal of theoretical biology*, *16*(1), 15-42.
- Witman, G. B. (1993). *Chlamydomonas* phototaxis. *Trends in cell biology*, *3*(11), 403-408.
- Wolf, S., Supatto, W., Debrégeas, G., Mahou, P., Kruglik, S. G., Sintes, J. M., Candelier, R. (2015). Whole-brain functional imaging with two-photon light-sheet microscopy. *Nature methods*, *12*(5), 379-380.
- Xiang, Y., Yuan, Q., Vogt, N., Looger, L. L., Jan, L. Y., & Jan, Y. N. (2010). Light-avoidance-mediating photoreceptors tile the *Drosophila* larval body wall. *Nature*, *468*(7326), 921.
- Yang, Z., Mei, L., Xia, F., Luo, Q., Fu, L., & Gong, H. (2015). Dual-slit confocal light sheet microscopy for in vivo whole-brain imaging of zebrafish. *Biomedical optics express*, *6*(5), 1797-1811.

- Ying, J., Liu, F., & Alfano, R. R. (1999). Spatial distribution of two-photon-excited fluorescence in scattering media. *Applied optics*, *38*(1), 224-229.
- Yuste, R. (2015). From the neuron doctrine to neural networks. *Nature Reviews Neuroscience*, *16*(8), 487-497.
- Yuste, R., & Denk, W. (1995). Dendritic spines as basic functional units of neuronal integration. *Nature*, *375*(6533), 682.
- Zernike, F. (1942). Phase contrast, a new method for the microscopic observation of transparent objects. *Physica*, *9*(7), 686-698.
- Zhang, B. B., Yao, Y. Y., Zhang, H. F., Kawakami, K., & Du, J. L. (2017). Left habenula mediates light-preference behavior in zebrafish via an asymmetrical visual pathway. *Neuron*, *93*(4), 914-928.
- Zhang, C., & Lewis, T. J. (2013). Phase response properties of half-center oscillators. *Journal of computational neuroscience*, *35*(1), 55-74.
- Zipfel, W. R., Williams, R. M., & Webb, W. W. (2003). Nonlinear magic: multiphoton microscopy in the biosciences. *Nature biotechnology*, *21*(11), 1369-1377.

REFERENCES

Annex 1

Tubiana, J., Wolf, S., & Debregeas, G. (2017). Blind sparse deconvolution for inferring spike trains from fluorescence recordings. *bioRxiv*, 156364.

Blind sparse deconvolution for inferring spike trains from fluorescence recordings

Jérôme Tubiana,^{1,*} Sébastien Wolf,^{2,3} and Georges Debregeas^{2,3}

¹*Laboratoire de Physique Théorique, Ecole Normale Supérieure and CNRS,
PSL Research, Sorbonne Universités UPMC, 24 rue Lhomond, 75005 Paris, France*

²*Sorbonne Universités, UPMC Univ. Paris 06, UMR 8237, Laboratoire Jean Perrin, F-75005 Paris, France*

³*CNRS UMR 8237, Laboratoire Jean Perrin, F-75005 Paris, France*

(Dated: June 27, 2017)

The parallel developments of genetically-encoded calcium indicators and fast fluorescence imaging techniques *in vivo*, opening a new arena for systems neuroscience. To fully harness the potential of functional imaging, one needs to infer the sequence of action potentials from fluorescence time traces. Here we build on recently proposed computational approaches to develop a blind sparse deconvolution algorithm (BSD), which we motivate by a theoretical analysis. We demonstrate that this method outperforms existing sparse deconvolution algorithms in terms of robustness, speed and/or accuracy on both synthetic and real fluorescence data. Furthermore, we provide solutions for the practical problems of thresholding and determination of the rise and decay time constants. We provide theoretical bounds on the performance of the algorithm in terms of precision-recall and temporal accuracy. Finally, we extend the computational framework to support temporal super-resolution whose performance is established on real data.

Introduction

In the last two decades, functional calcium imaging has emerged as a popular method for recording brain activity *in vivo*. This technique relies on calcium sensors, either synthetic or genetically expressed, that are designed to optically report the transient rise in intra-cellular calcium concentration that accompany spiking events. Calcium imaging offers several assets in comparison with standard electrophysiology methods: it is non-invasive, it allows monitoring extended neuronal networks (up to a few tens of thousands of units), and it can be combined with genetic methods in order to target specific neuronal populations.

The main limitation of calcium imaging is that it only provides a proxy measure of the neuronal activity. The kinetics of the calcium/reporter complexation being relatively slow, the spike-evoked fluorescence transients last much longer (0.1-1s) than the action potential itself (<5ms). As the fluorescence signal is generally noisy and/or weakly sampled, its interpretation heavily relies on deconvolution methods to infer approximated spike trains. With the rapid increase in data-throughput offered by current fast imaging techniques, these methods need to be fast and unsupervised, as any manual check of the produced inference signals would prove impractical.

Standard inference methods are based on a generative model, which describes the relationship between a spike train and the resulting fluorescence time trace. It reads:

$$F_i \equiv F(t_i) = a \int K(\tau) N(t_i - \tau) d\tau + b + \epsilon_i \quad (1)$$

where $t_i = i\Delta t$ is the time of measurement, $N(t) = \sum_j \delta_{t,t_j}$ denotes the spike train, b is the baseline fluorescence (spikeless signal), and ϵ_i is a discrete gaussian white noise: $\langle \epsilon_i \rangle = 0$, $\langle \epsilon_i \epsilon_j \rangle = \sigma^2 \delta_{i,j}$. The convolution kernel $K(t)$, which reflects the complexation kinetics, is of the form:

$$K(t) \propto (e^{-\frac{t}{\tau_d}} - e^{-\frac{t}{\tau_r}}) \mathbb{1}_{t \geq 0} \quad (2)$$

where the rise and decay time constants τ_r, τ_d – typically in the range of 10-100ms and 50-1000ms, respectively – mostly depend on the calcium indicator but can also vary with the targeted neuron. In the following, we normalize K such that $\max(K) = 1$, hence each spike produces a transient of maximum height a . The signal to noise ratio (SNR) is thus defined as $\text{SNR} = \frac{a}{\sigma}$. The noise stems from fluctuations of intra-cellular chemical concentration, light source and

*Electronic address: jerome.tubiana@ens.fr

Annex 2

Olive, R., Wolf, S., Dubreuil, A., Bormuth, V., Debrégeas, G., & Candelier, R. (2016). Rheotaxis of larval zebrafish: behavioral study of a multi-sensory process. *Frontiers in systems neuroscience*, *10*.



Rheotaxis of Larval Zebrafish: Behavioral Study of a Multi-Sensory Process

Raphaël Olive, Sébastien Wolf, Alexis Dubreuil, Volker Bormuth, Georges Debrégeas and Raphaël Candelier*

Laboratoire Jean Perrin, Université Pierre et Marie Curie, Sorbonne Universités, Centre National de la Recherche Scientifique 8237, Paris, France

Awake animals unceasingly perceive sensory inputs with great variability of nature and intensity, and understanding how the nervous system manages this continuous flow of diverse information to get a coherent representation of the environment is arguably a central question in systems neuroscience. Rheotaxis, the ability shared by most aquatic species to orient toward a current and swim to hold position, is an innate and robust multi-sensory behavior that is known to involve the lateral line and visual systems. To facilitate the neuroethological study of rheotactic behavior in larval zebrafish we developed an assay for freely swimming larvae that allows for high experimental throughput, large statistic and a fine description of the behavior. We show that there exist a clear transition from exploration to counterflow swim, and by changing the sensory modalities accessible to the fishes (visual only, lateral line only or both) and comparing the swim patterns at different ages we were able to detect and characterize two different mechanisms for position holding, one mediated by the lateral line and one mediated by the visual system. We also found that when both sensory modalities are accessible the visual system overshadows the lateral line, suggesting that at the larval stage the sensory inputs are not merged to finely tune the behavior but that redundant information pathways may be used as functional fallbacks.

Keywords: zebrafish, rheotaxis, behavior, vision, lateral line, multi-sensory integration

OPEN ACCESS

Edited by:

Mikhail Lebedev,
Duke University, USA

Reviewed by:

Hernan Lopez-Schier,
Helmholtz Zentrum Munchen,
Germany

Logan Ganzen,
Purdue University, USA

*Correspondence:

Raphaël Candelier
raphael.candelier@upmc.fr

Received: 24 December 2015

Accepted: 08 February 2016

Published: 23 February 2016

Citation:

Olive R, Wolf S, Dubreuil A, Bormuth V, Debrégeas G and Candelier R (2016) Rheotaxis of Larval Zebrafish: Behavioral Study of a Multi-Sensory Process. *Front. Syst. Neurosci.* 10:14. doi: 10.3389/fnsys.2016.00014

1. INTRODUCTION

Positive rheotaxis is the innate behavior shared by most fishes and amphibians to turn to face into an oncoming current, and hold position with minimum expenditure of energy (Arnold and Weihs, 1977). Its widespread nature and the fact that it imposes to manage many sensory cues of different nature (visual, vestibular, hydromechanical, proprioceptive) that are available to the animal makes the generic neuronal processes at play of great interest from a fundamental perspective.

The term *rheotaxis* actually encompasses two distinct behavioral phases, namely orientation of the body along stream lines and counterflow swim to hold position. Position holding is often considered to rely on the sole visual system and in particular on the so-called optomotor reflex (Orger et al., 2000, 2008; Portugues and Engert, 2009). Regarding body orientation, it has been considered for a long time that it could not originate from hydromechanical cues based on the false assumption that when a fish is carried away in a stream there is no relative motion between the fish and its surrounding medium (Lyon, 1904; Arnold, 1974). In real situations there are always

ABSTRACT

The first part of this thesis presents an historical overview of neural recording techniques, followed by a study on the development of a new imaging method for zebrafish neural recording: two-photon light sheet microscopy. Combining the advantages of two-photon point scanning microscopy and light sheet techniques, the two-photon light sheet microscope warrants a high acquisition speed with low photodamage and allows to circumvent the main limitation of one-photon light sheet microscopy: the disturbance of the visual system. The second part of the thesis is focused on goal-directed navigation in zebrafish larvae. After an exhaustive review on chemotaxis, phototaxis and thigmotaxis in various animal models, we report a study that reveals the neural computation underlying phototaxis in zebrafish. Combining virtual-reality behavioral assays, volumetric calcium recordings, optogenetic stimulation, and circuit modeling, this work shows that a self-oscillating hindbrain population called the hindbrain oscillator (HBO) acts as a pacemaker for ocular saccades, controls the orientation of successive swim-bouts during zebrafish larva navigation, and is responsive to light in a state-dependent manner such that its response to visual inputs varies with the motor context. This peculiar response to visual inputs biases the fish trajectory towards brighter regions (phototaxis). The third part provides a discussion on the neural basis of ocular saccades in vertebrates. We conclude with some recent preliminary results on heat perception in zebrafish suggesting that the same hindbrain circuit may be at play in thigmotaxis as well.

Keywords: calcium imaging – light-sheet – zebrafish – phototaxis – saccadic system – hindbrain – central pattern generator

Bases neuronales de la navigation dirigée chez le poisson zèbre et imagerie par nappe laser 2 photons de l'activité neuronale.

RESUMÉ

La première partie de cette thèse présente une revue historique sur les méthodes d'enregistrements d'activité neuronale, suivie par une étude sur une nouvelle technique d'imagerie pour le poisson zèbre : la microscopie par nappe laser 2 photon. En combinant, les avantages de la microscopie 2 photon et l'imagerie par nappe de lumière, le microscope par nappe laser 2 photon garantie des enregistrements à haute vitesse avec un faible taux de lésions photoniques et permet d'éviter l'une des principales limitations du microscope à nappe laser 1 photon: la perturbation du système visuel. La deuxième partie de cette thèse traite de la navigation dirigée. Après une revue exhaustive sur la chemotaxis, la phototaxis et la thigmotaxis, nous présentons des résultats qui révèlent les bases neuronales de la phototaxis chez le poisson zèbre. Grâce à des expériences de comportement en réalité-virtuelle, des enregistrements d'activité neuronale, des méthodes optogénétiques et des approches théoriques, ce travail montre qu'une population auto-oscillante située dans le rhombencéphale appelée l'oscillateur du cerveau postérieur (HBO) fonctionne comme un pacemaker des saccades oculaires et contrôle l'orientation des mouvements de nage du poisson zèbre. Ce HBO répond à la lumière en fonction du contexte moteur, biaisant ainsi la trajectoire du poisson zèbre vers les zones les plus lumineuses de son environnement (phototaxis). La troisième partie propose une discussion sur les bases neuronales des saccades oculaires chez les vertébrés. Nous concluons ce manuscrit avec des résultats préliminaires suggérant que chez le poisson zèbre, le même HBO est impliqué dans les processus de thigmotaxis.

Mots clefs: imagerie calcique – nappe laser – poisson-zèbre – phototaxis – système saccadique – cerveau postérieur – central pattern generator

